Characterizing Eclipsing Binaries and the Population of Planets Orbiting Around Them

Diana K. Windemuth

A dissertation
submitted in partial fulfillment of the
requirements for the degree of

Doctor of Philosophy

University of Washington

2020

Reading Committee:

Eric Agol, Chair

Rory Barnes

Tom Quinn

Program Authorized to Offer Degree:
Astronomy

University of Washington

Abstract

Characterizing Eclipsing Binaries and the Population of Planets Orbiting Around Them

Diana K. Windemuth

Chair of the Supervisory Committee:
Professor Eric Agol
Department of Astronomy

The majority of main sequence (MS) and pre-MS (PMS) stars reside in binaries or hierarchical multiples (Abt, 1979; Duchêne & Kraus, 2013). Understanding planetary processes and regimes of habitability in a general framework requires statistical studies of planets around all modes of stellar multiplicity. This thesis aims to constrain the demographics of planets orbiting binary stars (circumbinary planets; CBPs), using an independent, automated detection pipeline analysis. To do this, I exploit high cadence & high precision photometry and the transiting geometry to measure physical properties of eclipsing binaries (EBs) and detect CBPs around them. In particular, I create a modular eclipsing binary modeling code which leverages stellar evolution models with time-series, multi-band, and positional photometry to extract full system parameters, including stellar mass. This technique enables mass estimation for large ensembles of EBs, accurate to within 10% for detached MS systems, and I apply it to assemble a Bayesian catalogue of 728 fully characterized *Kepler* EBs. Next, I develop a hybrid transit detection method that is robust to large transit timing and duration variations associated with transiting CBPs. It corrects for large scale variations induced by binary reflex motion using a physical CBP model, and subsequently employs the Quasi-periodic Automated Transit Search algorithm (QATS; Carter & Agol, 2013) to empirically treat additional aperiodicities, due to model inaccuracies and assumptions. This dual accounting for quasi-periodicity improves CBP detection significance, by greater than a factor of 2 from previous efforts. Finally, I apply a CBP transit search on the *Kepler* EB subsample with full system solutions, and detect 8 robust candidates (corresponding to previously by-eye discovered CBPs) and 4 marginal candidates. Reconciling the detected CBP candidates with a thorough audit of detection and selection biases, I infer population-level trends for CBPs and contextualize my findings with complementary detection results, formation theories, as well as important directions for the future.

TABLE OF CONTENTS

Page

LIST OF FIGURES

Figure Number Page

LIST OF TABLES

ACKNOWLEDGMENTS

So many people and communities have lifted me throughout these years.

Thank you to the UW astro grads, you've been wonderful classmates, colleagues, friends, karaoke companions, and foosball partners. Special thanks to my cohort partner Grace Telford, B329 dream team inhabitants Nell Byler and Phoebe Upton Sanderbeck, and fellow ol' fogies Hannah Bish, Nicole Sanchez, and Trevor Dorn-Wallenstein – your wisdom, support, and friendship have been an endless source of inspiration. Thank you to GCAP and its members, brilliant scientists and humans who have enveloped me with a deep sense of belonging.

Thank you to the greater UW astronomy and astrobiology community, undergrads, grads, post docs, research scientists, faculty, and staff. It was a privilege to learn and work alongside you. A special thank you to Vikki Meadows for your advice, support, and advocacy.

To Katie Brennan, Marta Wolfshorndl, and Oriana Chegwidden, thank you. You've made the impossible possible – making zoom calls during the pandemic energizing.

Thank you to Cecilia Bitz and Miguel Morales, for serving as my AB rep and GSR; and to Rory Barnes and Tom Quinn, for serving on my reading committee and providing critical feedback.

To my advisor, Eric Agol, thank you so much for your mentorship and support. You're an amazing scientist and one of the kindest people I know.

Finally, thank you to my family, near and far. Your love and support mean everything and shape the person I am.

DEDICATION

To Obi and Evie

Chapter 1

INTRODUCTION

"Double, double toil and trouble" – Shakespeare, *Macbeth*

Understanding planet formation processes and identifying habitable environments and extraterrestrial biosignatures are major drivers in exoplanetary science and astrobiology[1]. Thus far, the focus has been on the discovery, demographics, and characterization of planets around single stellar hosts. The majority of main sequence (MS) and pre-MS (PMS) stars, however, reside in binaries or hierarchical multiples (Abt, 1979; Duquennoy et al., 1991; Duchêne & Kraus, 2013; Moe & Di Stefano, 2017). Therefore, understanding planetary processes and regimes of habitability in a general framework requires statistical studies of planets around all modes of stellar multiplicity.

The goal of this dissertation work is to build upon previous bodies of knowledge to bridge the gap between the demographics of planets orbiting around single stars (circumstellar; CS) and those around binary stars (circumbinary; CB). In particular, I exploit high cadence & high precision photometry and the transiting geometry – the fortuitous alignment of three bodies – to measure physical properties of binary stars that pass in front of one another, and to search for planets orbiting the center of mass of close binaries that pass in front of their stellar hosts. These studies facilitate a statistical analysis of the limits and occurrence rate of circumbinary planets (CBPs).

The transit technique is powerful because periodic changes to the integrated light of stars allows us to infer physical information about the target systems. Notably, the *Kepler* mission has served as a powerhouse for detecting transiting exoplanets, with ∼2300 confirmed

---

[1] https://astrobiology.nasa.gov/news/exoplanet-science-strategy/; accessed June 18, 2020

planets[2] at the time of this writing comprising >50% of the total confirmed planet count. In doing so, it has revolutionized our understanding of the diversity (e.g., Pierrehumbert, 2013; Jontof-Hutter et al., 2016), occurrence (e.g., Petigura et al., 2013; Batalha, 2014; Foreman-Mackey et al., 2014; Burke et al., 2015), and system architecture (e.g., Dawson, 2014; Steffen & Coughlin, 2016; Ballard & Johnson, 2016) of planets around single stars. These observational properties directly constrain, and in some cases, confound, circumstellar planet (CSP) formation and evolution models (see review by Winn & Fabrycky, 2015).

For example, there is an observed "radius desert" of close-in *Kepler* CS planets at 1.5-2$R_\oplus$, which persists even after completeness corrections (Fulton et al., 2017) and occupies the transition between rocky (super-Earth) and gaseous (sub-Neptune) planet regimes (Weiss & Marcy, 2014; Rogers, 2015; Wolfgang & Lopez, 2015; Chen & Kipping, 2017). Some physical process during formation or evolution sculpted this radius gap – perhaps photoevapouration of atmospheres due to high stellar irradiation (Owen & Wu, 2013; Jin et al., 2014; Lopez & Fortney, 2014; Chen & Rogers, 2016), preferential formation of super-Earths in gas-depleted disks (Lee & Chiang, 2016; Lopez & Rice, 2018), or atmospheric loss driven by planetary core accretion and cooling (Liu et al., 2015; Ginzburg et al., 2018). Moreover, the presence of compact, short-period multi-planet systems around single stars discovered in the *Kepler* data motivated the "inside-out" formation theory (Chatterjee & Tan, 2014). In this scenario, planets are sequentially formed out of rings of pebbles that collect at pressure maxima associated with the boundary of transition in disk viscosity, which moves outward successively.

A large, diverse sample of several thousand confirmed and candidate exoplanets has enabled multiple, independent studies on CSP population demographics and nuanced constraints on formation theories. These demographics also directly inform observational strategies to characterize habitable planets and to remote sense biosignatures, which are two primary objectives in astrobiology.

---

[2] https://exoplanetarchive.ipac.caltech.edu/docs/counts_detail.html; accessed June 17, 2020

Although there exists a rich literature in CBP observations and theory, compared to CSP counterparts, the landscape of CBP demographics is more uncertain, due to the small sample of discoveries. The majority of unambiguous detections are transiting systems detected by eye, which frustrates completeness corrections that are crucial for robust population-level analysis.

The remarkable discoveries and unambiguous detections of a dozen transiting circumbinary planets[3] demonstrate that planet formation in these environments is effective. An *apparent* trend emerges, revealing the bulk of detected CBPs as co-planar gas giants parked just outside the dynamical instability region of binaries with orbital periods in the 7-40 d range. Disentangling observational biases from physical trends is challenging as it is difficult to quantify "by eye" detection efficiency. Instead, efficiency estimation requires automated detection schemes.

Designing automated detection schemes for transiting CBPs is hard, as their transits may be strongly irregular, owing to dynamical and geometric effects associated with three body systems with large mass ratios. The geometric effect refers to reflex motion of the binary about the barycenter that may cause the transits to be no longer periodic and the relative planet-star velocity to vary for each transit (Agol et al., 2005). These effects, called transit timing variations (TTVs) and transit duration variations (TDVs), are well known in multi-planet systems around single stars. However, planet-induced TTVs and TDVs are *much* smaller than those in CBP systems. The former is typically tens of minutes to a few hours (e.g., Kepler-9 b&c; Holman et al., 2010), while the latter can on the order of days (e.g., Kepler-16b; Doyle et al., 2011). TTVs and TDVs may be especially large for CBPs around equal mass binaries, in which the barycenter is strongly offset from the primary. Additionally, the orbits of CBPs precess due to binary torque, causing a planet's inclination

---

[3] The 11 published *Kepler* CBPs are: Kep-16*b* (Doyle et al., 2011); Kep-34*b* & Kep-35*b* (Welsh et al., 2012); Kep-38*b* (Orosz et al., 2012b); PH1/Kep-64*b* (Schwamb et al., 2013; Kostov et al., 2013); Kep-47*b*, *c*, and *d* (Orosz et al., 2012a; Kostov et al., 2013; Hinse et al., 2015; Welsh et al., 2015a; Orosz et al., 2019); Kep-413*b* (Kostov et al., 2014); Kep-453*b* (Welsh et al., 2015b); Kep-1647*b* (Kostov et al., 2016); 12th system, KIC 10753734 has been reported but not yet published (Orosz et al., 2016). Recently, the first *TESS* CBP was discovered: TOI-1338 (Kostov et al., 2020).

relative to the observer to vary at the precession period (Farago & Laskar, 2010; Martin & Triaud, 2015; Li et al., 2016). These inclination variations induce additional variations in transit shape and timing, and lead to transits disappearing and reappearing over time. An optimized CBP transit search and analysis must therefore take these effects into account.

Using an automated approach, Armstrong et al. (2014b) pioneered a statistical analysis of the occurrence rate of CBPs and estimated that the frequency of gas giants with $P < 300$ d in *Kepler* CB systems, if preferentially co-planar, is ∼10%, consistent with those around single stars; however, their analysis was limited and insensitive to planets $<4\mathrm{R}_{\oplus}$. Klagyivik et al. (2017) systematically searched for transiting CBPs in *CoRoT* data and placed upper limits on the frequency of giant CBPs around $P < 10$ d binaries based on a null result, citing that they are more rare than CS hot Jupiters. Additional CBP demographic studies use the "by eye" *Kepler* discoveries as the base sample to study CBP system architecture (Li et al., 2016; Martin & Triaud, 2016) and their binary stellar host properties, such as binary period (Hamers et al., 2016; Muñoz & Lai, 2015; Martin et al., 2015; Fleming et al., 2018) and mass (Martin, 2019).

Here, I build upon these previous efforts to infer the population statistics of *Kepler* CBPs under a homogeneous and well-quantified detection scheme. Specifically, I characterize 728 *Kepler* EBs to create a catalogue of full stellar and orbital solutions. I then apply an automated and sensitive search for transiting CBPs, which accounts for large-scale, binary-induced TTVs. I use the search results and combine tests of pipeline completeness with analytic, time-dependent transit probabilities to infer CBP population statistics. Below (Chapter 1.1), I provide a more detailed outline for this thesis work.

1.1 Outline of This Thesis

The remainder of my thesis is organized as follows. In Chapter 1.2, I give a brief overview of planets around binaries in general, to better contextualize this work, which focuses on circumbinary planets around close binaries. It examines planet formation and occurrence in binary systems through the lens of binary separation, and is heavily drawn from the work of

Duchêne (2010). Then, in Chapter 1.3, I motivate the astrobiology relevance of this thesis, focusing on the connection between CBPs and habitability.

In Chapter 2, I present a newly developed photometric modeling code ("KEBLAT") capable of simultaneous or independent fits to the light curve (LC), spectral energy distribution (SED), and radial velocity (RV) of eclipsing binaries. I apply the code to simultaneously fit the LC and SED of 728 *Kepler* EBs, using the four-year *Kepler* time-series photometry and archival multi-band photometry from SDSS, WISE, and ground-based surveys. In particular, I leverage stellar evolution models to infer the absolute dimensions of the binary, including stellar masses, without the need for radial velocity measurements. In this work, I identify 35 new systems showing evidence for eclipse timing variations, create a homogeneous catalogue of stellar and orbital posteriors for 728 *Kepler* EBs, and lay the foundations for a comprehensive CBP search around these EBs in Chapter 4.

Next, in Chapter 3, I present an automated technique to detect transiting CBPs. The devised method accounts for large transit timing and duration variations (TTVs and TDVs), induced by binary reflex motion, in two important ways. First, it corrects for large-scale TTVs and TDVs in the light curves by using Keplerian models to approximate binary and CBP orbits; moreover, it allows additional aperiodicities on the corrected light curves by employing a Quasi-periodic Automated Transit Search algorithm (QATS; Carter & Agol, 2013). Because of these measures, this technique improves CBP detection significance from previous efforts, and augments the possibility to discover terrestrial-size CBPs.

Then, in Chapter 4, I apply the method outlined in Chapter 3 to the sample of EBs from Chapter 2, to search for CBP candidates and infer the occurrence rate of CBPs in the *Kepler* field. The automated target search identifies the most detectable, i.e., highest signal-to-noise, CBP in the system, and yields 12 candidates. In addition to CBP candidates, the search yields four multiply eclipsing candidates, including a newly discovered doubly eclipsing binary. I empirically test the completeness of our pipeline and analytically calculate the CBP transit probability window function to determine the total detection efficiency in bins of planet size and period. I infer that CBPs in coplanar orbits around longer-period

($P_b \gtrsim 5$) EBs in the Neptune to Saturn size range and with orbital periods within $35P_c$ have an occurrence rate of $18^{+7}_{-5}\%$. If instead the mutual inclinations between CBPs and host EBs are isotropically distributed, this occurrence rate rises to $83^{+31}_{-24}\%$.

Finally, in Chapter 5, I briefly discuss the findings of my thesis work in relation to CBP formation, habitability, and advocate for alternative modes of detection for future studies.

1.2 Towards a Separation-dependent Picture of Planet Occurrence and Formation in Binary Systems

The presence of stellar companions profoundly impacts the formation and evolutionary environment of planets in the system, especially for intermediate ($a_b \approx 1 - 100$ AU) and close ($a_b \lesssim 1$ AU) binaries, where their radiative and dynamical influences are large.

The two most common configurations in which planets exist stably around stellar binaries are S-type and P-type orbits, where planets orbit around a single stellar component and encircle both stellar components, respectively (Rabl & Dvorak, 1988). Through numerical simulations, Holman & Wiegert (1999) found empirically for both orbital configurations a critical planetary semi-major axis a_c which depends on the binary separation a_b, eccentricity e_b, and mass ratio $q = m_2/m_1$. For S-type planets, there exists a *maximum* critical planetary semi-major axis beyond which the planet is unstable, and in general the planet separation a_p must lie within $1/2\ a_b$. P-type planets, on the other hand, have a *minimum* critical planetary semi-major axis $a_c \approx 2 - 4a_b$ within which perturbations from the binary potential will either eject or ingest the planet. Many contemporary studies (Jaime et al., 2014; Chavez et al., 2014; Gong & Yan-Xiang, 2016; Sutherland & Kratter, 2019) have revisited this empirical stability criterion and extended it to resolve more details in orbital stability maps (e.g., mutual inclination, mean motion resonances, additional planets).

1.2.1 Wide Stellar Binaries

For wide ($a \approx 100 - 1000$ AU) stellar binaries, since gravity and tidal forces fall off as distance squared and cubed, respectively, the stellar companion's dynamical influence on a planet becomes vanishingly small, such that planet formation and evolution processes proceed as in the single stellar host limit (Duchêne, 2010). This is largely consistent with 1) sub-millimeter and infrared excess disk detections among PMS stars, which show similar occurrence rates between CS disks and circumprimary or circumsecondary disks (Duchêne, 2010; Harris et al., 2012); and 2) follow-up high-resolution imaging of *Kepler* Objects of Interest (KOIs), in which many of the planet-hosting systems have at least one wide stellar companion, suggesting that planet occurrence around single stars and in S-type orbits around wide binaries are comparable (Horch et al., 2014; Dressing et al., 2014; Hirsch et al., 2017; Furlan et al., 2017; Ziegler et al., 2017; Deacon et al., 2016).

1.2.2 Stellar Binaries at Intermediate Separations

For intermediate separations, presence of a closer-in companion significantly truncates the CS disk (Artymowicz & Lubow, 1994) for S-type systems. Optical, infrared, and millimeter surveys of the star forming regions reveal that the (apparent) CS disks around $\lesssim$35 AU binaries are depleted by $\gtrsim$2 in comparison to single star or wide binary hosts (Kraus et al., 2012), even within ∼1 Myr (Cheetham et al., 2015); moreover, the masses of protoplanetary CS disks are depleted by a factor of ∼25 for $\lesssim$35 AU binaries (Harris et al., 2012). It is unclear whether disks in <35 AU binaries have smaller masses and shorter lifetimes due to detection biases and incompleteness, because they are inherently less massive (from truncation), or if the depletion of material is an imprint of shorter-timescale planet formation processes at play, such as direct collapse from spiral density arms. Studies on populations of mature planetary systems, however, have begun to shed light on some of these uncertainties. Using adaptive optics imaging and aperture-mask interferometry, Kraus et al. (2016) found a lack of binary companions within <5 AU of KOI hosts, indicative that planet formation and survival is inhibited at these binary separations; Ngo et al. (2016) confirmed a paucity of 1–5 AU binary companions to transiting hot Jupiters, and found a higher stellar multiplicity rate at >50 AU separations for hot Jupiter hosts.

1.2.3 Close Stellar Binaries

For circumbinary systems with binary separations $\lesssim$1 AU, the picture is even more uncertain, although recent discoveries and surveys sensitive to gas giant CBPs have begun to fill in parameter space to test CBP formation and evolution. While the majority of CBPs in mature exoplanetary systems have been found around close-in ($P_b = 7 - 40$ d) binaries, only a handful of CB disks around ∼sub-AU T Tauri binaries are known (e.g., KH-15D Herbst et al., 2010), and the frequency of such CB disks is poorly constrained due to small sample size. The null detections of gas giant CBPs in radial velocity (e.g., BEBOP; Martin et al., 2019) and high-contrast imaging (e.g., SPOTS; Asensio-Torres et al., 2018) surveys – which probe different planetary separation regimes – suggest an occurrence upper limit of ∼10%. Using *Kepler* data and detections of transiting CBPs, Armstrong et al. (2014b) estimated the frequency of $>6\mathrm{R}_\oplus$ CBPs with $P < 300$ d to be ∼10%, if they are preferentially co-planar to binary hosts. For eccentric binaries, Doolin & Blundell (2011) find that polar CBP orbits are stable at 2 to 3 times the binary semi-major axis, and several studies (Martin & Lubow, 2018; Zanazzi & Lai, 2018; Cuello & Giuppone, 2019) predict that an initially misaligned CB disk tends toward one of two alignments with respect to the binary: co-planar and perpendicular. The discovery of a circumbinary ring in a polar configuration at ∼3.5 AU around the young HD 98800 system (Kennedy et al., 2019) suggests severely misaligned CBPs may be at least possible.

Traditional formation theories predict that circumbinary environments are hostile sites for planet formation and survival, especially near the inner regions, where observed (mature) CBPs are typically found. For example, in the classic "core accretion" scenario, small particles coagulate into large planetessimals via collisions. However, for close-in ($\lesssim 1 - 4$ AU) CB environments, even in the presence of gas drag, the binary potential excites eccentricities of inner disk particles, raising mutual velocities beyond the critical speed at which collisions are destructive rather than inelastic (Marzari & Scholl, 2000; Moriwaki & Nakagawa, 2004; Meschiari, 2012; Paardekooper et al., 2012; Rafikov, 2013; Lines et al., 2014; Bromley &

Kenyon, 2015).

Observations of transiting CBPs from *Kepler* and *TESS* reveal, however, that they somehow overcome this barrier to reside close to their binary hosts. This may be achieved through forming via planetessimal (Meschiari, 2012) or pebble accretion (Pierens et al., 2020) further out in the disk (e.g., deadzones, Martin et al., 2013), where the time-varying binary potential is weak, and then arriving at their current positions via inward migration (Pierens & Nelson, 2007, 2008; Kley & Haghighipour, 2014) and/or planet-planet scattering (Bromley & Kenyon, 2015; Smullen et al., 2016; Gong & Yan-Xiang, 2016; Gong & Ji, 2017; Sutherland & Kratter, 2019). Many 2D and 3D hydrodynamical simulations of CBPs in gaseous disks corroborate that the central cavity sculpted by binary tidal action (Artymowicz & Lubow, 1994) also provides a halting criterion or trap for CBPs migrating inwardly (Pierens & Nelson, 2013; Kley & Haghighipour, 2015; Thun & Kley, 2018; Pierens & Nelson, 2018; Kley et al., 2019; Yamanaka & Sasaki, 2019).

Furthermore, the *apparent* lack of transiting CBPs around very short period ($\lesssim$7 d) *Kepler* EBs has spurred investigations into dynamical paths to clear CBPs from these systems. In a triptych of independent analyses, Muñoz & Lai (2015), Hamers et al. (2016), and Martin et al. (2015) propose that the same physical mechanism that explains the formation of ultra-short period binaries, may also destabilize CBPs around them. The mechanism invokes the presence of a hierarchical, tertiary stellar companion, which are common in $\lesssim$ 3 d binaries (Tokovinin et al., 2006; Rappaport et al., 2013; Conroy et al., 2014). The tertiary star excites the inner binary eccentricity through Kozai-Lidov oscillations, allowing close encounters where tidal forces act to circularize and shrink the binary orbit (Fabrycky & Tremaine, 2007). CBPs that do survive the Kozai-Lidov + tidal decay (KLTD) regime have orbits that are somewhat misaligned and further away from the binary, and are thus more difficult to detect in the *Kepler* data. Additionally, Fleming et al. (2018) examine the coupled stellar-tidal evolution of isolated, short period binaries as a physical process to explain the observed dearth of CBPs. They find that a pre-MS binary's angular momentum evolution widens its initial orbit via spin-orbit coupling. Once a tidally-locked state is achieved, stellar magnetic braking extracts angular momentum from the binary orbit, causing it to decay. This early growth and decay in binary orbit likewise cause the edge of the critical stability region to expand and shrink, such that (proto-)CBPs located near the initial critical semi-major axis are destabilized. This mechanism likely operates within 1-100 Myr, depending on the choice of tidal model (Graham et al., submitted), and results in a lack of CBPs around mature systems for all binary orbital periods <7.5 d. If CBPs are readily formed and destabilized, the most likely fate for unstable CBPs is ejection and contribution to the population of free-floating planets (Sutherland & Fabrycky, 2016).

Additional detections and a sensitive, well-quantified detector are crucial to disentangle biases and to confirm, constrain, and compel CBP formation theories. This thesis work aims to build toward those goals.

1.3 Habitability & Astrobiology

The characterization of binary stars, detection of CBPs, and analysis of CBP demographics are directly relevant to astrobiology research goals. Since stellar multiplicity is a natural end product of the star formation process, understanding the distribution of habitable environments in the universe necessitates quantifying the abundance of CBPs. In the solar neighbourhood (<20 parsec), the frequency of multiple systems with solar-type (F, G, early-K) and later-type (late-K, M) primaries are $\sim$50% and $\gtrsim$30%, respectively (Duchêne & Kraus, 2013). A habitability census to evaluate the best targets for detailed characterization follow-up, is therefore not complete without investigating the population of planets orbiting binary stars. My work aims to shed light on the distribution of CBPs and what types of circumbinary environments host planets which may be incorporated into the realm of detectable habitable worlds.

Welsh et al. (2014) pointed out the fortuitous trend that known CBPs tend to lie close to their stability limit, which coincides with locations of Earth-like insolation and equilibrium temperature, known as the habitable zone (HZ). Whether the apparent “pile-up” of CBPs near the stability is an observational bias or a physical manifestation of tidal migration during planet formation is still a contentious topic (see, e.g., Quarles et al., 2018; Li et al., 2016). If this apparent "pile-up" is the result of a common physical process, then the fortuitous overlap between the stability limit and the HZ provides a beneficial bias toward detectable CBPs as habitable and boosts the frequency of habitable circumbinary worlds.

Below, I provide a short summary of habitability challenges and boons for CBPs.

1.3.1 The Radiative Habitable Zone

Because life on Earth requires liquid water as a universal solvent (Cockell et al., 2016), the conventional indicator for a habitable planet is the sustained presence of surface liquid water. This metric is the foundation of the radiative "habitable zone" (RHZ; Huang, 1960; Kasting et al., 1993), locations around a star where an Earth-like planet with a $CO_2/H_2O/N_2$ atmosphere receives the right amount of stellar radiation to sustain surface liquid water.

Traditionally, the inner and outer RHZ edges are defined as the onset locations of runaway greenhouse and maximum greenhouse, respectively (Kasting et al., 1993). In the runaway limit, a positive feedback loop occurs where rising temperature increases water vapour content in the atmosphere, which efficiently absorbs outgoing planet flux and traps surface heat, until the planet becomes desiccated, like Venus. At the maximum greenhouse limit, the warming effect of CO_2 fails to outperform cooling (increased albedo) via Rayleigh scattering by CO_2.

The atmosphere serves as an important buffering zone between the incoming stellar radiation, or instellation, and outgoing infrared planetary heat. Different atmospheric constituents, such as O_2, CO_2, and H_2O act as gatekeepers that allow (absorb) and reject (reflect) different wavelengths of radiation. The atmosphere's response to the incoming stellar spectral energy distribution (SED) dictates the boundaries of the HZ. Consequently, the HZ location exhibits curvature as a function of stellar type. Kopparapu et al. (2013) established a parameterized relationship between HZ stellar instellation and stellar effective temperature, for a range of input stellar spectral types.

Several studies have applied the concept of the traditional RHZ to CB systems using extensions of the Kopparapu et al. (2013) parameterization to include binary flux contributions (Kane & Hinkel, 2013; Cuntz & M., 2014; Haghighipour & Kaltenegger, 2013; Jaime et al., 2014; Mason et al., 2014; Wang & Cuntz, 2019; Cukier et al., 2019). In general, the traditional RHZ for two late-type MS stellar binaries is closer in than for a G-M dwarf binary, whose RHZ is in turn more close-in than solar twins. Moreover, more closely separated and circular binaries allow for wider RHZs, as the time-dependent binary potential/instellation more closely resembles that from the binary barycenter.

Owing to three-body dynamics, the CB habitable zone is a convolution of the RHZ with long-term stable orbits of CBPs. Because the location of the RHZ is dictated by the mass or spectral type of the binary components, while the location of the stability criteria is, to first order, a function of the binary period (Holman & Wiegert, 1999), scenarios arise where the HZ is interior to the stability limit, as is the case for Kepler-16b (Kane & Hinkel, 2013; Haghighipour & Kaltenegger, 2013), and for binaries with secondary stellar masses $< 0.12\mathrm{M}_\odot$ (Graham et al., submitted). Detailed habitability analysis, however, requires resolving the competing effects of the binary orbital period, eccentricity, and mass ratio on the locations and sizes of CBHZs (see, e.g., Fig. 8 from Cuntz & M., 2014).

It is important to note in the context of CBHZs that beyond the stability criterion, islands of instability exist, in particular near resonances, similar to the Kirkwood gaps of the asteroid belt. As eccentricity increases, the islands of instability grow and occupy more of the parameter space (Popova & Shevchenko, 2013; Kostov et al., 2014). This is not treated in current CBHZ boundary computations.

1.3.2 Climate Variations

More recently, detailed studies using general circulation models (GCMs) have explored the effects of rapidly varying stars-planet distances and thus levels of instellation a CBP receives, due to orbital motion and the geometry of the planet and binary. May & Rauscher (2016) used 1D latitudinal energy balance model (EBM) and GCM, coupled to a simplified dynamical model, and found that variable radiative forcing had no significant effects on the circulation patterns of gas giant atmospheres. Popp et al. (2017) used a 3D GCM to trace precipitation and surface temperature variations from binary-induced radiative forcing, for an aquaplanet with Earthlike atmosphere around the known CBP host Kepler-35. They showed that the global-mean surface temperature only varied by a few degrees, and a habitable climate is maintained. Using an analytic EBM, Haqq-Misra et al. (2019) demonstrated that the amplitude of surface temperature variations increases for terrestrial planets with higher land-to-ocean coverage, due to their lower effective heat capacity and thus lower atmospheric inertia; that is, the Popp et al. (2017) result is a best-case scenario.

Furthermore, owing to the multi-body dynamics, CBP orbits can undergo precession and oscillations in eccentricity and obliquity – Milankovitch cycles – which in turn modulates the amount of radiation received at the tops of atmospheres. Using a 1D latitudinal EBM model coupled to an N-body integrator with an obliquity evolution model, Forgan & Duncan (2016) investigated the coupled thermo-dynamical evolution of an Earthlike CBP around the $\sim$7 d solar and M-dwarf binary Kepler-47. They found that the amplitude of (secular) temperature variations due to $\sim$1000 yr Milankovitch cycles are comparable to binary-induced temperature variations on binary orbital timescales.

1.3.3 Effects of Stellar Activity

There exists a well-established stellar age-rotation-activity relation (Skumanich, 1972), in which younger stars tend to be rapid rotators and exhibit higher activity levels (e.g., flares, chromospheric emission, and mass loss). Low-mass stars, especially M-dwarfs – favoured for habitability studies due to their abundance, small size, and closer-in HZ – have significant flaring rates, which exhibit significant X-ray and UV (XUV) radiation as well as particle emission. For single, field M dwarfs, activity level correlates strongly with stellar rotation period, such that a faster spin rate results in stronger and more frequent flares (Mohanty & Basri, 2003). Although Segura et al. (2010) demonstrated an atmosphere's ability to recover from a single flare event, Tilley et al. (2019) subsequently showed that sustained, strong emission from flares and associated proton events may erode a planet's atmosphere.

In particular, they found that the ozone column of Earth-like atmospheres can be destroyed, leaving the surface vulnerable to shortwave radiation.

Intriguingly, Mason et al. (2013) proposed that the presence of a stellar companion, *in certain binary configurations*, may reduce stellar aggression via tidal braking, and therefore enhance atmospheric stability and domains of habitability. Mutual tidal interactions between the stellar components drive the system into a tidally locked or pseudosynchronous spin-orbit state, as well as circularize the orbit (Hut, 1981). For stars born as rapid rotators and with an initial separation of ∼0.15 AU ($P_b \sim 10$ d), the spin down of stellar rotation as the system tidally synchronize may significantly reduce magnetic activity relative to CS counterparts (Mason et al., 2014; Zuluaga et al., 2016; Johnstone et al., 2019), creating a habitability "niche."

The habitability studies reviewed here indicate that CBP habitability is possible, although more uncertain and complex, due to the plurality of stellar hosts. Building a strong foundation for CBP demographics is crucial to constrain the physical processes that shape them and to fill in the parameter space to explore modes of habitability. CBP discoveries are currently orders of magnitude more rare than CSPs, due to detection challenges and a smaller stellar target sample. However, there is a fortuitous overlap between the CBP radiative habitable zone and the critical stability region, which is readily accessible with current and future detection technologies, such as transit, RV, eclipse timing, and direct imaging. This fortuitous overlap should be exploited to populate the sample of habitable CBP candidates. In addition to Earth-size CBPs at the coincidence region, terrestrial-size moons around gas giant CBPs (Quarles et al., 2012) in the HZ may provide a potential habitat.

Chapter 2

MODELING *Kepler* ECLIPSING BINARIES: HOMOGENEOUS INFERENCE OF ORBITAL & STELLAR PROPERTIES

In this chapter, I report on the properties of eclipsing binaries from the *Kepler* mission with a newly developed photometric modeling code, which uses the light curve, spectral energy distribution of each binary, and stellar evolution models to infer stellar masses without the need for radial velocity measurements. I present solutions and posteriors to orbital and stellar parameters for 728 systems, forming the largest homogeneous catalogue of full *Kepler* binary parameter estimates to date. Using comparisons to published radial velocity measurements, I demonstrate that the inferred properties (e.g., masses) are reliable for well-detached main-sequence binaries, which make up the majority of our sample. The fidelity of the inferred parameters degrades for a subset of systems not well described by input isochrones, such as short-period binaries that have undergone interactions, or binaries with post-main sequence components. Additionally, I identify 35 new systems which show evidence of eclipse timing variations, perhaps from apsidal motion due to binary tides or tertiary companions. I plan to subsequently use these models to search for and constrain the presence of circumbinary planets in *Kepler* eclipsing binary systems.

Material from this chapter was previously published in collaboration with Eric Agol, Aleezah Ali, and Flavien Kiefer, in the October 2019 edition of the Monthly Notices of the Royal Astronomical Society, and is reproduced by permission of Oxford University Press.

2.1 Introduction

A significant fraction of stars live in binaries or higher-order multiple systems (Abt, 1979; Duchêne & Kraus, 2013); despite this, the effects of binarity on a system's formation, stellar evolution, and dynamical evolution, including planetary system evolution, are not well understood. These uncertainties propagate to other fields of astronomy. For example, they have profound implications on interpretations of stellar populations, the foundation of galactic and extragalactic astronomy (Eldridge et al., 2017; Izzard & Halabi, 2018). Constraining binary processes requires knowledge of their fundamental parameters, such as radii, temperatures, mass ratio, and age. Fortunately, the geometry of eclipsing binary (EB) stars allows for direct constraints on such parameters. This makes EBs excellent astrophysical tools not only to calibrate single star stellar evolution models (e.g., Stassun et al., 2009; Claret & Torres, 2018; del Burgo & Allende Prieto, 2018), but also to test models of binary tidal evolution (Birkby et al., 2012; Lurie et al., 2017; Fleming et al., 2019), along with their planetary systems (Martin et al., 2015; Fleming et al., 2018). However, direct measurements of binary absolute dimensions rely on the fortuitous condition that the binary is an eclipsing, double-lined spectroscopic system, and necessitate multi-band time-series and radial velocity (RV) information, which is observationally expensive to obtain for a large ensemble of systems. Making meaningful inferences about *populations* of binaries, therefore, may benefit from a different approach.

The goal of this work is to estimate absolute stellar and orbital dimensions for a large ensemble of ∼detached eclipsing binaries in the *Kepler* field, *relying only on photometry.* Rather than use time-intensive measurements of a small number of bright EBs to constrain stellar models, we leverage theoretical stellar isochrones to infer properties for a much larger sample of systems. The basis for our study begins with the Villanova *Kepler* EB Catalogue (VKEBC; Prša et al., 2011; Kirk et al., 2016), which contains over 2800 eclipsing and ellipsoidal binaries from the *Kepler* mission. The majority of these objects have only crude phenomenological estimates of eccentricity, temperature ratios, and sum of radii relative to orbits, without a full characterization of the binary parameters. Detailed, full parameter studies have typically focused on individual systems or smaller samples of binaries for e.g., asteroseismic (Guo et al., 2016; Gaulme et al., 2016), eccentricity-tidal (Kjurkchieva et al., 2016), and RV analysis (Matson et al., 2017). Here, we statistically combine the constraining power of both light curves and SEDs to derive full system solutions and posteriors to 728 *Kepler* EBs, creating a large homogeneous catalogue.

Such a catalogue has yet to be developed for the binaries in the *Kepler* field, although comparable analyses have been carried out for other catalogues of eclipsing binaries. The most similar study was applied to the Trans-Atlantic Exoplanet Survey (TrES; a pre-cursor survey to *Kepler*) by Devor et al. (2008) using light curves collected to discover transiting exoplanets from the ground, supplemented by multi-band photometry. The advantage of the *Kepler* field is that it forms a homogeneous dataset with high precision, continuous time-series photometry over a long baseline, and that it is extremely well studied in the characterization of single stars and exoplanets.

The original impetus for our catalogue is to characterize a large population of binaries to a sufficient degree to enable a search for transiting circumbinary planets (CBPs) and to quantify the frequency of CBPs as a function of stellar binary properties (Chapter 3-4). In addition to this, our analysis can provide the basis for additional studies of binary stellar populations. Time-intensive radial velocity follow-up of *Kepler* EBs would benefit from informative priors on masses, radii, temperatures, and ages of a large EB sample to select the preferred targets to observe. Our homogeneous parameter estimates could also permit more detailed statistical testing of physical processes, such as tidal circularization (Duquennoy et al., 1991; Van Eylen et al., 2016) and rotational synchronization (Lurie et al., 2017), and could facilitate detection of additional bodies in the system, such as tertiary stars (e.g., Borkovits et al., 2015; Borkovits et al., 2016). Our methodology may be applied to current and upcoming surveys in the era of large-scale precision photometry such as OGLE, *TESS*, and LSST, which have all-sky coverage, opening up an avenue for binary star galactic archaeology.

With these goals in mind, here we present a Bayesian characterization of 728 well- to semi-detached EBs using *Kepler* time-series photometry and archival multi-band imaging, as well as *Gaia* parallaxes when available; that is, we derive full system parameters with only photometry and astrometry, and no RV information. Simultaneous modeling of the light curve (LC) and spectral energy distribution (SED) provides joint constraints on EB orbital (e.g., period, eccentricity, argument of periastron, inclination) and stellar (e.g., mass, radius, temperature, age) properties, subject to the assumption that the two stars fall on a single isochrone. The chapter is organized as follows. In section 2.2, we describe our sample selection and the simultaneous LC + SED model. We present the results of our analysis in section 2.3, and discuss our results in the context of stellar evolution, systematic biases, previous EB radial velocity and population studies in section 2.4. In section 2.5, we conclude and summarize our key findings.

2.2 Methods

We developed a Python code, dubbed "KEBLAT", to simultaneously fit the light curves and SEDs of 728 *Kepler* EBs to obtain their orbital and stellar parameters. The open-source code is available on Github[1]. In this section we describe the target selection process (§2.2.1), the datasets gathered (§2.2.2), the light curve modeling (§2.2.3), spectral energy distribution modeling (§2.2.4), and joint LC+SED modeling of each binary (§2.2.5 and 2.2.6). To test the accuracy of our model inference, we also extract RVs for 3 EBs in our sample that have not been studied previously (§2.2.7); we add these to published EBs with RV mass solutions to compare to our inferred masses below (§2.4.1). Throughout this work, we refer to properties of the primary and secondary components with subscripts 1 and 2, respectively, and define the primary component as the eclipsed star that exhibits the deeper light curve minimum.

---

[1] `https://github.com/savvytruffle/keblat/`

2.2.1 Sample Selection

We selected our binary systems from the Villanova *Kepler* EB Catalogue or VKEBC (Prša et al., 2011; Kirk et al., 2016). This sample, totaling 2877 targets, has been compiled from the entire *Kepler* prime mission and includes binaries which are not eclipsing (e.g., ellipsoidal variables). We made selection cuts to reduce grazing (i.e., non-constraining) geometries and the effects of close binarity that are not included in our model (e.g., tidal distortions and Doppler boosting of the binary components).

First, to diminish the presence of background, grazing, or non- eclipsing binaries, we required primary and secondary eclipse depths to be >5% and >0.1% of the normalized flux, respectively. Next, we excluded targets which exhibit strong distortions in the light curve by selecting for binaries with morphology parameter `morph` < 0.6. This morphology parameter, provided by VKEBC, is based on a locally linear embedding scheme that classifies light curve shape, such that a low value correlates with well-detached systems exhibiting clearly separated eclipses, and higher morphology value correlates with over-contact (OC) systems with sinusoidal variations (Matijevič et al., 2012).

In total, we investigated 728 ∼detached eclipsing binary systems. The large reduction in the number of systems from the full VKEBC is related to the fact that short-period binaries have the highest eclipse probability, but also have the largest tidal distortions; our sample emphasizes the longer period eclipsing binaries.

2.2.2 Data Acquisition

Kepler *Photometric Time Series Data*

We extracted light curves from *Kepler* long-cadence (∼30 min) simple aperture photometry (SAP) based on Data Release 24, spanning ∼4 years or 17 quarters. To correct for slight variations in instrumental sensitivity across quarterly rotations, whereby light from a target may fall upon different detector and pixels, we normalized the raw SAP flux by the quarterly median value. To lessen the impact of outliers in the data, we then de-weighted data points with quality flags > 8 (signifying cosmic ray hits, space craft re-pointing, etc) by inflating their error bars 10-fold. We did not fit the entire *Kepler* light curve for our final analysis. Instead, we clipped the light curve around each eclipse with a window 1.5–2.0 times eclipse durations, which were initially taken from VKEBC, and then iteratively refined during the optimization process. This window around each eclipse allowed us to fit a polynomial to the variable component of each binary which is not included in our physical model, while minimizing the model evaluation and computational time.

Spectral Energy Distribution Data

As we did not have radial velocity data for most of our targets, we required additional constraints to infer the absolute parameters of each system. We collected literature photometric data on each target, and modeled these with stellar evolution models (see §2.2.4). We identified extant photometry for each target by cross-matching our sample against sources from the Howell-Everett (HE, Everett et al., 2012), Sloan Digitial Sky Survey (SDSS, Ahn et al., 2012), Two-Micron All-sky Survey (2MASS, Skrutskie et al., 2006), and Wide-field Infrared Survey Explorer (WISE, Cutri & et al., 2014) catalogues on Vizier using a $2''$ search cone. We gathered together the available archival photometry to construct SEDs, excluding targets which had fewer than five photometric data points.

Having multiple measurements spanning a broad wavelength range is crucial to leverage the shape of stellar SEDs to constrain the stellar properties. The U and B flux, in particular, distinguish young and hot stars from cooler, older stars. While the HE and 2MASS campaigns have nearly complete coverage of the *Kepler* field, the WISE footprint on our sample covers only ∼50%, and the SDSS footprint covers only ∼10%. Therefore, we supplemented SDSS photometry with $g'\,r'\,i'\,z'$ estimates from the *Kepler* Input Catalogue (KIC), which were designed to mimic SDSS bandpasses. The typical agreement between KIC and SDSS *griz* measurements for our sample is of order ∼0.05 mag. Furthermore, we used the measured ephemerides to identify that about 10–15% of the photometric observations had been taken during an eclipse; we inflated their error bars to 3 mags to diminish their influence during fitting.

2.2.3 Light Curve Model

The LC module couples a Keplerian orbit solver to the analytic Mandel & Agol (2002) transit model with a quadratic limb-darkening law to fit the observed light curve. The Keplerian orbital model determines the instantaneous relative positions of the binary stars, which are used, in conjunction with radius ratio and a limb darkening prescription, to compute the obscured-to-unobscured system flux. We apply a triangular parameterization of the quadratic limb darkening coefficients to allow uniform prior sampling (Kipping, 2013); these coefficients are allowed to float and are not explicitly coupled to model atmospheres.

Using this model, KEBLAT constructs a template light curve with high temporal fidelity at ∼1min, incrementally summed to produce a ∼30 min integration, i.e., the *Kepler* long-cadence exposure time. The code then uses this high fidelity template to linearly interpolate the flux at each observed cadence. This method speeds up the computation time and accounts for distortions in the light curve due to finite integration times (Kipping, 2010). For stellar eclipses, which are much higher signal-to-noise than exoplanet transits, this step is especially important; the effect of finite integration time is strongest during ingress and egress, which in turn can affect inference of eccentricity, inclination, radii, and limb darkening coefficients. We test this interpolation scheme against direct computation of the light curve and found that the maximum error is $\sim 10^{-6}$, at least 2–3 orders of magnitude smaller than typical in-eclipse residuals due to dynamical and stellar variability. We apply quarterly contamination values from *Kepler* to model (varying) third-light contributions, and allow each quarter's contamination value to float during optimization.

In total, the light curve model has $13+N_{\mathrm{quarters}}$ free parameters describing stellar properties (M_{sum}, $\frac{R_2}{R_1}$, R_{sum}, $\frac{F_2}{F_1}$), orbital elements ($e\sin\omega$, $e\cos\omega$, b, P, $\mathrm{t_{PE}}$), limb darkening ($q_{11}, q_{12}, q_{21}, q_{22}$), a systematic error term σ_{sys} to account for underestimated observational uncertainties, and crowding values for quarter j (c_j). Note that we define the impact parameter with respect to the primary, such that $b = a\cos i/R_1$. Transformed parameters such as $e\sin\omega$, $e\cos\omega$, and limb darkening coefficients have finite bounds. For non-transformed variables, we place broad bounds; see Table 2.1 for a detailed summary of each parameter.

During each model evaluation, we simultaneously fit a second order local polynomial around each eclipse to marginalize the background continuum flux, which may be influenced by instrument variations and/or stellar activity. We used a window of 1.5 – 2 times the primary eclipse duration to ensure our polynomial choice is appropriate, and found that a second order polynomial was typically sufficient. Because the eclipses are masked during polynomial marginalization, higher order polynomials may overfit the data and potentially introduce spurious signals.

2.2.4 Stellar Evolution and Photometric models

The SED model assumes a co-eval binary specified by age τ, metallicity z, and masses M_1 and M_2. We utilize PARSEC (Bressan et al., 2012) stellar evolution isochrones, a large grid of stellar models featuring properties such as luminosity, $\log g$, effective temperature, and flux in various bandpasses. We adopt a fine grid spacing, with $z_{\rm grid}$ = [0.001, 0.002, 0.004, 0.008, 0.01, 0.015, 0.02, 0.03, 0.04, 0.05, 0.06], $\Delta\tau_{\rm grid} = 0.02$, and median $\Delta M_{\rm grid} = 0.006$. For a specified set of mass, age, and metallicity, KEBLAT performs a bi-linear interpolation over the PARSEC grid to determine the predicted temperatures and absolute magnitudes in *UBV griz JHK* W_1W_2 bandpasses, i.e., the stellar SED. We calculate the effective radius of each star from the bolometric luminosity via the Stefan-Boltzmann law; these radii values are necessary to couple to the LC module.

To fit the archival data, we sum the predicted SEDs of both stellar components, compute the distance modulus, and correct for dust extinction along the line of sight assuming an exponential dust distribution with scale-height $h_0 = 119$ pc (Kruse & Agol, 2014):

$$\mathrm{mag}_{\lambda,\mathrm{binary}} = \mathrm{Mag}_{\lambda,\mathrm{binary}} + 5\log_{10}\left(\frac{d}{10}\right) + A_\lambda E(B-V)\left(1-\exp\left(\frac{-d\sin b_G}{h_0}\right)\right) \qquad (2.1)$$

where b_G is a target's galactic latitude, d is distance in pc, and $E(B-V)$ and A_λ are reddening and band specific extinction computed from a Milky Way extinction law with

$R = 3.1$ (Fitzpatrick, 1999). The integrated absolute magnitude of the binary in a given bandpass is

$$\mathrm{Mag}_{\lambda,\mathrm{binary}} = \mathrm{Mag}_{\lambda,1} - 2.5\log_{10}\left(1 + 10^{-0.4(\mathrm{Mag}_{\lambda,2}-\mathrm{Mag}_{\lambda,1})}\right) \ . \tag{2.2}$$

We use cross-matched *Gaia* distances derived from Bailer-Jones et al. (2018) and Schlafly & Finkbeiner (2011) dust maps results, when available, to place Gaussian priors on d and $E(B-V)$ in our model. Accurate distances from parallax may be used to place better constraints on EB masses since mass correlates tightly with luminosity on the main sequence. Well-calibrated eclipsing binaries can be used as standard candles to calibrate parallaxes (Southworth et al., 2005), and the converse should also be true for systems with well-constrained geometries (Stassun & Torres, 2016). In particular, accurate distances may better constrain masses for binaries with non-total or non-annular eclipses by precisely determining total system luminosities. However, rather than using reported uncertainties as fixed σ_d, $\sigma_{\mathrm{E(B-V)}}$, we allow the widths of these Gaussian priors to float to tolerate inaccuracies in the dust map or *Gaia* data due to source confusion or presence of tertiary companions, which has an occurrence rate of $\sim 15-20\%$ in the *Kepler* field (Gies et al., 2012; Rappaport et al., 2013; Conroy et al., 2014; Orosz, 2015). Frequent eclipses or nearby long-period binaries may also deleteriously affect the accuracy of *Gaia* astrometry.

As with the LC model, the SED model fits for a systematic error, σ_{SED}, to account for underestimated observational errors and uncertainties in the isochrone models. This systematic error also encapsulates any contaminant flux to the binary by additional components, as we do not fit for a third star given the limited number of available SED measurements. As a result, we expect this systematic term to be relatively large compared to reported observational uncertainties.

In practice, we use the sum and ratio of masses ($M_{\mathrm{sum}} = M_1 + M_2$, $Q = M_2/M_1$), instead of individual masses (M_1, M_2), to optimize the SED fits. The SED module has in total 10 possible free parameters describing the fundamental stellar properties (M_{sum}, Q, age, metallicity), dust scaleheight h_0, σ_{SED}, and distance d and reddening $E(B-V)$, with their associated uncertainties σ_d, $\sigma_{\mathrm{E(B-V)}}$; for this work, we fix $h_0 = 119$ pc. We give descriptions of each parameter and associated bounds in Table 2.1.

2.2.5 Joint SED and LC model

We couple the isochrone interpolator to the light curve solver for simultaneous SED + LC fitting. During a joint fit, the SED model provides binary radii and *Kepler* bandpass fluxes, which are used as inputs to the LC module; this effectively reduces the number of free parameters from 13+$N_{\rm quarters}$+10 to 20+$N_{\rm quarters}$. The full set of parameters is listed in Table 2.1. We express the joint likelihood function as the product of likelihoods given all sets of data (e.g., LC, SED, extinction, and distance), assuming that each data point is uncorrelated and uncertainties are Gaussian:

$$\begin{aligned}\log L = &-\frac{1}{2}\sum_i \left(\frac{\Delta \mathrm{LC}_i^2}{(\sigma_{\mathrm{LC},i}^2+\sigma_{\mathrm{LC,sys}}^2)} + \log(\sigma_{\mathrm{LC},i}^2+\sigma_{\mathrm{LC,sys}}^2)\right)\\ &-\frac{1}{2}\sum_j \left(\frac{\Delta \mathrm{SED}_j^2}{(\sigma_{\mathrm{SED},j}^2+\sigma_{\mathrm{SED,sys}}^2)} + \log(\sigma_{\mathrm{SED},j}^2+\sigma_{\mathrm{SED,sys}}^2)\right)\\ &-\frac{1}{2}\left(\left(\frac{\Delta d}{\sigma_d}\right)^2+\log(\sigma_d^2)\right)-\frac{1}{2}\left(\left(\frac{(\Delta \mathrm{E(B-V)}}{\sigma_{\mathrm{E(B-V)}}}\right)^2+\log(\sigma_{\mathrm{E(B-V)}}^2)\right)+C\end{aligned} \tag{2.3}$$

Here, ΔLC, ΔSED, Δd, and ΔE(B-V) are the light curve, spectral energy distribution, distance, and reddening fit residuals, respectively. The distance and E(B-V) uncertainties σ_d and $\sigma_{\mathrm{E(B-V)}}$ are allowed to float. The systematic error terms for LC and SED are added in quadrature to the observed uncertainties, and importantly the log quantities penalize inflating the error bars. This prevents the model from converging to a poor fit compensated by over-inflating the error bars, and allows the model to weight the LC or SED differently, if the data prefers it. The best-fit solution corresponds to the maximum likelihood model.

2.2.6 Model Initialization, Optimization, and Bayesian Parameter Estimation

Due to the non-linear nature of the SED and light curve models, we fit the time-series and multi-band photometry in three stages:

1. A fit to only the *Kepler* light curve.
2. A fit to only the spectral energy distribution.
3. A combined fit to the *Kepler* light curve and spectral energy distribution, using the prior stages to initialize the fit.

For each stage, we optimize the solutions via `lmfit` (Newville et al., 2014), a non-linear least squares minimization algorithm based on the Levenberg-Marquardt algorithm (Moré, 1978). We find that the optimization routine is highly sensitive to initial parameters; for initial solutions far away from local minimum, the optimization scheme may become stuck, or tend toward boundary values. Consequently, we initialize the optimizer with a combination of gridded parameters and parameter guesses from observables. We describe our fitting procedures in practice below.

For LC fitting, we use observed eclipse depths, durations, and times to estimate initial parameters, and pad these guesses with a grid in radius ratio, $e\cos\omega$, $e\sin\omega$, and impact parameter. We then optimize each set of initial parameters and save the solution with the smallest chi-square value. For SED fitting, we use a brute-force grid method to find the best-fit SED model(s) with stellar parameters consistent with the light curve solution: we initialize each set of SED fits in a grid of $M_{\text{sum}} \in \{0.5, 1.0, 1.5, 2.0, 2.5, 4.0\} M_{\odot}$, $Q \in \{0.1, 0.3, 0.5, 0.9\}$, z value from KIC, $E(B-V)$ value from Schlafly & Finkbeiner (2011) and d from Bailer-Jones et al. (2018). Then, for each set of M_1, M_2, z, we determine the upper age limit given the initial mass in the PARSEC model, and evenly sample age values in log space. For each nested subgrid, we optimize the fit via `lmfit` and save solutions with the lowest χ^2 value.

The best-fit parameters from the separate SED and LC solutions seed the joint-fit optimization. When radii values from SED optimization are in tension with LC-derived ones, we pad the separately derived best-fit parameters with a grid of values in mass sum, mass ratio, and age, and step through a grid of these initial parameters for simultaneous SED+LC fitting.

To quantify uncertainties and degeneracies in the model, we use the best-fit solution from the joint SED+LC optimization to seed Monte Carlo Markov Chain (MCMC) simulations. We use an affine-invariant MCMC ensemble sampler, `emcee` (Foreman-Mackey et al., 2013), with 128 walkers to sample the posterior distribution of parameters for each binary. We place log-uniform priors on the systematic error terms, Gaussian priors on d and E(B-V), and flat priors on all other parameters; see Table 2.1 for details on parameter bounds. In addition, uniform sampling of age and eccentricity, under parameter transformation to $\tau = \log_{10}(\text{age [yr]})$ and $(e \sin\omega,\ e \cos\omega)$, requires placing a prior of $\exp(\tau \ln 10)/\ln 10$ and $1/e$, respectively. As the model already contains a large number of free parameters, we fix the crowding parameters during posterior sampling to the values found from the optimization stage.

We generate Markov chains with 128 walkers for N_{iter} = 100,000 – 700,000 iterations, discarding chains before burn-in for posterior analysis. We define the burn-in period as when the chains cross 5 times the median log-likelihood value of the entire ensemble population, adapting the methodology of Tegmark et al. (2004). Because the chains are initialized from a high-dimensional Gaussian distribution centered on the `lmfit` optimized solution, burn-in is typically low ($\lesssim 10,000$ iterations), and a long burn-in period may signify that the optimized solution was located at a local minimum. For systems exhibiting this behaviour, we restart the Markov chains using the previous run's maximum-likelihood solution.

We use multiple diagnostics to assess convergence. First, we check that the acceptance fraction is between 0.01 and 0.4. Next, we estimate the integrated autocorrelation time, τ_{acf}, of the ensemble and verify that it is appropriate for the chain length. Finally, we visually inspect that the chains appear well-mixed in trace plots. Longer autocorrelation times typically correlate with smaller acceptance fractions, and large τ_{acf} values may indicate a parameter is not well constrained by the data, the parameter space is multi-modal, or that the observed binary cannot be fully captured by co-eval model isochrones. We note that for shallowly eclipsing systems or those exhibiting tidal distortions, the autocorrelation times for b, age, metallicity, and mass may be long, with effective chain length $N_{\text{iter}}/\tau_{\text{acf}} = 15$ –

20, even after >500,000 generations of 128 walkers. This is because grazing geometries do not well constrain the light curve model, and isochrone models do not well predict stars modified by additional physics. Rather than excluding these EBs from our final sample, for completeness, we report their parameter estimation and discuss at length the factors that limit those results in §2.4.1 and §2.4.2. In contrast, flat-bottomed light curves indicative of total or annular eclipses completely break any degeneracy with inclination. For non-grazing, well-detached systems, our median chain lengths are >50 times $\tau_{\rm acf}$. We find that period, times of eclipse, and $e\cos\omega$ converge well for all EBs.

2.2.7 Radial Velocities

In order to validate our method, we compare our inferred stellar masses against RV masses from existing literature studies (see §2.4). To supplement the number of RV comparison targets, we mine spectroscopic data from The Apache Point Observatory Galactic Evolution Experiment (APOGEE; Majewski et al., 2017), and extract RVs for three EBs in our sample: KICs 5284133, 5460835, and 6610219. They compose a small overlap of double-lined spectroscopic systems (SB2s) with ≥6 number of APOGEE visits and were not being studied by the EB Working Group.

The radial velocities of the SB2 spectra are derived using a multi-order version of the Two-Dimensional Cross-Correlation algorithm called `TODMOR` (Zucker & Mazeh, 1994; Zucker et al., 2003; Kiefer et al., 2018). We refer the reader to Kiefer et al. (2016) for a full description of the method and summarize the technique in brief here. First, we normalize each APOGEE spectrum by a percentile rank-filtered version of itself (Hodgson et al., 1985; Faigler et al., 2015; Halbwachs et al., 2016). Empirically, we fix the percentile at the 75%-level and the window size at 50 Å, a compromise to suppress undesirable deformation of the pseudo-continuum but conserving the narrower stellar lines. For each target, the spectra with the largest separation of the components are then matched by χ^2-optimization with 2 synthetic spectra from the PHOENIX library (Hauschildt et al., 1999). The synthetic spectra are also normalized with the same procedure, and broadened to match the line spread function of APOGEE. Averaging over all selected spectra, we obtain stellar parameters for both components of each binary system, including effective temperature, surface gravity, metallicity, flux ratio at 1.6μm, and $v \sin i$. Finally, we calculate the two-dimensional cross-correlation function of each observed spectrum and the two synthetic spectra, as explained in Zucker et al. (2003), to derive the RVs of both binary components simultaneously.

2.3 Results

We present the results of our simultaneous SED + LC modeling of 728 *Kepler* EBs. We find that the majority of our models are good fits to the data. In Tables 2.2 and 2.3, we list orbital and stellar solutions for a small subset of EBs in our sample, respectively; these inferred binary parameters correspond to the 50th percentile values of the MCMC chains after burn-in, with error bars corresponding to 16th and 84th percentile values.

The formal uncertainties on mass, age, and metallicity, likely underestimate true, physical uncertainties, as they are reliant on the input stellar isochrone models. *Kepler* light curves, with their continuous, high-precision 30 min cadence data, offer exquisite constraints on the timing and shapes of eclipses, which map onto the precision of retrieved orbital elements. The inferred geometric elements are particularly precise if the system exhibit flat-bottomed primary and/or secondary eclipse, as total or annular eclipses break degeneracies associated with inclination. For low signal-to-noise or shallow eclipses, however, there is less constraining power in parameters that influence the duration and shapes of the eclipses, such as $e \sin \omega$ vector, impact parameter (inclination), radius ratio, and flux ratio. This degeneracy is a general problem in eclipse modeling, and may be ameliorated by additional spectroscopic (e.g., flux ratios if systems are SB2s) or astrometric constraints. We note that about 10% of our total EB sample have shallow eclipse depths (PE and SE depths < 0.05), which are susceptible to degeneracies associated with inclination, and thus may not have unique solutions.

Furthermore, the 50th percentile values for each parameter frequently correspond to a model which is a poor fit to the data, because the probability distributions are highly asymmetric; therefore, we also report parameter values corresponding to the maximum likelihood (ML) model in Table 2.4. We show the ML fits to the SED and light curves, for 5 targets in Figures 2.1 to 2.5; these exhibit a range of orbital and stellar parameters, and demonstrate both the versatility and pitfalls of our modeling technique. The full suite of data products for all EBs modeled, including maximum likelihood fits and posterior parameter distributions plots, are available in the Github repository[2].

2.3.1 Goodness of Fit

To quantify the goodness of fit for our EB sample using our technique, we measure median absolute scatter between our models and LC+SED data. Figure 2.6 shows the distribution of residuals for the time series *during eclipse* (top) and multi-band (bottom) photometric fits, in log space. For a majority (75%) of EBs in our sample, the median residuals are $\lesssim$1 parts per thousand and $\lesssim$0.1 mag for light curve and SED, respectively, indicating that in general model solutions well describe the data (see, e.g., Figures 2.1, 2.2, and 2.5). We quantify light curve jitter or "white" noise by computing the median absolute difference (MAD) in out-of-eclipse flux, and overplot the MAD distribution (red dashed line) against the residual distribution for comparison. Note that the MAD noise level computed here typically underestimates true noise in the *Kepler* light curves, because it does not account for correlated noise due to e.g., spot modulation, Doppler beaming, and third body perturbation (see e.g., Figure 2.3). Nevertheless, the majority of systems have model residuals comparable to the white noise, while about 25% of modeled systems appear to have residuals larger than measured jitter. Systems with morphology parameter >0.5 (shown in orange) systematically exhibit larger residuals in the light curve and in the SED; these are typically short period ellipsoidal or interacting binaries (see, e.g., Figure 2.4). We further discuss sources of noise that may cause additional scatter during eclipse, as well as sources for the long tail of large residual distributions in §2.4.2.

---

[2] `https://github.com/savvytruffle/keblat/`

2.3.2 Orbital Properties

The observed sky-projected orbits of binaries can be described by their period P, eccentricity e, argument of periastron ω, inclination i, and semi-major axis a. We generate population statistics and histograms using the 50th percentile MCMC posterior values. These distributions provide consistency checks and insight into the physical processes that shaped the binary systems' dynamical states and histories, in the context of observation and selection biases. To fit each distribution, we compute the 50th percentile x-axis values in each bin, and assign Poisson error to bin counts. We adopt this method to generate histograms over convolving posterior probability densities for simplicity, and confirm that this approximation is valid by checking that the 1σ uncertainties for each system are much smaller than the histogram bin width. Figure 2.7 shows the resulting distributions for relative orbital size, eccentricity, inclination, and period.

The binary period distribution of our sample (upper left panel of Figure 2.7) peaks around $P \sim 4$ d and follows a gamma distribution with $\alpha = 7.6, \beta = 4.7$. The shape reflects our target selection process; for reference, the period distribution of the entire VKEBC is shown in dark orange and given half weight to keep the y-axis within range. The decline in the number of $P < 3$ d EBs in our sample relative to the full catalogue is a direct consequence of selecting for `morph`<0.6 binaries, i.e., at least semi-detached (SD) systems, as over-contact systems are more likely found around binaries with small separations; by contrast, the underlying *Kepler* EB distribution peaks around $P \sim 0.5$ d.

The inclination distribution is shown in the top right panel, where we fold the values about 90°. The distribution peaks around ~edge-on, as expected for eclipsing geometries, and can be roughly fit by an exponential distribution with $\lambda = 0.28$. The tail of the distribution is somewhat heavy because a large portion of the EBs in our sample have short periods ($P \approx 1-2$d), which allows for smaller inclination values (less edge-on) to satisfy the condition for eclipse: $|a \cos i| \leq R_1 + R_2$ for circular orbits. We expect this tail may be even larger if we relaxed the `morph` < 0.6 criteria, as higher morphology values correlate strongly with shorter periods and thus higher eclipse probability.

The eccentricity distribution (bottom left panel) cannot be described by a single population, as evidenced by the bimodal distribution in $\log e$ with peaks around -1.6 and -0.5 ($e \approx 0.03, 0.3$, respectively). The excess of ~circular binaries is expected, given the predominance of shorter period $P < 10$ d binaries in the sample, which are typically tidally circularized (Zahn & Bouchet, 1989); this peak near circular orbit would be even stronger if we included the full VKEBC sample, which contain more short period EBs. The lower right panel of Figure 2.7 shows the distribution of binary orbital separations as the sum of stellar radii relative to the semi-major axis, $\frac{R_1+R_2}{a}$. This is to first order a proxy for light curve morphology; smaller values indicate the stars take up a small fraction of the average orbital separations, while larger values mean the sizes of the stars are comparable to their orbital separation. In the latter case, the stars would experience large tidal forces, resulting in orbital circularization and ellipsoidal deformation of stellar surfaces. Indeed, EBs in our sample with higher morphology values (`morph`> 0.5) represent the bulk of systems with large fractional radii. The turnover at larger $\frac{R_1+R_2}{a}$ values is a consequence of our input criteria to exclude `morph`>0.6 binaries, which are more likely to be tidally interacting.

Figure 2.8 illustrates the morphology (top), inclination (middle), and eccentricity (bottom) of EBs in our sample as a function of their period. Morphology parameter values are truncated at our input cut-off of 0.6, and decline with increasing period, such that $P \gtrsim 10$ d systems are typically well-detached binaries. This trend encapsulates the effect of tidal forces which scale inversely and steeply with orbital separation. Shorter period binaries ($P < 5$ d) have higher ellipsoidal amplitudes and are more likely to interact, and thus have larger morphology values in general. Roughly 18% of our total sample have `morph`$\geq$0.5.

As expected, binary inclination tapers to ~edge-on (90°) at longer orbital periods (middle panel), due to observational bias in the geometry of detecting eclipses. The orbital separations of very short period binaries ($P < 4$ d) are small enough that grazing eclipses still occur for orbits that are inclined significantly with respect to the observer ($i \sim 70^\circ$). Eclipsing binaries that harbour circumbinary planets (Doyle et al., 2011; Welsh et al., 2012; Orosz et al., 2012b,a; Schwamb et al., 2013; Kostov et al., 2014; Welsh et al., 2014; Kostov et al., 2016) are highlighted as orange stars; they are well-aligned systems with $P \approx 10 - 50$ d.

The eccentricity-period plot (bottom panel) shows the prevalence of tidal circularization in binaries with orbital periods $\lesssim$10 d. This result is consistent with findings from previous studies of *Kepler* binaries (Van Eylen et al., 2016; Price-Whelan & Goodman, 2018), although we do not recover a significant difference in the fraction of eccentric binaries with respect to hot and cold stellar components (Van Eylen et al., 2016).

2.3.3 Stellar Properties

Next, we present the distributions of stellar parameters ($\tau = \log_{10}(\text{age [yr]})$, mass ratio Q, surface gravity $\log g$, and temperature T) of our EB sample in Figure 2.9. The age distribution (upper left panel) is bimodal, with a strong peak between ∼1-10 Gyr as expected, and another broad but much smaller distribution at younger ages, centered around $\tau \sim$7, or 10 Myr. Were the stellar distribution drawn from a uniform distribution in formation timescale over 10 Gyr, which approximates the star formation of the Galactic disk from which this sample is drawn, then we would only expect ≈1% of stars with ages < 100 Myr and ≈0.1% with ages less than 10^7 yr, rather than the ≈10% for $\tau < 7$ and ≈25% for $\tau < 8$ which comprise our sample. The over-representation of young ages corresponds to instances where single-star isochrones poorly predict the observed stellar properties, and we discuss the age results further in §2.4.2

The $\log g$ distribution (upper right panel) shows that the majority of detached EBs in the *Kepler* sample are dwarfs ($\log g \sim$4.5), although about 10% of them have started to evolve off the main sequence as subgiants with $\log g < 4$. We decompose the $\log g$ distributions of primary (dark grey) and secondary (light grey) components, and stack them vertically. The $\log g$ distributions for EB primaries and secondaries peak at slightly different values: 4.2 and 4.5, respectively. For reference, we overplot (in dark orange) the distribution of $\log g$ from the full *Kepler* Objects of Interest catalogue (KOI), i.e., single stars. The combined (primary + secondary) $\log g$ distribution is similar to the underlying KOI $\log g$ distribution in that both KOI and KEBLAT EB surface gravity distributions $\log g \sim 4.5$, consistent with main sequence dwarfs. However, there is a discrepancy between KOI and overall KEBLAT EB samples in the $\log g \approx 3.8 - 4.2$ range, where slightly evolved sub-giants are overrepresented in our sample compared to KOIs. The $\log g$ distribution for our sample's primary stars also peaks at a lower $\log g$ value than the full KOI sample. These differences may not be significant, given typical uncertainties in KOI $\log g$ values are 0.4 (Brown et al., 2011), although it may be related to the higher eclipse probability for stars of larger radius.

The mass ratio distribution ($Q = M_2/M_1$; lower left panel) shows a general positive trend. Typically, $Q > 1$ systems indicate one or both of the components are not normal stars, i.e., non-MS or mass exchange has modified a system's nascent binary mass ratio. For plotting purposes here, however, we invert the mass ratios for $Q > 1$, and stack the resulting histogram on top of the $Q \leq 1$ population, so that the values are in the range [0, 1]. The combined distribution contains a dearth of low-mass companions ($Q < 0.3$) and strongly favours similar-mass binaries ($Q \sim 0.95$), consistent with spectroscopic results of solar-type binaries by Raghavan et al. (2010) and Tokovinin et al. (2006). This increasing Q trend, *if physical*, should reflect formation values, as our morphology cut disfavours semi-detached binaries and excludes overcontact binaries, e.g., W Uma systems, which are able to exchange mass and evolve away from their nascent Q values (see, e.g., Rucinski, 2001; Yakut & Eggleton, 2005; Gazeas & Niarchos, 2006). We further discuss the reliability of mass ratio inference in §2.4.1.

Here, we briefly consider how observational biases (e.g., eclipse probability) and the input selection criteria (e.g., `morph`<0.6, SE depths) may affect this apparent mass ratio trend; quantifying the combined selection function of *Kepler*, the VKEBC, and our sample is beyond the scope of this work. Since eclipse probability and morphology values decrease with increasing period (see Figure 2.8), we examine the distribution of mass ratios in different period bins. The lower right panel of Figure 2.9 shows Q distributions (for $M_2/M_1 \leq 1$ only) for very short ($P < 4$ d; blue solid), short ($4 \leq P < 10$ d; orange dashed), and long ($P > 10$ d; green dotted) period binaries, where mass bins are widened relative to the cumulative Q distribution to account for low bin counting. Within Poisson counting noise, we find no significant deviations in Q distributions across different binary period bins. We expect eclipse probability to be relatively uniform across Q and not affect their distribution per orbital period bin, except at very low mass ratios which preferentially produce extremely shallow secondary eclipses.

2.3.4 H-R Diagram for Kepler *EBs*

Using predictions from stellar isochrones based on best-fit SED+LC models, we plot luminosity in absolute *Kepler* magnitudes, temperature, and metallicity for our EB sample in Figure 2.10. The resulting H-R diagram shows a spread in the main sequence, with a smattering of evolved stars, but no prominent red giant branch. The lack of giants is likely due to a combination of bias in isochrone fitting and target selection. The target selection is affected both by 1) colour cuts in the *Kepler* catalogue and 2) the morphology cut we made for our sample of ~detached EBs. In the first case, *Kepler* was designed to detect Earth-size planets around Sun-like stars and selected for FGK dwarfs. In the second case, our morphology cut may bias the sample because red giants are low density, and thus much more easily distorted by gravity and produce (over-)contact morphologies, which are preferentially excluded. Although there is some giant contamination, the majority of *Kepler* input catalogue targets are dwarfs. Berger et al. (2018) recently measured precise radii for ~200,000 *Kepler* stars using *Gaia* DR2 parallaxes and properties from the DR25 Kepler Stellar Properties Catalog (Mathur et al., 2017), and found that only 23% and 12% of the stars are subgiants and giants, respectively. We find $\sim 18\%$ and $\sim 10\%$ of the primaries and secondaries in our sample have $\log g < 4$ (see upper right panel of Figure 2.9). We discuss how isochrone fitting may bias the age and $\log g$ results for KEBLAT EBs in Section 2.4.

2.3.5 ETV Systems and Triple Candidates

In addition to extracting binary properties, we visually inspected the light curve fits of all EBs modeled and identified 84 systems with eclipse timing variations (ETVs), potentially due to perturbations by a tertiary companion or apsidal motion from tidal deformation of binary components. Out of these 84 systems, one is a confirmed circumbinary planet host (i.e. Kepler-16/KIC 12644769, see Figure 2.5) and 48 have been previously identified and characterized (Gies et al., 2012; Rappaport et al., 2013; Conroy et al., 2014; Orosz, 2015; Borkovits et al., 2016), leaving 35 newly identified candidates. We list all ETV systems identified in this work in Table 2.5, where additional lettering denotes provenance of previous identification, and reported periods, mass ratios, and eccentricities correspond to maximum-likelihood solutions.

The ETVs typically manifest in the light curve residuals as additional scatter around eclipse ingress and egress, with a "pinching" at the center of eclipse, see, e.g., Figures 2.3 and 2.5. Because ETVs cause eclipses to shift back and forth in time, the residuals take on a shape proportional to the derivative of the light curve. They are largest when the slope of the eclipse is steepest but decline to zero mid-eclipse where the slope is zero, which is responsible for the pinch. Stellar pulsations or starspot modulations may confound ETV signals or lead to false positives; however, these stellar variations tend to affect the entire range of the eclipse and take on a shape similar to the shape of the eclipse. We note that because the systems reported here are inspected by eye, they are typically cases with strong ETV signals and do not comprise a homogeneous sample. Both Conroy et al. (2014) and Orosz (2015) refer to a large, comprehensive study of triples in well-detached *Kepler* EBs still in development by Orosz, in prep, which would be a source of detailed characterization not carried out here.

2.3.6 APOGEE-derived Mass Ratios

As a part of our investigation into the reliability of KEBLAT (non-RV) mass ratio estimates as compared to RV-derived Q, we measured and modeled RVs from APOGEE spectra for three SB2 systems in our sample, KICs 5284133, 5460835, and 6610219 (see §2.2.7 for a description of the RV extraction and model). This is an independent analysis from KEBLAT, without LC or SED information or priors, and relies on software from Kiefer et al. (2018).

Absolute masses of the individual components require the inclination constraint from the light curve and cannot be derived from the RV alone; however, the mass ratios depend only on the ratio of RV semi-amplitudes. We present mass ratio solutions for the three SB2s in Table 2.6, and show the best-fit radial velocity solutions in Figure 2.11. We discuss these results in the context our larger SED+LC modeling effort in §2.4.1.

2.4 Discussion

Here, we examine the robustness and limitations of our binary model and results. In particular, we determine the accuracy of our EB properties by comparing them to various previous studies published in literature, including RV studies which yield direct measurements on mass (see §2.4.1). We are able to reliably infer masses using only photometry for detached, main-sequence binaries. Our solutions are not broadly applicable for EBs with components modified by mass transfer or with red giant companions, as they are not well captured by theoretical isochrones. In §2.4.2, we discuss these caveats and devise diagnostics to identify them using observables and model parameters.

2.4.1 Reliability of Parameter Estimation

Mass Measurements

We compile from several radial velocity studies a list of *Kepler* EBs with published mass solutions common to our sample in Table 2.7. These masses represent RV "truths" with which we compare our photometry-only mass inferences. We adopt the mass ratio Q, a quantity independent of inclination, to compare our results; this allows us to use the APOGEE-derived mass ratios from our independent RV analysis.

Figure 2.12 compares KEBLAT mass ratios to RV solutions from the literature for an overlap sample of 55 EBs. The majority of data points lie close the one-to-one line, with a cluster of discrepant values around KEBLAT $Q \sim 0.75$. We hypothesize that differences in the sub-population of binaries within the overlap sample may explain the varying levels of Q

agreement. We use a mixture model to test our hypothesis and quantify the degree of fitness. Following the convention of Hogg et al. (2010), we include a linear trend (the "foreground" model) and assume the outliers are drawn from a Gaussian distribution (the "background" model). We sample the mixture model with `emcee` and compute the marginalized posterior probability that each data point belongs to the foreground model P_{FG}. We use a threshold $P_{FG} = 10^{-16}$ to split the sample into "foreground" (42 EBs) and "background" (13 EBs) populations for additional analysis.

We investigate the EBs from the "background" or outlier distribution and find they cluster toward two distinct groups: (i) binaries with morphology values > 0.5 (e.g., ellipsoidal or Algol-type binaries) and (ii) binaries with one or more red giant components. These systems are not robustly fit by KEBLAT because of the inherent model assumptions; our method does not treat non-Keplerian effects such as tidal deformations that may be present in higher morphology systems, and it is reliant on theoretical isochrones, which cannot self-consistently describe systems that have undergone mass transfer. Moreover, the post-MS evolutionary phases are short lived, where small perturbations in mass or age can lead to large differences, or discontinuities in radius, making it difficult to capture via isochrone fitting. While KEBLAT successfully retrieved the mass ratios of *some* `morph`>0.5 and red giant binaries, it typically failed to reproduce physically self-consistent solutions. Instead, the solutions tended toward young, $Q > 1$ massive stars with large radius ratios to satisfy the light curve eclipse constraints. One underlying symptom of these mass ratio outliers is that they typically have artificially young derived ages; we discuss this in further detail in §2.4.2.

We perform linear regression on the "foreground" EB population (e.g., with outliers removed) in our mixture model and use a systematic uncertainty term $\sigma_{Q,\mathrm{sys}}$ to quantify the accuracy of KEBLAT-derived masses with respect to RV solutions. We find that they correlate linearly with slope $m = 0.95 \pm 0.06$, intercept $b = 0.01 \pm 0.05$, and systematic error $\sigma_{Q,\mathrm{sys}} = 0.1 \pm 0.02$. This agreement indicates that KEBLAT mass ratios are reliable to $\sim$0.1 for well-detached, main-sequence binaries. Additionally, we demonstrate the agreement for absolute masses between KEBLAT and RV analyses. Figure 2.13 shows primary (filled circle) and secondary (open circle) masses in the overlap sample, after removing EBs with red giant components and `morph`>0.5. The inferred masses from photometry-only are in accord with RV values to within 15% of the mass of the star (represented by the grey region). We note that not all of the RV studies included simultaneous light curve modeling in their analysis, which may introduce $\sin i$ corrections in the RV absolute masses at the 2% level; this bias is small relative to the scatter between RV and KEBLAT values, and so we do not account for it.

In addition to the RV studies, a small number of *Kepler* EBs in our sample overlapped with systems observed by the Trans-atlantic Exoplanet Survey (TrES) and modeled by Devor et al. (2008). Their method (MECI) was similar to ours, and used ground based light curves and archival 2MASS photometry in conjunction with isochrones to predict binary masses, but does not use parallax as a constraint upon the model. We applied a quality cut to their catalogue, and selected only for overlap binaries with reduced $\chi^2 < 2$. Figure 2.14 shows the agreement in primary and secondary mass between KEBLAT and MECI analysis; in general, the masses agree to 20%, despite both analyses relying only on photometry and adopting different isochrones, data sets, and model details.

For mass inference, the comparison results above indicate that masses derived from photometry here are reliable for well-detached, main-sequence binaries, which comprise the majority of our sample. We recommend approaching systems that have morphology parameter > 0.5, young age estimates ($\tau \lesssim 7.5$), and large radius ratio ($R_2/R_1 \gtrsim 2$; indicative of red giant secondaries) with caution.

Orbital Elements and Stellar Radii & Temperatures

We compare our inferred eccentricities, inclinations, radii, and temperatures to solutions from the RV studies mentioned above. We supplement this comparison analysis with values from coarse ensemble parameter studies using light curve (Kjurkchieva et al., 2017) and SED (Armstrong et al., 2014a) information. Because the literature studies used here have varying degrees of robustness based on their model assumptions and data quality, we only consider their qualitative agreement. In general, KEBLAT solutions agree with published values from small-sample RV studies to within the measurement uncertainties, and share bulk trends with existing larger-scale light curve or SED studies of *Kepler* EBs.

Figure 2.15 shows that eccentricity, inclination, and radii values between KEBLAT and literature studies generally lie close to 1:1 relationships, denoted by the dashed black lines. The inclination values show good agreement with RV analyses (see lower left panel), with the exception of Matson et al. (2017) values; we suspect this is because their inclinations are based on machine learning results from phenomenological LC modeling rather than a physical LC model. The eccentricity values (upper left panel) are also generally in very good agreement with published RV work. Our values are broadly consistent with those from Kjurkchieva et al. (2017), although there is large scatter as their approach suffers from using binned phase data and only fitting e and ω while holding other parameters fixed at approximate relation values (see their §2). That is, they assume the eccentricity vectors do not correlate with radius, temperature, and other orbital parameters. However, binning or down-sampling the LC can change the eclipse profiles, especially at ingress and egress where the shapes are sensitive to eccentricity vectors, inclination, and stellar radii. Therefore, we expect our full forward modeling on the entire light curve to yield more robust results.

The upper and lower right panels show that our inferred radii demonstrate very good fidelity to results from RV studies. In particular, the red giant systems (Gaulme et al., 2016) show much better agreement in radii than mass (see Figure 2.12); while the eclipse shape tightly constrains binary radii, the isochrone fitting prefers a more massive MS secondary to a low-mass post-MS component to reproduce its large secondary radius. This may be due to large systematic errors in the isochrones for post-MS evolutionary phases (del Burgo & Allende Prieto, 2018) and/or insufficient parameter sampling of complex isochrone morphologies (see §2.4.2 for further discussion).

Figure 2.16 compares general *Kepler* EB properties derived in this study to those reported in Armstrong et al. (2014a). The goal of their work was to generate binary temperatures for the entire VKEBC, using Castelli-Kurucz (Castelli & Kurucz, 2003) model atmospheres to fit SEDs constructed from UBVJHK magnitudes. Their analysis differs significantly from ours; in particular, they did not utilize the light curves, except to use eclipse depths reported in the VKEBC to constrain T_2/T_1. As shown in the upper left panel, the effective temperatures of primary components inferred by KEBLAT generally agrees with Armstrong et al. (2014a) values as well, although there is a discrepant clump near KEBLAT $\log T_1 \sim 4.1$ vs. Armstrong $\log T_1 \sim 3.8$. This latter clump represents the eclipsing Algol population in our sample, previously mentioned in §2.4.1 and discussed further in §2.4.2. Armstrong et al. (2014a) used Gaussian priors centered around KIC values, with an adaptive upper limit of 13000K (see their Table 1), or $\log T$ ∼4.1, which explains the dearth of $\log T_1 > 4$. The temperature ratios generally agree (lower left panel), although there is a large scatter. This is to be expected, since Armstrong et al. (2014a) inferred the ratio of temperatures based on relative depth of eclipses as reported by the VKEBC, whereas here, we derive T_2/T_1 from a full forward model based on light curve and SED data. The upper right panel shows that primary radii values, normalized by estimated EB distance, agree well, while radius ratio as derived from KEBLAT and Armstrong et al. (2014a) has significant scatter (see lower right panel). In particular, the inset overlay shows that for a small range of KEBLAT R_2/R_1 values, there is a large, nearly uniform spread (0.5-1.0) in Armstrong radius ratios, which the authors state are poorly constrained in their study (see, e.g., Figures 4 and 5 and section 5.2.2 in Armstrong et al. (2014a)). Furthermore, we note that the data points with very large radius ratio values ($R_2/R_1 > 2$) are systems with confirmed red giant components (Gaulme et al., 2016).

2.4.2 Limitations & Diagnostics

We have demonstrated that our models produce good fits to the data for the majority of our sample and accurate parameter inferences for a subset of EBs with RV overlap. Here, we examine our model assumptions, the inherent limitations to our method, and their effects on our results. We recommend using age ($\tau \lesssim 7.5$) and morphology (`morph`>0.5) as diagnostics for systems which may be poorly described by our model, and comment on future improvements.

Correlated Noise in the Light Curve

In addition to stochastic “white” noise, *Kepler* light curves exhibit correlated noise, due to both instrumental systematics, e.g., telescope drift, and astrophysical effects, e.g., stellar variability, contaminant light from nearby sources (see Gilliland et al. (2015) for a discussion of *Kepler* noise properties); sources of astrophysical “noise” may be equivalently considered as “signals.” A low-order, local polynomial fitting around each eclipse is typically sufficient for light curves of detached systems and minimal stellar variability. For EBs with strong quasi-periodic out of eclipse variation, such as those with `morph`>0.5 which comprise the majority of poor fits in Figure 2.6, a low-order polynomial may not sufficiently capture the variability, giving rise to larger residuals.

For single star targets, stellar variability, typically in the form of starspot rotation (Giles et al., 2017), stellar oscillation and granulation (Bastien et al., 2013; North et al., 2017), flares (Davenport, 2016), confound astrophysical signals. For EBs in our sample, the presence of a secondary star adds two levels of confusion: 1) stellar variability associated with the companion itself and 2) light curve effects due to dynamical interactions and binary evolution, such as ellipsoidal variations, gravity darkening, Doppler beaming, and reflection (Faigler et al., 2013). For case 2, the amplitudes of Doppler beaming and reflection/ellipsoidal effects for similar-mass, P$\lesssim$5 d solar-type binaries can be of order 1 and 10 ppt, respectively (Zucker et al., 2007). Binaries in our sample with morphology parameter $\gtrsim 0.5$ are most affected by these effects, in particular ellipsoidal variations, and account for some of the population with larger residuals in Figure 2.6 (see orange vs. blue bins).

For the goal of large ensemble binary parameter inference from only photometry using MCMC, including a full physical treatment of tidal distortions and other photodynamical effects would be significantly more computationally expensive. Well-established numerical codes that include detailed physics already exist, such as `ELC` (Orosz & Hauschildt, 2000) and the Wilson & Devinney (1971) based code `PHOEBE` (Prša et al., 2016), where stellar surfaces are modeled on a mesh or grid and allowed to deform. These numerical codes provide higher fidelity to the physics of close binaries at the expense of computational speed. A more computationally tractable method may be to use analytic approximations to explicitly describe ellipsoidal, beaming, and reflection effects, such as the `BEER` algorithm (Faigler & Mazeh, 2011). However, this approach would still benefit from an appropriate treatment of additional correlated instrumental noise and stellar variability.

In principle, using Gaussian process (GP) kernels to model instrumental and astrophysical noise in conjunction with a simple physical binary model may lead to better light curve fitting fidelity. The kernel parameters may additionally give insight into the physical processes that underlie the observed quasi-periodic variations. For example, Angus et al. (2018) applied GPs to infer stellar rotation periods for a subset of *Kepler* objects of interests. In practice, however, we found that including GPs in our method to model *Kepler* EB light curves significantly increased computational time and required more user input on specific systems to assess kernel type and initial parameter choice; using GPs on *K2* or *TESS* light curves, which typically has ~month long coverage rather than ~year, may be more computationally tractable. We leave implementing GPs on correlated noise as future work, and note that `celerite`, a newly developed algorithm that scales with the number of data points, i.e., $\mathcal{O}(N)$, might make significant improvements to computation time and fitting flexibility.

Third Light Contamination

Here, we consider the effects of "third light contamination," or photometric contamination associated with background/foreground source(s) coincident to or companion(s) gravitationally bound to the binary. As mentioned in §2.2.3 and §2.2.4, we fit for quarterly *Kepler* contamination values during model optimization; however, we do not explicitly and self-consistently model flux dilution in the SED by additional sources, due to the limited number of SED measurements, as well as increased model complexity associated with specifying a third isochrone and differential point spread functions (PSFs) with wavelength. Instead, the SED module fits for a single systematic error term, i.e., any additional error beyond observational uncertainties, including third light contamination. This systematic error term should sufficiently capture contributions to the SED from relatively faint contaminators.

Kepler photometry is more susceptible to flux contamination than the Johnson, SDSS, 2MASS bands because of the instrument's large pixel scale and aperture radius[3] (e.g., Schwamb et al., 2013; Morton, 2012). While WISE bands 1 and 2 share similarly large aperture radii ($\sim 6''$; Kennedy & Wyatt, 2012), the PSFs from optical and near-IR observations are small. As a result, many of the sources that apppear blended in *Kepler* and WISE photometry are expected to be resolved and contribute minimally to the bulk of the SED data in the optical and near-IR.

Unresolved contaminators (e.g., point sources at small angular separations $<1''$) that are bright relative to the binary (e.g., giants or similar mass dwarfs) will introduce wavelength-dependent bias to the observed SED. If their contribution deviates significantly from *Kepler* quarterly estimates, they will also dilute the expected depth of eclipses. As we explain below, overall, we expect that only a small fraction (few percent) of our sample are deleteriously affected by bright, unresolved contaminants.

We estimate the extent to which these sources may affect our sample in two ways: 1) by using order of magnitude statistical arguments and 2) by identifying correlated characteristics in inferred model parameters. In the former case, we make the assumption that the majority of these unresolved sources are gravitationally bound, co-eval tertiaries. Tokovinin et al. (2006) found that the fraction of SB2s with tertiary companions in the period range $P_{\rm tertiary} = 2 - 10^5$ yr depends strongly on the inner binary period, reaching $\sim$90% for $P \lesssim 3d$ and $\sim$35% for $P \gtrsim$10 d. Studies of triples around largely short period ($P < 10$ d) *Kepler* EBs, with $P_{\rm tertiary} \lesssim 4$ yr, have converged on an occurrence rate of $\sim$15% (e.g., Gies et al., 2012; Rappaport et al., 2013; Conroy et al., 2014). Based on these values, we assume that $\sim$30% of our EBs host additional unresolved companions. Since the majority of tertiaries have

---

[3] https://keplerscience.arc.nasa.gov/the-kepler-space-telescope.html

detected masses smaller than the binary mass (Tokovinin, 2008; Borkovits et al., 2015), we estimate that 1/3 of triples, or ∼10% of EBs in our sample may harbour companions with significant flux contribution.

In our analysis, we expect that systems with substantial wavelength dependent flux contamination will introduce bias to the total spectral shape (skew) and to the distance modulus (offset). As a result, they may exhibit large inferred systematic SED errors $\sigma_{\rm sys,SED}$ and distance errors σ_d. We find that 5% of our sample have $\sigma_{\rm sys,SED} > 0.1$ mag and $\sigma_d > 200$ pc. This value of a few percent appears consistent with the order of magnitude estimate from the statistical approach. However, as discussed in §2.2.4, §2.4.2, and §2.4.2, other effects can also cause large σ_d and $\sigma_{\rm sys,SED}$ values.

As an example, we note that KIC 4862625 is a binary with a pair of companions separated by $0.7''$ in a hierarchical quadruple configuration. The companion binary contributes ∼10% and ∼20% of the total flux in the *Kepler* and K_s bands (Schwamb et al., 2013). Despite this, our stellar inferences ($M_1 = 1.33{\rm M}_\odot$, $M_2 = 0.38{\rm M}_\odot$) agree remarkably well with published values ($M_1 = 1.38 - 1.53{\rm M}_\odot$, $M_2 = 0.387 - 0.408{\rm M}_\odot$; Schwamb et al., 2013; Kostov et al., 2013).

Isochrone Inaccuracies & Fitting Biases

An inherent limitation to our model is that it relies on theoretical stellar models, which may contain inaccuracies and generate fitting biases. In particular, the complex morphology of isochrones challenges uniform parameter space sampling (Jørgensen & Lindegren, 2005), and the predictive power of isochrones is weak for low mass dwarfs (e.g., the radius inflation problem; Stassun et al., 2012), post-MS evolutionary phases (e.g., red giants; Cassisi, 2017), and stars that exchange(d) mass. These factors lead to discrepant mass values when compared to RV studies (§2.4.1) and the population of over-represented young ($\tau < 8$) stars in our general sample (§2.3.3). While young ages may be used as consistency checks to the fidelity of stellar isochrones, stringent tests and calibration of stellar evolution models will require the bulk collection of precise radial-velocity measurements of these eclipsing binaries, such as expanding upon the initial survey of EBs with APOGEE (Zasowski et al., 2013; Badenes et al., 2018).

The morphology of stellar isochrones, in which small perturbations in mass, age, or metallicity can lead to large differences in radius, temperature, and luminosity, challenges uniform sampling of input parameters based on observables. This is particularly true during post-MS evolutionary phases, which apply to RG binaries in our sample. While masses do not always agree, KEBLAT radius values track RV solutions remarkably well for them (see Figure 2.15). This indicates that the isochrones are converging to young, higher mass MS secondaries with large radius values in order to reconcile $R_2/R_1 \gg 1$ based on the eclipses. One means of improving isochrone interpolation for future implementations may be to adopt an "Equivalent Evolutionary Phases" method (Dotter, 2016), in which isochrones are transformed onto a uniform basis that samples evenly different evolutionary phases, rather than evenly in absolute timesteps. Another potential solution for better sampling is to fit the isochrones with a multi-dimensional Gaussian process and compute derivatives of the GP with respect to model parameters; these derivatives would enable more robust optimization and Hamiltonian Markov Chain (Duane et al., 1987) analysis[4] to more efficiently sample parameter space.

Another reason why isochrone fitting might fail for red giants is that theoretical radius predictions may be too uncertain (e.g., poor constraints on mass loss, convective overshooting parameters) for the level of precision needed to fit flat-bottomed eclipses in the *Kepler* light curves. Astereoseismic studies of red giants, which have been revolutionized in the era of *Kepler* and *CoRoT*, can provide more reliable and physically motivated constraints on mass relative to our method, and better calibrate stellar models.

In addition to post-MS evolution uncertainty, theoretical models do not reproduce observations of M-dwarfs well. Several studies have shown that low-mass ($M \approx 0.1 - 0.8\mathrm{M}_\odot$)

---

[4] Hamiltonian Markov Chain or HMC uses concepts from Hamiltonian dynamics to sample the posterior distribution of parameters, by introducing a momentum state. It modifies Metropolis Markov chain update procedures with position and momentum state proposals/trajectories found using a leapfrog integrator. See Neal (2012) for details.

dwarfs have radii inflated relative to theoretical models, up to ∼ 15% (Stassun et al., 2012; Kraus et al., 2011; Cruz et al., 2018). This radius inflation is coupled by a corresponding decrease in effective temperature, such that the mass-luminosity relationship (for MS stars) is preserved. The presence of radius discrepancies appears to be agnostic to stellar multiplicity (Kesseli et al., 2018). Multiple studies agree that radius inflation is associated with magnetic field activity, although they diverge in their conclusions about the relative importance of rotation-induced surface magnetic fields and their potential effects on stellar radii via convective inhibition, dark spot coverage, and tidal synchronization in binaries (Chabrier et al., 2007; Stassun et al., 2012; Feiden & Chaboyer, 2014; Kesseli et al., 2018).

The PARSEC isochrones we used in our SED+LC model included improved calibration for low mass stars with radius discrepancy at the ∼ 5% level (Chen et al., 2014). Binaries with anomalously young M-dwarfs may be explained by the model attempting to compensate for a larger radius than theoretical models predict; stars that have not yet started core H fusion, i.e., reached the main sequence, are still contracting, and thus have larger radii compared to their MS counterparts. For M dwarfs, the pre-MS stage may last ∼ 10 Myr to ∼ 2.5 Gyr, consistent with inferred youthful ages. Allowing a factor for radius inflation might help in modeling these stars. However, because the luminosity-mass relation for M dwarfs is well calibrated, a radius inflation factor necessarily requires a corresponding scaling relation to lower the effective temperature, which in turn affects the predicted SED. This makes treating the issue in a self-consistent way difficult.

Finally, our model assumes that stars fall on coeval isochrones, an assumption which can be strongly violated in binaries which have undergone mass-transfer. The majority of binaries with anomalously young ages in our general sample and with discrepant masses in our RV comparison sample appear to be Algol-type binaries. These are systems with primary masses between 2-4 $M_\odot$ (Ibanoğlu et al., 2006), V-shaped eclipses, and typically exhibiting semi-detached morphologies (see e.g., Figure 2.4). In these eclipsing Algol systems, mass transfer occurs from the more evolved and initially more massive component which has filled its Roche lobe onto the less massive companion; as the companion accretes more mass, it is “rejuvenated” becoming hotter, more massive, and delaying evolution away from main sequence. Stellar evolutionary tracks of single-stars cannot accurately capture masses and ages of stars in Algol-type binaries because they do not take into account modification due to binary evolution. Because the primary components of Algol-type binaries are typically “main sequence” stars with high mass (O, B, A dwarfs), we expect the ages of this population to be skewed toward young populations. One possible ad-hoc solution to these rejuvenated systems is to allow the ages of both stars to vary independently, although such a treatment may not be physically self-consistent, and the additional degree of freedom may pose further difficulties in efficiently sampling the full parameter space. Alternatively, the same mechanism that enables mass transfer, i.e., when a star fills its Roche lobe, can be used to constrain mass ratios in EBs with semi-detached or over-contact light curve morphologies; this method has demonstrated success for totaling eclipsing SD or OC systems (Wyithe & Wilson, 2002).

2.5 Conclusions

We have modeled the light curves and SEDs of 728 ∼detached *Kepler* eclipsing binaries, using Bayesian inference for full binary parameter estimation. Our forward model couples Padova stellar isochrones to a Mandel & Agol (2002) transit model to solve the system’s stellar and orbital parameters with only photometric information. The entire set of posteriors and maximum likelihood solutions are available online.

We are interested in obtaining reliable orbital and mass solutions, in particular as the basis of an automated and optimized search for circumbinary planets. We find that binary orbital parameters are typically very well constrained by the light curve data, and comparisons for a subset of our sample with previous studies indicate that the majority are reliable.

Moreover, we show that detached, main sequence binaries give accurate masses relative to RV “truths.” Binary systems which have been affected by stellar evolution, or contain stars which are otherwise discrepant with isochrone predictions, however, may give poor agreement. The latter exhibit symptoms of higher morphology values (`morph`$\gtrsim$0.5) and artificially young stellar ages ($\tau \lesssim 7.5$), which may be used as a filter for quality check. These symptoms are manifestations of the inherent limitations associated with our approach: namely, that we do not account for non-Keplerian effects like ellipsoidal variations, and that we rely on co-eval isochrone models; the inferred stellar parameters are only as accurate as input theoretical models. On the other hand, discrepant results that arise from these limitations may help inform which binary targets warrant more time-intensive follow-up observations, to better calibrate theoretical stellar models. For future work, our methodology may be improved by additional *Gaia* systemic radial velocities. Currently *Gaia* does not provide these for targets flagged as binaries; once *Gaia* releases its spectroscopic catalogue, systemic RV can be estimated and, in conjunction with proper motion, the full 3-dimensional motion can provide additional constraints to binary ages based on galactic kinematics. Additionally, as we have discussed in §2.4.2, incorporating Gaussian processes into the time series and isochrone modeling may improve the robustness of our model to non-Keplerian light curve effects and post-MS stars.

We conclude by summarizing our key takeaways below:

1. We have created the largest, homogeneous catalogue of *Kepler* eclipsing binaries with full system parameters and posteriors from Bayesian inference. This catalogue is of interest to identify compelling targets for RV follow-up (e.g., M-dwarf binaries), and to binary population studies which require mass estimates and precise measurements of orbital elements (e.g., eccentricities), such as tidal theory and circumbinary planet searches.

2. We additionally identify 35 new systems with eclipse timing variations, perhaps arising from apsidal motion due to binary tides and/or tertiary companions.

3. We demonstrate that we can reliably retrieve mass using only photometry for well-detached, main sequence binaries, using comparisons to RV “truths.” These systems make up the majority of our sample.

4. For a subset of binaries with post-main sequence components or significant tidal defor-

mations (e.g., semi-detached systems where mass exchange have occurred), our inferred masses are not universally reliable, as our model does not account for non-spherical distortions and are limited by the fidelity of input stellar isochrones. We recommend using $\tau \lesssim 7.5$ and `morph`>0.5 to diagnose potentially problematic systems. Fortunately, photometric masses may be derived using asteroseismology (Gaulme et al., 2016) for red giants and by exploiting Roche lobe-filling configurations for semi-detached and over-contact binaries (Wyithe & Wilson, 2002).

5. The technique used here can be applied to OGLE, TESS, and other large time-domain photometric surveys coming online, such as LSST, to characterize large numbers of eclipsing binaries. As many of these surveys have all-sky coverage, this poses an intriguing opportunity to probe binary galactic archeaology.

Table 2.1. Model Parameters

Parameter	Meaning	Module†	Constrained by	Priors
P	period (d)	LC	time of eclipses	flat (0, 4000)
$e\sin\omega$	transformation of eccentricity	LC	ratio of PE + SE durations	flat (-0.95, 0.95)
$e\cos\omega$	& longitude of periastron	LC	time of PE + SE	flat (-0.95, 0.95)
$t_{\rm PE}$	time of primary eclipse (BJD-2454833)	LC	LC minimum	flat (0, 4000)
b	impact parameter $\frac{a\cos i}{R_1}$	LC	shape of eclipse	flat (-10, 10)
q_{11}, q_{12}	transformed quadratic limb darkening	LC	shape of eclipse	flat [0, 1]
q_{21}, q_{22}	coeffs for primary & secondary	LC	shape of eclipse	flat [0, 1]
$F_{\rm rat}$	Kepler flux ratio $\frac{F_2}{F_1}$	LC only	relative depth of eclipse	flat [1e-8, 100]
$R_{\rm sum}$	sum of radii (R$_{\odot}$)	LC only	duration of eclipse	flat [0.1, 1e6]
$R_{\rm rat}$	ratio of radii $\frac{R_2}{R_1}$	LC only	eclipse shape + relative depth	flat [1e-6, 1000]
$M_{\rm sum}$	sum of masses (M$_{\odot}$)	SED, LC*	shape of SED	flat [0.2, 24]
Q	ratio of masses $\frac{M_2}{M_1}$	SED	shape of SED	flat [0.0085, 2]
z	binary metallicity ($z_{\odot} = 0.015$)	SED	shape of SED	flat [0.001, 0.06]
τ	binary $\log_{10}$ age ($\log_{10}$(yr))	SED	shape of SED	flat [6, 10.1]
d	distance to system (pc)	SED	SED offset	Gaussian‡ $d_{\rm Gaia}, \sigma_d$
$E(B-V)$	reddening, assuming $R_V = 3.1$	SED	shape of SED	Gaussian $\{\mu, \sigma\}_{\rm Schlafly}$
h_0	dust vertical scaleheight (pc)	SED	shape of SED	fixed at 119
σ_d	uncertainty in *Gaia* distance prior (ln)	SED		flat [-1, 7]
$\sigma_{\rm E(B-V)}$	uncertainty in reddening prior (ln)	SED		flat [-12, 2]
$\sigma_{\rm sys,SED}$	systematic SED error (ln)	SED		flat [-25, 0]
$\sigma_{\rm sys,LC}$	systematic LC error (ln)	LC		flat [-25, -4]
c_j	crowding parameter for quarter j	LC	depth of eclipses	flat [0, 1]

Note. — †All parameters belong to the simultaneous SED+LC module, unless otherwise specified, e.g., "LC only."

*When only light curve data available, $M_{\rm sum}$ is a proxy for a, to obtain the sizes of stars relative to their separation.

‡ When no *Gaia* parallax available, the distance prior is flat on [10, 15000] pc.

Table 2.2. Eclipsing Binary Orbital & Distance Parameter Posteriors

KIC	P (d)	t_{PE} (BJD-2454833)	$e\sin\omega$	$e\cos\omega$	i (rad)	d (pc)
10031409	$4.143879363^{+4.5e\text{-}8}_{-4.6e\text{-}8}$	$124.5491837^{+9.6e\text{-}6}_{-1.0e\text{-}5}$	$0.0047^{+0.0014}_{.0012}$	$0.000007^{+0.000004}_{-0.000004}$	$1.4923^{+0.0002}_{-0.0002}$	941^{+23}_{-22}
10198109	$17.91874241^{+3.8e\text{-}7}_{-3.9e\text{-}7}$	$146.3930259^{+1.8e\text{-}5}_{-1.8e\text{-}5}$	$0.2787^{+0.0025}_{-0.0024}$	$0.2484^{+0.0002}_{-0.0002}$	$1.5825^{+0.0003}_{-0.0003}$	637^{+48}_{-22}
12356914	$27.30822669^{+9.3e\text{-}6}_{-9.4e\text{-}6}$	$143.5001244^{+2.7e\text{-}4}_{-2.8e\text{-}4}$	$0.4245^{+0.0154}_{-0.0153}$	$0.1213^{+0.0009}_{-0.0010}$	$1.5642^{+0.0014}_{-0.0013}$	1344^{+1}_{-14}
10619109	$2.045166167^{+3.4e\text{-}8}_{-4.7e\text{-}8}$	$122.139347^{+1.7e\text{-}5}_{-1.6e\text{-}5}$	$0.0676^{+0.0043}_{-0.0043}$	$0.00136^{+0.00008}_{-0.00013}$	$1.2260^{+0.0027}_{-0.0027}$	1081^{+24}_{-22}
12644769	$41.07759097^{+1.4e\text{-}6}_{-1.4e\text{-}6}$	$132.6583057^{+2.8e\text{-}5}_{-2.9e\text{-}5}$	$0.1641^{+0.0005}_{-0.0005}$	$0.017971^{+0.000004}_{-0.000004}$	$1.57659^{+0.00002}_{-0.00001}$	$68.6^{+0.5}_{-0.5}$

Note. — Posteriors for orbital & distance parameters for a subset of our sample which corresponds to Figures 2.1 to 2.5, to demonstrate the table's form and content. Full posteriors for all parameters available in online table. See Table 2.1 for details on parameter meanings.

Table 2.3. Eclipsing Binary Stellar Parameter Posteriors

KIC	z	τ (log(yr))	M_1 ($M_\odot$)	M_2 ($M_\odot$)	R_1 ($R_\odot$)	R_2 ($R_\odot$)	F_2/F_1
10031409	$0.011^{+0.002}_{-0.002}$	$9.37^{+0.16}_{-0.20}$	$1.13^{+0.04}_{-0.05}$	$1.08^{+0.04}_{-0.05}$	$1.183^{+0.009}_{-0.009}$	$1.085^{+0.022}_{-0.028}$	$0.7689^{+0.0245}_{-0.0289}$
10198109	$0.006^{+0.001}_{-0.002}$	$9.57^{+0.28}_{-0.71}$	$1.01^{+0.15}_{-0.08}$	$0.36^{+0.03}_{-0.01}$	$1.078^{+0.045}_{-0.025}$	$0.347^{+0.014}_{-0.008}$	$0.00473^{+0.00002}_{-0.00002}$
12356914	$0.007^{+0.002}_{-0.001}$	$9.77^{+0.20}_{-0.33}$	$0.94^{+0.08}_{-0.06}$	$0.60^{+0.02}_{-0.02}$	$1.026^{+0.014}_{-0.018}$	$0.587^{+0.014}_{-0.015}$	$0.0602^{+0.0020}_{-0.0013}$
10619109	$0.0023^{+0.0003}_{-0.0002}$	$6.25^{+0.01}_{-0.01}$	$2.48^{+0.04}_{-0.05}$	$1.87^{+0.02}_{-0.02}$	$2.619^{+0.016}_{-0.020}$	$3.038^{+0.018}_{-0.018}$	$0.2093^{+0.0131}_{-0.0118}$
12644769	$0.0100^{+0.00005}_{-0.00004}$	$10.0796^{+0.0003}_{-0.0006}$	$0.6002^{+0.0005}_{-0.0003}$	$0.1913^{+0.0003}_{-0.0002}$	$0.6092^{+0.0004}_{-0.0002}$	$0.2161^{+0.0003}_{-0.0002}$	$0.01582^{+0.00003}_{-0.00003}$

Note. — Posteriors for stellar parameters for a subset of our sample which corresponds to Figures 2.1 to 2.5, to demonstrate the table's form and content. Full posteriors for all parameters available in online table. See Table 2.1 for details on parameter meanings.

Table 2.4. Maximum Likelihood Parameter Solutions

Parameter	KIC 10031409	KIC 10198109	KIC 12356914	KIC 10619109	KIC 12644769
$M_{\rm sum}$	2.2751	1.2485	1.5222	4.3590	0.7919
Q	0.9536	0.3731	0.6604	0.7520	0.3188
z	0.0138	0.0079	0.0087	0.0023	0.0100
τ	9.2752	9.9106	9.8953	6.2404	10.0800
d	963.48	608.77	1343.87	1073.79	68.63
E(B-V)	0.2117	0.2395	0.2214	0.5907	0.0664
h_0	119	119	119	119	119
P	4.143879379	17.9187423	27.30822721	2.04516617	41.07759104
$t_{\rm PE}$	124.549181	146.3930288	143.5001619	122.1393461	132.6583081
$e\sin\omega$	0.003968	0.276679	0.443474	0.066164	-0.163677
$e\cos\omega$	0.000006	0.248540	0.120055	0.001243	-0.017973
b	0.9400	-0.3405	0.3313	1.4283	-0.4410
q_{11}	0.1732	0.2798	0.4472	0.9994	0.1763
q_{12}	0.3858	0.4381	0.8051	0.0002	0.9990
q_{21}	0.3624	0.6030	0.9237	0.5990	0.2659
q_{22}	0.1984	0.9802	0.8589	0.3190	0.8639
$\ln\sigma_{\rm sys,LC}$	-7.2	-8.1	-4.3	-6.5	-8.0
$\ln\sigma_{\rm sys,SED}$	-3.5	-3.7	-3.0	-2.4	-3.4
$\ln\sigma_{\rm E(B-V)}$	-11.1	-2.0	-2.0	-0.7	-6.4
$\ln\sigma_{\rm d}$	0.0	6.7	-6.1	0.0	2.4
c_0	0.9917	0.0000	0.0000	0.9885	0.9847
c_1	0.9909	0.9927	0.9339	0.9885	0.9784
c_2	0.9898	0.9909	0.9846	0.9901	0.9859
c_3	0.9864	0.9910	0.9930	0.9897	0.9902
c_4	0.9867	0.9902	0.9793	0.9886	0.9902
c_5	0.9910	0.9927	0.9362	0.9884	0.9849

Table 2.4 (cont'd)

Parameter	KIC 10031409	KIC 10198109	KIC 12356914	KIC 10619109	KIC 12644769
c_6	0.9927	0.9925	0.9884	0.9897	0.9874
c_7	0.0000	0.9910	0.9932	0.0000	0.9929
c_8	0.9888	0.9902	0.9617	0.9885	0.9849
c_9	0.9887	0.9927	0.8870	0.9884	0.9842
c_{10}	0.9925	0.9925	0.9718	0.9897	0.9928
c_{11}	0.0000	0.9909	0.9667	0.0000	0.9888
c_{12}	0.9887	0.9892	0.9872	0.9885	0.9922
c_{13}	0.9899	0.9927	0.9442	0.9885	0.9814
c_{14}	0.9851	0.9925	0.9958	0.9897	0.9955
c_{15}	0.0000	0.9909	1.0000	0.0000	0.9859
c_{16}	0.9877	0.9892	0.9902	0.9885	0.9949
c_{17}	0.9904	0.9927	0.9388	0.9885	0.9818
`morph`†	0.35	0.07	0.03	0.55	0.03

Note. — Maximum likelihood solutions for a subset of our sample which corresponds to Figures 2.1 to 2.5, to demonstrate the table's form and content. Full version available online. See Table 2.1 for details on parameter meanings and units. Values of 0.0 denotes no data was available. † `morph` is the morphology value taken directly from the Villanova *Kepler* Eclipsing Binary Catalogue (Prša et al., 2011; Kirk et al., 2016).

Table 2.5. ETV candidates identified in our sample

KIC	P (d)	Q	e	Other Sources[†]
10095512	6.01720794	0.83	2.0e-03	brc
10215422	24.84708632	0.64	2.9e-01	
10268903	1.10397904	0.82	4.5e-03	b
10292238	143.11911400	0.86	6.2e-01	
10296163	9.29674544	0.52	3.8e-01	b
10352603	32.77898645	1.01	4.7e-01	
10549576	9.08935880	0.52	6.9e-02	b
10583181	2.69635500	0.58	3.2e-07	b
10619109	2.04516617	0.75	6.6e-02	
10686876	2.61841459	0.46	1.0e-03	b
10736223	1.10509420	0.72	1.2e-02	
10909274	39.23813527	1.00	7.3e-01	
10979716	10.68409498	0.80	1.5e-01	b
11071207	8.04963317	1.01	3.1e-01	
11234677	1.58742711	0.45	1.6e-01	b
11499757	12.31440178	0.89	2.6e-01	
11558882	73.91782410	0.60	4.2e-01	b
11724091	1.55909021	0.50	1.9e-02	
11923819	33.15943126	1.02	3.3e-01	
12356914	27.30822721	0.66	4.6e-01	b
12459731	14.18110967	0.77	4.1e-02	b
12644769	41.07759104	0.32	1.6e-01	
1995732	77.36197359	1.09	1.3e-01	
2305372	1.40469172	0.77	2.8e-02	b
2306740	10.30698967	0.86	3.1e-01	
2576692	87.87820528	1.00	2.1e-01	b
3241619	1.70334728	0.76	6.5e-03	

Table 2.5 (cont'd)

KIC	P (d)	Q	e	Other Sources[†]
3247294	67.42012708	1.33	6.0e-01	o
3440230	2.88110019	0.72	1.0e-01	b
3757778	36.51436879	0.43	3.6e-01	
4077442	0.69284258	0.74	1.2e-01	
4544587	2.18911101	0.88	2.8e-01	
4753988	7.30445219	0.71	1.1e-02	b
4773155	25.70600971	0.92	4.4e-01	
4848423	3.00364489	0.96	2.5e-03	b
4948863	8.64355067	0.68	4.8e-03	b
5039441	2.15138428	0.52	2.8e-03	brc
5113053	3.18509078	0.87	6.0e-05	
5269407	0.95887119	0.53	2.3e-04	b
5288543	3.45707832	0.80	6.4e-03	
5513861	1.51021130	0.95	2.2e-06	b
5553624	25.76208222	0.83	5.6e-01	
5632781	11.02520265	1.01	2.7e-01	
5731312	7.94636806	0.77	4.7e-01	b
5955321	11.63787579	0.98	4.8e-01	
5962716	1.80459191	0.71	2.8e-01	b
6029130	12.59165677	0.94	1.5e-02	
6042116	5.40715640	0.64	9.7e-02	
6449358	5.77679432	0.43	4.0e-04	
6464285	0.84365137	0.61	1.6e-02	
6525196	3.42059775	0.94	7.1e-05	brc
6543674	2.39103076	0.97	4.5e-02	b
6545018	3.99145640	0.83	2.7e-03	brc
6610219	11.30099291	1.01	2.1e-01	

Table 2.5 (cont'd)

KIC	P (d)	Q	e	Other Sources†
6877673	36.75871004	0.81	2.0e-01	b
7021177	18.64532032	0.97	5.9e-01	
7025540	2.14821893	0.96	1.2e-02	
7137798	2.25353766	0.46	1.1e-01	
7177553	17.99645567	1.45	4.2e-01	b
7257373	10.46690066	0.99	9.6e-04	
7385478	1.65547318	0.48	1.2e-01	b
7630658	2.15115515	0.94	2.2e-04	b
7670617	24.70372529	0.49	1.8e-01	b
7812175	17.79408320	0.49	1.4e-01	b
7821010	24.23823475	0.96	6.8e-01	b
8143170	28.78745177	0.68	1.2e-01	b
8210721	22.67317786	0.36	1.3e-01	b
8411947	1.79767532	0.86	1.8e-02	
8429450	2.70515393	0.87	9.7e-03	b
8444552	1.17809835	0.79	1.5e-01	b
8553788	1.60616375	0.70	1.6e-01	b
8553907	42.03215831	1.02	5.1e-01	o
8701327	8.50883607	0.91	5.3e-03	
9007918	1.38720670	0.48	2.8e-04	b
9053086	1.27484170	0.55	1.5e-01	
9110346	1.79055388	0.93	9.4e-05	b
9392702	3.90931364	0.58	1.6e-02	b
9451096	1.25039078	0.64	2.4e-02	brc
9637299	1.88243818	0.59	3.1e-03	
9711751	1.71152733	0.79	5.3e-05	b
9714358	6.47419566	0.20	1.4e-02	brc

Table 2.5 (cont'd)

KIC	P (d)	Q	e	Other Sources†
9715925	6.30827736	0.77	2.2e-01	b
9777062	19.23003836	0.94	3.6e-01	
9850387	2.74849856	0.93	2.8e-03	b

Note. — Systems visually identified as exhibiting eclipse timing variations (ETVs). Note the period, mass ratio, and eccentricity included in this table correspond to maximum-likelihood solutions and not the median posterior values. †Triple candidates previously identified by Borkovits et al. (2016), Rappaport et al. (2013), Conroy et al. (2014), and Orosz (2015) contain flags 'b', 'r', 'c', 'o', respectively.

Table 2.6. Mass Ratios from APOGEE RVs

KIC	P (d)	ΔP (d)	Q	ΔQ
5284133	8.7778	0.0178	0.5358	0.0110
5460835	21.47	2.64	0.8285	0.0346
6610219	11.300689	0.000301	0.96134	0.00248

Table 2.7. RV-derived EB Mass Values from Literature

KIC	$P(d)$	$M_1(M_\odot)$	$\Delta M_1(M_\odot)$	$M_2(M_\odot)$	$\Delta M_2(M_\odot)$	Provenance
2305372	1.40469145	1.2	0.1	0.62	0.04	Matson et al. (2017)
3241619	1.70334707	1.24	0.04	0.86	0.02	Matson et al. (2017)
3440230	2.88110031	1.6	0.1	0.4	0.03	Matson et al. (2017)
4285087	4.4860314	1.137	0.013	1.103	0.014	Clark Cunningham et al. (2019)
4544587	2.1891143	1.69	0.1	1.42	0.09	Matson et al. (2017)
4574310	1.30622004	1.38	0.06	0.31	0.01	Matson et al. (2017)
4665989	2.248067589	1.77	0.09	1.32	0.05	Matson et al. (2017)
4848423	3.0036461	1.22	0.05	1.08	0.04	Matson et al. (2017)
4851217	2.47028283	1.43	0.05	1.55	0.05	Matson et al. (2017)
4862625	20.000214	1.47	0.08	0.37	0.035	Kostov et al. (2013)
5284133	8.7845758	–	–	–	–	F. Kiefer, independent analysis
5285607	3.89940111	1.557	0.038	1.346	0.033	Clark Cunningham et al. (2019)
5444392	1.51952889	1.17	0.01	1.19	0.1	Matson et al. (2017)
5460835	21.5392662	–	–	–	–	F. Kiefer, independent analysis
5473556	11.258818	1.2207	0.0112	0.9678	0.0039	Kostov et al. (2016)
5513861	1.51020825	1.5	0.04	1.32	0.03	Matson et al. (2017)
5738698	4.80877396	1.52	0.03	1.44	0.02	Matson et al. (2017)
5786154	2.00827091	1.06	0.06	1.02	0.04	Gaulme et al. (2016)
6131659	17.5278276	0.942	0.010	0.703	0.008	Clark Cunningham et al. (2019)
6206751	1.24534281	1.5	0.05	0.198	0.007	Matson et al. (2017)
6525196	3.42059774	1.0351	0.0055	0.9712	0.0039	Hełminiak et al. (2017)
6610219	21.5392662	–	–	–	–	F. Kiefer, independent analysis
6762829	18.79537	0.949	0.06	0.2492	0.06	Orosz et al. (2012a)
6778289	30.1301383	1.51	0.022	1.091	0.018	Clark Cunningham et al. (2019)
6781535	9.12208635	1.01	0.03	1.03	0.03	Clark Cunningham et al. (2019)
6864859	40.8778419	1.354	0.029	1.411	0.028	Clark Cunningham et al. (2019)
7037405	207.1083	1.25	0.04	1.14	0.02	Gaulme et al. (2016)

Table 2.7 (cont'd)

KIC	$P(d)$	$M_1(M_\odot)$	$\Delta M_1(M_\odot)$	$M_2(M_\odot)$	$\Delta M_2(M_\odot)$	Provenance
7605600	3.32619385	0.53	0.02	0.17	0.01	Han et al. (2019)
7821010	24.238235	1.289	0.015	1.231	0.015	Hełminiak et al. (2017)
7943602	14.69199	1.0	0.1	0.78	0.05	Gaulme et al. (2016)
8262223	1.61301476	1.96	0.006	0.21	0.001	Guo et al. (2017)
8552540	1.06193426	1.32	0.03	1.04	0.02	Matson et al. (2017)
8560861	31.9732937	1.93	0.12	1.06	0.08	Borkovits et al. (2014)
8572936	27.7958103	1.0479	0.0033	1.0208	0.0022	Welsh et al. (2012)
8823397	1.5065037	2.1	0.2	0.21	0.02	Matson et al. (2017)
9159301	3.04477215	1.61	0.08	0.4	0.02	Matson et al. (2017)
9246715	171.2768599	2.149	0.007	2.171	0.007	Gaulme et al. (2016)
9602595	3.5565129	3.0	0.1	0.60	0.03	Matson et al. (2017)
9632895	27.322037	0.934	0.01	0.1938	0.002	Welsh et al. (2014)
9641031	2.17815425	1.2041	0.0076	0.9498	0.0046	Hełminiak et al. (2017)
9837578	20.733666	0.8877	0.0053	0.8094	0.0045	Welsh et al. (2012)
9970396	235.2985	1.14	0.03	1.02	0.02	Gaulme et al. (2016)
10001167	120.3903	0.81	0.05	0.79	0.03	Gaulme et al. (2016)
10020423	7.44837695	1.043	0.055	0.362	0.013	Orosz et al. (2012b)
10031808	8.5896432	1.741	0.009	1.798	0.013	Hełminiak et al. (2017)
10156064	4.855936446	2.1	0.1	1.44	0.08	Matson et al. (2017)
10191056	2.427494881	1.59	0.32	1.427	0.036	Hełminiak et al. (2017)
10581918	1.80186366	1.3	0.06	0.169	0.009	Matson et al. (2017)
10619109	2.04516616	1.5	0.4	0.31	0.07	Matson et al. (2017)
10736223	1.105094186	1.6	0.1	0.35	0.03	Matson et al. (2017)
10935310	4.128795224	0.92	0.05	0.5	0.03	Han et al. (2017)
10987439	10.67459809	0.9862	0.0034	1.4215	0.0045	Hełminiak et al. (2017)
11922782	3.512934275	1.067	0.010	0.836	0.006	Hełminiak et al. (2017)
12351927	10.116146	0.82	0.015	0.5423	0.008	Kostov et al. (2014)

Table 2.7 (cont'd)

KIC	$P(d)$	$M_1(M_\odot)$	$\Delta M_1(M_\odot)$	$M_2(M_\odot)$	$\Delta M_2(M_\odot)$	Provenance
12644769	41.07922	0.6897	0.0035	0.20255	0.00066	Doyle et al. (2011)

Note. — Note for binary studies which contain multiple mass estimates (e.g., from asteroseismology and RV), we adopted the RV-only derived values for consistency. ΔM_1 and ΔM_2 are uncertainties associated with published mass values.

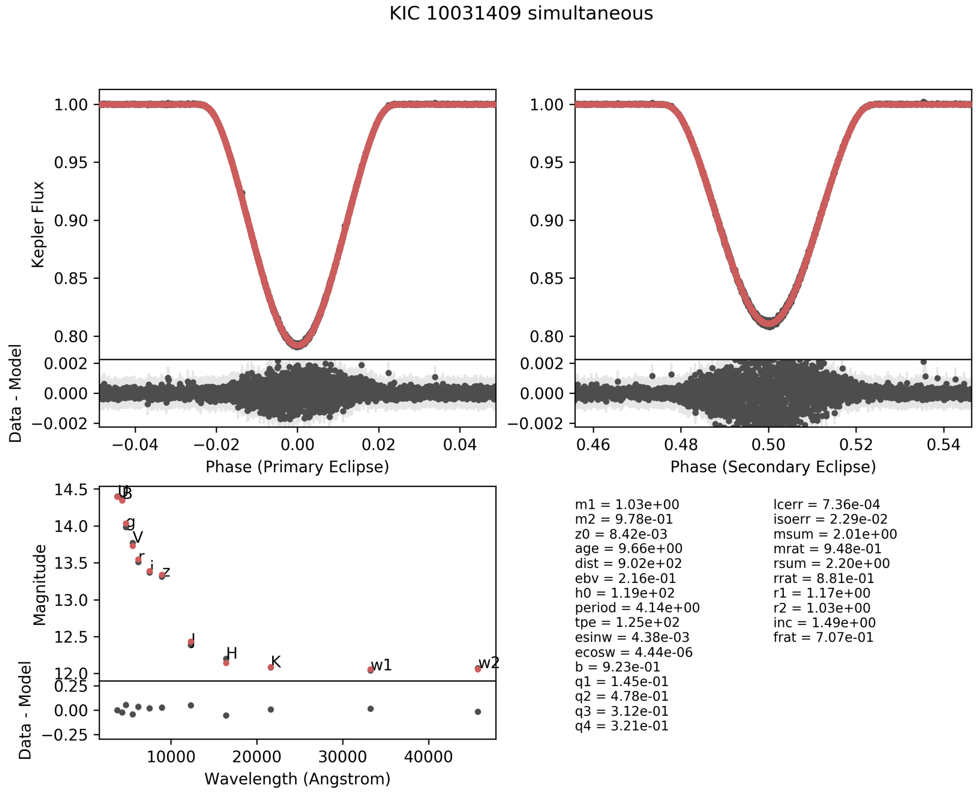

Figure 2.1 Maximum-likelihood (ML) solution for KIC 10031419, a G-dwarf binary in a ~4 d, circular orbit. The upper panels show the normalized, detrended, and phase-folded primary and secondary eclipse flux data (black) and the light curve fit corresponding to the ML model (red), while the bottom left panel shows the SED fit. Data points with *Kepler* quality flags >8 are masked for visual clarity here (although they are not removed during fitting, see §2.2.2). The ML parameters are reported for reference. Both the light curve and SED residuals belong to the mean and mode bin from Figure 2.6, and indicate a good fit to the data; the scatter during eclipse is consistent with starspot modulations.

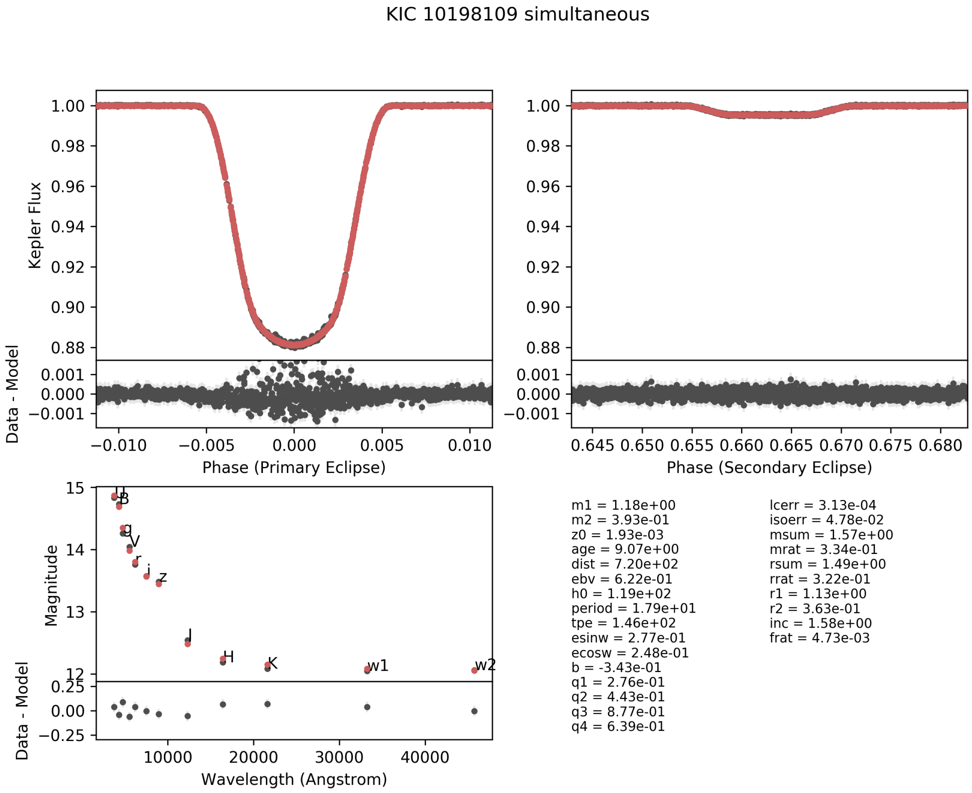

m1 = 1.18e+00
m2 = 3.93e-01
z0 = 1.93e-03
age = 9.07e+00
dist = 7.20e+02
ebv = 6.22e-01
h0 = 1.19e+02
period = 1.79e+01
tpe = 1.46e+02
esinw = 2.77e-01
ecosw = 2.48e-01
b = -3.43e-01
q1 = 2.76e-01
q2 = 4.43e-01
q3 = 8.77e-01
q4 = 6.39e-01

lcerr = 3.13e-04
isoerr = 4.78e-02
msum = 1.57e+00
mrat = 3.34e-01
rrat = 3.22e-01
rsum = 1.49e+00
r1 = 1.13e+00
r2 = 3.63e-01
inc = 1.58e+00
frat = 4.73e-03

Figure 2.2 Same as Figure 2.1, except for KIC 10198109, an eccentric, 18 d binary with $Q \sim 0.3$. The in-eclipse scatter is small, $\lesssim$1 ppt, and again likely due to starspots.

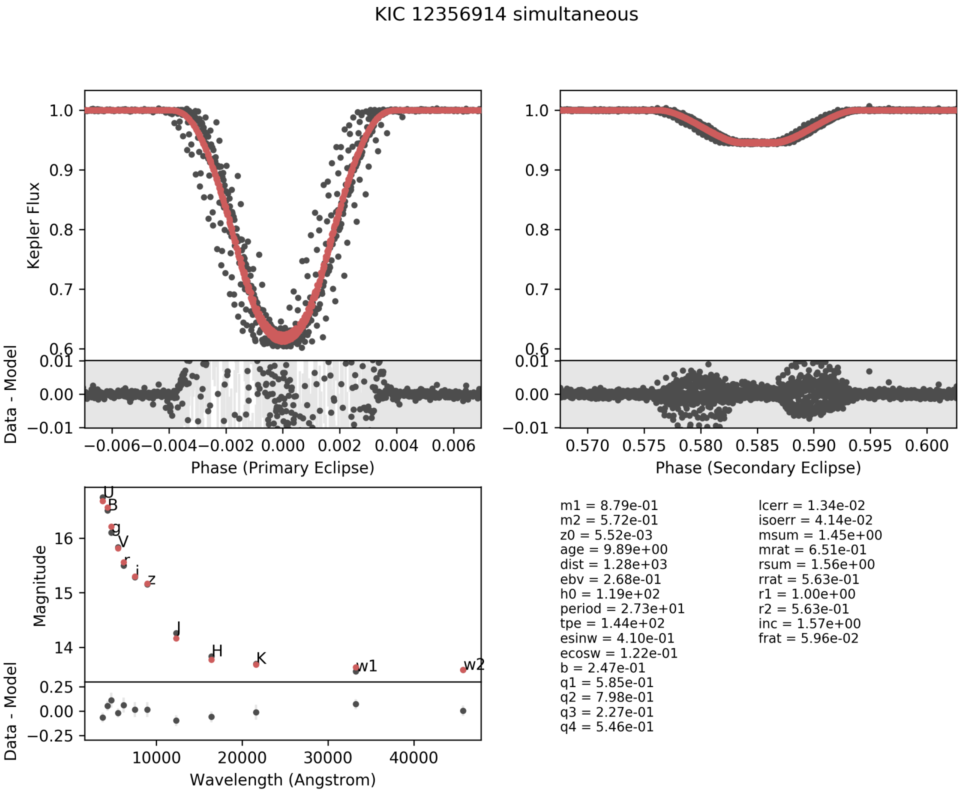

Figure 2.3 Same as Figure 2.1, but for KIC 12356914, a pair of low mass stars in an eccentric, 27 d orbit around each other. The strong eclipse timing variations present in primary and secondary eclipse pull $\sigma_{\text{sys,LC}}$ toward very large values, and indicate the presence of a third companion in a wider orbit around the central binary, consistent with the more rigorous analysis of Borkovits et al. (2016).

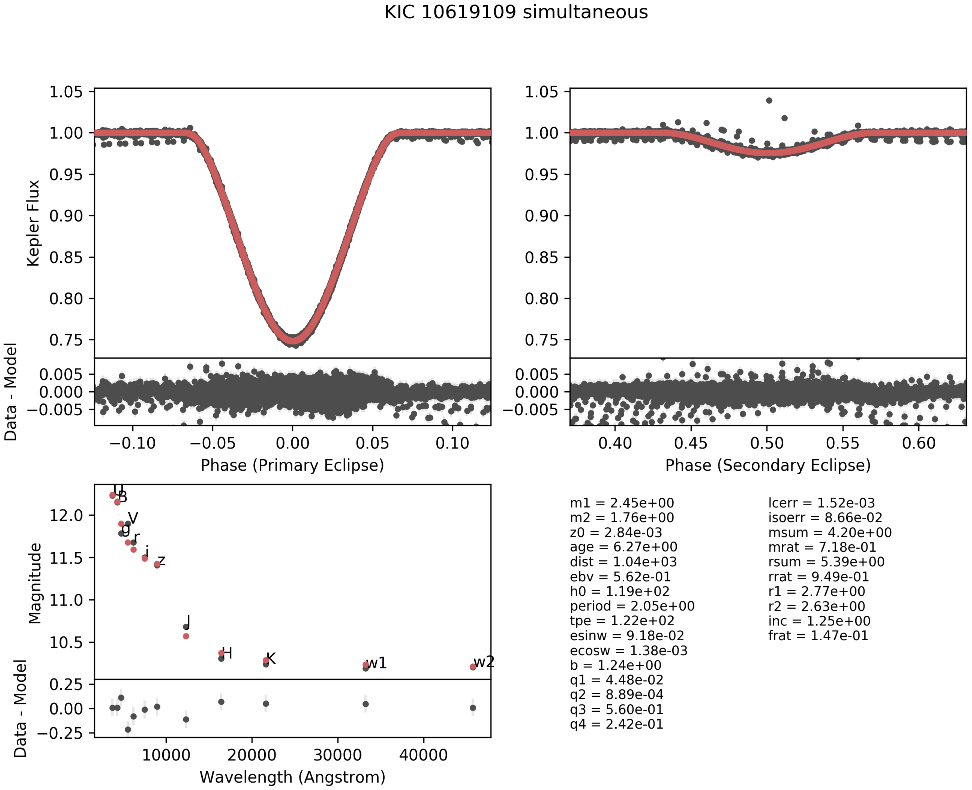

Figure 2.4 Same as Figure 2.1, but for KIC 10619109, a 2 d, nearly circular orbit binary. Note the relatively large light curve scatter out of eclipse and 0.2 mag scatter in the SED residuals. This is an example of a marginally good fit, but with anomalously young ages, relatively high mass components, and morph parameter >0.5, indicative of an Algol-type system (see §2.4.2 for further discussion). The outlier data points are an artifact of poor polynomial fitting, due to missing data near/during a particular eclipse.

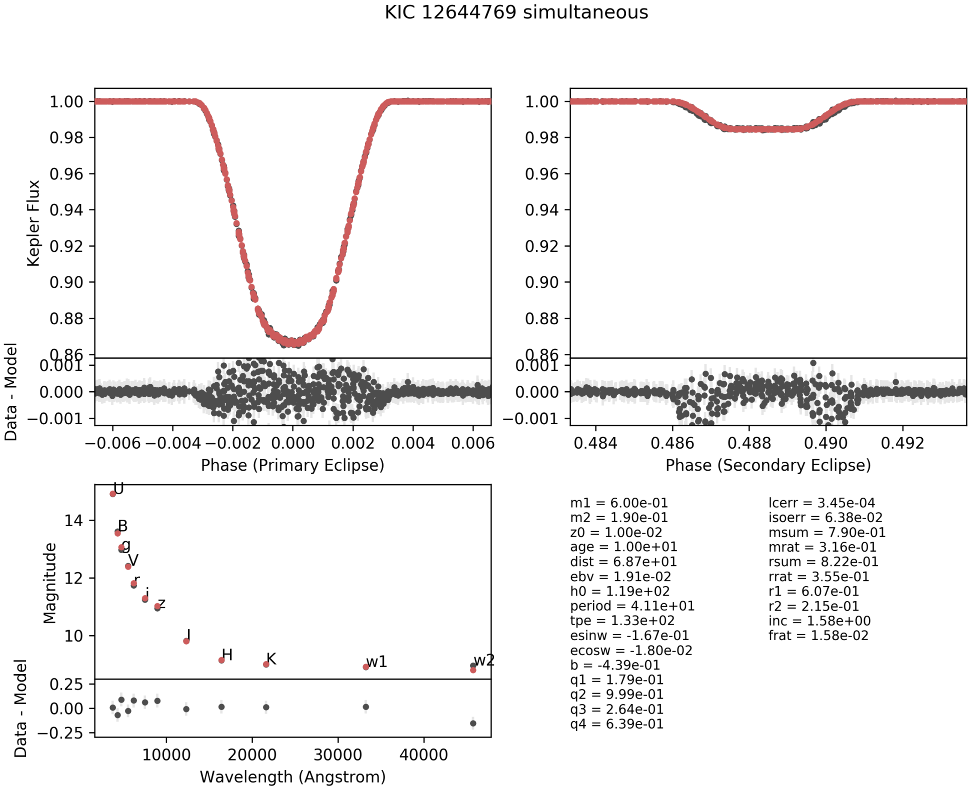

Figure 2.5 Same as Figure 2.1, but for KIC 12644769, a system in which two M dwarfs orbit each other every 41 days in a slightly eccentric fashion. The scatter in-eclipse is relatively small at <1 ppt, but nevertheless exhibit interesting phenomena. Residuals during primary eclipse are consistent with starspot modulations (on the primary star), while residuals at secondary ingress and egress indicate small ETVs by a small tertiary component. Indeed, KIC 12644769, aka Kepler-16, is a known circumbinary planet host (Doyle et al., 2011).

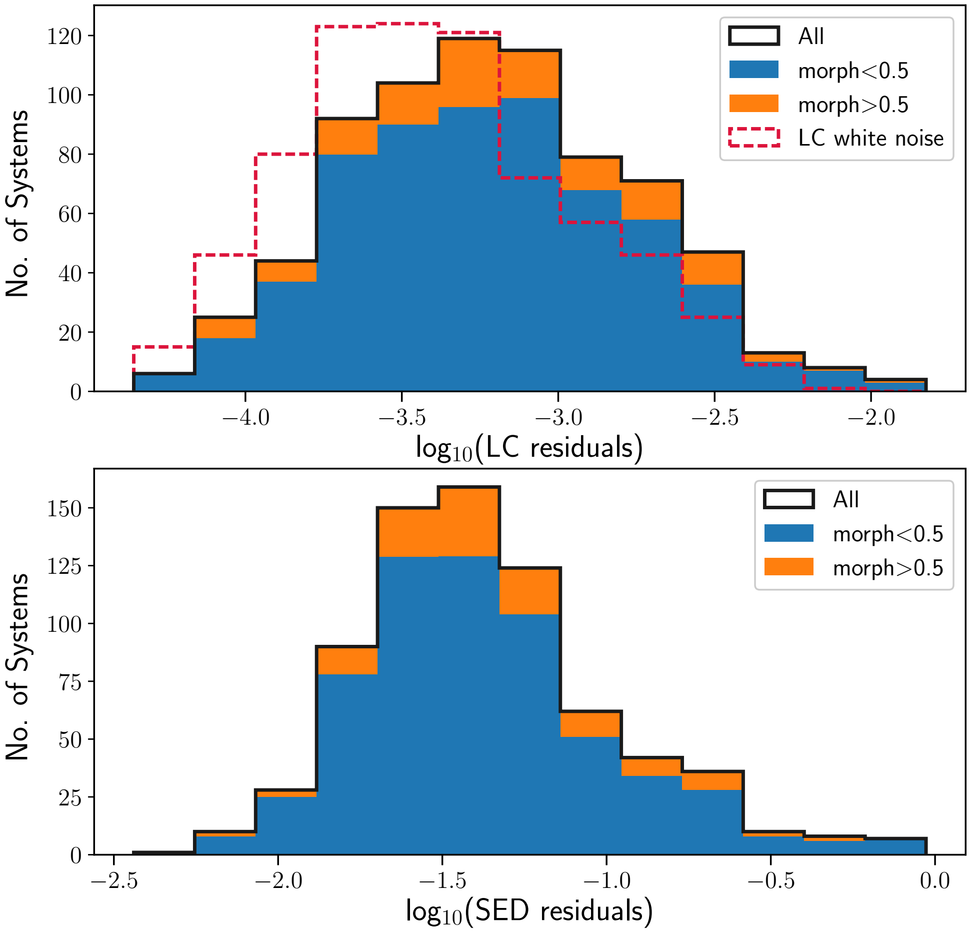

Figure 2.6 The median absolute data-model residual distribution (black curve) for our EB fits in log space; we decompose the distributions between `morph`<0.5 (blue) and `morph`>0.5 (orange) systems and stack them vertically. The majority of systems modeled exhibit residual levels comparable to light curve "jitter," quantified by the median absolute difference (MAD) in out-of-eclipse flux (red dashed curve). However, this proxy for LC noise does not capture correlated noise well, so light curves which exhibit e.g., large Doppler or ellipsoidal amplitudes, starspot variation, quasi-periodic stellar variability, or third light dilution that varies within each quarter, will have underestimated noise values. This contributes to the difference between in-eclipse model residuals and inherent light curve jitter distributions; systems with large eclipse timing variations, starspot or ellipsoidal variations compose the tail of large residuals ($\gtrsim$ 0.01). Indeed, `morph`>0.5, e.g., short period EBs likely to exhibit ellipsoidal variations and/or have undergone interactions, have larger residuals relative to `morph`<0.5 systems.

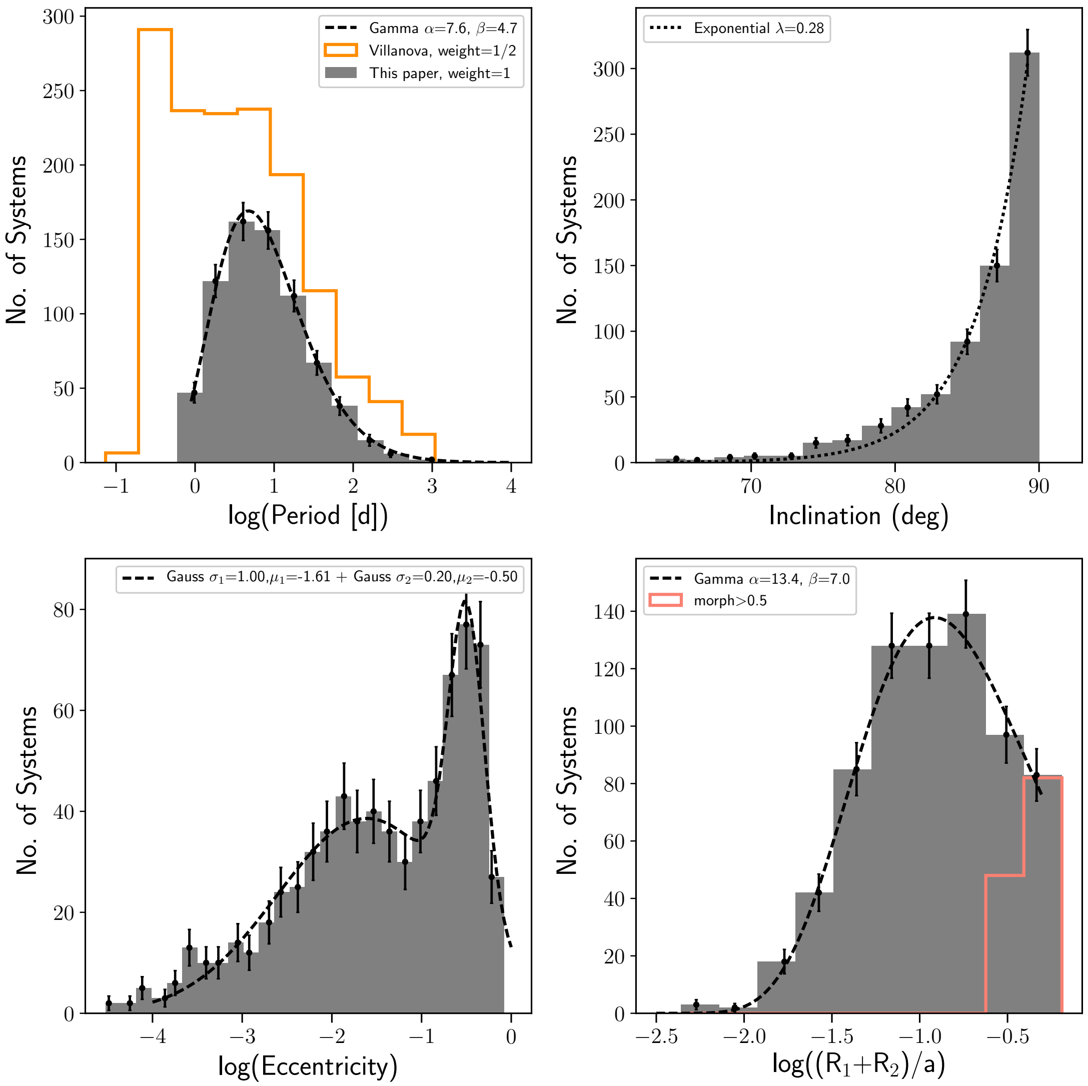

Figure 2.7 Distribution of orbital parameters: period, inclination, eccentricity, and orbital separation relative to stellar size, for EBs in our sample. The period distribution peaks around 3 days, and follows a gamma distribution in shape. The inclination distribution peaks near edge-on and declines exponentially. Note that our fits allow inclinations from 0° to 180°, but here we wish to illustrate the distribution of edge-on vs. grazing systems, so we folded the data about 90 degrees. The eccentricity distribution is bimodal, peaking around $\log e \sim -1.6, -0.5$ corresponding to $e \approx 0.03,\, 0.3$. We also plot the distribution of orbital semi-major axis relative to stellar radius, which to first order is a proxy of light curve morphology; about 3/4 of our sample have $(R_1 + R_2)/a < 0.2$.

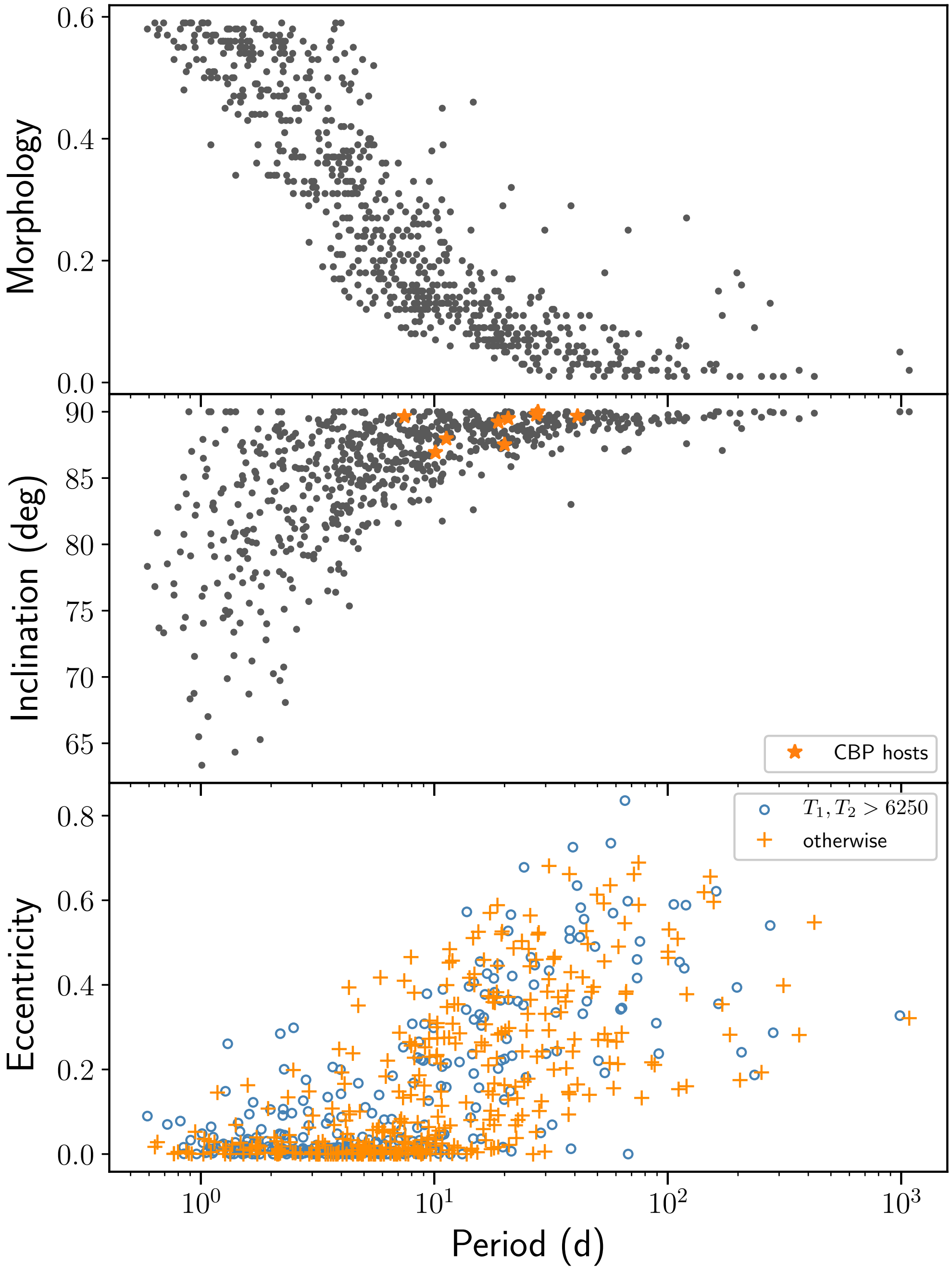

Figure 2.8 Morphology (top), inclination (middle), and eccentricity (bottom) of EBs in our sample as a function of their orbital period.

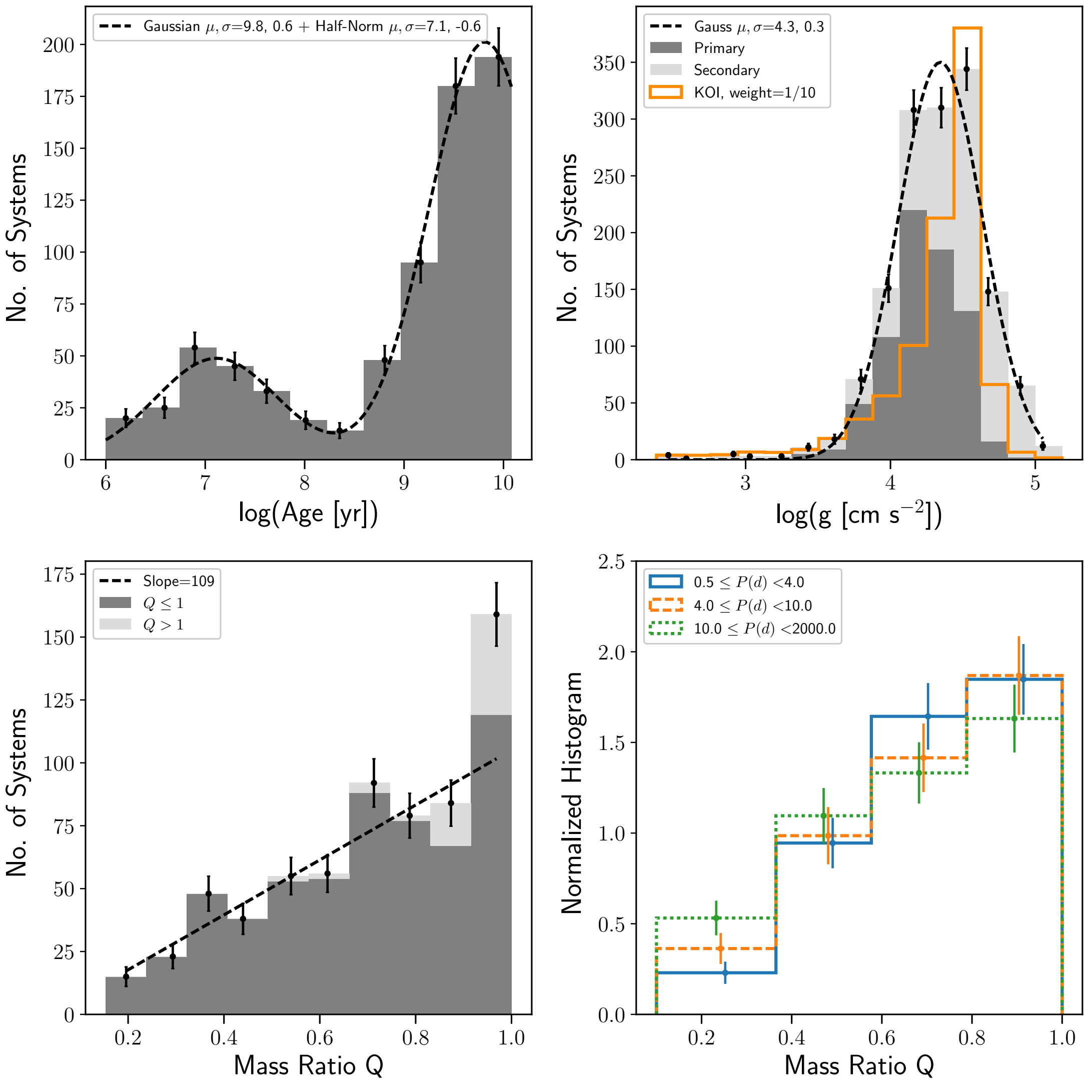

Figure 2.9 Distribution of stellar parameters: age, $\log g$, and mass ratio Q, for EBs in our sample. The age distribution (upper left) is bimodal, such that the majority of EBs contain ~billion-year-old stars, with a small but notable excess of young (<100 Myr) stars (see text for discussion). The surface gravity distribution (upper right) peaks around $\log g \sim 4.3$, indicating the prevalence of main sequence binaries in our sample. The mass ratio distribution (lower left) shows an increasing slope toward similar-mass binaries, consistent with observations of solar-type binaries in the field (Raghavan et al., 2010). Note that for systems where $Q > 1$ (light grey), we invert the mass ratio such that $Q = M_1/M_2$ to keep values in range [0, 1]. The mass ratio distribution for $Q \leq 1$ (lower right) is relatively uniform across $P < 4$, $P = 4 - 10$, and $P > 10$ d binaries.

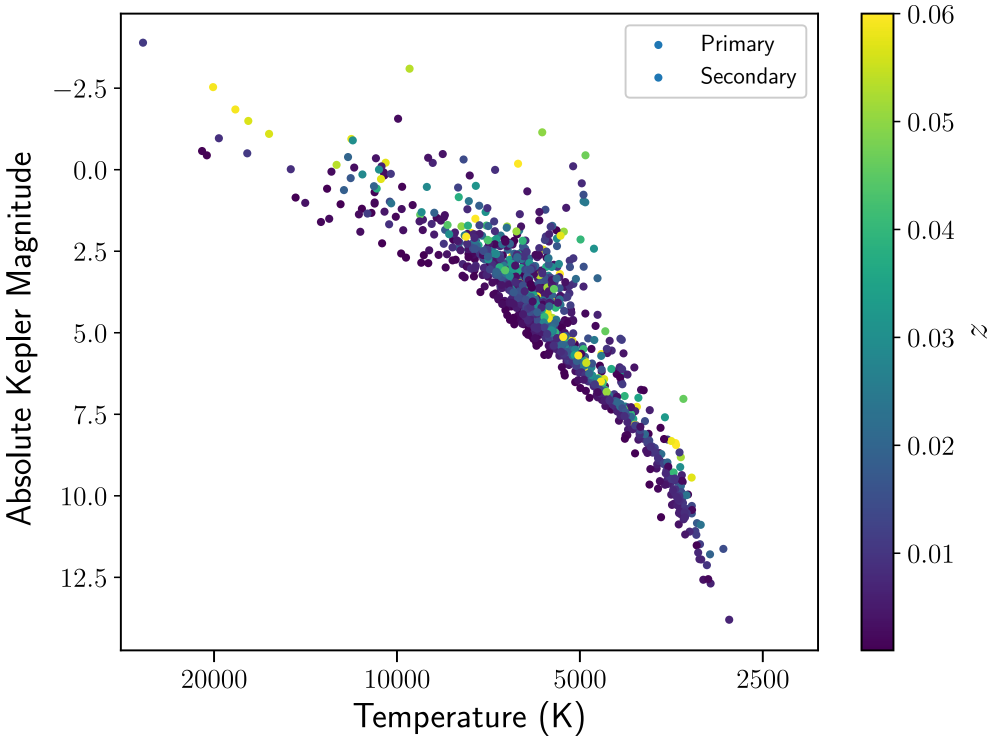

Figure 2.10 EBs from our sample, with temperature and absolute *Kepler* magnitude of each stellar component, plotted on the HR diagram; the color bar denotes inferred metallicity z of the system. While there is a small population of sub-giants starting to turn off the main sequence, there is an absence of red giant branch. The lack of giants may be due to a combination of isochrone fitting bias and Kepler target selection (see text for discussion).

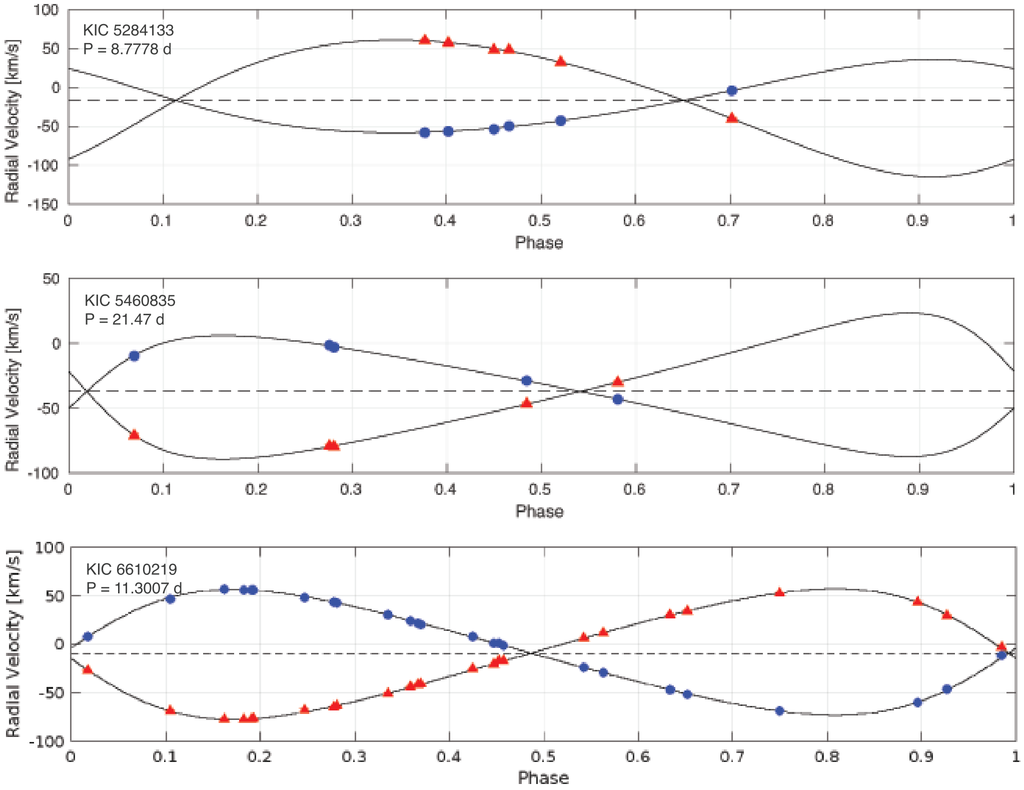

Figure 2.11 Radial velocity solutions in an independent analysis to three SB2 systems in our sample, using the method of Kiefer et al. (2018).

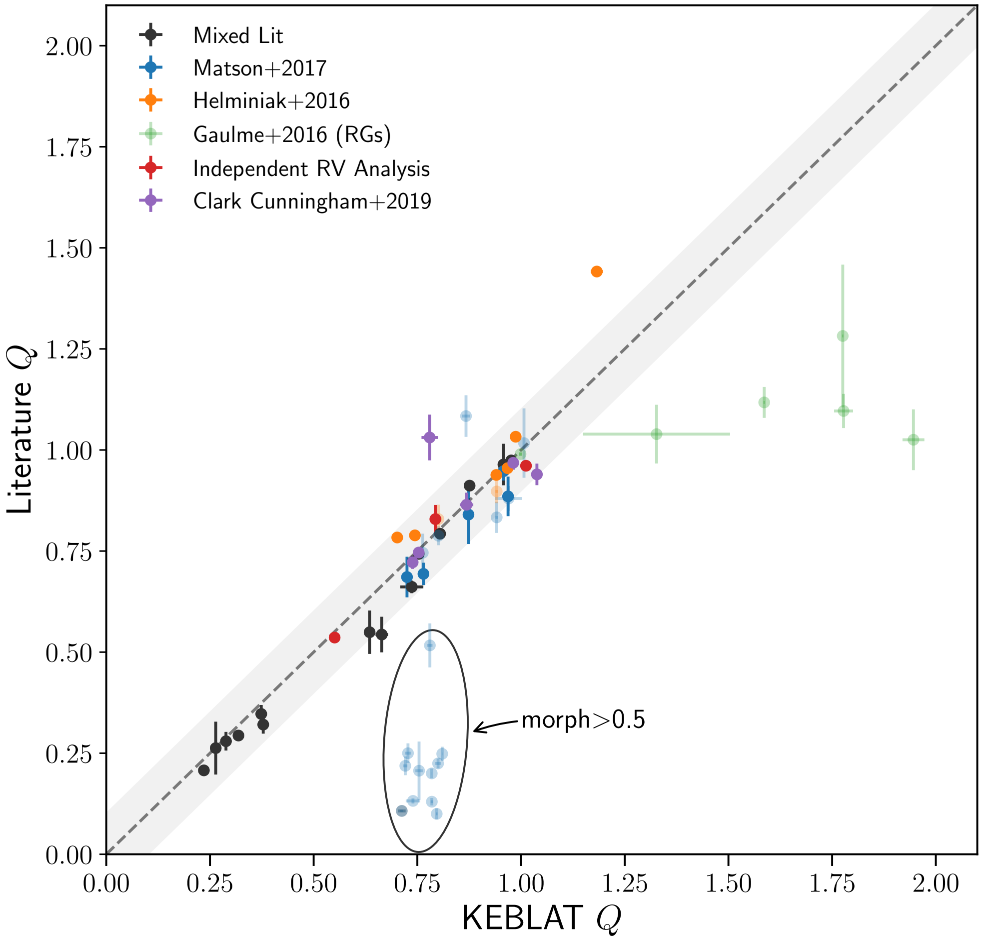

Figure 2.12 Comparison of RV-derived mass ratio values as reported in literature vs. KEBLAT values using the SED+LC fitting method. The dashed black line denotes 1:1 relationship, with light grey regions representing ±0.1 uncertainty in Q. In general, there is broad agreement with literature values. Binaries which are not well described by stellar isochrones (represented by lighter alpha values), e.g., red giants and binaries that exchange(d) mass, give discrepant mass ratio values.

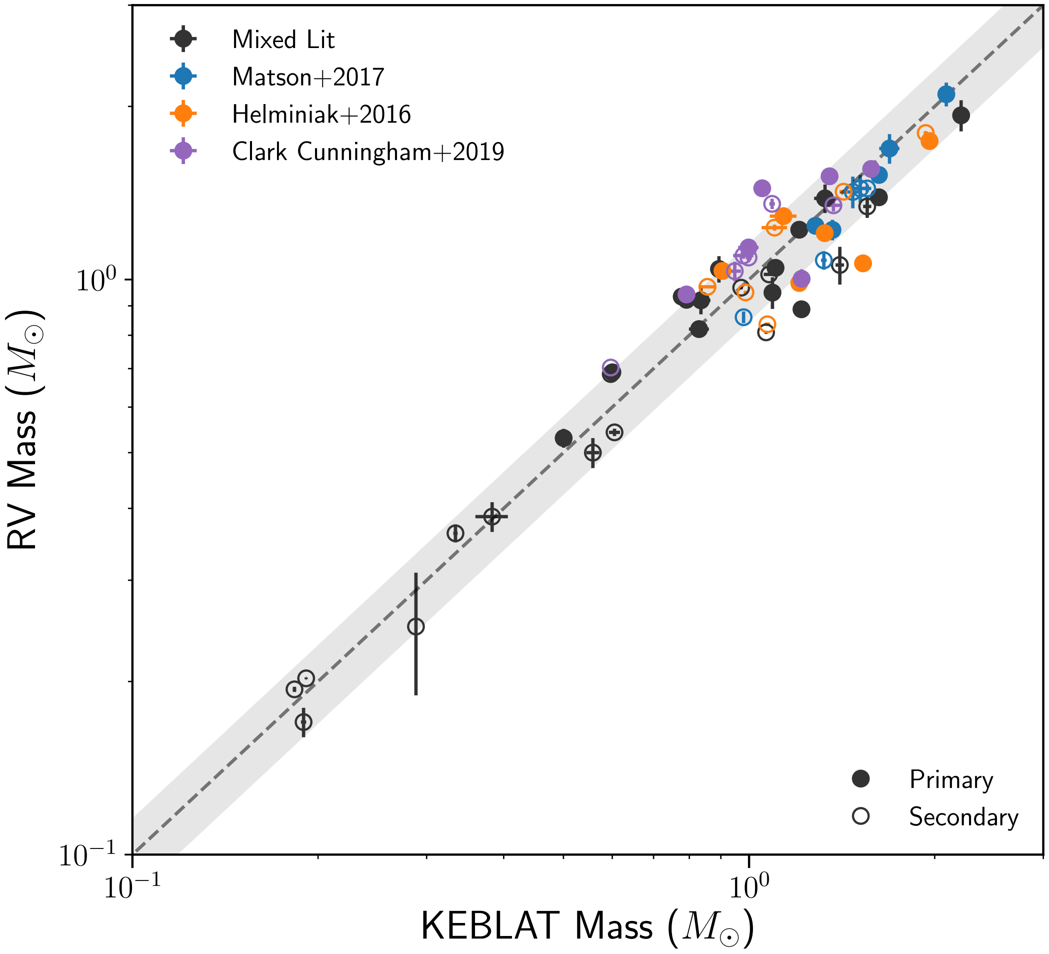

Figure 2.13 Comparison of absolute mass values between KEBLAT and RV-derived values from literature, after removing EBs with red giant components and `morph`>0.5 (see §2.4.1). The closed and open circles represent primary and secondary components of the binary. The dashed black line denotes 1:1 relationship, with light grey regions representing 15% of the mass uncertainties. The photometric masses show good agreement with RV values.

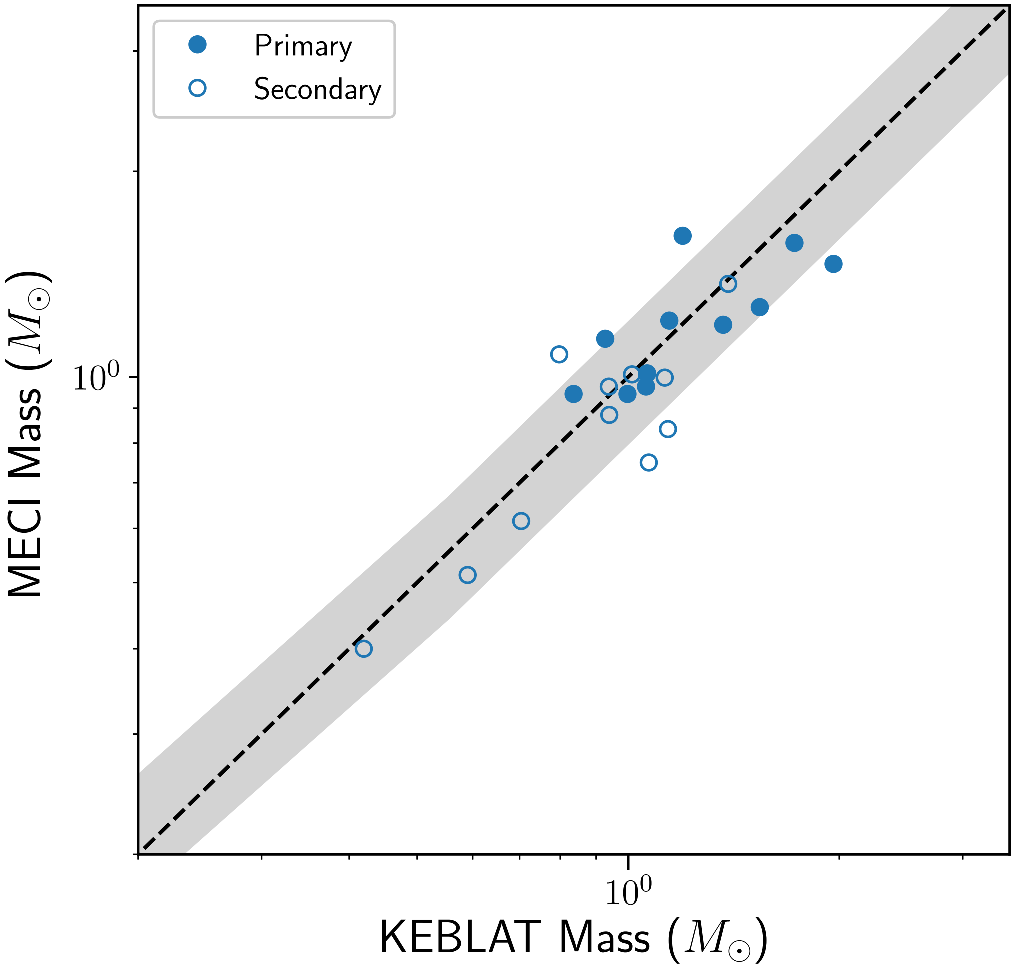

Figure 2.14 Comparison of mass values from our analysis and that of Devor et al. (2008) for a small number of overlap binaries. Both studies used light curve and SED data with stellar isochrones to derive masses, although predicated on different data and details of each method are different. The mass values show relatively good agreement.

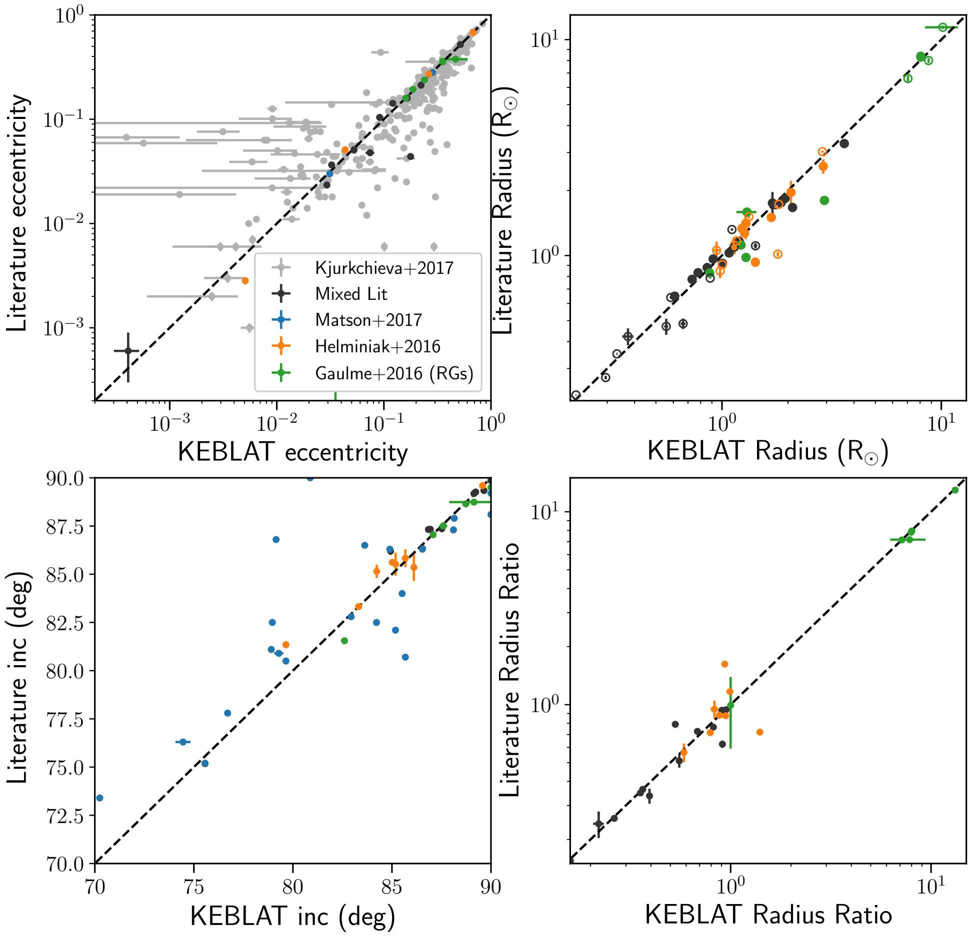

Figure 2.15 Comparison of eccentricity, inclination, and radii values from KEBLAT and various literature studies, which show overall good agreement. The values are collected from the same RV studies from mass comparison, plotted in Fig. 2.12, and we supplement additional eccentricity estimates from (Kjurkchieva et al., 2017). While the masses of red giant components (Gaulme et al., 2016) were poorly inferred, the absolute radii show good fidelity to literature values. There is also greater scatter among inclination values from Matson et al. (2017) (blue), however these were fixed to be Slawson et al. (2011) neural network inference values based on phenomenological light curve modeling rather than physical model, which may explain some of the discrepancies.

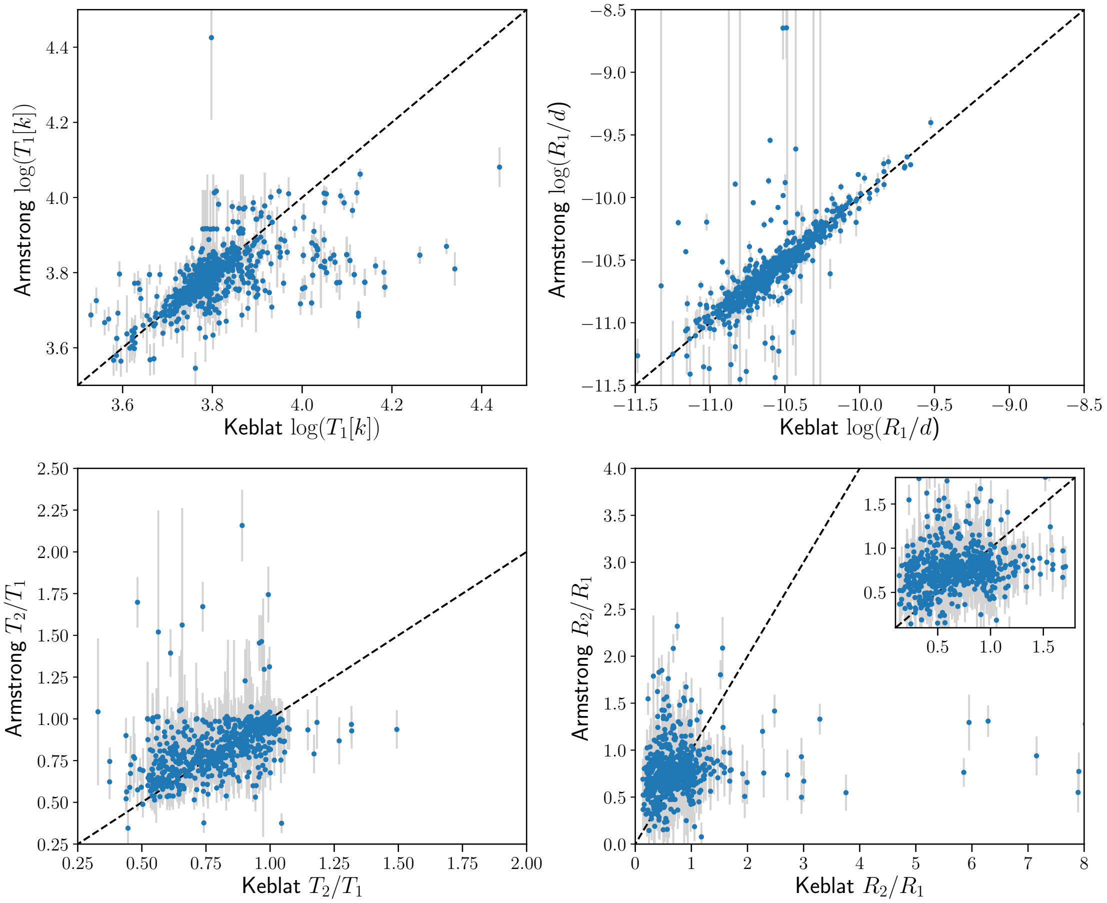

Figure 2.16 Comparison of parameters as derived here and values presented in Armstrong et al. (2014a) for temperature of the primary star (top left), primary radius normalized by distance to system (top right), temperature ratio (bottom left), and radius ratio (bottom right). While T_1 and R_1/d show bulk agreement, their temperature and radius ratios estimates are relatively crude and show significant scatter with respect to values derived in this work (see text for discussion).

Chapter 3

AN AUTOMATED METHOD TO DETECT TRANSITING CIRCUMBINARY PLANETS

To date a dozen transiting “Tatooines” or circumbinary planets (CBPs) have been discovered, by eye, in the data from the *Kepler* mission; by contrast, thousands of confirmed circumstellar planets orbiting around single stars have been detected using automated algorithms. Automated detection of CBPs is challenging because their transits are strongly aperiodic with irregular profiles. Here, we describe an efficient and automated technique for detecting circumbinary planets that transit their binary hosts in *Kepler* light curves. Our method accounts for large transit timing and duration variations (TTVs and TDVs), induced by binary reflex motion, in two ways: 1) We directly correct for large-scale TTVs and TDVs in the light curves by using Keplerian models to approximate binary and CBP orbits; and 2) We allow additional aperiodicities on the corrected light curves by employing the Quasi-periodic Automated Transit Search algorithm (QATS). We demonstrate that our method dramatically improves detection significance using simulated data and two previously identified CBP systems, *Kepler*-35 and *Kepler*-64. *Material from this chapter was previously published in collaboration with Eric Agol, Josh Carter, Eric B. Ford, Nader Haghighipour, Jerome A. Orosz, and William F. Welsh in the November 2019 edition of the Monthly Notices of the Royal Astronomical Society, and is reproduced by permission of Oxford University Press.*

3.1 Introduction

The discovery rate of extrasolar planets orbiting around single stars has increased exponentially in the past two decades. This was largely enabled by the *Kepler* mission and the transit technique in synergy with ground-based radial velocity surveys. In stark contrast to the thousands of confirmed and candidate *circumstellar* planets (CSPs), spanning Earth to Jovian in size, only 11 published transiting *circumbinary* planets (CBPs) have been discovered in the *Kepler* data[1]. The transits of these CBPs across their binary hosts are sufficiently deep that they were identified by eye, while transit detections of planets around single stars were facilitated by automated detection pipelines (e.g. Petigura et al., 2013; Foreman-Mackey et al., 2016; Thompson et al., 2018).

Here, we present an automated technique to detect transiting CBPs. Our method assumes a single test planet in a circular and co-planar orbit around the binary, and reconciles changes in transit timing and shapes in CBP systems in two ways: 1) We correct for circular and eccentric binary orbits using Keplerian models, creating a regularized light curve in which the CBP transit shape and timing are more uniform. 2) We apply the Quasi-periodic Automated Transit Search (QATS; Carter & Agol, 2013) algorithm on the regularized light curves, which allows for additional timing deviations due to inaccuracies in the binary model (e.g., mass ratios) and CBP model (e.g., planet eccentricity, perturbations of the planet's orbit by the binary or other planetary companions). This two-fold TTV treatment increases detection significance and decreases false alarm probability, and enables a systematic search for smaller, perhaps terrestrial, circumbinary worlds.

Automatic transit detection algorithms not only enable larger-scale discoveries, they also permit statistical testing of detector efficiency, bias, and completeness. These quantities are imperative to robustly infer the underlying physical distribution of exoplanets, e.g., occur-

---

[1] The 11 published *Kepler* CBPs are: Kep-16*b* (Doyle et al., 2011); Kep-34*b* & Kep-35*b* (Welsh et al., 2012); Kep-38*b* (Orosz et al., 2012b); PH1/Kep-64*b* (Schwamb et al., 2013; Kostov et al., 2013); Kep-47*b*, *c*, and *d* (Orosz et al., 2012a; Kostov et al., 2013; Hinse et al., 2015; Welsh et al., 2015a; Orosz et al., 2019); Kep-413*b* (Kostov et al., 2014); Kep-453*b* (Welsh et al., 2015b); Kep-1647*b* (Kostov et al., 2016); 12th system, KIC 10753734 has been reported but not yet published (Orosz et al., 2016).

rence rates and system architectures (Batalha et al., 2013; Petigura et al., 2013; Foreman-Mackey et al., 2014; Ballard & Johnson, 2016; Hsu et al., 2019). A successful transit detection algorithm is optimized for speed and detection significance, and is typically conditioned on periodic signals. Notable exceptions to strict periodicity include the QATS algorithm, which allows a user-specified TTV window and have been applied to multi-planet systems around single stars, and algorithms tailored to detect transiting CBPs (Jenkins et al., 1996; Ofir, 2008; Armstrong et al., 2014a; Klagyivik et al., 2017).

Automated detection of CBP transits poses unique challenges and have lagged behind their CSP counterparts. This is because time-varying radiative and dynamical effects from the binary make transit pulses irregular in the time-series data. In particular, the reflex motion of the binary about the barycenter leads to "roaming conjunctions" and induces large transit timing and duration variations (TTVs and TDVs), as well as transit depth variations in binary systems with unequal surface brightness. In fortuitous configurations, multiple transit events across the same or both stellar disks may occur near one syzygy (conjunction of observer-planet-stellar component). There may be additional variations in transit shape and timing due to precession of the CBP orbit (Martin & Triaud, 2015), which can cause transits to disappear and reappear over time, and due to second-order dynamical effects, e.g., perturbations from additional planets in the system. The latter is negligible compared to the geometric effect due to binary motion. Binary-induced TTVs can be of order days to even weeks (e.g., Kepler-16b; Doyle et al., 2011), orders of magnitude larger than TTVs due to perturbing companions in multi-planet systems around single stars (Agol et al., 2005).

Previous work on transiting CBP detection addressed TTVs either by using a modified Box-fitting Least-Square (BLS; Kovács et al., 2002) with a large, variable width (Armstrong et al., 2014a; Klagyivik et al., 2017), or by directly correcting for binary motion and then applying a periodic search (Jenkins et al., 1996; Ofir, 2008). In particular, Armstrong et al. (2014a) applied their algorithm to non-contact *Kepler* eclipsing binaries (EBs) to estimate the occurrence rate of CBPs, using a constant transit duration and analytic approximations

(Armstrong et al., 2013) to inform the maximum variable BLS window for each binary. Klagyivik et al. (2017) used a similar method to search for transiting CBPs in CoRoT data, but allowed the depth and duration of model transits to vary. Both studies, however, used a large TTV window in which to look for transits, which introduces a higher false-alarm probability.

Jenkins et al. (1996) and Ofir (2008) proposed to directly correct for binary motion by solving the binary orbit to predict planet-binary positions. However, they required precise periodicity of planet transit times after an exact correction for the binary orbit, neither of which will be realized in practice.

Here, we introduce a hybrid technique that corrects for geometric transit effects due to binary motion with a physical circumbinary orbit model *and* relaxes the subsequent assumption of strict periodicity using the QATS algorithm. In doing so, this paper is organized as follows. In Section 3.2, we describe the geometry of CBP transits and detail our detection technique, including the physical binary and CBP models used for transit regularization. In Section 3.3, we apply our method to simulated data, and also demonstrate its robustness on two known *Kepler* CBPs, *Kepler*-35*b* (Welsh et al., 2012) and *Kepler*-64*b*/PH1*b* (Kostov et al., 2013; Schwamb et al., 2013), which were tested with existing automated algorithms (Armstrong et al., 2014a; Klagyivik et al., 2017). A detailed comparison of CBP detection techniques, such as one for generic transit detection algorithms by Tingley (2004), is beyond the scope of this paper. In Section 3.4, we discuss the improvements on detection significance and comment on the limits of our detection technique. We conclude this study and summarize key takeaways in Section 3.5.

3.2 Methods

Our detection technique, dubbed "QATS-EB," differs from traditional transit search methods and addresses the aperiodic transits of circumbinary planets in a two-component approach. First, we use a semi-analytic CBP model to account for the influence of the binary hosts, which induce large-scale TTVs and TDVs on the planet. Second, we utilize the QATS algorithm (Carter & Agol, 2013), which relaxes strict periodicity in the transit search window with a user-specified inter-transit duration, i.e., allows room for error in timing predictions due to model inaccuracies. These two improvements work in conjunction to boost CBP detection signal-to-noise ratio (S/N) and decrease the false alarm probability.

Figure 3.1 illustrates the overall QATS-EB procedure, which we preview in brief here. First, our method uses an EB model (Windemuth et al., 2019a) to solve for binary parameters and remove eclipses from the light curve (panels 1a–1b). Then, it performs, at each observed cadence, a likelihood ratio (chi-square difference $\Delta\chi^2$) test for a null hypothesis against a CBP transit across one of the binary stars, with predicted depth, duration, timing given by binary parameters and test planet period and size (panels 2a–2c). Finally, at each proposed planet parameters, it runs a quasi-periodic search on the time-series likelihood ratios and computes the detection S/N (panels 3a–3b).

QATS-EB can search for CBP transits across the primary and secondary stars, in series. The predicted transit depth, duration, and timings are different for each stellar component, and the primary star is typically more luminous than the secondary. Thus, one can apply the method to search for CBP transits across the primary, then mask the detected transits and perform a subsequent, self-consistent search for transits across the secondary. Unless otherwise specified, we assume transits are across the primary star for the remainder of this paper.

In the subsections to follow, we give an overview of definitions and the CBP transit geometry (§3.2.1) and provide detailed descriptions of the auomated CBP transit detection procedure (§3.2.2).

3.2.1 Definitions & Geometry of CBP Transits

Throughout the paper, we use the following convention to describe the components of a circumbinary system. We use "eclipses" to specify when the stellar components pass in front of each other, and use "transits" when the planet passes in front of one of the stars. A primary eclipse (PE), i.e., the deeper eclipse, occurs when the primary (hotter) stellar component is

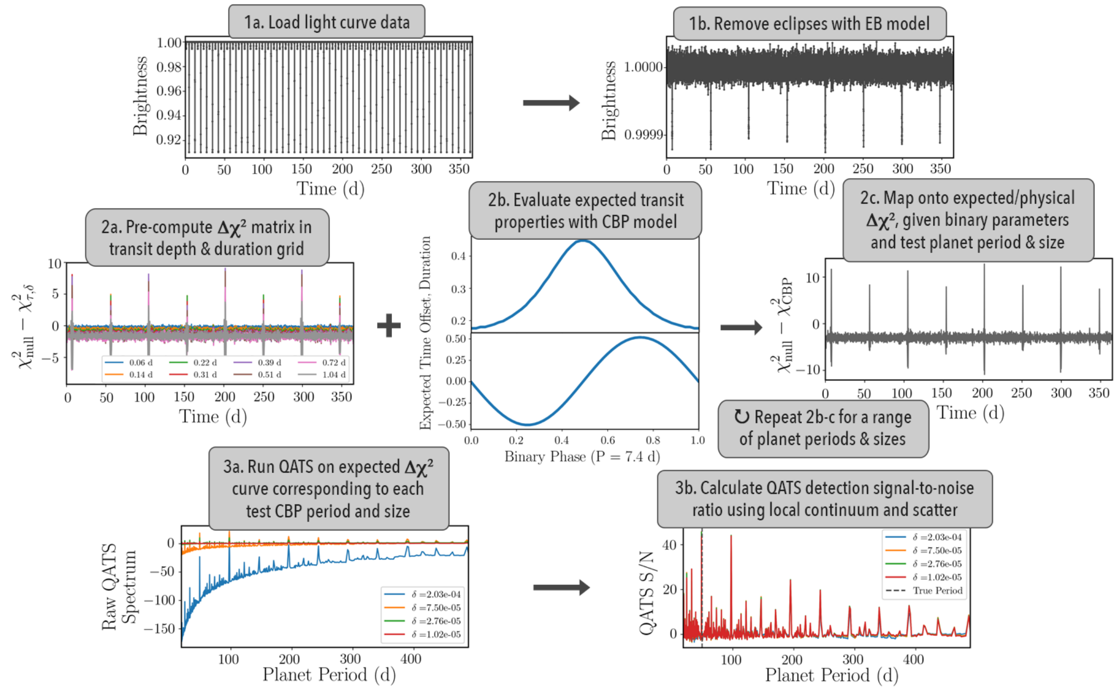

Figure 3.1 A schematic diagram depicting procedures in the QATS-EB algorithm to detect circumbinary planets. (1) Use an EB model (Windemuth et al., 2019a) to remove eclipses in the light curve. (2a) Test EB-removed light curve for the presence of a transit with fixed depth and duration at each light curve cadence, creating a corresponding $\Delta\chi^2$ -curve. (2b) Using a physical CBP model, compute the expected transit properties (depth, duration, barycentric timing offset) as a function of binary phase (or time), for a specified test CBP planet period and size. (2c) Interpolate the expected, regularized $\Delta\chi^2$ -curve using (2a) and (2b). (3a) Run QATS on the expected $\Delta\chi^2$ -curve, and loop through different test periods and sizes to build up maximum CBP likelihood as a function of period and size (QATS spectrum). (3c) Normalize each QATS spectral continuum to produce QATS signal-to-noise for detection statistic. See text in §3.2 for details.

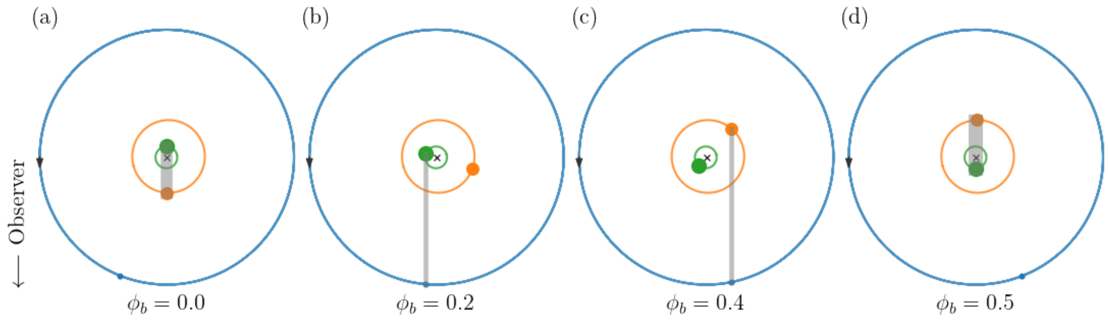

Figure 3.2 Geometry of a CBP system (21 d G + M binary with a 92 d planet), where ‘x’ marks the barycenter of the binary, and the green, orange, and blue symbols denote the position and orbit of the primary star, secondary star, and CBP, respectively. In this top-down view, the observer is located in the page, toward the direction indicated, such that the eclipsing geometry is met; the system is moving counterclockwise, as indicated by the arrow. Panels (a) through (d) depict consecutive snapshots of the system for *one instance* of the 3-body orbit, during primary eclipse (PE), transit across the primary (TAP), transit across the secondary (TAS), and secondary eclipse (SE), respectively. The grey regions represent the shadow of the occluding body. The orbits are scaled to each other, but the relative sizes of the bodies are exaggerated for visual clarity. The conjunctions are indicated as a function of binary phase ϕ_{b}, since they depend upon binary parameters; however, transits will not always occur at those binary phases.

being eclipsed by the secondary; while a secondary eclipse (SE) occurs when the secondary is occulted by the primary. We abbreviate when the planet transits either the primary or secondary star as transit across the primary (TAP) or secondary (TAS), respectively. While occultations of a CBP by its binary hosts may occur, they are typically not detected in the system light curve, as the planet's brightness is usually negligible compared to the sum of flux output by the binary. Throughout the paper, we denote quantities associated with the binary and planet with subscripts 'b' and 'p', and use subscripts 1 and 2 to describe the primary and secondary stellar component, respectively.

Figure 3.2 shows a subset of eclipse/transit geometries for an illustrative CBP system, in which the planet orbits every 92 d around a 21 d G+M dwarf binary. The timing and duration of stellar eclipses and planetary transits depend on the relative positions and velocities between each pair of bodies. These are determined, to first order, by binary parameters, which set the binary orbit and stable configurations for the CBP orbit.

In order for a CBP to be dynamically stable against perturbations by the binary, the planet must be located beyond a critical stability region. This critical semi-major axis a_c was first quantified numerically by Holman & Wiegert (1999) and subsequently confirmed and expounded upon by several authors (e.g., Li et al., 2016; Quarles et al., 2018; Sutherland & Kratter, 2019). Typically, $a_c \approx (2-3)a_{\mathrm{b}}$, or equivalently, $P_c \approx (3-5)P_{\mathrm{b}}$. This inner stability limit sets the inner boundary to the CBP search period.

3.2.2 CBP Transit Detection

Time-series Likelihood Ratio Test

Our detection algorithm relies on a model comparison technique, the likelihood ratio test. In essence, it compares the likelihood that a test CBP, corresponding to size R_{p} and period P_{p}, transits one of the stellar components at every time, t, in the light curve data, relative to a null hypothesis that no transit is present. We quantify this ratio of likelihoods as the difference in χ^2 between no-transit and transit, $\boldsymbol{\Delta\chi}^2 = \boldsymbol{\chi}^2_{\mathrm{null}} - \boldsymbol{\chi}^2_{\mathrm{CBP}}$. The $\Delta\chi^2$ centered around cadence i is given by

$$\begin{aligned}\Delta\chi_i^2 = &\sum_{i-N/2}^{i+N/2}\left(\frac{F_i - F_{\mathrm{CBP},i}(R_{\mathrm{p}}=0, P_{\mathrm{p}}, \boldsymbol{\theta_{\mathrm{b}}})\cdot P_i(k)}{\sigma_i}\right)^2 \\ &-\sum_{i-N/2}^{i+N/2}\left(\frac{F_i - F_{\mathrm{CBP},i}(R_{\mathrm{p}}, P_{\mathrm{p}}, \boldsymbol{\theta_{\mathrm{b}}})\cdot P_i(k)}{\sigma_i}\right)^2,\end{aligned} \tag{3.1}$$

where $\boldsymbol{F}$ and $\boldsymbol{\sigma}$ are the time-series data and associated uncertainties; $N+1$ is the length of the data segment being fit, which encompasses the duration of the test transit and continuum window surrounding it; $\boldsymbol{F}_{\mathrm{CBP}}$ is the model CBP transit light curve, which is a function of R_{p}, P_{p}, and binary parameters $\boldsymbol{\theta_{\mathrm{b}}}$; $\boldsymbol{P}(k)$ is a kth order polynomial, which is used to locally detrend the light curve. So, around each observed cadence i, we evaluate the difference in χ^2 between a polynomial-only fit and a CBP transit centered at i times a polynomial fit. We describe the CBP model which predicts $\boldsymbol{F}_{\mathrm{CBP}}$ in §3.2.2.

This formalism assumes that every $\Delta\chi_i^2$ or $\boldsymbol{F}_{\mathrm{CBP},i}$ samples the same number of data points $N+1$. As a result, any transit outside $N/2$ at the edges of a light curve will be missed. This problem is exacerbated in real observations, which may contain long gaps that separate the light curve into several data chunks. Therefore, in practice, we soften the requirement for strictly uniform $N+1$ sampling near edges, and adopt the reduced χ^2 as a metric to evaluate the time-series likelihood ratios, to mitigate against edge effects.

When a transit is present at cadence i (time t) in the data, the fit which includes the transit will give a lower χ_i^2 than the fit without the transit, so $\Delta\chi_i^2$ will be positive when a transit is present, and conversely it will be negative when there is no transit. In evaluating the likelihood that a transit corresponding to a test CBP with period P_{p} and size R_{p} occurs at every observable cadence in the light curve, we construct a time-series $\Delta\chi^2$ -curve. From here on, we drop the explicit arrow vector notation, and distinguish the vector (time-series) likelihood ratios as simply $\Delta\chi^2$ and scalar (specified time) likelihood ratio as $\Delta\chi_i^2$.

EB Model

To remove eclipses (see panel 1b of Figure 3.1) and predict transit depths, durations, and times during CBP-star conjunctions, we must determine the dimensions and orbital properties of the binary. We have previously characterized 728 well- to semi-detached *Kepler* EBs selected from the *Kepler* Eclipsing Binary Catalogue[2] (Prša et al., 2011). We refer the reader to Chapter 2 or Windemuth et al. (2019a) for a detailed description and discussion of our EB modeling process.

We use $\boldsymbol{\theta}_\mathrm{b}$ corresponding to the maximum-likelihood EB solution to predict the sky-projected binary positions as a function of time t, or binary phase ϕ_b. We consider the descending node of the binary orbit Ω to be 180° along the x-axis, following the convention of Winn (2010). The x, y, and sky-projected positions r_sky of each binary component are then

$$\begin{aligned} x_{1,2} &= -\mu_{1,2} r_\mathrm{b} \cos(\omega_{1,2} + f_\mathrm{b}), \\ y_{1,2} &= -\mu_{1,2} r_\mathrm{b} \sin(\omega_{1,2} + f_\mathrm{b}) \cos i_\mathrm{b}, \\ r_{\mathrm{sky};1,2} &= -\mu_{1,2} r_\mathrm{b} \sqrt{1 - \sin^2(\omega_{1,2} + f_\mathrm{b}) \sin^2 i_\mathrm{b}}\ , \end{aligned} \tag{3.2}$$

where

$$\begin{aligned} \mu_{1,2} &= \frac{M_{2,1}}{M_1 + M_2}, \\ r_\mathrm{b} &= \frac{a_\mathrm{b}(1 - e_\mathrm{b}^2)}{1 + e_\mathrm{b} \cos f_\mathrm{b}}, \\ \omega_1 &= \omega_2 + \pi \end{aligned} \tag{3.3}$$

with $a_\mathrm{b}, e_\mathrm{b}, i_\mathrm{b}$ being the semi-major axis, eccentricity, and inclination of the binary, and $f_\mathrm{b} = f_\mathrm{b}(t)$ is the binary true anomaly.

CBP Model & Transit Regularization

The CBP model uses the EB model (§3.2.2) and assumes that the planet is a test body, i.e., $M_\mathrm{p} = 0$, in a circular, edge-on Keplerian orbit around the binary barycenter. This approach

---

[2] http://keplerebs.villanova.edu/

makes simplifying assumptions to the 3-body problem. In reality, tidal or non-spherical distortions will alter the Keplerian binary orbit, and the changing binary potential modifies the CBP orbit. However, because the goal of this method is *detection* rather than detailed characterization, our approximations are valid for their speed and accuracy, greatly reducing the size of parameter space which must be explored to make a detection (see also §3.4).

We do not know *a priori* the period of the planet and the binary phase or time at which transits occur, except that the planet period must be greater than the critical period for stability P_c (Holman & Wiegert, 1999). Therefore, we sample, i.e., test for the presence of a CBP transit, at every cadence in the observed light curve. Furthermore, we test the entire light curve for every trial P_p and R_p, in a user-defined search grid. This is because the depth, duration, and timing of CBP transits depend on binary parameters $\boldsymbol{\theta}_\mathrm{b}$ as well as trial planet parameters.

For a particular planet period and size, QATS-EB calculates the time-dependent positions of and relative separations between the planet and a stellar component *at a proposed mid-transit time.* To regularize transits, we use the relative planet-star sizes and stellar flux ratio to determine the expected transit depth δ, and use the time of first and fourth contact to evaluate the transit duration τ as a function of time t or binary phase ϕ_b (see panel 2b of Figure 3.1).

Additionally, we correct for the large-scale, binary-induced TTVs by realigning test transits across one of the binary components (a "moving target") such that they occur at the (stationary) binary barycenter at $x = 0$. We refer to the time between transit in front of a stellar component to transit in front of the barycenter as the barycentric time offset t_bary . This t_bary changes as a function of ϕ_b and is approximately given by

$$t_\mathrm{bary} = \frac{x_\mathrm{p}(t_\mathrm{tran}) - x_\mathrm{bary}}{v_{x,\mathrm{p}}(t_\mathrm{tran})} = \frac{x_1(t_\mathrm{tran})}{v_{x,\mathrm{p}}(t_\mathrm{tran})} \tag{3.4}$$

which assumes that the planet is moving at constant velocity across the distance between the stellar component and binary barycenter, in the x-direction. Since the $\Delta\chi^2$ -curve is a time-series likelihood ratio test for the presence of CBP transits, we apply this timing offset to all proposed mid-transit times, i.e., observed cadences. In doing so, we transform the entire $\Delta\chi^2$ from observed times t to $t' = t - t_{\rm bary}$.

Thus, for a given set of light curve data, binary parameters, and test CBP period and size, QATS-EB computes a regularized matrix $\Delta\chi^2(P_{\rm p}, R_{\rm p}, t')$. This timing transformation effectively reduces the observed, large-amplitude binary-induced TTVs.

To demonstrate the efficacy of the timing transformation, we show an example of its application to *Kepler*-35*b* in Figure 3.3. The figure illustrates the differences in TTV amplitudes for *Kepler*-35*b* with and without time correction. Here, we apply QATS-EB with the same search parameters except using $f = 0.005$ and $f = 0.02$ to t' and t, respectively, where f is the fractional TTV window relative to the search $P_{\rm p}$ (see §3.2.2 for further discussion of f). The transit light curves and corresponding $\Delta\chi^2$ (left panels) are folded to their respective best detected periods, with the mean transit aligned to an arbitrary planet phase. For visual presentation, we vertically stack QATS-detected transit events and plot linearly detrended light curves, with dark circles denoting the QATS-detected times of transits. The left panels clearly demonstrate a significant reduction in TTVs when timing correction is applied; the mean TTV scatter decreases from ∼0.5 d to ∼0.05 d (see right panel).

Finally, because CBP transit duration varies strongly as a function of binary phase (see panel 2b of Figure 3.1), a $\Delta\chi^2$ -curve corresponding to a particular physical CBP model will also vary strongly as a function of binary phase. This is because for a CBP system, the majority of its light curve does not contain transits. Thus, in general, $\Delta\chi_i^2$ values are smaller for $\phi_{\rm b}$ or t where the model predicts shorter CBP transits than for $\phi_{\rm b}$ with longer predicted transits, artificially causing the continuum of the $\Delta\chi^2$ -curve to be sinusoidal. This quasi-periodic signal in the $\Delta\chi^2$ continuum must be removed, as the standard QATS algorithm is not optimized for non-Gaussian noise.

To this end, and to make the search more computationally tractable, we adopt the following procedure in practice. First, we pre-compute a $\Delta\chi^2$ (τ, δ, t) matrix, i.e., in a 2D grid of duration τ and depth δ, using a U-shape transit profile (see panel 2a of Figure 3.1). Because the χ^2 is quadratic as a function of depth, we can compute the $\Delta\chi^2$ at any δ by evaluating

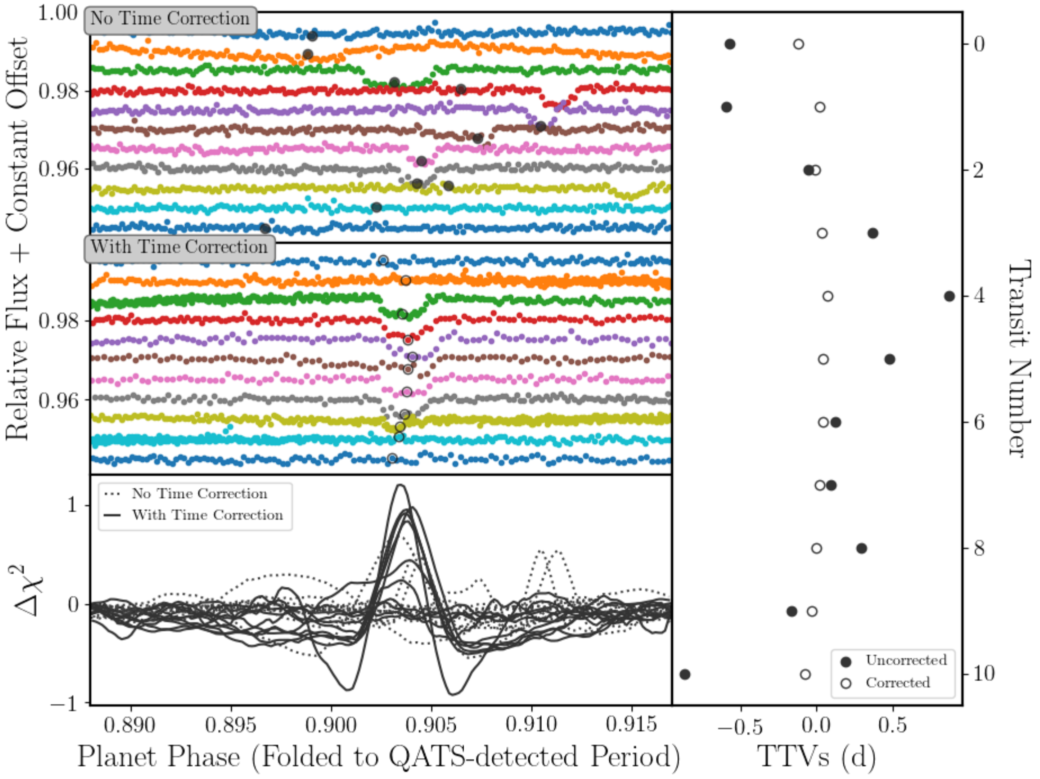

Figure 3.3 Comparison of transits for *Kepler*-35b in regular time t and resampled time $t' = t - t_{\rm bary}$, where we apply QATS-EB with $f = 0.02$ and $f = 0.005$ to uncorrected and corrected cases, respectively. The left panels show the transits folded to their respective QATS-detected period, with arbitrary mean phase offset. Top panels show *Kepler* data, detrended with a linear polynomial and each transit number plotted with a constant flux offset, for visual effect. The dark circles denote the indices corresponding to the best QATS-detected period; note in the uncorrected case, the best detected period some times misses when true transits occur, due to their large TTVs. The bottom panel illustrates the corresponding expected $\Delta\chi^2$ with the best QATS-detected transit depth and period. The transits are clearly more aligned when the barycentric timing offset is applied; the TTVs are reduced by an order of magnitude, from ∼0.5 d to ∼0.05 d (see right panel).

the U-shape transit model at three grid points in δ (Kruse et al., 2019). Then, we construct a CBP template, containing predicted transit depth, duration, and $t_{\rm bary}$ as a function of binary phase (see panel 2b of Figure 3.1). Finally, we use that CBP template to linearly transform from the pre-computed $\Delta\chi^2$ (δ, τ, t) to the expected, or physical $\Delta\chi^2$ (P_p, R_p, t') (see panel 2c of Figure 3.1).

In detail, we standardize the "raw," pre-computed $\Delta\chi^2$ (τ, δ, t) matrix before using the CBP template to interpolate $\Delta\chi^2$ as a function of physical parameters $R_{\rm p}$ and $P_{\rm p}$. Recall that at cadences without transits, $\Delta\chi^2_i$ changes strongly with duration. Thus, for each time-series slice of the pre-computed $\Delta\chi^2$ (τ, δ, t), larger duration values lead to more negative zero-point and higher scatter in the $\Delta\chi^2$ continuum (see Figure 3.1 panel 2a), so that interpolating the raw $\Delta\chi^2$ will introduce a variable continuum at the binary period. To avoid this correlated signal, we subtract each time-series $\Delta\chi^2$ vector by its median, i.e., 50th percentile value and then normalize by the 68th percentile absolute difference value, a 1σ estimate on the continuum scatter.

Then, for a given test CBP $P_{\rm p}$ and $R_{\rm p}$, we linearly interpolate the expected $\Delta\chi^2_i$ value from the expected transit duration at each time t and the standardized, pre-computed $\Delta\chi^2$ grid. This removes binary phase dependence during interpolation and preserves the height of $\Delta\chi^2$ "pulses" – when transits are actually present – relative to the continuum (see panel 2c of Figure 3.1). Finally, we transform to the barycentric time frame by resampling in uniform cadence $t' = t - t_{\rm bary}$.

QATS Detection Significance

We feed the regularized $\Delta\chi^2$ $(P_{\rm p}, R_{\rm p}, t')$-curves into standard QATS, which returns the maximum stacked transit signal $S_{\rm best}(P_p, R_p, f)$, where P_p, R_p are the search period and size (depth), and f is the user-specified, fractional transit timing variation window per $P_{\rm p}$. We build up a QATS quasi-periodogram or "spectrum" (see panel 3a of Figure 3.1) by searching through a range of planet periods, or, more precisely, range of minimum and maximum periods bounded by f.

The choice of the quasi-periodic window is non-trivial, as a larger window is more likely to encompass transits with larger TTVs, but at the expense of including more background noise. Carter & Agol (2013) recommended a constant fraction f of the (average) search period, such that the difference between minimum and maximum quasi-periodic intervals scales linearly with the planet's orbit. This strategy is motivated by theoretical predictions of TTVs on a transiting CSP by additional perturbing bodies (Agol et al., 2005). In the CBP case, the large-scale, binary-induced TTVs scale with $(P_\mathrm{b}/P_\mathrm{p})^{2/3}$ (see, e.g., Armstrong et al., 2013). This motivates a choice for f that increases more slowly with search period, which is attractive in that it includes less background noise at larger planet search periods. However, inaccuracies in the binary model and eccentricities in the planet's orbit will introduce additional timing error or variations, which can grow with planet period. For this paper, we adopt the fixed f approach and find it effective in detecting the $P_\mathrm{p} < 150$ d simulated and known *Kepler* CBPs.

The continuum behaviour of the raw QATS spectrum depends on the noise properties of the light curve and corresponding $\Delta\chi^2$ -curve and the input search parameters. To flatten the continuum, we fit a linear combination of polynomials in P_p, the number of QATS-detected transits N_tran, and the width of the transit timing variation window per search period, in cadences. We then subtract the linear combination model and normalize by the local QATS noise around each P_p (see panel 3b of Figure 3.1; Kruse et al., 2019). This forms the final QATS "signal-to-noise" and quantifies the detection significance.

3.3 Example Applications

3.3.1 Simulated Data

We first test our technique on simulated data. We use the N-body integrator `rebound` (Rein & Liu, 2012) to simulate a system with orbital and binary properties similar to *Kepler*-47*b* (Orosz et al., 2012a), but place an Earth-mass and Earth-size planet around the G and M dwarf binary. We integrate the system for 200 days (roughly 26.5 times the binary period), and tabulate the exact binary and planet parameter values used to initialize the simulation in Table 3.1. The sky-positions of each body are used to determine the system flux at every conjunction event via the Mandel & Agol (2002) model. We inject white noise to the simulated light curve with $\sigma = 5 \times 10^{-5}$. The top panel of Figure 3.4 shows the EB-removed light curve of the simulated system. It contains 4 transits across the primary component ($\delta \approx 0.0001$). Because the secondary star is much fainter than the primary ($F_2/F_1 \approx 0.006$), transits across the secondary are extremely shallow, below the level of injected noise σ.

We apply QATS-EB to the light curve shown in the top panel of Figure 3.4, using binary parameter values listed in Table 3.1 to compute expected $\Delta\chi^2$ and a fractional TTV window $f = 0.01$. That is, at each trial planet period, QATS computes the maximum total transit signal-to-noise with quasi-periodic bounding between successive transits which is 1% of the search period wide. The resulting QATS detection significance is plotted in the bottom panel of Figure 3.4, where blue and orange colors indicate a QATS-EB search with and without timing corrections, respectively, as outlined in §3.2.2. The Earth-size planet is detected at higher signal-to-noise ratio (S/N=20) when barycentric timing offsets are applied, about 1.4 times more significant than the non-regularized case (S/N=14).

Table 3.1 Binary and Circumbinary Planet Parameters

System	P_b (d)	e_b	i_b (°)	M_1 ($M_\odot$)	M_2 ($M_\odot$)	R_1 ($R_\odot$)	R_2 ($R_\odot$)	F_2/F_1	P_p (d)	e_p	i_p (°)	R_p ($R_\oplus$)	M_p ($M_\oplus$)
Simulated*	7.448	0.0288	89.34	1.04	0.36	0.964	0.351	0.00568	49.514	0.02	90	1	1
Kep-35b†	20.733666	0.1421	90.4238	0.8877	0.8094	1.0284	0.7861	0.3941	131.458	0.04	90.76	8.16	40
Kep-64b‡	20.000214	0.2117	87.36	1.384	0.387	1.75	0.422	0.00153	138.317	0.05	90.022	6.18	<168

Note: * modeled after *Kepler*-47b (Orosz et al., 2012a); † Welsh et al. (2012); ‡ Schwamb et al. (2013).

3.3.2 Known Kepler *CBPs*

Next, we demonstrate improved detection significance using QATS-EB on two known CBP systems, *Kepler*-35*b* (Welsh et al., 2012) and *Kepler*-64*b*/PH1*b* (Kostov et al., 2013; Schwamb

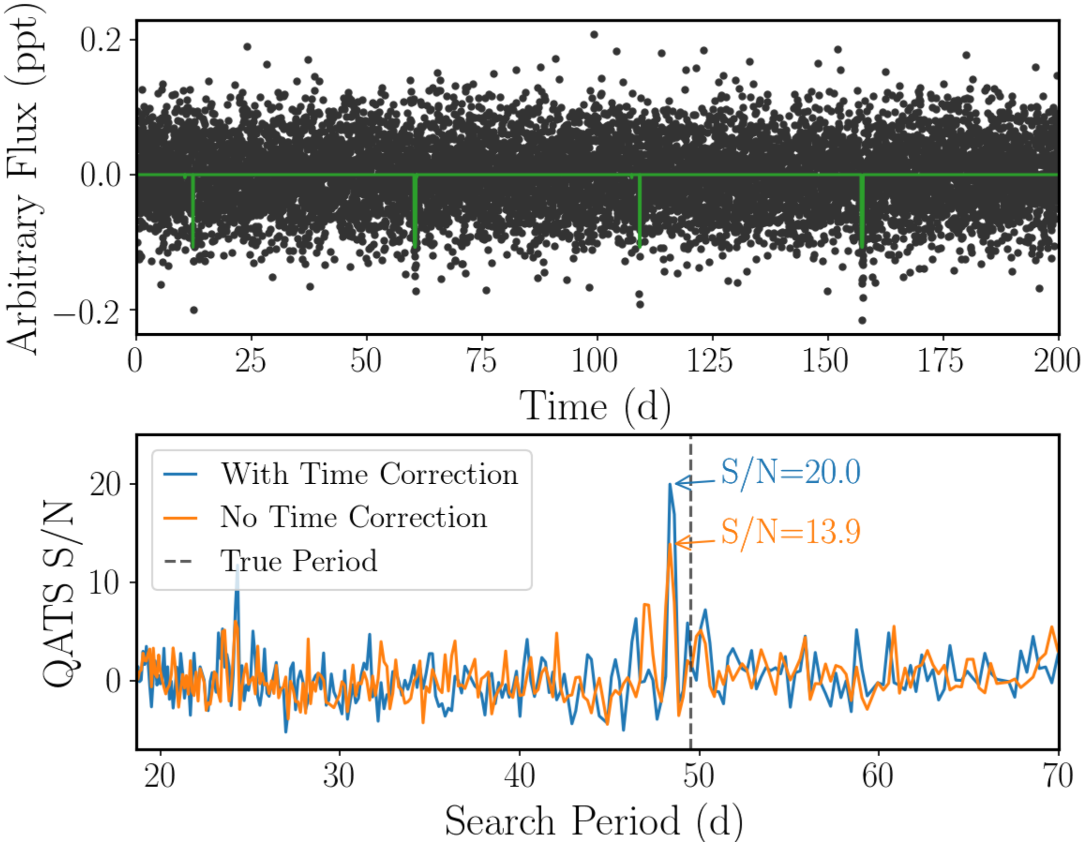

Figure 3.4 Top: Simulated data (EB-removed) for a $1M_{\oplus}$, $1R_{\oplus}$) CBP around a 7.5 d G+M-dwarf binary with orbital and binary properties similar to *Kepler*-47 system (Orosz et al., 2012a, 2019) (see Table 3.1). The simulated light curve, in arbitrary normalized, median-subtracted flux in parts-per-thousand (ppt), contains 4 transits across the primary ($\delta = 0.0001$; the noiseless light curve is shown for reference). Transits across the secondary stellar component are not observed above the injected white noise threshold ($\sigma = 5\times10^{-5}$). Bottom: Recovered QATS signal-to-noise spectrum with a fractional TTV window f=0.01, i.e., 1% of the search period. Blue and orange lines indicate QATS detection significance with and without barycentric timing offset correction. While the Earth-size planet is clearly detected in both instances, including timing correction yields a detection at the true period with a significance that is 1.4 times higher than the uncorrected case.

et al., 2013). We show, for reference, the binary and CBP parameter values for both systems from their discovery papers in Table 3.1. Although both CBPs were discovered by eye, they were used as benchmarks for previous automated detection algorithms (Klagyivik et al., 2017 with *Kepler*-35*b*; Armstrong et al., 2014a with *Kepler*-64*b*) and provide a good baseline for comparison.

We utilize *Kepler* simple aperture photometry (SAP) data, normalized by the median SAP flux of each observing quarter, spanning a total duration $\mathcal{T} \sim 4$ years at a cadence of 0.0204 d (30 min). We subtract eclipse signals using the best-fit models from Windemuth et al. (2019a), and remove data points with quality flags >0, filling missing cadences with neighboring median flux values. We then apply QATS-EB to the "cleaned" light curves. We employ a logarithmic depth grid of 1–30 times the median absolute difference in flux and a finely-spaced duration grid of 3–61 cadences (0.06–1.2 d) to construct the $\Delta\chi^2$ (δ, τ, t) matrix. We then transform this matrix to the expected $\Delta\chi^2$ $(R_{\rm p}, P_{\rm p}, t')$ using the best-fit binary parameters. We execute the quasi-periodic search with fractional TTV windows $f = 0.005, 0.02$, initial and final planet periods $P_{{\rm p},i} = 2.5P_{\rm b}$ and $P_{{\rm p},f} = \mathcal{T}/3$, i.e., requiring at least three primary transits. On a 2012 Intel® Core™ i5-3570 3.4GHz Linux machine with 4GB of memory, the QATS-EB search over ∼3x400 test CBP radii and periods takes ∼5 mins on each cleaned light curve (∼65,000 cadences). This is approximately two orders of magnitude slower than standard QATS; however, the number of *Kepler* EBs around which to search for CBPs is roughly two orders of magnitude fewer than *Kepler* single stars. Thus, the total computation times are comparable.

We show a subset of the EB-removed light curve of *Kepler*-64, on which we apply QATS-EB, and the resulting QATS detection spectrum with $f = 0.005$ in the upper and lower panels of Figure 3.5, respectively. The QATS detection spectrum shows a strong peak (S/N=26) near the true period of 138 d with weaker peaks at P/2, 2P, and 3P aliases, at higher significance than Armstrong et al. (2014a) values (grey region). They defined detection significance as the mean value of the maximum peak and associated aliases, divided by the median periodogram value. This differs somewhat from the QATS S/N definition, which more closely resembles the Signal Detection Efficiency, defined as

$$\mathrm{SDE} = \frac{S_{\mathrm{peak}} - \mathrm{avg}(S)}{\mathrm{stdev}(S)} \ , \tag{3.5}$$

where S is the signal (Kovács et al., 2002). From Figure 1 of Armstrong et al. (2014a), we estimate an equivalent $\mathrm{SDE}_{\mathrm{hi}}$=(1.0-0.37)/0.05≈12.5 and $\mathrm{SDE}_{\mathrm{lo}}$=(1.0-0.37)/0.1≈6.5, which are 2 to 4 times smaller than the QATS-EB S/N.

Finally, we show the detection of *Kepler*-35*b* in Figure 3.6, and demonstrate how regularizing the transits using a physical model (2a–2c in Figure 3.1) substantially improves the detection S/N. The top panel illustrates a slice in depth of the pre-computed $\Delta\chi^2$ (δ, τ, t) matrix, i.e., $\Delta\chi^2$ as a function of time for different test transit durations and fixed depth ($\delta = 4.58 \times 10^{-4}$). The bottom panel plots the QATS S/N spectrum as a function of the quasi-periodic search period at fixed depth, under different search conditions.

Without the barycentric timing offsets to regularize transit times, QATS-EB requires a larger TTV window, i.e., includes more noise, for detection (see green vs. orange lines). Applying time corrections enables a reduction in f and greatly increases detection significance (blue line). The CBP is clearly detected near the true period ($P_{\mathrm{p}} = 131.5$ d) at S/N=35.6, with additional strong peaks at 1:2, 2:1, and 3:1 aliases of the period. This detection significance is 1.5 times higher than the case with $f = 0.02$ and no timing correction. For comparison, we overplot detection results from Klagyivik et al. (2017) as black stars (see their Figure 1), where the highest peak from their analysis occurs near the 2:1 period alias, corresponding to a S/N of 17. They also recover the true period, although at lower detection significance (S/N≈7).

3.4 Discussion

We have demonstrated the efficacy of QATS-EB to detect single transiting CBPs in §3.3. QATS-EB yields a 40% increase in detection significance compared to standard QATS (Carter & Agol, 2013), and outperforms previous automated techniques applied to known *Kepler* CBPs (Armstrong et al., 2014a; Klagyivik et al., 2017) by factors of 2 to 4. Here, we

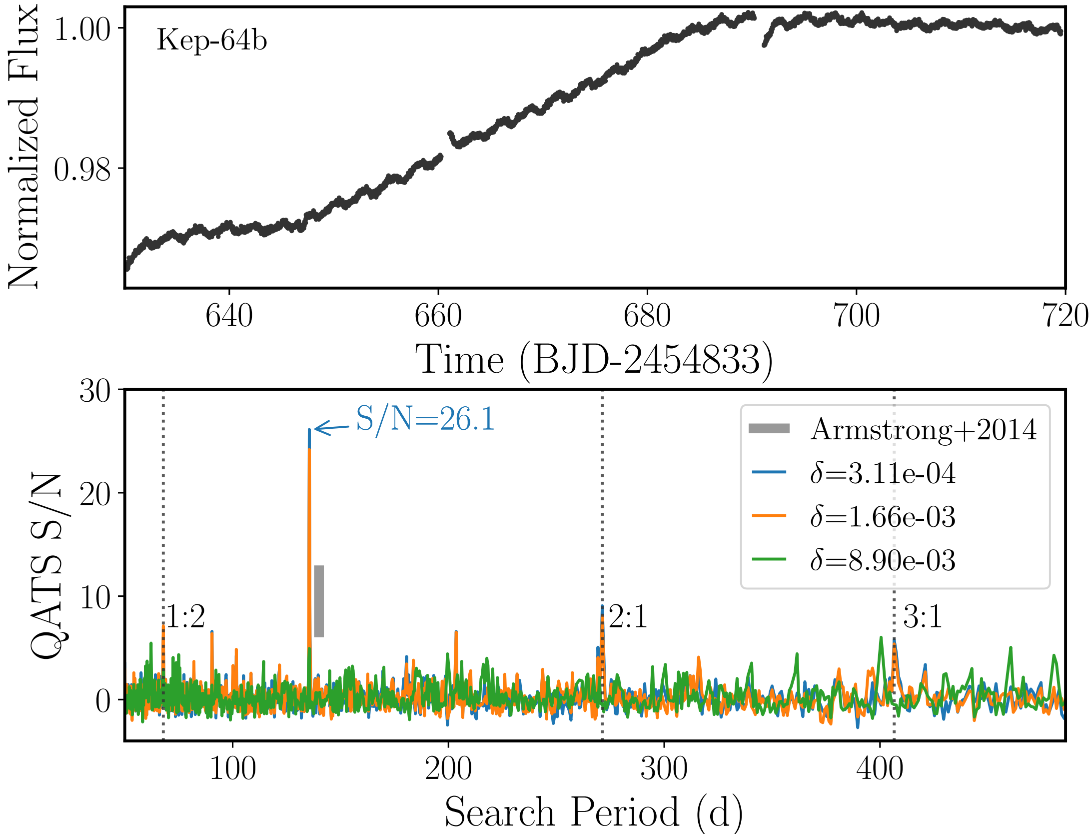

Figure 3.5 Detection of *Kepler*-64*b*. Top: a subset of the EB-removed SAP light curve, which shows high frequency stellar variability. Bottom: QATS-EB detection significance for different transit depths δ (CBP size). The grey region represent the relative detection significance from Armstrong et al. (2014a), based on estimated values from their Figure 1. Dotted lines mark P/2, 2P, 3P harmonics of the planet period.

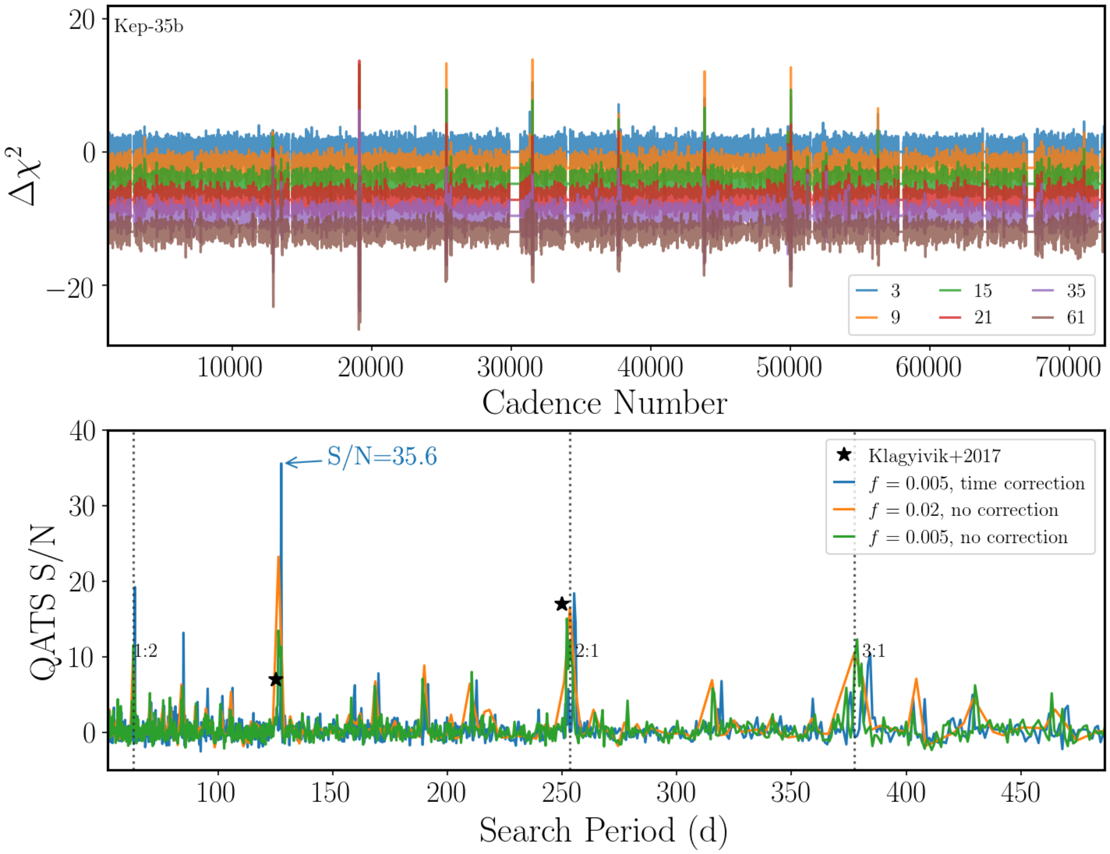

Figure 3.6 Detection of *Kepler*-35*b*. Top: $\Delta\chi^2$ -curves as a function of test transit duration (in cadences), arbitrarily offset for visual effect, at a fixed transit depth ($\delta = 4.58 \times 10^{-4}$); the $\Delta\chi^2$ (δ, τ, t) matrix is used to compute the expected $\Delta\chi^2$ $(R_\mathrm{p}, P_\mathrm{p}, t')$. Bottom: Resulting QATS-EB detection significance as a function of planet period in days, where different colors represent different search parameters and dotted lines denote aliases of the most likely period. Using the barycentric timing offset allows for smaller TTV windows f in the QATS-EB search and significantly increases the detection S/N. With the timing correction, the planet is clearly detected near the true period of 131.5 d, at a S/N of 35.6. For comparison, Klagyivik et al. (2017) (shown as black stars) detected the 2:1 period alias at S/N=17 (comparable to QATS-EB with $f = 0.02$ and no timing correction; orange line) and the true period at S/N=7.

revisit the underlying assumptions of QATS-EB and discuss their motivations and validity for this two-component technique.

The original QATS algorithm maximizes the likelihood of transits in uniform cadence under the condition of quasi-periodicity and homogeneous transit duration. Applying this in its standard form to CBPs suffers from requiring a wide timing window, given their large, binary-induced TTVs, as well as from breaking the assumption of uniform transit duration. Instead, an ideal method for the detection of transiting circumbinary exoplanets would be to create a physical model for a CBP system, and to exhaustively search the parameter space of that model for the presence of a transiting planet (e.g., Doyle et al., 1995). However, this approach is extremely computationally expensive: given six CBP orbital elements and a radius relative to the size of the occulted stellar component, combined with the uncertainty in the number of CBPs in a system, this approach would require an initialization at an enormous number of models on a grid of instantaneous planet orbital periods, eccentricities, longitudes of periastron and ascending node, inclinations, phases, and radius ratios.

QATS-EB is a compromise between these extremes: we account for large-scale duration and timing variations using a simple, semi-analytic physical CBP model, while the flexibility of the standard QATS algorithm absorbs some of the inaccuracies incurred in this approximate model. The approximate CBP model, as detailed in §3.2, operates under the following assumptions:

1. It assumes that the binary parameters are perfectly known. This assumption can be thwarted by inaccuracies in the modeling of the eclipsing binary, and/or by difficulties with detrending the light curves.

2. It assumes a circular orbit for the planet. Although the majority of known CBPs have small eccentricities ($\lesssim$0.05), the effect of eccentricity, when unaccounted for, may introduce error in transit shape and timing predictions.

3. It assumes that the planet's orbit is edge-on and that its impact parameter does not

change significantly over the range of observed transits, i.e., that the depth of TAP and TAS is constant over the duration of observation.

4. It assumes that each transit event across one of the binary stars results in a single dip, rather than multiple dips during conjunction, which can occur when the star catches up and passes the planet multiple times.

5. It assumes a single, test circumbinary planet. In principle, one can iteratively apply QATS-EB to detect additional planetary companions by masking transits associated with a detected candidate, as planet-planet perturbations are typically much smaller than binary-induced transit variations. However, multi-planet configurations with large transit timing and duration variations will require relaxing f and reduce QATS S/N.

In the following subsections, we further discuss the scope of the limitations that assumptions 1–4 impose, as well as possible avenues for improvement. We argue that in most cases, the assumptions should not severely limit the performance of the search algorithm. We acknowledge that a more rigorous approach to quantify the algorithm's completeness and false alarm probability requires applying QATS-EB en masse to a large grid of CBP simulations, *with noise properties from or closely mimicking the data set upon which a transiting CBP search is applied.* This is beyond the scope of this current paper, and we leave performing a detailed injection and recovery analysis as a future task.

3.4.1 Mass Ratio and Orbital Eccentricity

The standard QATS algorithm can mitigate the effects of assumptions 1 (exact binary solution) and 2 (circular planet orbit) when they are partly violated. If the mass ratio of the binary is inaccurate, this will affect the transit timing and duration amplitudes. Figure 3.7 shows the expected transit duration and timing offset as a function of binary phase, for a rocky CBP orbiting every 60.9 d around a 7.45 d binary with different mass ratios $Q = M_2/M_1$ and eccentricities e_b. For reference, primary eclipse occurs at phase=0, while secondary eclipse occurs near phases of 0.5 and 0.4, for circular and eccentric binary cases, respectively. The expected transit duration and timing offset are largest for equal mass, eccentric binaries, in which binary reflex motion is greatest. Moreover, the greatest change in TAP duration occurs near phases surrounding secondary eclipse, when the sky-projected velocities of the primary star and planet are at their maximal amplitude and in the same direction.

Likewise, deviations from a circular orbit of the planet will introduce differences in the transit timing and duration amplitudes relative to true values. We explore the effects of planet eccentricity by initializing `rebound` CBP models on a coarse grid of binary mass ratios $Q \in \{0.3, 0.9\}$, binary eccentricities $e_{\rm b} \in \{0.02, 0.2\}$, and planet longitudes of periastron $\omega_{\rm p} \in [0, 2\pi]$ in steps of 0.5, to populate transits in binary phase. We hold constant all other parameters: $P_{\rm b}$=7.45 d, $P_{\rm p}$=60.9 d, $\omega_{\rm b}$=226.4^o, $i_{\rm b}$=89.5^o, $i_{\rm mutual}$=0.2^o. We then compare QATS-EB predictions of transit duration (τ) and barycentric time offset ($t_{\rm bary}$) to simulation "truths."

We show the scatter distributions of τ and $t_{\rm bary}$, marginalized over binary phase, as "violin" plots (Hintze & Nelson, 1998) in Figure 3.8. Here, the color regions ("violins") represent kernel density estimations of the scatter, i.e., $\Delta t_{\rm bary}$ and $\Delta\tau$ distributions, where the white circles denote median values. The dark boxes span first to third quartiles, or the inner quartile range (IQR; $\pm 0.67\sigma$), and the whiskers span ±1.5 IQR of the first and third quartiles ($\pm 2.7\sigma$). For small planet eccentricities (see $e_{\rm p}$=0.02 cases), QATS-EB predictions typically agree with simulation values to within 0.01 d. For eccentric planets (see $e_{\rm p}$=0.2 cases), QATS-EB predictions typically differ by ∼0.05 d and ∼0.1 d – roughly 0.1% and 0.2% of the planet period – for low and high mass ratio binaries, respectively. The largest deviations in transit duration ($\gtrsim$ 0.5 d) occur near binary phases where the transit duration changes rapidly, i.e., when the projected x-velocity of the stellar component changes direction to match that of the planet's (see region around $\phi_{\rm b}$=0.3-0.7 in Figure 3.7). Thus, even for modestly eccentric CBPs, applying $t_{\rm bary}$ reduces binary-induced TTVs by a factor of 5–10.

The QATS algorithm can, in principle, correct for the error in the transit timing amplitude

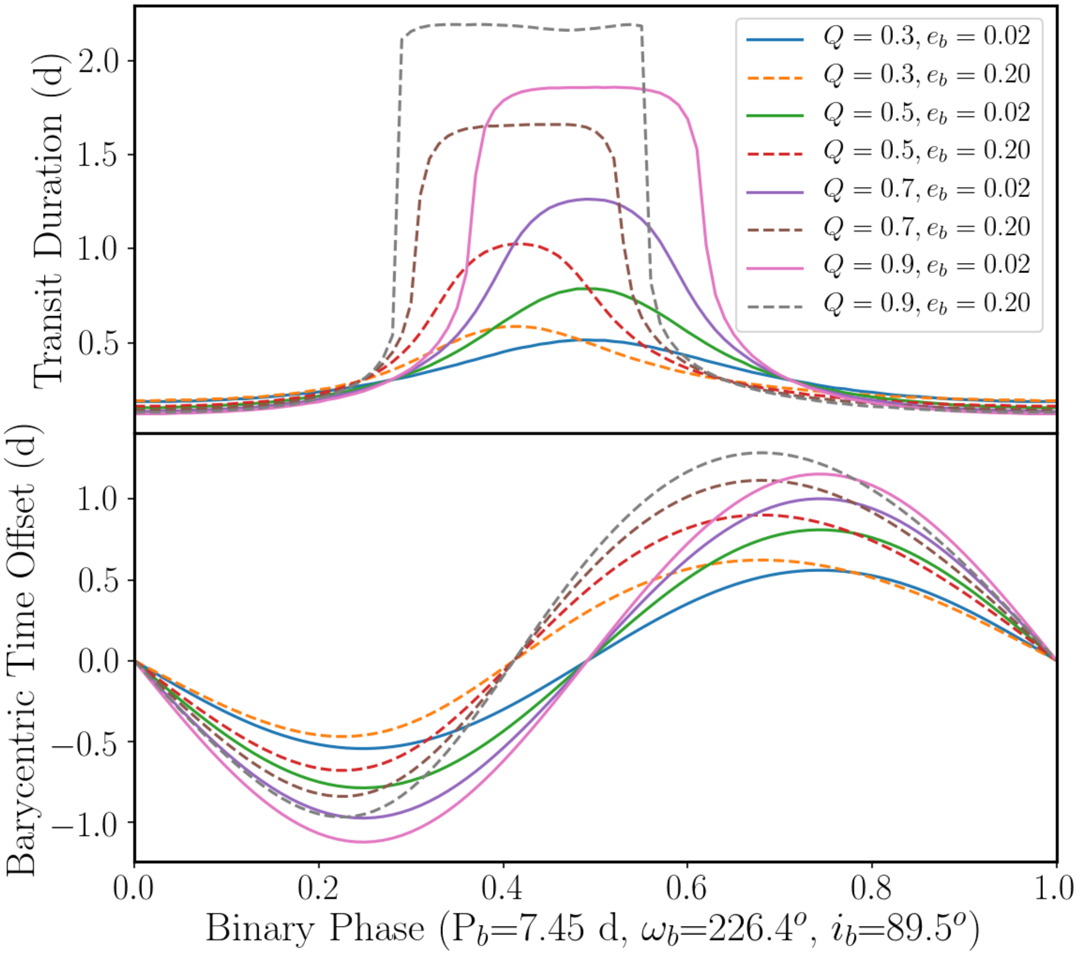

Figure 3.7 The expected transit properties for an Earth-size CBP (P$_p$=60.9 d) in a circular, edge-on orbit around a 7.45 d binary as a function of binary mass ratio $Q = M_2/M_1$ and eccentricity $e_{\rm b}$. All other system parameters are held fixed.

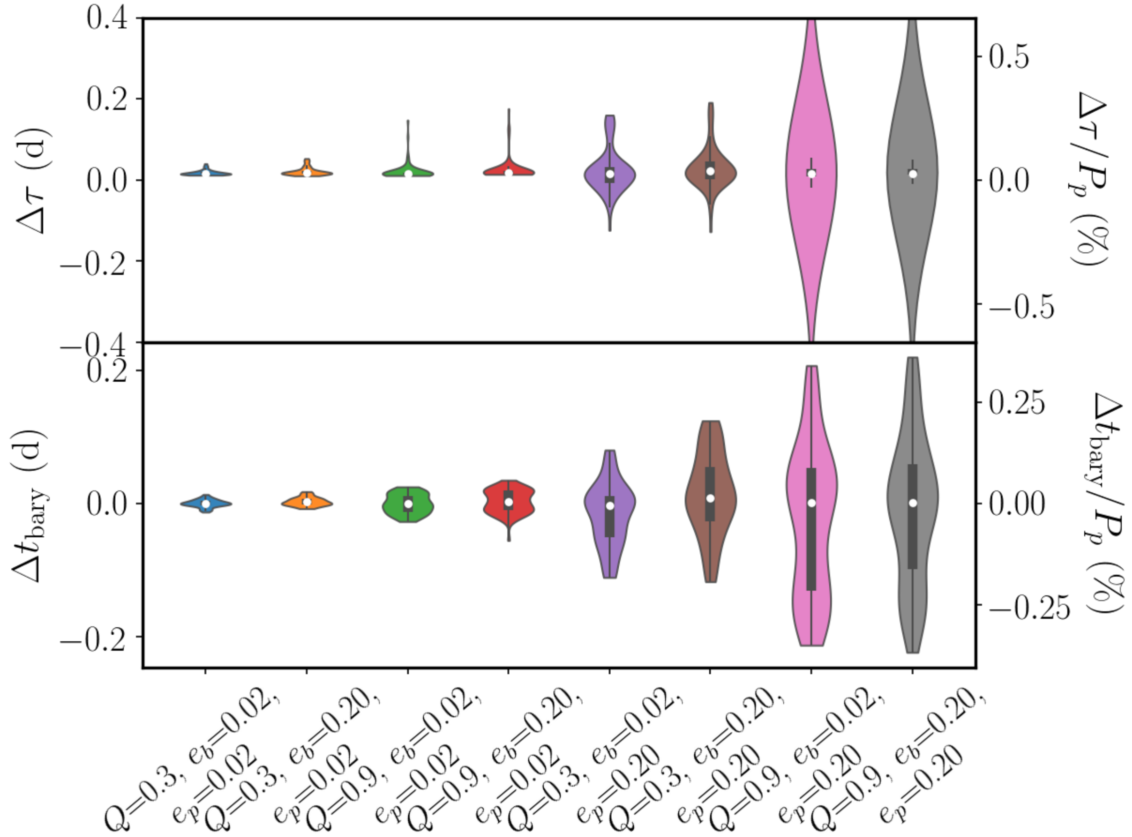

Figure 3.8 The scatter distribution, marginalized over binary phase, between expected QATS-EB model values and simulation "truths," for different CBP model initializations (x-axis). Top and bottom panels show differences in transit duration τ and barycentric timing offset $t_{\rm bary}$ in days (left axis) and per $P_{\rm p}$ = 60.9 d (right axis), respectively. The colored, shaded regions ("violins") represent the full distribution of difference values, where the widths indicate frequency of the dependent variable. The white circles correspond to second quartile (median) values; the thick dark box represents the inner quartile region (IQR), from first to third quartile range ($\pm0.67\sigma$). The thin dark lines or "whiskers" denote the ±1.5 IQR of the first and third quartiles ($\pm2.7\sigma$). Note that for $e_{\rm p}$=0.02 cases, the difference between true and QATS-EB values is ∼0.01 d, shorter than *Kepler* long cadence. For eccentric planets, QATS-EB predictions have larger error, as expected, with the bulk of scatter ∼0.1 d, about 0.2% of the planet period.

by using a wider user-specified window, but the variation in duration will lead to a slight loss in detection signal-to-noise. Fortunately, widening the QATS window causes the false-alarm floor to rise logarithmically, and so in many cases will not severely impact the transit detection capability of the algorithm (Carter & Agol, 2013). For comparison, we tested QATS-EB on a circular ($e_\mathrm{p} = 0.02$) vs. eccentric ($e_\mathrm{p} = 0.2$) Earth-size CBP orbiting every 60 d around a $Q = 0.9, e_\mathrm{b} = 0.2, P_\mathrm{b} = 7.5$ d EB, and found a S/N reduction factor of 1.5 for $f = 0.01$.

3.4.2 Time-varying CBP Orbital Elements

QATS-EB assumes that the orbit of a CBP is edge-on when computing expected transit properties. For small deviations from this configuration, the change in expected τ and t_bary is small ($\lesssim 0.05$ d). However, the orientation of a CBP and its mutual inclination with respect to the binary are not constant in time, even in stable configurations. Indeed, CBP orbits are perturbed by the time-varying binary potential, leading to precession and, in the case of eccentric binaries, libration of planet orbital elements (Schneider, 1994; Farago & Laskar, 2010; Doolin & Blundell, 2011); this oscillation of orbital elements can cause transits to disappear (e.g., *Kepler*-413*b*; Kostov et al., 2014) or to appear (e.g., *Kepler*-47*c*; Orosz et al., 2019) over time, as the system departs from and enters into a transiting geometry. In particular, the precession timescale for circular binaries is proportional to P_p and $(a_\mathrm{p}/a_\mathrm{c})^2$. For CBPs close to the stability region around short-period ($P_\mathrm{b} \approx 10$ d) binaries, which describes the majority of the discovered population thus far, this timescale can be of order 1000s d, comparable to the length of observation for, e.g., *Kepler*. In such instances, the disappearance of transits during the total observing timespan, as is the case for *Kepler*-413*b* (Kostov et al., 2014), leads to a detection signal-to-noise loss, as S/N $\propto \sqrt{N_\mathrm{tran}}$.

Since it is highly inefficient for a detection algorithm to explore non-transiting parameter space, quantifying the limits of detection requires separately deriving geometric transit probabilities. This is non-trivial for CBPs, due to precession. For more details, we refer the reader to Li et al. (2016) and Martin & Triaud (2016), who studied the transit probability of CBPs around circular binaries under finite observing times.

3.4.3 Single vs. Multiple Transits during Conjunction

Because the stellar components move along an orbit interior to a circumbinary planet, the differential relative speeds and sky positions may lead to multiple transits during one conjunction. Strictly speaking, there are two scenarios which result in multiple transits near one conjunction: (a) Near barycenter crossings, when the stellar components themselves are near eclipse, a CBP may consecutively transit one star then another; (b) When a CBP moves slowly relative to a stellar component, the star may pass through the planet's shadow multiple times, causing multiple transits across the same star (Deeg et al., 1998; see their Fig. 1). QATS-EB can, in principle, treat scenario (a), although in its current implementation it must search for transits across the primary independently of transits across the secondary, and vice versa. Scenario (b) forms a corollary to assumption 4, that a single transit or dip occurs each time the planet crosses one component of the binary. As we show below, this assumption, which we call the "single-transit-per-stellar-conjunction" or "single-transit" criterion for short, is typically satisfied.

The single-transit criterion can be met if the speed of the planet is sufficiently large compared to that of the primary (or secondary) star, such that the star does not have time to loop around and intersect the planet's shadow along the line-of-sight multiple times. We explore in Appendix A the range of parameters for which there will be a single vs. multiple transits of the primary and secondary stellar component by the planet when it crosses the binary, in the limit of circular, edge-on orbits for both planet and binary. We derive the critical planet velocity for single-transits marginalized over binary phase and compute the fraction of time corresponding to single-transits of the primary and secondary (see appendix). We show that for CBP systems with semi-major axis ratios $a_{\rm p}/a_{\rm b}$ ranging from 3 to 10 and binary star mass ratios $Q = M_2/M_1$ ranging from zero to one, the probability of a single-transit exceeds 86% for both the primary and secondary star in the circular edge-on case. We expect that for modest binary eccentricities this will also hold true. The single-transit constraint required by QATS-EB, then, applies to the bulk of parameter search space, except for pathological cases.

3.5 Conclusions

We have developed an automated transit detection algorithm tailored to find circumbinary planets, which exhibit large transit timing, duration, and depth variations due to reflex motion of binary hosts. Our technique, dubbed “QATS-EB,” uses a physical EB+CBP model to regularize the transits with respect to the binary barycenter, and constructs a time-series in CBP transit likelihood. QATS-EB permits additional TTVs after regularization, i.e., due to model inaccuracies, by using the quasi-periodic search algorithm developed by Carter & Agol (2013). This two-component technique enhances overall detection significance, which is particularly important when searching for CBPs that are small and/or exhibit sparse transits. Figure 3.1 shows a summary of the search procedure and detection statistic.

To balance computational efficiency and model complexity, the semi-analytic CBP model component of our technique makes several simplifying assumptions. Namely, it is conditioned on edge-on, circular planet orbits. For modest eccentricities, typical errors in regularization of transit timing and duration are small ($\lesssim$0.05 d). Moreover, the quasi-periodic nature of the standard QATS algorithm is able to alleviate larger timing deviations with a wider user-specified window, although doing so encompasses more background noise.

As demonstrated for *Kepler*-35 and *Kepler*-64 systems, our method significantly improves detection signal-to-noise ratio, by factors >2. This improvement boosts our chances to detect smaller circumbinary planets, e.g., in the terrestrial regime. We plan to use our technique for a blind CBP search around *Kepler* EBs and test detection completeness to infer CBP population statistics in a following paper. Although we intend to search for CBPs in *Kepler* data, our technique can be applied to other time-series data with uniform cadence and sufficient monitoring baseline, such as those from *K2*, the continuous viewing zones of *TESS*, or the upcoming PLATO mission.

Chapter 4

THE POPULATION OF CIRCUMBINARY PLANETS AROUND *Kepler* ECLIPSING BINARIES

In this chapter, I devise an automated pipeline to search for transiting CBPs around a quarter of the EB population from the *Kepler* mission, using the transit detection technique from Chapter 3. I present the results of our search, i.e., the candidate catalogue, which comprises 8 known CBP systems and 4 marginal candidates. In addition to the CBP candidates, the pipeline yields four multiply eclipsing candidates, including a new doubly eclipsing binary KIC 3848919. To disambiguate observational and detection effects from the underlying CBP distributions, we create a synthetic CBP catalogue and quantify both the pipeline detection efficiency and geometric CBP transit probability, which is a complex function of binary and CBP parameters. We then use our candidate and mock catalogue to statistically infer the physical population of CBPs. We infer that the frequency of Neptune- and Saturn-size CBPs with orbital periods < 450 d around low morphology ($P_b \gtrsim 5$ d) EBs is $18^{+7}_{-5}\%$, if planets are preferentially coplanar relative to binary orbits. If instead CBPs are distributed isotropically in mutual inclination with respect to host binaries, the occurrence rate grows to $83^{+31}_{-24}\%$. We find that the relative abundance of circumbinary Jupiter-size or larger gas giants is significantly lower, and constrain its occurrence rate to be $< 4\%$ and $< 15\%$ for coplanar and isotropic mutual inclination distributions, respectively. Given the data, we do not find strong evidence that the apparent trend for CBPs to lie close to the stability limit remains after correcting for detection and transit geometry biases. Moreover, if CBPs are isotropically distributed relative to their binary hosts, they are less frequent around $P \lesssim 5$ d than $P \gtrsim 5$ d EBs. However, owing to the small target sample for high morphology ($P_b \lesssim 5$ d) EBs, our analysis cannot robustly constrain the relative abundance of CBPs around $P \lesssim 5$ d and $P \gtrsim 5$ d binaries with more coplanar mutual inclinations.

The work conducted in this chapter is done in collaboration with Eric Agol, Daniel Fabrycky, Eric B. Ford, Nader Haghighipour, Jerome A. Orosz, and William F. Welsh.

4.1 Detection Pipeline

We start with an overview of the general infrastructure of the CBP transit detection pipeline. For each target in our input EB catalogue (see §4.1.1), the pipeline loads in the normalized, *Kepler* simple aperture photometry (SAP) and the maximum-likelihood binary LC model of Windemuth et al., 2019a (hereafter W19a; see also Chapter 2) to remove eclipses. The eclipse-removed light curves are further detrended (see §4.1.2) to remove data outliers, *Kepler* systematics such as flux jumps or steps, and periodic, out-of-eclipse binary signals such as ellipsoidal variation. Given user-specified planet search parameters, the pipeline uses a (Keplerian) physical CBP model to predict transits, evaluates the likelihood ratio ($\Delta\chi^2$) between the predicted transit and noise only model at each LC cadence, and tests the total CBP transit likelihood using the Quasiperiodic Automated Transit Search Algorithm (QATS; see §4.1.3). The significance of detection is evaluated using the QATS likelihood as a function of planet period, which compose the QATS spectrum or quasi-periodogram. A CBP detection occurs when the QATS signal is above a specified detection cut and passes multiple, automated false positive vetting (see §4.1.4).

4.1.1 Binary Target Selection & Properties

In this study, we use the W19a EB catalogue, a uniformly modeled subset of systems from the Villanova *Kepler* Eclipsing Binary Catalogue (Prša et al., 2011). This sample is advantageous because it contains full stellar and orbital parameter estimates, including binary mass ratio, period, inclination, and eccentricity vectors, which set the scale of geometric timing variations due to line-of-sight binary reflex motion. We refer the reader to Chapter 2 for details of the binary modeling process.

We divide our sample of 728 EBs into two subsamples: detached or low morphology (LM; `morph`<0.5) and semi-detached or high morphology (HM; 0.5≤`morph`≤0.6) systems. HM systems exhibit large out-of-eclipse variations and typically have short periods ($P_b = 0.5 - 4$ d) and circular orbits, while the distribution of binary eccentricity and period for LM systems

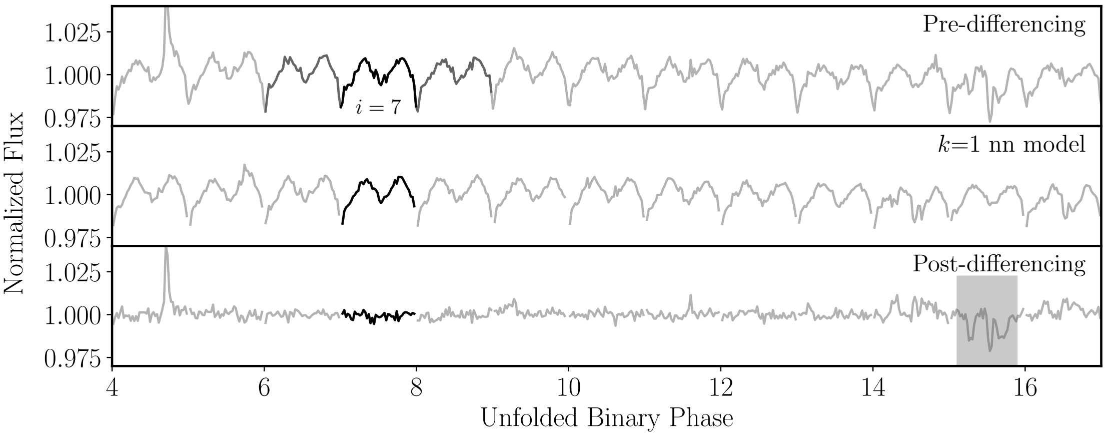

Figure 4.1 Demonstration of phase differencing technique for EBs with large out-of-eclipse variations at binary orbital frequencies. Top panel shows the eclipse model subtracted light curve (light grey) as a function of binary phase number, where black is the LC segment of the current binary epoch E_i and dark grey denotes the $k = 1$ nearest-neighbour phase numbers. The middle panel shows the fiducial model constructed by averaging the outlier-rejected k nearest-neighbour light curve segments to E_i. Finally, the bottom panel shows the post-differencing, or original minus computed (O-C) light curve. The light grey box highlights CBP transits present in the data, which appears more easily identifiable after differencing.

are centered at higher values with larger ranges.

For each target light curve, we quantify quarterly third light contamination using values from Chapter 2, which are typically within 1-5% of *Kepler* crowding estimates.

4.1.2 Light Curve Detrending

In order to optimally search for transit signals and minimize false positives in the *Kepler* light curves, we prime, or "detrend" each LC to remove instrumental (e.g., thruster firings, cosmic ray hits) and stellar (e.g., eclipses, flares) features that may confuse transit signals. Specific subsets of EBs also exhibit persistent LC features that require additional detrending (e.g., eclipse timing variation & ellipsoidal variation candidates; see discussion below). We describe our systematic approach below and highlight component procedures that differentiate subpopulations of EBs.

First, for all input LCs, we remove eclipse signals using the best-fit light curve and polynomial models derived from EB fitting (see Chapter 2), and in place of the cadences, we add white noise comparable to neighboring data segments. Then, we remove positive single-point outliers with a 5σ clipping, as well as data with quality flags > 16. Next, we split the entire light curve into chunks demarcated by the start of new quarters and data gaps > 0.4 days in duration, and normalize each chunk by the median. Within each light curve segment, we linearly interpolate over smaller gaps (< 0.4 days) and data points exhibiting instrumental glitches not flagged by *Kepler* but that were common to many *Kepler* light curves (Welsh, private communication).

As mentioned earlier, subsets of EBs in our sample show additional, correlated LC features which may artificially introduce artifact noise and degrade overall transit detection ability. In particular, light curves with eclipse timing variations require eclipses to be fit individually in order to fully remove eclipse signals and minimize residuals. To address this potential detrending artefact, the pipeline flags systems with large eclipse residuals as potential ETV candidates; specifically, when the median absolute eclipse residuals exceed seven times the median absolute out-of-eclipse residuals. Systems marked as ETV candidates then go through an ETV module, which individually fits each time of eclipse while holding all other LC parameters constant and generates an output O-C diagnostic.

Furthermore, light curves with strong out-of-eclipse variations modulated by binary period (e.g., ellipsoidal variations, as systems identified by high morphology values (`morph` $\geq$ 0.5), undergo a detrending procedure called binary "phase differencing" (Fabrycky et al., in prep). This phase differencing technique uses k nearest-neighbours (nn) binary epochs E (i.e., phase numbers) to construct a fiducial template for E_i, the ith binary epoch. To create the E_i template, we transform the k-nn and ith data so that they are uniformly sampled in phase. Then, we construct a self-similarity matrix by comparing $\{i-k, ..., i, ..., i+k\}$ epochs against each other, and mask data points with low self-similarity values (i.e., outliers). The template is then the phase averaged mean of the self-similar neighbouring epochs. By marching forward in epochs and subtracting the fiducial model from input data, the entire light curve is detrended.

Figure 4.1 illustrates the "phase differencing" procedure for a short period binary with strong ellipsoidal variations. The top, middle, and bottom panels show the eclipse-removed input light curve, the $k = 1$ nn model, and the post-differencing residuals, respectively. This technique removes gradual evolution of the light curve as a function of epoch, and preserves signals that occur on timescales different from the binary period, such as planetary transits, stochastic stellar flares, or instrumental systematics. One caveat of this differencing method is that it may produce "ghost signals" or detrending artefacts. For example, a low signal-to-noise flare in epoch E_i that is missed by outlier rejection will imprint negative flares (dips, potentially resembling transits) in E_{i-1} and E_{i+1}. Nevertheless, in bulk injection & recovery tests we find that this detrending method generally outperforms the LM technique, for HM EBs. Figure 4.2 shows the difference in QATS detection spectrum when using the phase differencing method (top panel) vs. the nominal LM technique to detrend the light curve data, for an example simulated HM system. Using the former detrending technique, the QATS-detected peak period coincides with the true (injected) period, while the latter detrending technique results in noisy signals at the wrong period, i.e., a false positive.

We use the median absolute flux difference (MAD) in the time-series data as a proxy measure for the light curve's white noise. We also estimate the amplitude and timescale of the correlated noise component from the first zero-crossing or minimum of the LC autocorrelation function (ACF). The correlated noise component helps inform the order of the polynomial for detrending and computing $\Delta\chi^2$. Targets with large correlated noise amplitudes at timescales $\lesssim 2$ d, the maximum CBP search duration, are assigned fifth order polynomials, while less noisy light curves are fit with third order polynomials.

Finally, for all LCs, non-stationary noise due to *Kepler* systematics (e.g., sudden pixel sensitivity dropout) and stellar activity (e.g., flares) require additional detrending measures. One of the inherent limitations of QATS-EB is that it is sensitive to the presence of stochastic noise/events. As a result, light curve continuum variations such as flares, pointing drift,

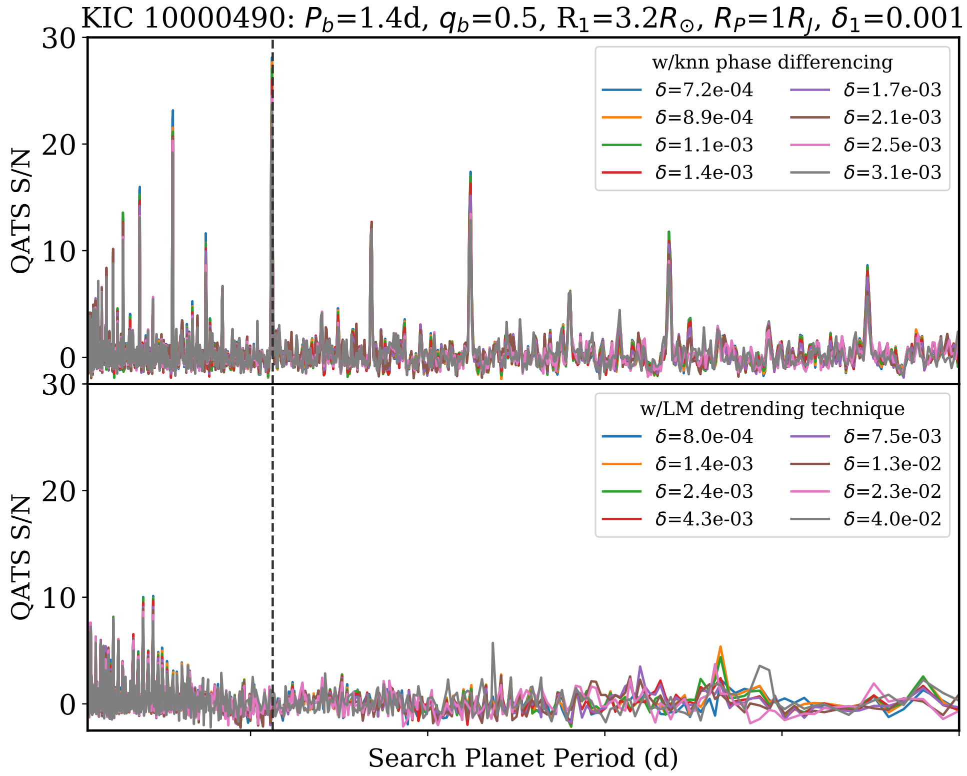

Figure 4.2 QATS detection quasi-periodogram when using phase differencing detrending (top) vs. using LM detrending technique (bottom) for an example (simulated) HM system. The phase differencing technique dramatically improves detection signal-to-noise.

complex rotational modulation of starspots, etc can introduce false positives in the detection algorithm. To mitigate these false alarms (FA), we use model selection based on the reduced χ^2 statistic on LC portions with signals strongly *inconsistent* with a simple polynomial model (third or fifth order, depending on LC correlated noise timescale amplitude). We choose χ^2_r as the selection criterion to stay consistent with the QATS-EB $\Delta\chi^2$ search methodology, which compares the likelihood ratio of transit+polynomial and polynomial-only models given observed data for a grid of transit parameters (see §4.1.3).

We use a finite set of FA models, including a flare model (Davenport et al., 2014), a step function, a U-shaped transit model, a polynomial-only model, a sinusoidal model, and a sudden pixel sensitivity dropout model (SPSD; Mullally et al., 2016). We show an example set of fits to the data using these various models in Figure 4.3. Ideally, evaluating this suite of models, i.e., model comparison at *every* light curve cadence would yield a better performance to vet light curve systematics. This is however computationally expensive. In practice, we select for the strongest FA signals by testing the top ∼10 peaks in a training set of $\Delta\chi^2$ against each of the models. If a non-transit signal is "preferred," i.e., yields a 15% lower χ^2_r than transit + polynomial or polynomial only fits, then the signal in the light curve is removed with the best-fit model.

To summarize, the procedure is:

1. Create full EB light curve model $\mathbf{F}_{\mathrm{EB}}$ using *Kepler* data $\mathbf{F}$ and maximum-likelihood solution from W19a.

2. Assess if a system is potential ETV candidate; if so, perform light curve fit *per* eclipse to create $\mathbf{F}_{\mathrm{EB}}$ and compute ETV amplitude.

3. Remove eclipse signals $\mathbf{F}_{\mathrm{EB}}$ from light curve data.

4. Assess if a system is ellipsoidal candidate; if so, perform k nearest-neighbour phase differencing to remove quasiperiodic variations, i.e., construct a "template" from the

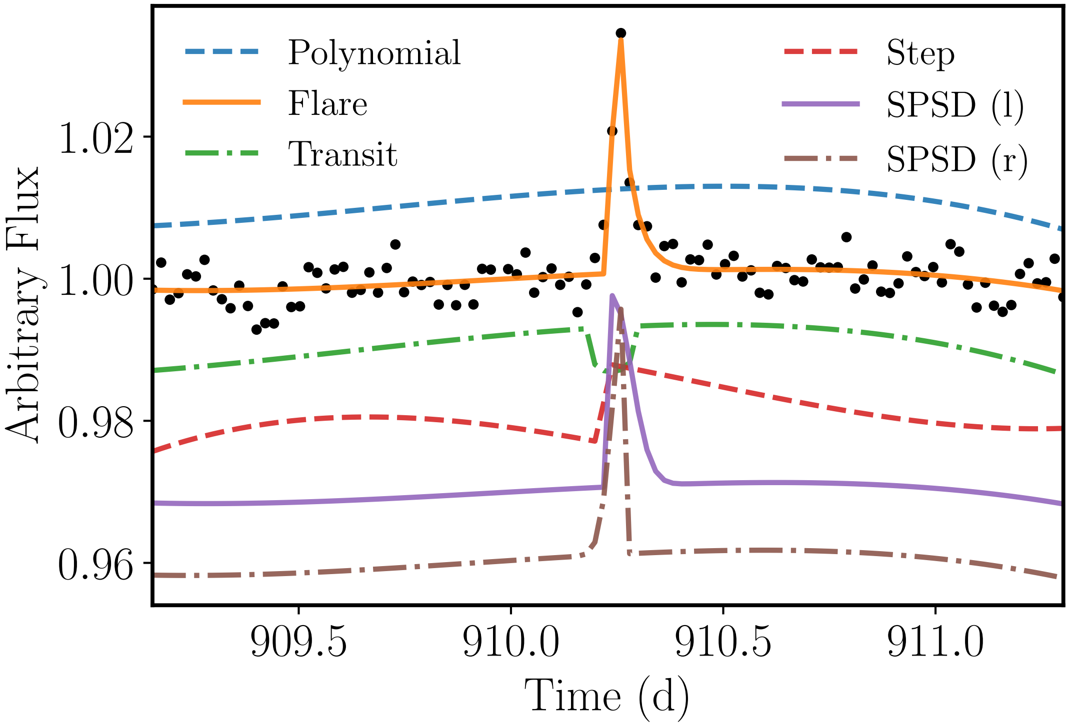

Figure 4.3 Example model selection fits: Light curve data (black points) overlaid with a subset of the false alarm (FA) models used in this work. In particular, the blue dashed line corresponds to the polynomial-only model; orange solid line corresponds to a flare and polynomial model; green dash dotted line corresponds to transit and polynomial models; red dashed line corresponds to step function and polynomial; purple solid line and brown dash dotted line correspond to left-sided and right-sided sudden pixel sensitivity drop-off model, respectively, multiplied by a polynomial model. For visual clarity, each FA model fit is offset by 0.01. See text for more details.

average of light curve segments corresponding to previous and next k phase numbers, and subtract it from the light curve of the current phase number. In practice, we found using $k = 1$ gave the best results.

5. Remove single-point positive outliers with 7-sigma clipping, low quality data points, and data segments within 0.1 day of "bad cadences" visually identified to be common to many *Kepler* light curves.

6. Split entire light curve into chunks according to *Kepler* quarter gaps and data gaps > 0.4 days.

7. Within each light curve segment, linearly interpolate across short-duration data gaps and inject normally distributed white noise with σ_w=MAD($\mathbf{F}$) to make uniform cadences.

8. Train coarse-grid $\Delta\chi^2$ on the "detrended" light curve to identify top $\sim$10 $\Delta\chi^2$ peaks and their corresponding cadences; vet the light curve at these cadences by using model selection, i.e., optimize the light curve segment using a suite of "false alarm" models (e.g., a step function model, a U-shaped transit model, a polynomial-only model, a flare model, a sinusoidal model, and a SPSD (sudden pixel sensitivity dropout) model.

4.1.3 QATS-EB

We have previously established an efficient transit detection algorithm tailored to search for circumbinary planets in Windemuth et al., 2019b (hereafter W19b) and in Chapter 3. In brief, QATS-EB processes input flux time-series information $F(t)$ as output chi-square difference time-series $\Delta\chi^2(t, R_p, P_p, \theta_b)$, and accounts for binary-induced transit variations using an approximate physical CBP model and QATS, the Quasiperiodic Automated Transit Search algorithm (Carter & Agol, 2013).

Search Parameters & Detection Thresholds

For each target, the pipeline searches for CBPs on a grid of trial planet periods and transit depths (planet-to-star radius ratios). The minimum search period is set to the critical stability limit ($P_p \approx 3P_b$) and the maximum search period to one-third the total light curve duration (i.e., require three transits). The depth grid is set to $\{1.0, 1.7, 3.0, 5.3, 9.4, 16.4, 28.6, 50\} \times$ the white noise σ_w.

In addition to specifying the planet search parameters, the quasi-periodic nature of the search algorithm requires a prescription for the minimum and maximum range in the search period; this range or search window allows for signals to deviate more from periodicity at the expense of additional noise; conversely then, correcting for aperiodicities in a physically consistent manner allows us to make the search window more narrow, producing a boost to the signal-to-noise ratio (SNR). Typically for CSPs, the search window covers transit timing variations due to additional planets in the system, which scales linearly as a fraction of the planet period, e.g., $\Delta P_p = f P_p$ (Agol et al., 2005). Because our CBP transit likelihood calculation already accounts for large-scale planetary transit timing variations due to line-of-sight reflex motion of the binary, we may choose a search window that increases less steeply as a function of trial planet period, e.g., $\Delta P_p^{2/3}$. Figure 4.4 demonstrates the different scaling regimes in the QATS search window. At longer periods, the search window employed here is significantly smaller than a constant f, allowing for more sensitivity at those periods. We opt to use a ΔP_p search window that scales as $0.02 P_p^{2/3}$.

Finally, we establish a QATS-EB signal as a detection when it is above a SNR threshold > 7.1 and > 8.1 for HM and LM targets, respectively. These detection thresholds were empirically chosen from the injection & recovery analysis (see §4.3.1) to maximize pipeline completeness while minimizing false positives.

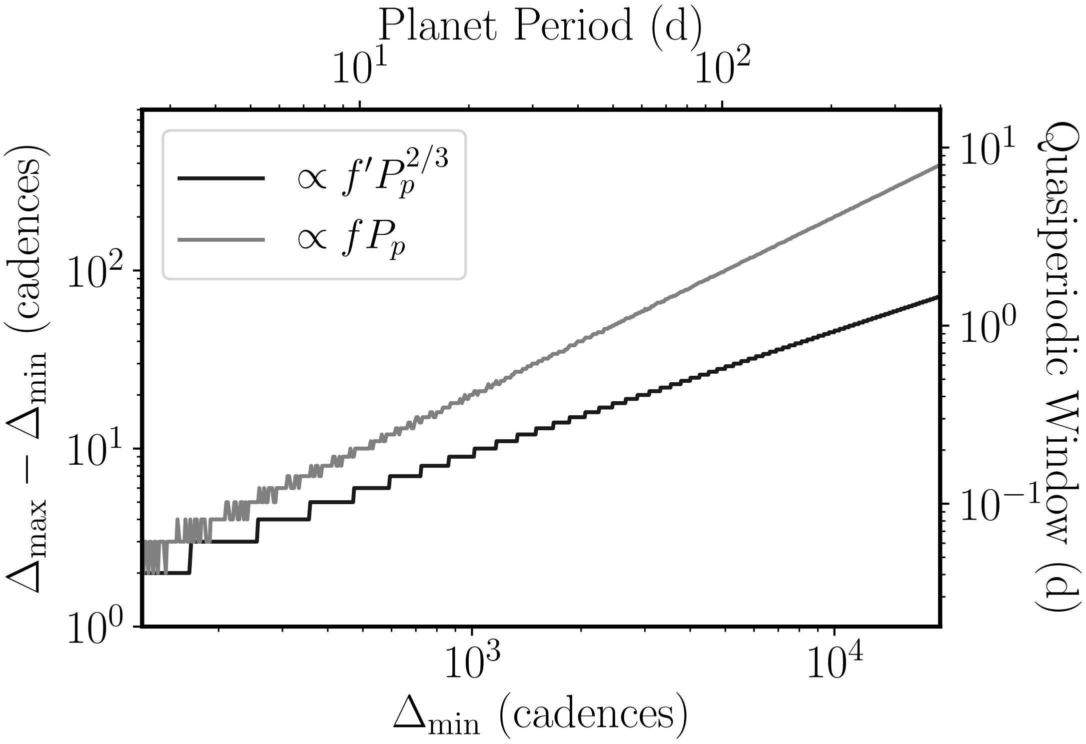

Figure 4.4 The quasiperiodic (TTV) window as a function of the search period.

4.1.4 False Positive Vetting

A QATS signal above the detection threshold does not necessarily meet our criteria as a successful detection. Because the QATS algorithm is sensitive to stochastic noise (Carter & Agol, 2013), we further vet each "detection" with a set of automated procedures to evaluate the likelihood that the detection is a false positive (FP). Given each quasi-periodic detection, the pipeline iterates over the QATS detected transit times and individually fits each data segment with a transit model. To assess the likelihood that each detected event is best fit with a transit, we use model selection, by comparing the reduced χ^2 values of false alarm models (U-shaped transit, flare, step-function, sinusoid, polynomial-only; see §4.1.2) optimized to the data. A detected event is considered a FA when non-transit fits produce a lower χ_r^2. This is distinguished from a false positive, which refers to a QATS-EB detection in the quasiperiodogram above the SNR threshold but contains spurious signals, i.e., individual events.

We devise a set of heuristic measures to assess if a QATS-EB detection is a false positive. These measures are adopted based on results of the injection & recovery analysis (see §4.3.1) to maximize pipeline completeness while minimizing false positives, and are therefore specific to this particular detrending and detection pipeline. A false positive flag is raised when:

- Fewer than three QATS-detected transit events are detected
- No detected event with $\Delta\chi^2 > 0$
- More than half of detected events occur during times coinciding with binary eclipses, for LM EBs
- More than half of the detected events are better fit by FA models
- The number of "strong" $\Delta\chi^2$ events corresponding to FA models is greater than the number corresponding to transit models, where "strong events" are signals with $> 5\sigma$ $\Delta\chi^2$ values.

Only QATS signals above the detection threshold that do not have FP flags count as "successful detections," i.e., CBP candidate. Out of 91 target systems above the detection threshold, 12 candidates remain after the vetting.

4.2 Search Results: Circumbinary Planet Candidates

We perform a CBP search on the EB sample for transits across the primary stellar component, and record QATS-EB detections above SNR thresholds that pass false signal vetting as candidates. We do not consider planet multiplicity, i.e., additional, less detectable companions in our analysis.

The target search yields 12 CBP candidates, 11 around LM systems and 1 around a HM system. Table 4.1 shows their detection properties (columns 7–9), binary parameters (columns 2–6; W19a), estimated noise properties (columns 10-12), and post-detection transit fit statistics (columns 13–15). The detection properties include the peak SNR value associated with each detection and its corresponding period and detected number of transit events. The noise statistics uses the median absolute difference of the LC as a proxy for white noise, and uses the autocorrelation of the LC data to estimate the correlated noise timescale and amplitude. The transit fits are initialized with QATS-EB detected transit times, durations, and depths, and then optimized with the `L-BFGS-B` algorithm, a quasi-Newtonian method that computes approximations to the inverse Hessian by using only gradient information, as implemented in `scipy` (Virtanen et al., 2020).

We show QATS-EB detection and diagnostic plots for two candidates in our sample: KIC 4862625 (Kep-64b; Figure 4.5) and KIC 12351927 (Kep-413b; Figure 4.6). Additional detection and diagnostic plots for all candidates (plus KIC 10753734b) may be found in Appendix B. Each detection plot shows the raw QATS signal in the upper panel and the continuum removed signal-to-noise spectrum in the bottom panel. A strong detection typically contains multiple aliases, i.e., harmonics of the peak period signal. The diagnostic plots display individual transit events in square panels, with fits to the light curve data (upper); residuals of the fits (middle); and optimized transit models overplotted against the continuum-normalized data via a local polynomial (lower). Transit panels shaded grey correspond to $\Delta\chi^2$ values (long bottom panel) > 0.

Out of 12 candidates, 8 are previously discovered and confirmed CBPs (Kep-16b, Kep-453b, Kep-64b, Kep-35b, Kep-34b, Kep-38b, Kep-47c, Kep-413b); these are detected at high significance (SNR=13–135). Four other known transiting CBPs are not in the candidate list: Kep-47b & d, Kep-1647b, and KIC 10753734b. Kep-1647b, the longest transiting CBP with $P \sim 1100$ d (Kostov et al., 2016), was missed by the pipeline due to insufficient number of transits. KIC 10753734b was detected at a SNR of 7.3 (see Appendix B), below the 8.1 threshold for LM systems. While we detected additional planets of the Kep-47 system, for consistency, we do not include them here in our analysis, so that the list of candidates constitute the most detectable signals in those systems.

Four candidates are not previously identified, and deserve additional scrutiny to preclude false positives. KICs 6042116, 8111622, and 8302455 are marginal detections. Both KICs 6042116 & 8302455 are EBs with period ~ 5 d and are classified as LM, but show (quasi-)sinusoidal light curve continuum. In particular, the light curve of KIC 8302455 exhibits starspot modulation, and the QATS-detected transit events do not appear convincingly transit-like. For KIC 6042116, the light curve has correlated features, perhaps due to Doppler beaming, reflection, and/or tidal distortions, and the QATS-detected transit events occur near the same binary phase. The detection around high morphology EB KIC 3851193 has a SNR of 11, and if true, would make the first transiting CBP candidate around a short-period binary at $P_b = 1.34$ d, with a wide planet orbit ($\sim$100 d). Such a configuration is consistent with the results of dynamical interactions with tertiary stars (Muñoz & Lai, 2015; Martin et al., 2015; Hamers et al., 2016), and the theoretical modeling of tidal-stellar evolution in Fleming et al. (2018) and Graham et al., submitted. However, the light curve is HM and noisy, and the timing of the transit events near binary eclipse is suspect. Further testing is needed for these systems to disambiguate the plausibility of detected signals.

Due to uncertainty in the plausibility of some candidates, we separate them into two samples, with HMd/LMd referring to all 12 detected candidates (“dirty”) around HM/LM

Table 4.1 CBP Candidates from Target Search

KIC	mor	P_b (d)	P_c (d)	e_b	$i_b(^\circ)$	SNR	P_p (d)	N_t	σ_MAD	σ_corr	P_ACF	$N_\mathrm{t,fit}$	δ_fit	$\chi^2_{r,\mathrm{fit}}$	Notes
12644769	0.03	41.08	204.5	1.6E-01	90.33	135.5	224.73	7	7.E-05	7.E-03	14.95	6	1.7E-02	34.3	Kep-16
9632895	0.06	27.32	102.8	5.2E-02	89.76	65.5	237.96	6	1.E-04	5.E-03	10.14	6	4.9E-03	1.5	Kep-453
4862625	0.06	20.00	109.1	2.2E-01	87.54	22.1	135.16	10	2.E-04	1.E-03	2.66	10	1.2E-03	1.3	Kep-64
9837578	0.08	20.73	96.7	1.3E-01	89.49	20.8	126.79	11	5.E-04	2.E-03	3.00	10	4.2E-03	1.2	Kep-35
8572936	0.04	27.80	193.9	5.2E-01	90.03	19.0	284.73	5	3.E-04	2.E-03	4.67	5	2.8E-03	1.2	Kep-34
6762829	0.15	18.80	79.1	9.2E-02	89.25	17.4	102.81	14	2.E-04	8.E-04	2.07	13	5.6E-04	1.2	Kep-38
10020423	0.15	7.45	28.7	2.9E-02	89.67	14.9	302.05	4	3.E-04	2.E-02	7.56	4	2.1E-03	1.2	Kep-47
12351927	0.07	10.12	41.0	3.4E-02	86.97	13.1	64.30	23	6.E-04	5.E-03	5.18	22	2.5E-03	1.4	Kep-413
3851193	0.55	1.34	4.9	1.8E-07	90.10	11.0	100.68	14	3.E-04	2.E-03	2.14	13	1.7E-03	1.9	
6042116	0.27	5.41	24.7	9.7E-02	83.08	9.4	97.72	15	7.E-05	3.E-03	2.71	9	3.0E-04	1.2	
8111622	0.07	15.45	116.2	5.3E-01	89.45	8.7	248.50	6	4.E-04	8.E-03	3.67	4	1.8E-03	1.4	
8302455	0.29	4.88	18.0	1.3E-05	84.37	8.2	61.70	24	1.E-04	1.E-02	4.91	9	5.1E-04	0.7	

Note on column names: mor, P_b, P_c, e_b, i_b are the morphology, period, critical stability period, eccentricity and inclination associated with the binary, respectively; SNR, P_p, N_t are the signal-to-noise ratio, planet period, and number of transits associated with the QATS-EB detection; σ_MAD, σ_corr, P_ACF are estimates for the white noise amplitude, correlated noise amplitude, and correlated noise period; $N_\mathrm{t,fit}$, δ_fit, $\chi^2_{r,\mathrm{fit}}$ are the number of transits, average transit depth, and average reduced chi-square values associated with post-detection model selection fits which favoured U-shaped transit models over false alarm models.

targets, and HMc/LMc referring to the 8 conservative candidates ("clean").

We emphasize we do not claim new discoveries here. These candidates are transit detection yields from our pipeline that passed empirical, automated false alarm tests (see §4.1.4), and may not be true CBPs. Further vetting (e.g., noise testing, photodynamical modeling) is necessary to rule out false positive scenarios, due to light curve noise (e.g., stellar variability, unanticipated detrending artefact) and/or astrophysical contaminants (e.g., background eclipsing binary blend).

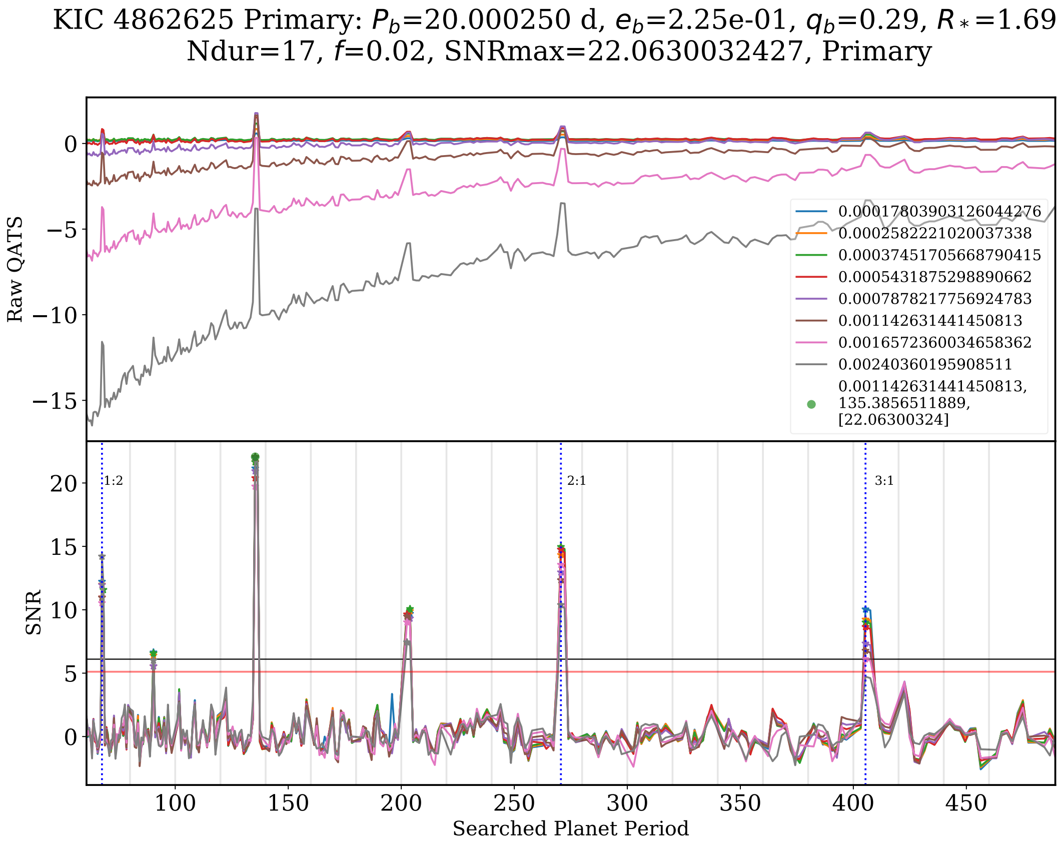

Figure 4.5 QATS-EB detection plot for KIC 4862625, where the upper panel shows "raw" QATS signal, and the bottom panel shows the signal-to-noise spectrum. The dotted lines denote aliases of the peak period, and different colour lines correspond to the searched depth grid. While QATS searches using the depth grid enable detections, $\delta_{\rm fit}$ values (see Table 4.1) from post-detection transit fits are more robust estimators for the actual transit depths.

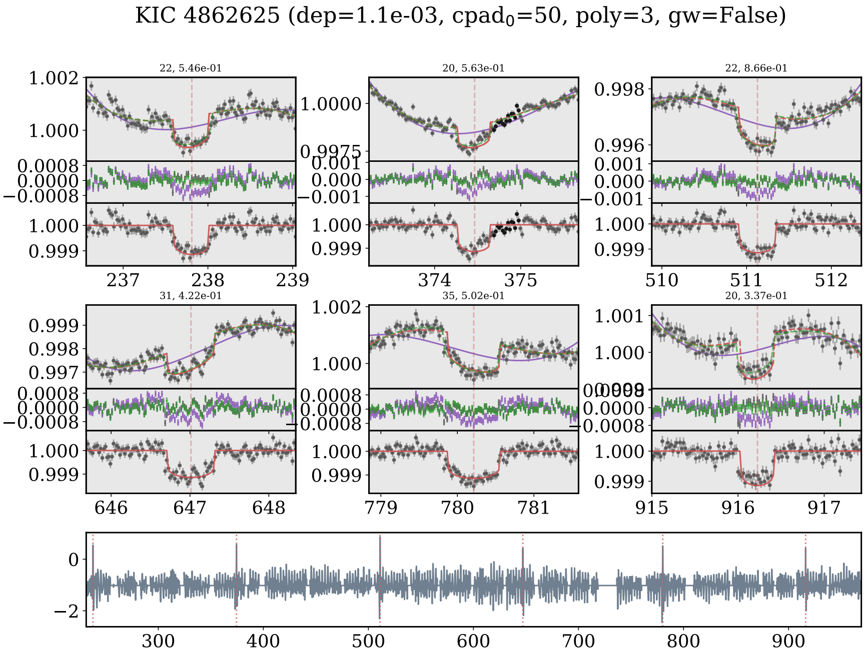
KIC 4862625 (dep=1.1e-03, cpad$_0$=50, poly=3, gw=False)

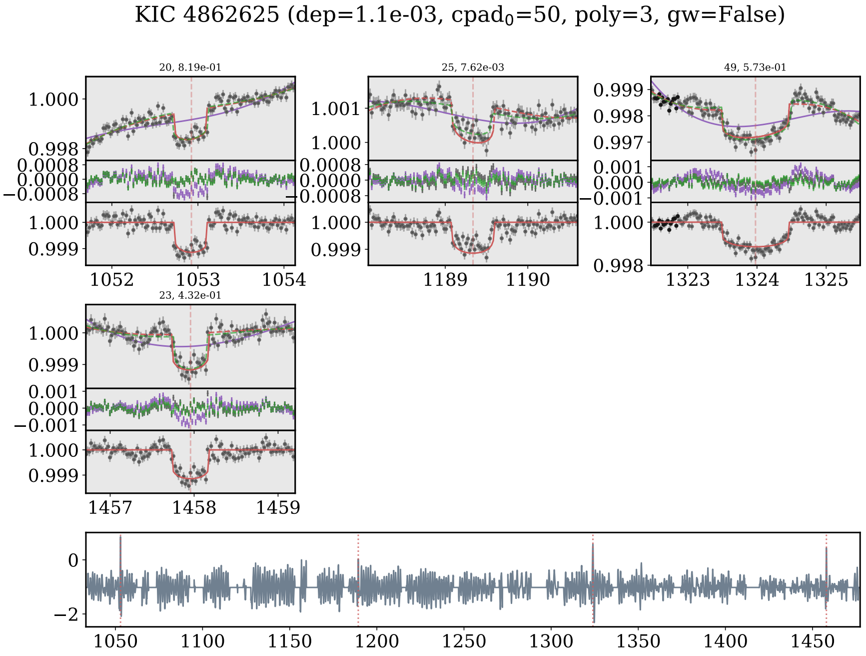
KIC 4862625 (dep=1.1e-03, cpad$_0$=50, poly=3, gw=False)

Figure 4.5 Continued; QATS-EB diagnostic plot for KIC 4862625, where each panel corresponds to a detected transit time showing the post-detection fits to the LC data (top), residuals (middle), and fits to local polynomial detrended data (bottom). Transit depths are ~0.1%. Panels shaded in light grey correspond to $\Delta\chi^2$ values >0.

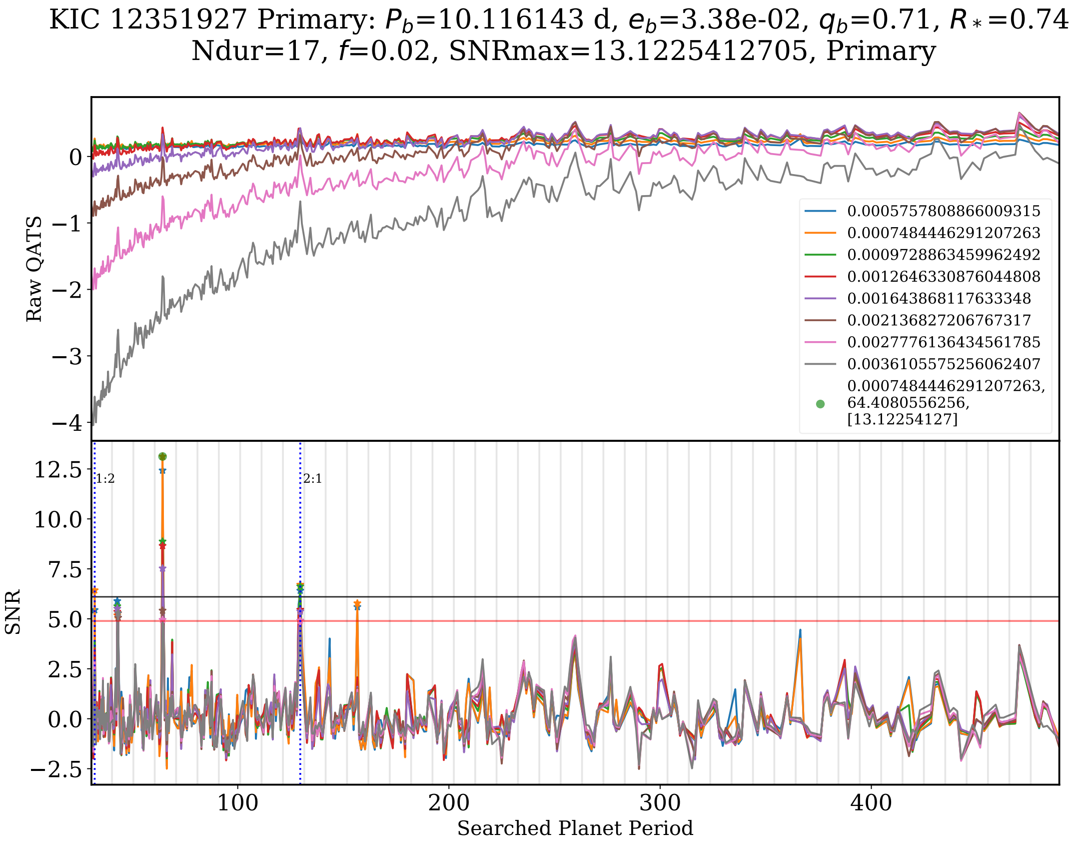

Figure 4.6 Same as Figure 4.5, but for KIC 12351927. Note that the transits come and go, due to precession, and change in depths.

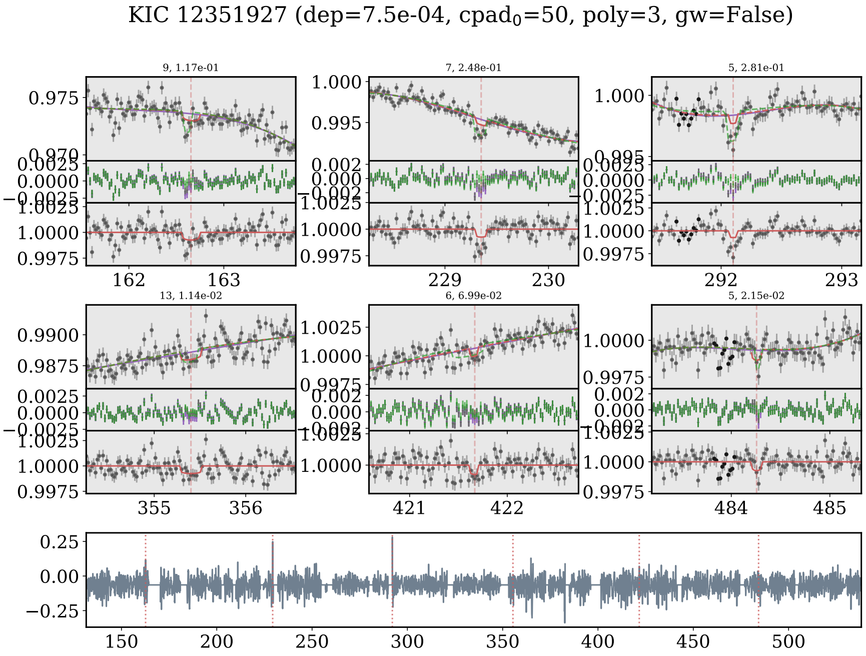

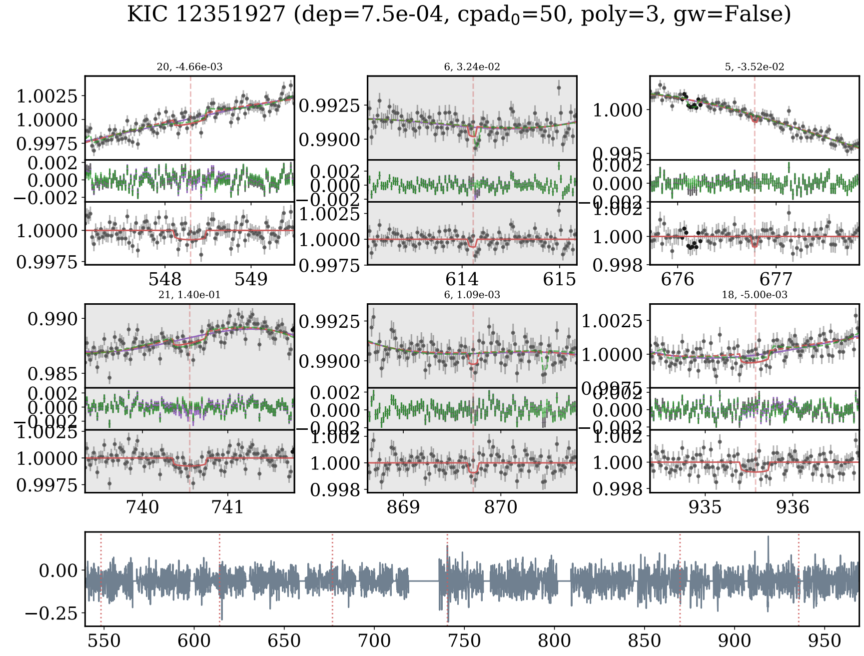

Figure 4.6 Continued.

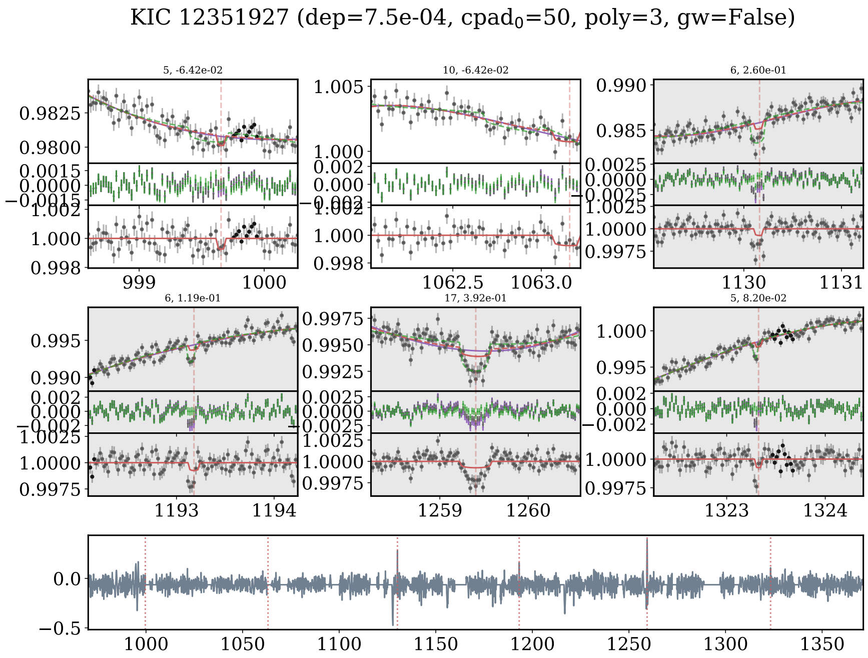
KIC 12351927 (dep=7.5e-04, cpad$_0$=50, poly=3, gw=False)

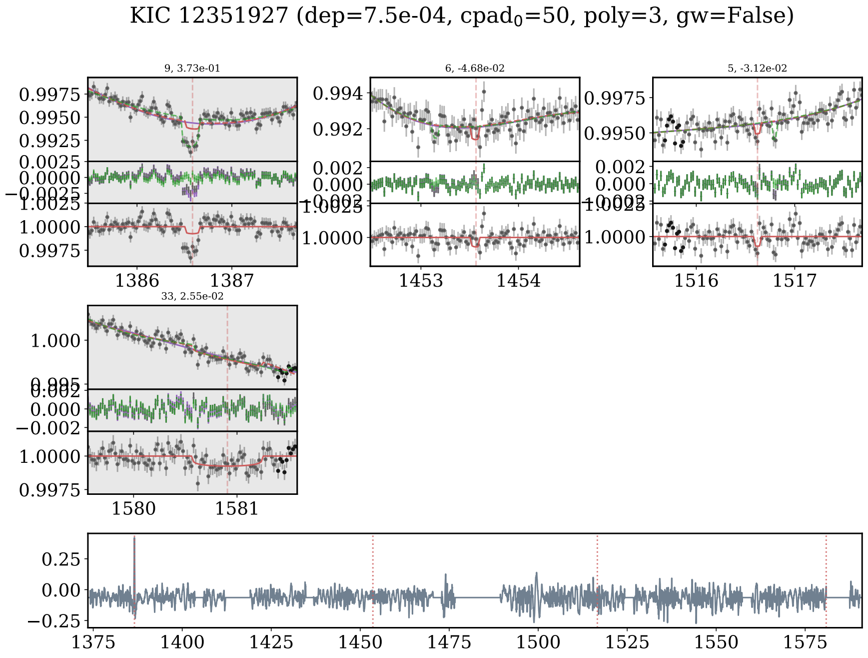
KIC 12351927 (dep=7.5e-04, cpad$_0$=50, poly=3, gw=False)

Figure 4.6 Continued.

4.3 Detection Completeness

Debiasing detection deficiencies is crucial to robustly infer the underlying frequency of CBPs. We consider the total detection efficiency as the joint probability of the QATS-EB pipeline detection probability (§4.3.1) and CBP transit probability under finite time (§4.3.2). While these quantities depend on the full set of binary and planet parameters, we examine detection completeness as a function of planet radius, period, and mutual inclination distribution, and binary period. In §4.3.3, we present the cumulative detection efficiency of our method, marginalized over mutual inclinations.

4.3.1 Pipeline Sensitivity

Synthetic Catalogue

We create a synthetic catalogue, which we call Catalogue B, to test and quantify recovery fraction or pipeline completeness. Using `rebound` (Rein & Liu, 2012), we directly inject physically consistent CBPs around the EBs from our target search. This method takes advantage of the fact that CBP transits are sparse/rare in the EB data, and preserves the noise properties of light curves in the target search.

We use the W19a maximum-likelihood binary parameters, and simulate $N = 500$ CBPs around each EB target, drawing from planet parameter distributions outlined in Table 4.2. EBs with light curve properties that are guaranteed to produce undetectable transits (e.g., with total light curve duration $< 3P_c$ or with noise amplitudes $\gg$ predicted transit depth of a Jovian-size planet around that primary) were removed; 664 EBs remain from the original 728 sample. In total, the mock catalogue contains ∼332,000 simulated CBP systems. The full procedure for each EB target is as follows

1. Load EB parameters and *Kepler* SAP light curve.

2. For each of 5 mass bins ($M_p/M_\oplus \in \{1, 2, 10, 33, 100, 1000\}$), draw 100 CBPs with planet parameters according to Table 4.2, totaling 500 CBPs per target.

Table 4.2 Simulated CBP Parameter Distributions

Parameter	**Distribution**	**Notes**
Period (d)	$\log_{10} P_\mathrm{p} \sim \mathcal{U}\,(1.1P_c, \min(35P_c, \mathcal{T}/3))$	critical stability period P_c (Holman & Wiegert, 1999); total LC duration $\mathcal{T}$
Eccentricity	$e_\mathrm{p} \sim$ Rayleigh(σ=0.06)	Motivated by CSPs, see text for details
Inclination (rad)	$i_\mathrm{p} = \pi/2$	Relative to observer; held constant
Longitude of Periastron (rad)	$\omega_\mathrm{p} \sim \mathcal{U}(0, 2\pi)$	
Time of periastron (d)	$t_\mathrm{peri} = 0$	Held constant
Longitude of Ascending Node (rad)	$\Omega_\mathrm{p} = \pi$	Held constant
Mass ($M_\oplus$)	$M_\mathrm{p} \sim \mathcal{U}\left(M_{\mathrm{p,bin};i}, M_{\mathrm{p,bin};i+1}\right)$	$M_\mathrm{p,bin} \in \{1, 2, 10, 33, 100, 1000\}M_\oplus$
Radius ($R_\oplus$)	$R_\mathrm{p} \sim$ Broken Power Law	From Chen & Kipping, 2017

3. Simulate each CBP system with `rebound` at a time resolution of 10 times finer than *Kepler* long cadence. Compute the corresponding CBP transit light curve with a Mandel & Agol (2002) model, integrating to the *Kepler* long cadence, and multiply to the observed target EB light curve. If fewer than 3 transits occur in the *total duration* of the observed light curve, resample planet parameters P_p and ω_p. Note that the final synthetic LC may contain fewer than 3 transits, due to *Kepler* data gaps and poor quality cadences (which are removed; see Chapter 4.1.2). We relax the ideal assumption of Armstrong et al. (2014a) who required transits to be consecutive; instead, CBPs are allowed to precess as a natural consequence of multi-body dynamics, so that transits may come and go and change depths, as is observed in known systems.

We choose the Rayleigh distribution as a simplified functional form for the planet eccentricity distribution (see Table 4.2). In reality, the final eccentricity distribution of planets depends on planet mass, period, multiplicity, and proximity to resonance (Hadden & Lithwick, 2014; Shabram et al., 2016, e.g.,). Without strong priors from CBP simulations and observations, we use a single Rayleigh distribution, motivated by 1) qualitative comparison to CBP planet-planet scattering simulations (Gong & Ji, 2017), and 2) empirical fits to short-period population of *Kepler* CSPs.

We show the planetary properties of our mock simulations in Figure 4.7, where the top

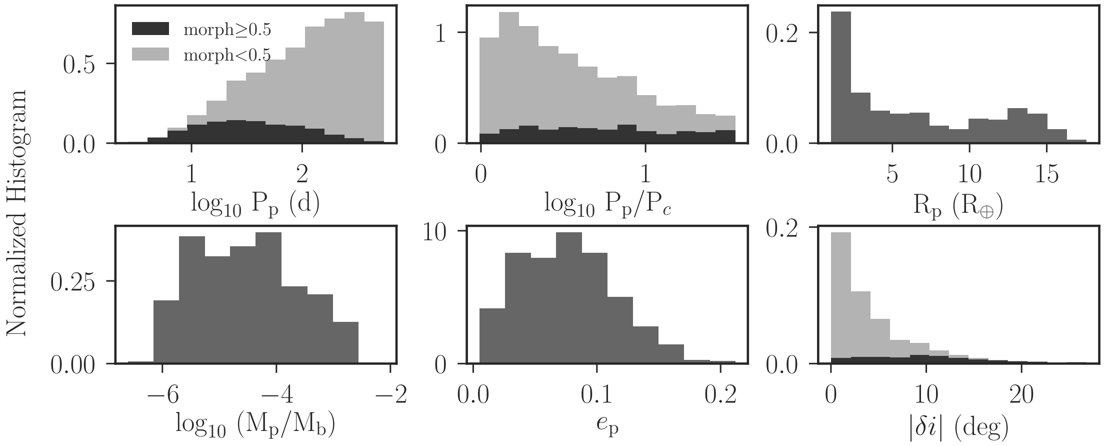

Figure 4.7 Distribution of planet properties in the mock catalogue. The top panels show the simulated CBP period distribution (left), planet-to-critical period distribution (right) in log space, and CBP radius distribution (right). Because high morphology (≥0.5) EBs tend to be short period ($P_\mathrm{b} \approx 0.5 - 5$ d), the simulations span a uniform distribution in $\log_{10}(P_p/P_c)$ from $\sim 1 - 35$. Although CBPs around lower morphology EBs skew toward longer planet period (because morph<0.5 EBs span a larger range in binary periods), their planet periods relative to binary period skew toward smaller values. This is because at longer binary periods, only CBPs with small P_p/P_c values have periods $< 3 \times$ the target EB's total light curve duration $\mathcal{T}_\mathrm{obs}$. The bottom left panels show the CBP mass relative to the binary (left), CBP eccentricity distribution (middle), and mutual inclination distribution in degrees (right).

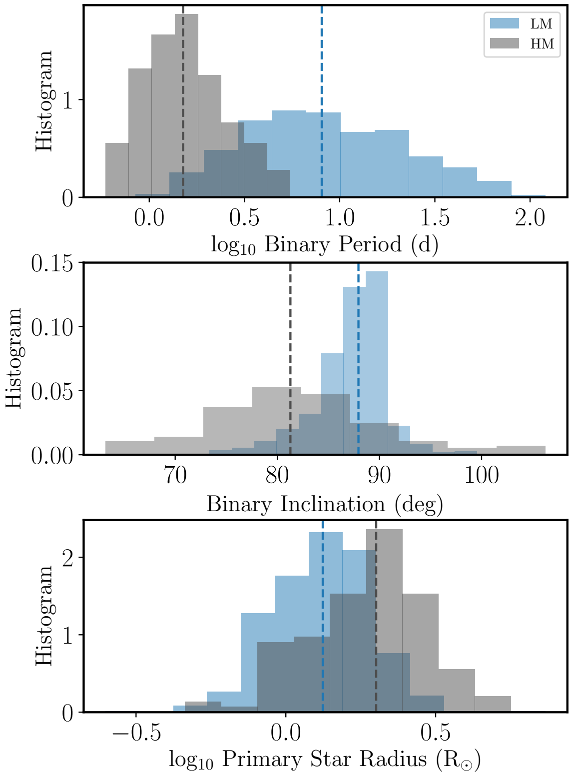

Figure 4.8 Binary period (top), binary inclination (middle), and primary star radius (bottom) distributions for HM (morph≥0.5) and LM (morph<0.5) EB targets. The dotted lines show the the 50th percentile values of each distribution.

panels (left to right) show the CBP raw period P_p, planet-to-critical-stability period P_p/P_c, and radius distributions R_p; and the bottom panels (left to right) show the CBP mass M_p, eccentricity e_p, and mutual inclination distribution δi in degrees. To illustrate how planet properties are affected by binary parameters – due to dynamical or geometrical considerations – we split the sample between low (morph<0.5) and high morphology (morph≥0.5) EB hosts. For reference, the distributions in binary period, inclinations, and stellar radii for HM and LM systems are illustrated in Figure 4.8.

Because high morphology EBs are short period ($P_{\rm b} \approx 0.5 - 4$ d peaking at ∼1.6 d), the simulations span a uniform distribution in $\log_{10}(P_p/P_c)$ from $\sim 1 - 35$. CBPs around LM EBs skew toward longer (absolute) planet period and smaller planet-to-critical period values, because their binary hosts span a larger period range ($P_b \approx 4 - 100$ d). The fall-off in $\log_{10}(P_p/P_c)$ distribution for low morphology EBs is due to the windowing effect of finite *Kepler* observing time $\mathcal{T}_{\rm obs}$, which is on average 4 years, but may vary from target to target. That is, CBPs around longer period EBs are more likely to have at least 3 transits in $\mathcal{T}_{\rm obs}$ at smaller P_p/P_c values.

The mutual inclination distribution (lower right panel of Figure 4.7) here simply follows the binary inclination distribution (middle panel of Figure 4.8), as $\delta i = i_b - \pi/2$ for $\Delta\Omega = 0$, $i_p = \pi/2$. Shorter period EBs have a broader inclination distribution, as the condition for eclipses to occur scales inversely with semi-major axis.

Figure 4.9 shows a contour map of the 2D distribution in planet period P_p and median timing variations of transits across the primary star (TAP) $\Delta t_{\rm TAP}$, based on a kernel density estimate (KDE). For reference, we overplot the KDEs of LM and HM sub-populations in dashed and dotted contour lines, respectively. The marginalized distributions in TTV and planet period are also shown on the top and right sub-panels. There is a strong linear log-log correlation between timing variations and planet period (yellow line). This encompasses the geometric effect due to reflex motion of the binary. More specifically, we expect $\Delta t_{\rm TAP} \propto (P_{\rm p} P_{\rm b}^2)^{1/3}$ (Armstrong et al., 2013). Assuming $P_{\rm p} \sim P_{\rm b}$ based on the drawn planet period distribution, $\Delta t_{\rm TAP} \propto P_{\rm p}$.

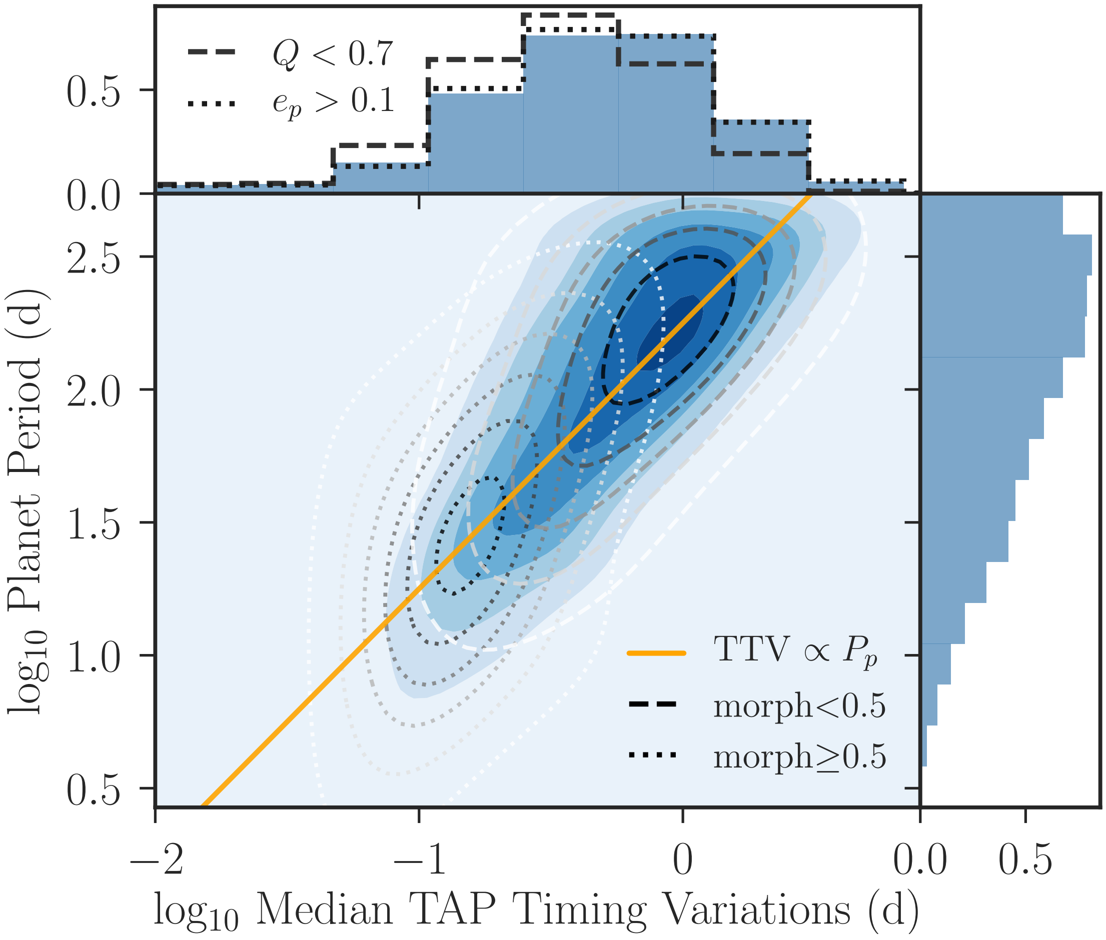

Figure 4.9 Median timing variations in days for CBP transits across the primary stellar component, as a function of planet period. In general, longer period planets tend to have larger TTVs. The top panel shows the normalized distribution of TAP timing variations, while the right panel shows the normalized distribution of planet period. For reference, the distributions of TAP timing variations for the $Q < 0.7$ (lower binary mass ratio) systems and for the $e_p > 0.1$ (eccentric planet) systems are overplotted as dashed and dotted lines, respectively. The TTV distributions between the overall sample and the subsample of eccentric CBPs remain similar, which suggests additional TTVs due to model inaccuracies, i.e., assumption of circular planet orbits, are relatively small-scale. In contrast, the TTV distribution skews smaller for the subsample of lower binary mass ratio systems, which reinforces that the timing effects due to binary reflex motion dominate CBP TTVs.

The additional scatter about the log-log $\Delta t_{\rm TAP} - P_{\rm p}$ relation derives from additional effects of binary period, eccentricity, and mass ratio $Q = M_2/M_1$. For example, primaries in binaries with shorter period and lower mass ratio have smaller maximum orbital deviations from their barycenter, and therefore the CBP transit timing deviations due to reflex binary motion tend to be smaller. Because geometric effects due to binary orbital motion contribute the most to CBP TTVs, planetary effects such as planet eccentricity contribute significantly less to the overal TTVs. In the upper panel of Figure 4.9, the scales of $\Delta t_{\rm TAP}$ contribution by binary mass ratio and planet eccentricity are shown in dashed and dotted lines, respectively. The $e_p > 0.1$ TTV distribution remains similar to the bulk population, while $Q < 0.7$ distribution is skewed toward smaller TTV values relative to the bulk population.

Pipeline Completeness Maps

We report the results of direct injection & recovery on EB targets here. We define a successful recovery as a positive detection at multiple (known) injected transit times. That is, a simulated system is successfully recovered if it passes the same QATS-EB detection criteria as the target search (see § 4.1.3 and 4.1.4) and contains at least two detected transits coinciding within a transit duration from the true injected signals. We adopt this set of criteria, rather than simply requiring recovered periods to match the true period or aliases of it, because noise can conspire to produce a signal peak near the true period, especially at integer multiples of the binary period. Furthermore, CBP systems may precess during *Kepler* mission duration timescales, causing transits to become more shallow and disappear (or re-appear). This can cause QATS to pick up on the precession timescale, some alias of it, or some other beat frequency of the orbital and precession periods. Finally, because injected transits may also fall into missing data gaps, the QATS-detected period may be different from the true period.

We distinguish these successful recoveries, or true positives (TP), from false positives (FP). False positives are systems flagged as positive detections but those detections fail to recover transits near the injected values. Systems that fail to pass the detection SNR threshold or vetting process are flagged as true negatives (NG).

We tune the detection SNR threshold to balance the true and false positive rates. We use a SNR floor of 7.1 and 8.1 for HM and LM subsamples, which corresponds to an overall FP rate of <10% and <1%, respectively. The SNR floor is lower for HM systems to accommodate for the lower overall true positive rates.

Additionally, for some systems in our mock catalogue, the pipeline recovery analysis returned a single detected period common to different injected planet sizes and periods *for that particular EB target.* Recall that the simulated CBPs are directly injected into the target EB light curves. When the pipeline recovers the same period signal for multiple simulations with the same EB light curve template, this suggests the QATS-EB detection corresponds to signals (or noise) from the target EB light curve, and not from the injected CBP transits.

We visually inspected these "common periods" to assess their provenance. For a few targets, these "common" periods are the result of transit signals from tertiary stellar companions or doubly eclipsing binaries. We list these systems in Table 4.3, including the discovery of a doubly eclipsing system KIC 3848919, not previously identified in literature (see Appendix C for brief analysis). In other cases, we find that these recovery periods common to specific EB target light curves are the result of obviously spurious signals due to correlated noise or poor data detrending. We use the list of common periods to identify additional and reject false positives, both in the injection & recovery and target search. Detections in the mock catalogue and target search are excluded from the final completeness analysis or candidate catalogue, if they correspond to one of the target EB "common periods."

We express the pipeline completeness as a 2D histogram in bins of planet radius and planet period relative to the critical stability period, i.e., marginalized over the other input system properties. The pipeline efficiency in the jth bin is then the number of TPs divided by the total number of systems within each bin

$$Q_{\mathrm{pipe},j} = \frac{N_{\mathrm{TP},j}}{N_{\mathrm{TP},j} + N_{\mathrm{FP},j} + N_{\mathrm{NG},j}} \ . \tag{4.1}$$

Figures 4.11 and 4.12 show the pipeline completeness for HM and LM systems, respec-

Table 4.3 Additional Eclipsing Companions Detected in QATS-EB

KIC	P_b (d)	$P_{\mathrm{companion}}$ (d)	Type	Discovery Paper
3832716	1.1419	2.1703	Doubly eclipsing binary	Fedurco & Parimucha (2018)
3848919	1.04726	0.92726	Doubly eclipsing binary	
4247791	4.1009	4.0497	Doubly eclipsing binary	Lehmann et al. (2012)
7670485	8.4677	>1500	Triple or companion binary	Zhang et al. (2017)

tively. The pipeline is more sensitive to CBP size, i.e., changes in transit depths, relative to CBP period, i.e., changes in number of transits. This relative insensitivity to planet period (within $\lesssim 14P_c$) was also noted by Armstrong et al. (2014a). The overall CBP pipeline completeness is lower compared to CSP counterparts, in major part due to the difference in stellar properties between the target samples. In particular, the radius distribution of the primary stars in our sample (see Figure 4.8) peaks at $\sim 2\mathrm{R}_\odot$ (HM) and $\sim 1.3\mathrm{R}_\odot$ (LM), larger than the radii of GKM stars around which most terrestrial CSP searches target. Moreover, inaccuracies in the corrections for large-scale binary-induced TTVs would act to lower detection SNR.

For HM, the detection efficiency floor at large CBP sizes is lower at $\sim 50\%$, compared to $\sim 80\%$ for Jovian-size CBPs within $10P_c$ in the LM sample. Given our target sample, the pipeline appears insensitive to terrestrial-size CBPs, and marginally sensitive to sub-Neptune size ($R = 2 - 4R_\oplus$) CBPs around LM systems. This is a disappointing reality to contend with, as one of the goals of this work is to quantify the distribution of terrestrial-size CBPs. In addition to transit depth reduction due to larger stellar radii, we suspect light curve variability or noise associated with stellar binarity plays a major role.

We test this hypothesis by creating a CBP catalogue analogous in system properties to our fiducial Catalogue B, but using KOI light curves as noise templates, i.e., injecting the transit signals to single star *Kepler* light curves. We refer to the single-star noise template

CBP mock catalogue as Catalogue A[1]. For reference, we show the distribution of *Kepler* magnitudes for single star templates from mock Catalogue A (dashed blue line) and for EB targets from mock Catalogue B (solid grey line) in Figure 4.10. The bulk of the two brightness distributions overlap, suggesting similar photon noise properties, although there is an excess of ∼15 *Kepler* mag in Catalogue A relative to Catalogue B and a dearth of $\gtrsim 16$ *Kepler* mag. We plot the CBP recovery results up to $P_c = 10P_c$ for Catalogue A in Figure 4.13. The recovery rates are indeed higher, especially in the 1–4$R_\oplus$ bins, suggesting binary LC noise properties (e.g., starspots associated with rotation of one or both stellar components; reflection, beaming, and ellipsoidal effects) are the likely culprit and may significantly hinder signal detection.

We further investigate the detection efficiency in LM systems as a function of binary mass ratio $Q = M_2/M_1$. Figure 4.14 compares the pipeline completeness for $Q > 0.7$ and $Q < 0.7$ systems, and illustrates a detection bias against high mass ratio binaries. This bias is most noticeable in the 2–4$R_\oplus$ and 4–8$R_\oplus$ range, where detection efficiency drops by a factor of ∼2.2 and ∼1.5 for CBPs within $10P_c$, respectively. This detection bias against higher mass ratio binaries is not surprising (see also Martin, 2019) and may be understood in two contexts. First, the flux contribution of the secondary becomes comparable in equal-mass (MS) binaries, diluting the depth of transit given the same size CBP. Second, the binary-induced TTVs are larger for high Q systems, due to larger primary orbits relative to binary barycenters, and so inaccuracies in the geometric TTV corrections scale accordingly.

4.3.2 Transiting Criterion Sensitivity

In the previous section, we quantified the pipeline efficiency in detecting CBPs, *given that they transit either stellar component during the* Kepler *observing window.* Now, we consider the probability that CBPs transit their stellar hosts, under finite observing time and given their planet and binary parameters. This probability is the complement of fraction of CBPs

---

[1] Continuing the age-old astronomy tradition of confusing naming conventions/alphabetical ordering.

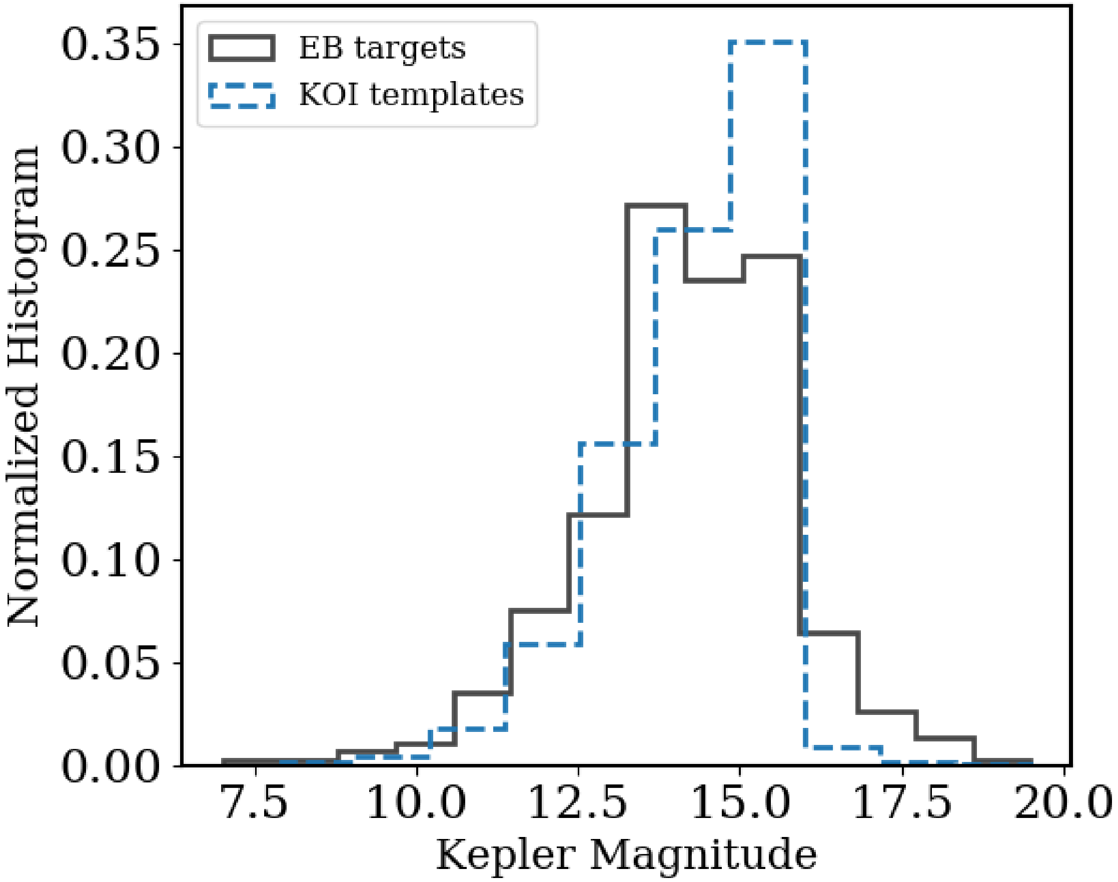

Figure 4.10 Distribution of Kepler magnitudes for KOI single stars used in mock Catalogue A (dashed blue) and EB targets used in Catalogue B.

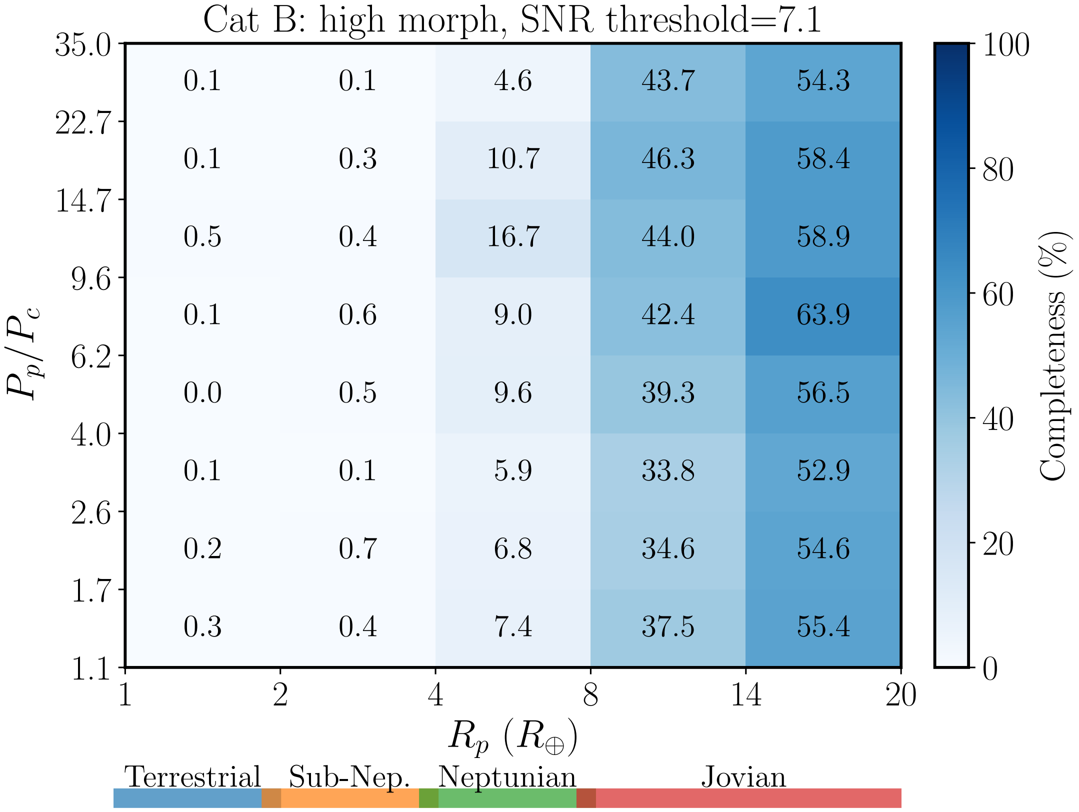

Figure 4.11 The detection completeness map as a function of CBP period (in multiples of the critical stability period P_c) and size corresponding to the injection & recovery of systems in the high morphology sample of Simulated Catalogue B. For reference, the bottom inset shows the approximate planet type (terrestrial, sub-Neptune, Neptune, and Jovian) corresponding to the different size bins.

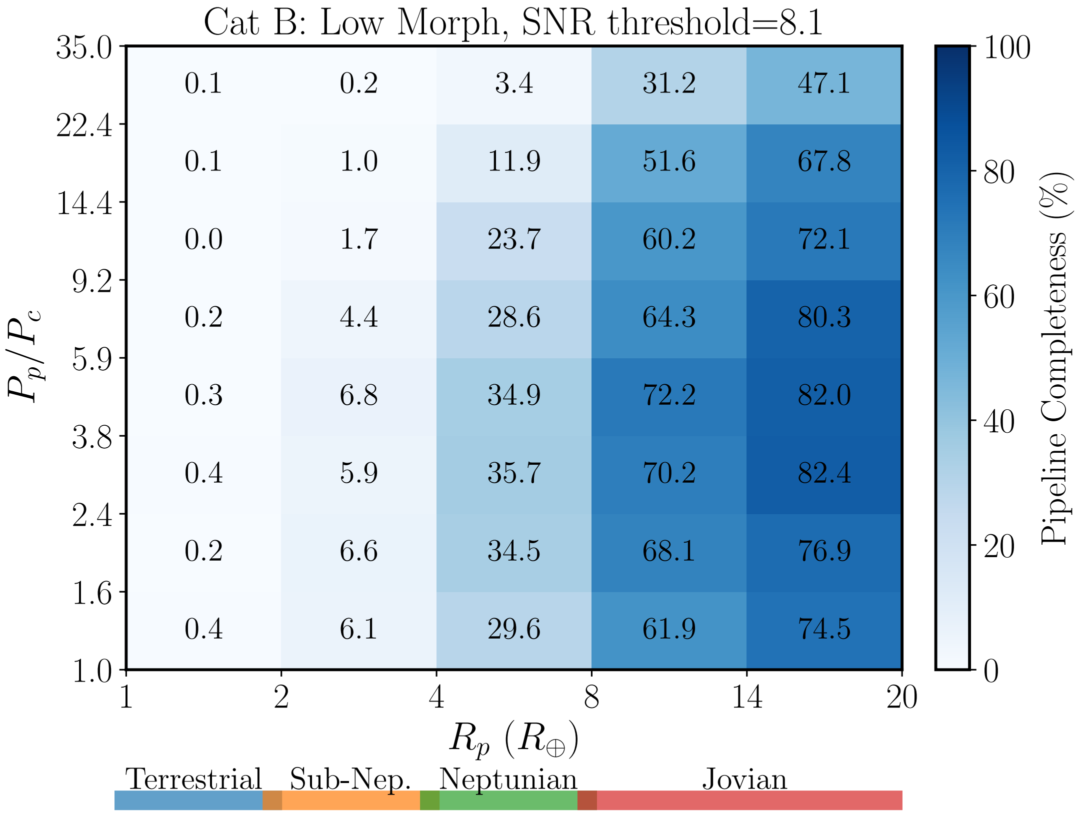

Figure 4.12 Same as Figure 4.11, but for the low morphology sample of Simulated Catalogue B.

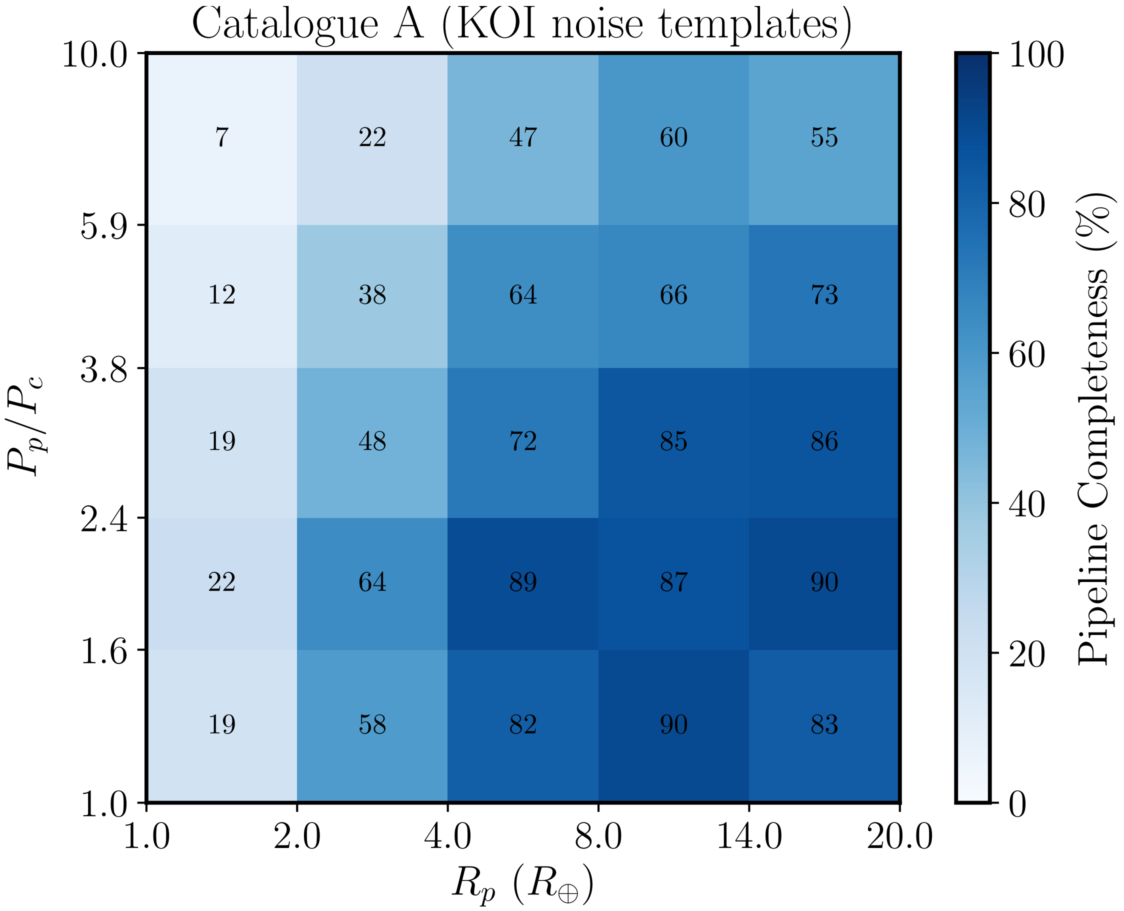

Figure 4.13 Recovery results for Catalogue A – a mock CBP catalogue with same system properties as our fiducial Catalogue B but using *Kepler* single star light curves as noise templates.

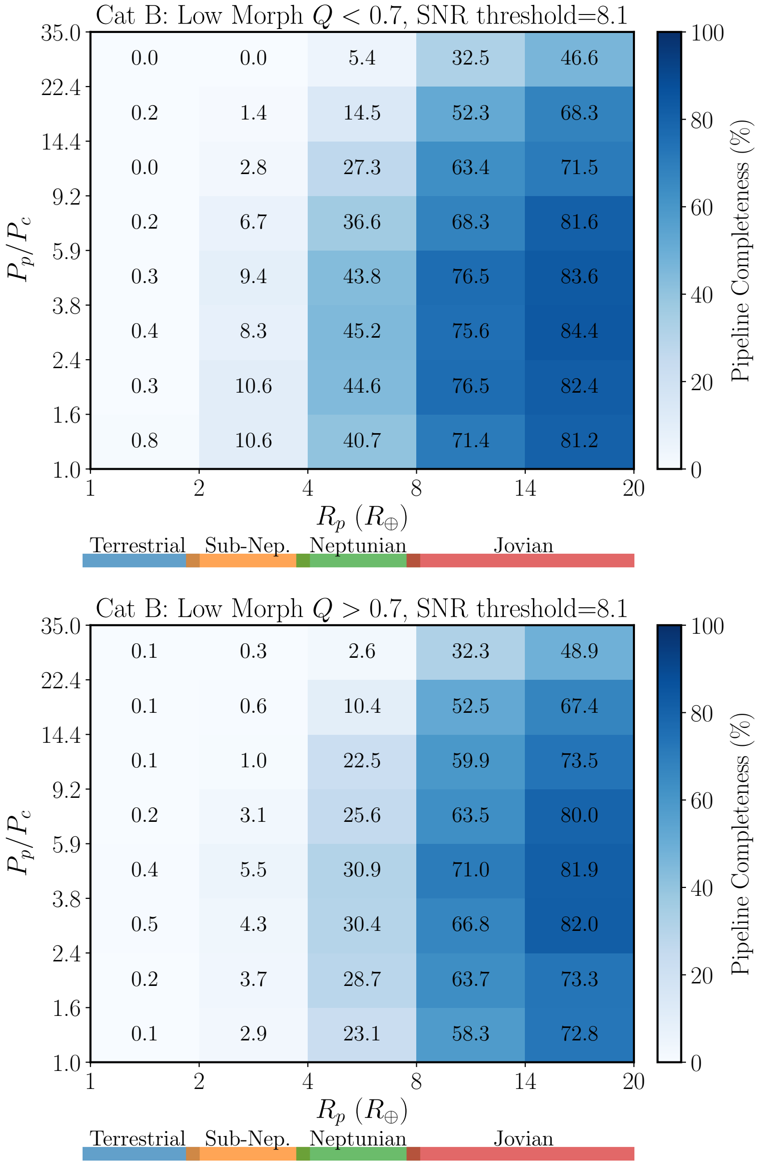

Figure 4.14 Similar to Figure 4.12, but comparing LM detection efficiency for low mass ratio $Q = M_2/M_1 < 0.7$ (upper) and high mass ratio $Q > 0.7$ (lower) binaries. In the 2–8R$_\oplus$ and P_p/P_c <10 region, CBPs around low mass ratio binaries are more efficiently detected than high Q binaries, by a factor of ~ 1.5 for Neptunes and ~ 2.2 for sub-Neptunes.

missed because they did not transit during the *Kepler* (prime) mission in the first place. The statistical correction for CBP transit probability under finite time is crucial to compute the total detection efficiency.

We estimate the statistical correction analytically, as it is computationally inefficient to simulate a large ensemble of CBPs filling out all parameter space and run QATS-EB on systems that may not transit. This approximate approach to compute missing planets due to non-transiting geometry has been adopted by many CSP transit detection pipelines or population analyses (Petigura et al., 2013; Burke et al., 2015; Foreman-Mackey et al., 2016).

The analytic expression for CBP transit probability is considerably more complex than for CSPs. In particular, CBP orbits may evolve toward or away from crossing the line-of-sight binary orbit due to precession. For circular binary orbits, a CBP's longitude of node circulates, i.e., changes linearly with time, and the precession timescale is (Schneider, 1994; Farago & Laskar, 2010)

$$T_{\mathrm{prec}} = \frac{4}{3\cos\delta i}\left(\frac{P_p^7}{P_b^4}\right)^{1/3}\frac{(M_1+M_2)^2}{M_1M_2} \tag{4.2}$$

where δi is the mutual inclination between planet and binary orbital planes, which remains constant in the circular binary regime. It is related to the longitude of nodes and inclinations relative to the observer via (Martin, 2017)

$$\cos\delta i = \cos(\Omega_b - \Omega_p)\sin i_b \sin i_p + \cos i_b \cos i_p \tag{4.3}$$

For constant δi, changes to $\Omega_b - \Omega_p$ manifests as sinusoidal variations in i_p, allowing potential windows of transits.

Thus, the probability that an ideal detector observes CBP transits during some time interval is regulated by planetary orbit, precession, and observing properties and timescales. Li et al. (2016) and Martin (2017) have previously derived the transit probability of CBPs around circular binaries, accounting for precession and finite observing time. We adopt their methodology and assumptions, namely that planet mass $\ll$ binary mass, that binary and planet orbits are circular, and that observations are uniform cadence (i.e., no data gaps); we revisit these assumptions at the end of this subsection.

We define the probability of at least k CBP transits during the *Kepler* mission as $Q_{\mathrm{t},\geq k}$, and separate it into two components, such that:

$$\begin{aligned} Q_{\mathrm{t},\geq k} &= P(\mathrm{tran} \geq k|\boldsymbol{\theta}_{\mathbf{b}}, \boldsymbol{\theta}_{\mathbf{p}}, \boldsymbol{\theta}_{\mathbf{survey}}) \\ &= P(\mathrm{tran} \geq k|\mathrm{xing}) \cdot P(\mathrm{xing}|\boldsymbol{\theta}) \end{aligned} \tag{4.4}$$

where "xing" denotes binary orbit crossing, $\boldsymbol{\theta} = \{\boldsymbol{\theta}_{\mathbf{b}}, \boldsymbol{\theta}_{\mathbf{p}}, \boldsymbol{\theta}_{\mathbf{survey}}\}$ are binary and planetary parameters, and survey parameters associated with the *Kepler* observations, e.g., duty cycle f_{duty} and total observing window length $\mathcal{T}_{\mathrm{obs}}$ of light curves. The first component is the probability that the planet transits a stellar component at least k times during binary orbit crossings, while the second component is the "geometric" probability that the planet crosses the binary orbit with respect to the observer during $\mathcal{T}_{\mathrm{obs}}$, given that its orbit precesses according to $\boldsymbol{\theta}_{\mathbf{p}}$ and $\boldsymbol{\theta}_{\mathbf{b}}$ (Martin, 2017 refers to the latter as "transitability").

Following the approach of Burke & McCullough, 2014, we define the probability of observing k or more transits as

$$P_{\geq k} = 1 - \sum_{i=0}^{k-1} P_k \ , \tag{4.5}$$

where P_k is the probability of observing exactly k transits, which is implicitly a function of $\{\boldsymbol{\theta}_{\mathbf{p}}, \boldsymbol{\theta}_{\mathbf{b}}, \boldsymbol{\theta}_{\mathbf{survey}}\}$, and $\sum P_k$ term is the probability of observing *fewer* than k transits. In the high duty cycle regime, which applies to *Kepler* targets (see, e.g., Burke et al., 2015; Foreman-Mackey et al., 2016), Burke & McCullough (2014) have shown that a binomial approximation to compute P_k agrees well with numerical results for CSPs. We adopt this approach to estimate P_k for CBPs, where each independent planet-binary orbit crossing is a binomial trial

$$P_k = \binom{M}{k} P_0 (1 - P_0)^{M-k} \ , k = 0, 1, 2, ..., M \tag{4.6}$$

Here, M is the expected number of binary orbit crossings (see equation 18 of Li et al., 2016), and $P_0 = f_{\mathrm{duty}} P_{\star}$ is the probability of transit across the stellar disk of a binary component (see equation 17 of Li et al., 2016) weighted by the average fraction of time spent observing. For comparison, in the CSP limit and with no substantial dynamical forcing by additional bodies, $M = \mathcal{T}_{\mathrm{obs}}/P_{\mathrm{p}}$ and $P_0 = f_{\mathrm{duty}}$; such a planet will always transit its host star and every planet period interval is an orbit crossing event, *given that the system satisfies the CSP geometric transit criterion.*

We expand Equations 4.5 and 4.6 to $P_{\geq k=3}$, as we rejected simulations with fewer than 3 transits during $\mathcal{T}_{\mathrm{obs}}$. Combining the expansion with Equation 4.4,

$$
\begin{aligned}
Q_{\mathrm{t}}(\star) &= P_{\geq k}(\star|\mathrm{x})P(\mathrm{x}|\boldsymbol{\theta}) \\
&= \Big(1-(1-f_{\mathrm{duty}}P_\star)^M - Mf_{\mathrm{duty}}P_\star(1-f_{\mathrm{duty}}P_\star)^{M-1} \\
&\quad - M(M-1)/2(f_{\mathrm{duty}}P_\star)^2(1-f_{\mathrm{duty}}P_\star)^{M-2}\Big)P(\mathrm{x}|\boldsymbol{\theta}) \ ,
\end{aligned}
\tag{4.7}
$$

where "$\star$" and "x" denote planet crossing the stellar disk and orbit, respectively, and other quantities are the same as in Equation 4.6. $P(\mathrm{x}|\boldsymbol{\theta})$, the probability of orbit crossing accounting for precession, is explicitly derived in equation 16 of Li et al. (2016). The above equation describes the probability a planet transits one stellar component at least 3 times under $\mathcal{T}_{\mathrm{obs}}$.

To compute the probability that a CBP transits *either* stellar component at least 3 times (our simulations were created with this specific set of criteria), we combine the individual transit probabilities for each stellar component and use complement rules for probability. Following the logic of Li et al. (2016), the probability of at least k transits across either stellar components can be expressed as

$$
\begin{aligned}
Q_{\mathrm{t}\geq k}(\star_1\mathrm{or}\star_2) &= P(\mathrm{x}_2|\boldsymbol{\theta})\Big(1-P_{<\mathrm{k}}(\star_2|\mathrm{x}_2)P_{<\mathrm{k}}(\star_1|\mathrm{x}_2)\Big) \\
&= P(\mathrm{x}_2|\boldsymbol{\theta})\Big(1-P_{<\mathrm{k}}(\star_2|\mathrm{x}_2)\big[P_{<\mathrm{k}}(\star_1|\mathrm{x}_1)P(\mathrm{x}_1|\mathrm{x}_2)+P_{<\mathrm{k}}(\star_1|!\mathrm{x}_1)P(!\mathrm{x}_1|\mathrm{x}_2)\big]\Big) \\
&= P(\mathrm{x}_2|\boldsymbol{\theta})\left(1-P_{<\mathrm{k}}(\star_2|\mathrm{x}_2)\left[P_{<\mathrm{k}}(\star_1|\mathrm{x}_1)\frac{P(\mathrm{x}_1)}{P(\mathrm{x}_2)}+\frac{P(\mathrm{x}_2)-P(\mathrm{x}_1)}{P(\mathrm{x}_2)}\right]\right)
\end{aligned}
\tag{4.8}
$$

where "!" denotes the Boolean operator "not," i.e., $P(!\mathrm{x}_1|\mathrm{x}_2)$ is the probability a planet does not cross the primary's orbit given that it crosses the secondary's orbit; $P_{<\mathrm{k}}(\star_{1,2}|\mathrm{x}_{1,2})$ is probability of observing *fewer* than k transits of the primary (secondary) star, and can be solved using Equations 4.5 and 4.6; $P_{<k}(\star_1|!\mathrm{x}_1)$, the probability of fewer than k transits of star 1 given that its orbit is *not* crossed by the planet, is 1, and $P(!\mathrm{x}_1|\mathrm{x}_2)$ is $\frac{P(\mathrm{x}_2)-P(\mathrm{x}_1)}{P(\mathrm{x}_2)}$.

We use Equation 4.8 to compute each simulated CBP's transit probability, given its input binary (e.g., masses, period, inclination), planet (e.g., period, mutual inclination), and transit survey properties (e.g., observing duration, duty cycle).

We now revisit the validity of our assumptions – CBP as test particle, circular binary orbits, and continuous observing data. Figure 4.7 shows that the majority of systems have $\frac{M_{\rm p}}{M_1+M_2} < 10^{-4}$, and 95% of simulations have $\frac{M_{\rm p}}{M_1+M_2} < 10^{-3}$, satisfying the massless particle approximation. A larger caveat is that ∼25% of our target EB sample have $e_b > 0.2$ (∼16% $e_b > 0.3$). In the limit of eccentric binaries, the secular behaviour of CBP orbits is more complex, such that for certain configurations their inclinations and longitudes of node may librate around $\pm\pi/2$ (Farago & Laskar, 2010). While this remains a caveat, we note that Li et al. (2016) compared their analytic transit probability calculations (derived under circular binary approximation) to numerical results, and showed that they agree, even for CBPs with eccentric hosts Kep-64 & Kep-1647 ($e \sim 0.2$) and Kep-34 ($e \sim 0.5$). Finally, although *Kepler* does have quarterly gaps and missing cadences due to poor data quality, the mean duty fraction in the target light curves is ≈91%.

4.3.3 Cumulative Detection Efficiency & Mutual Inclination Considerations

We now derive the cumulative detection efficiency or completeness Q_c, which depends on the distribution of mutual inclinations between CBP and host binary orbits. The connection between these two quantities is as follows. Recall that Q_c is the total probability of detection, given the pipeline efficiency and the time-dependent transit efficiency, both of which can be directly computed using known properties of the synthetic catalogue $\boldsymbol{\theta} = \{\boldsymbol{\theta}_{\mathbf{b}}, \boldsymbol{P}_{\mathbf{p}}, \boldsymbol{R}_{\mathbf{p}}, \boldsymbol{\delta i}$, ... $\}$. However, the mock simulations are seeded with a small range in mutual inclinations, so that the ≥3 transits criterion may be more efficiently achieved. Consequently, we must correct for any bias due to this choice by marginalizing over various distributions of δi, as the true distribution is not known.

To make this intuitive, consider the following toy universes where all system parameters mirror each other except for mutual inclination. For simplicity, let's make the (unphysical) assumption that $\Omega_b = \Omega_p$ such that $\delta i = i_b - i_p$ at all times (in reality, CBPs precess such that for constant δi, i_p and $\Omega_p - \Omega_b$ are varying sinusoidally with time, which underscores the importance of marginalizing over δi). In universe 1, nature has no preference on δi and fills CBPs around binaries uniformly from $\delta i = 0 - 180°$, while in universe 2, nature has a strong preference to create CBPs coplanar to binary hosts. In both universes, the pipeline detection efficiencies are the same, because we have (by design) only tested the detection completeness on CBPs that transit. However, we would observe many more CBP systems in universe 2 than universe 1, because universe 2 creates more CBPs with mutual inclinations that allow fortuitous transit alignment. Since we do not know *a priori* if we live in universe 1, 2, or n, we must condition our detection efficiency and CBP frequency estimation on different prior distributions of δi.

Following Li et al. (2016), we specify δi distribution as a Fisher distribution

$$f_\kappa(\delta i) = f(\delta i|\kappa) = \frac{\kappa}{2\sinh\kappa} \exp\left(\kappa\cos\delta i\right)\sin\delta i \ , \tag{4.9}$$

where κ is a free parameter controlling the spread in mutual inclination, such that $f_\kappa(\delta i)$ is isotropic when $\kappa \to 0$, and peaks near coplanarity and approaches a Rayleigh distribution for $\kappa \gg 1$. This distribution is adopted from Fabrycky & Winn (2009), who used it to model how angles between stellar spin and planetary orbit ("spin-orbit alignment") are 3D directionally distributed in CSP systems. Figure 4.15 illustrates the probability density functions (per radian) of mutual inclination for $\kappa = \{0.1, 1, 3, 10, 30, 100\}$.

The marginalized cumulative detection efficiency for the mth simulated system in the mock catalogue can be expressed as

$$\begin{aligned} Q_{c,m}(\kappa) &= Q_{\mathrm{pipe},m}\bar{Q}_{t,m}(\kappa) \\ &= Q_{\mathrm{pipe},m}\int_0^\pi Q_{t,m}(\delta i)p(\delta i|\kappa)d(\delta i) \ , \end{aligned} \tag{4.10}$$

where $p(\delta i) = f_\kappa(\delta i)$ from Equation 4.9, $Q_{t,m}$ is given by Equation 4.8, $\bar{Q}_{t,m}(\kappa)$ is the marginalized transit detection efficiency, and we have dropped the explicit dependence on $\boldsymbol{\theta}$, the rest of the system properties, for legibility. Additionally, we make the assumption that

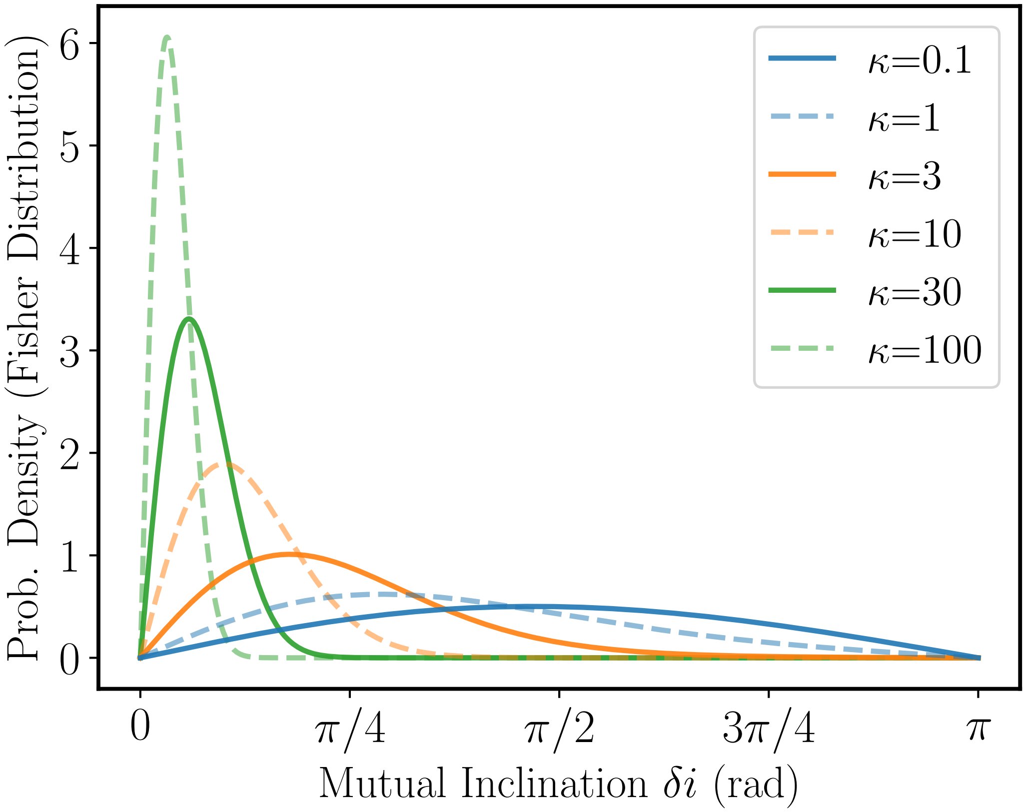

Figure 4.15 Modeling CBP mutual inclination distribution as a Fisher distribution, where the different colour and line styles correspond to different choices of scale parameter κ. As κ increases, the mutual inclination distribution becomes more narrowly peaked at smaller values.

the *pipeline* efficiency does not vary strongly across mutual inclinations *that allow at least 3 transits* in the target light curve, given otherwise identical system parameters. We revisit this assumption at the end of this section.

Figure 4.16 shows $\bar{Q}_{t,m}(\kappa)$ as a function of P_p/P_c based on simulated CBPs from the HM subsample of Catalogue B, for various κ. Within each κ panel, the vertical spread in Q_t reflects the spread in target binary parameters. At large kappa values, the mutual inclination distribution is more strongly peaked toward 0, i.e., aligned with the binary orbital plane. This means for EBs with i_b away from $\pi/2$ (i.e., less edge-on orientation), i_p is also strongly misaligned *relative to observer*, and even short-period planets are less likely to transit, due to viewing geometry. The consequence of this is that for short-period EBs, which may take on a larger spread in i_b and still satisfy the eclipsing geometry, CBPs are more likely to transit if they are more misaligned *with respect to the binary*. We see this effect in the $\kappa \rightarrow 700$ panel of Figure 4.16: the marginalized transit probability takes on larger spread from 0 to 1 at shorter planet(-to-binary stability) periods around short-period EBs. For smaller κ, mutual inclinations tend towards an isotropic distribution. Therefore, when marginalized over all possible mutual inclinations, the strongest predictor for transit probability is planet(-to-binary) period.

In practice, we create completeness maps in bins of R_p and P_p/P_c, i.e,. for the jth bin, $Q_{c,j}$ is the sum over all $Q_{c,m}$ for $\boldsymbol{\theta_m}$ that belong to bin j. Figures 4.17 and 4.18 show the percent change between the cumulative (marginalized) detection completeness and pipeline-only completeness as a function of κ, for HM and LM systems, respectively. For reference, Figures 4.11 and 4.12 show the absolute values of pipeline completeness for HM and LM subsamples. As is expected, in both HM and LM, the greatest change in detection efficiency, when transit bias is accounted for, occurs at longer planet orbital periods (e.g., $P_p > 4P_c$) for all κ. Within the inner range in $P_p/P_c = 1 - 4$, we observe that the relative change decreases (less negative) for larger κ values in LM systems, while the relative change increases (more negative) for larger κ values in HM systems. This is the effect of binary inclination distribution, which has a larger spread in HM targets due to eclipse geometry.

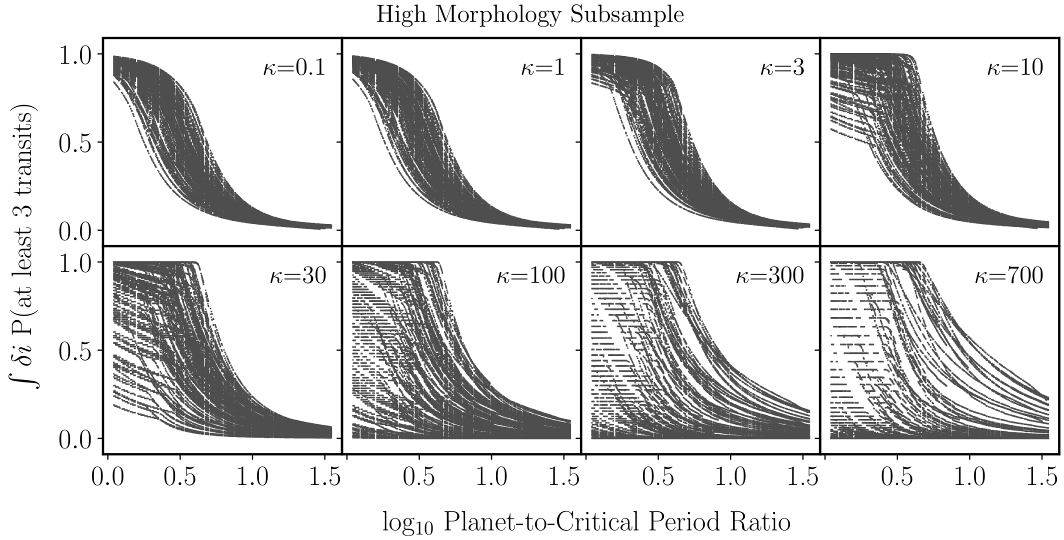

Figure 4.16 Marginalized CBP transit probability Q_t as a function of $\log_{10}(P_p/P_c)$ in the high morphology subsample of Catalogue B, for various κ. Concretely, each point represents the probability that a CBP (with given planet and binary parameters) will transit the binary at least 3 times during *Kepler* observations, marginalized over different CBP-EB mutual inclination distributions (parameterized by κ). In general, CBP transit probability drops as planet period increases; this geometric effect dominates in CSPs as well – the further out a planet is, the more aligned it must be to transit its host star relative to the observer. However, for CBPs, there is an additional geometric effect modifying Q_t, a time-dependent aspect due to precession of the planet around its host binary. This series of plots show the averaged effects of precession on CBP transit probability, conditioned on different mutual inclination distributions.

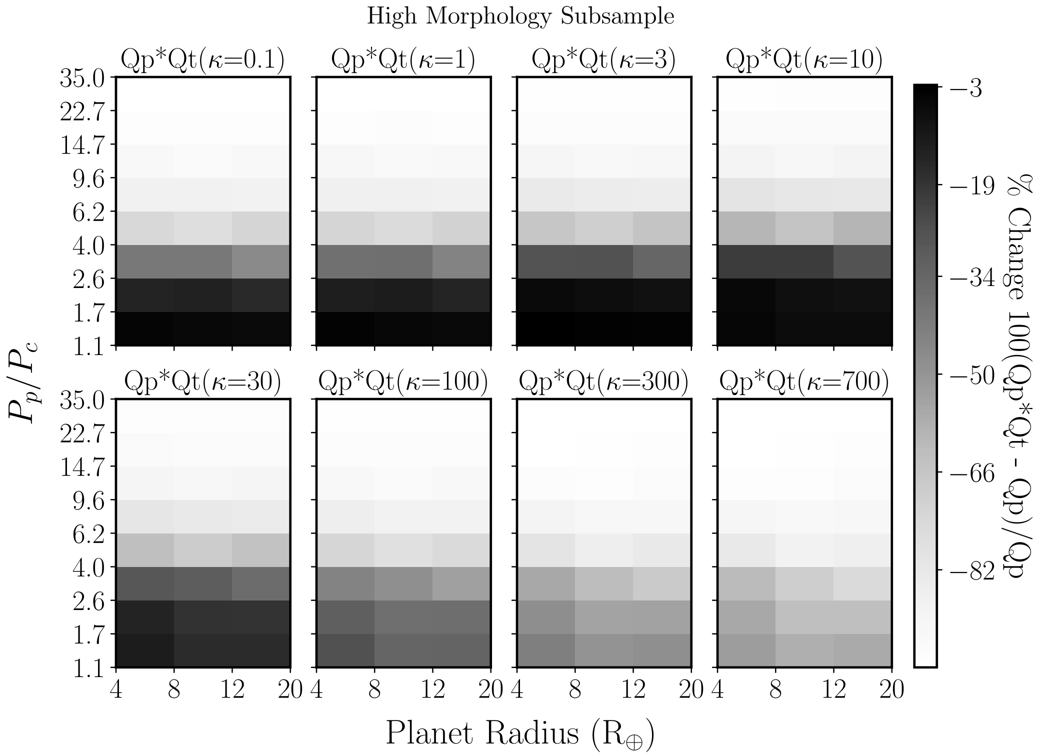

Figure 4.17 The percent change in cumulative detection efficiency ($Q_pQ_t(\kappa)$) from pipeline detection efficiency (Q_p) for the high morphology sample of Catalogue B, at different CBP radius and period bins. The absolute values for high morphology Q_p are shown in Figure 4.11; smaller CBP size bins are excluded in the percent change analysis, due to pipeline insensitivity at $R_p < 4R_\oplus$ for the high morphology subsample.

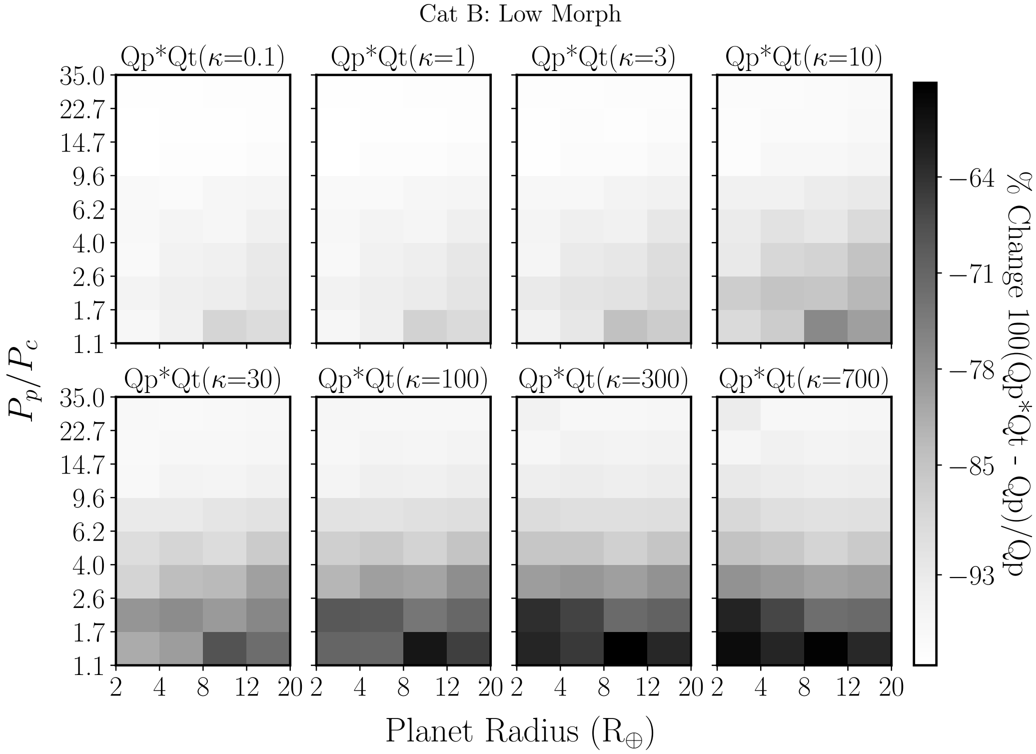

Figure 4.18 Same as Figure 4.17, but for LM sample of Catalogue B.

Finally, we return to Equation 4.10 and examine the validity of assuming that $Q_{\mathrm{pipe},m}$ is constant for δi producing at least 3 transits, given otherwise identical systems. In general, the number, timing, and duration of transits may vary as a function of δi, which would introduce subtle differences to the pipeline detection efficiency. For example, a higher number of transit events would boost the pipeline detection SNR; while larger than expected transit timing variations would smear the stacked transit signals across a larger range in period, and longer duration transits may become lost in light curves with correlated noise on similar timescales – both yielding a lower pipeline SNR.

Because we directly simulate CBPs around each target EB and marginalize detection efficiency over bins of planet radius and period, each bin samples a range in $\delta i = \pi/2 - i_b$. We expect poor sampling in *pipeline* efficiency at large δi does not significantly bias cumulative detection efficiency results, as $Q_{t,\geq 3}$ drops exponentially at large δi.

A finer complexity to consider is that at fixed i_b, many different combinations of $\Delta\Omega$ and i_p can satisfy a specific δi value. Therefore, because Catalogue B simulations held $\Delta\Omega$ constant at 0, we briefly explore potential correlations between the choice of $\Delta\Omega$ and number of transits, to determine if Catalogue B's simulations with $\Delta\Omega$=0 would introduce strong biases in the efficiency calculations.

Figures 4.19 and 4.20 show the number of transits across the primary (in the ~4 year *Kepler* span) at various mutual inclinations for a 7.4d CBP around a 2d binary and a 55.3d CBP around a 10.1d binary, respectively. In both cases, the binary components are solar, with circular orbits tilted slightly at 89°. The dashed line represents the analytic approximation from (Li et al., 2016), which shows remarkable agreement. Each δi grid contains 300 simulated systems with 30 random, possible pairs of ($\Delta\Omega$, i_p) × 10 different initial planet phase $f_{0,p}$, while all other system parameters are held constant. The light grey violin plots show the distribution in number of TAPs marginalized over $\Delta\Omega, i_p, f_{0,p}$, while the dark grey boxes cover the first and third quartile values. The white markers represent the median number of TAPs for $\Delta\Omega = 0$ simulations ($\Delta\Omega$=0 is forbidden at $\delta i > 90°$ for ~edge-on binaries). In both numerical experiments, the number of transits in $\Delta\Omega = 0$ cases lie within the quartile ranges of all allowable $\Delta\Omega$ cases, and exhibit no large, systematic bias. We therefore conclude that our assumption in Equation 4.10 is valid for the purposes of this study.

4.4 CBP Population Inference

We now estimate the underlying circumbinary planet population from the catalogue of CBP candidates (§4.2) and the total detection efficiency (§4.3). The formalism in this section relies heavily on the work of Youdin (2011) and Foreman-Mackey et al. (2014). We use a Hierarchical Bayesian framework, as illustrated in Figure 4.21, to conceptualize the generational relationship between population statistics and observable statistics. In this framework, some underlying physics (e.g., planet formation, migration) shape population-level parameters $\boldsymbol{\alpha}$ (e.g., planet radius, period, and mutual inclination distribution; binary mass ratio and period distribution), which seeds a set of parameters for each individual system $\boldsymbol{\theta_i}$ (a vector of physical parameters describing the binary and planet); these systems are then detected with observables $\boldsymbol{x_i}$ (the light curves).

We seek to infer the unknown population parameters – the frequency of CBPs as a function of physical parameters of interest. To keep consistent with CSP literature, we define η as the frequency of CBPs (within some interval of physical properties), and $\Gamma = \frac{d\eta}{d\boldsymbol{\theta}}$, the occurrence rate density (frequency *per* interval of physical properties). In the derivations below (§4.4.1), we use intervals of planet size $\ln R_p$ and normalized planet period $\ln \frac{P_p}{P_c}$, i.e., $\Gamma = \frac{d^2\eta}{d\ln R_p d\ln(P_p/P_c)}$, and define V_j as the area of the jth cell. The normalization in period by P_c is motivated by dynamical considerations, as CBPs within the critical period are unstable to perturbations from the binary (recall that we seeded CBP simulations from uniform distribution in $\ln \frac{P_p}{P_c}$), and absolute values of CBP period are not meaningful in assessing habitability. We also investigate the CBP frequency as a function of mutual inclination distribution and host binary period, although these quantities are not explicitly treated in the equations below, by repeating the $\frac{d^2\eta}{d\ln R_p d\ln(P_p/P_c)}$ analysis while varying κ (mutual inclination distribution), and by splitting our sample into high- and low- morphology EB

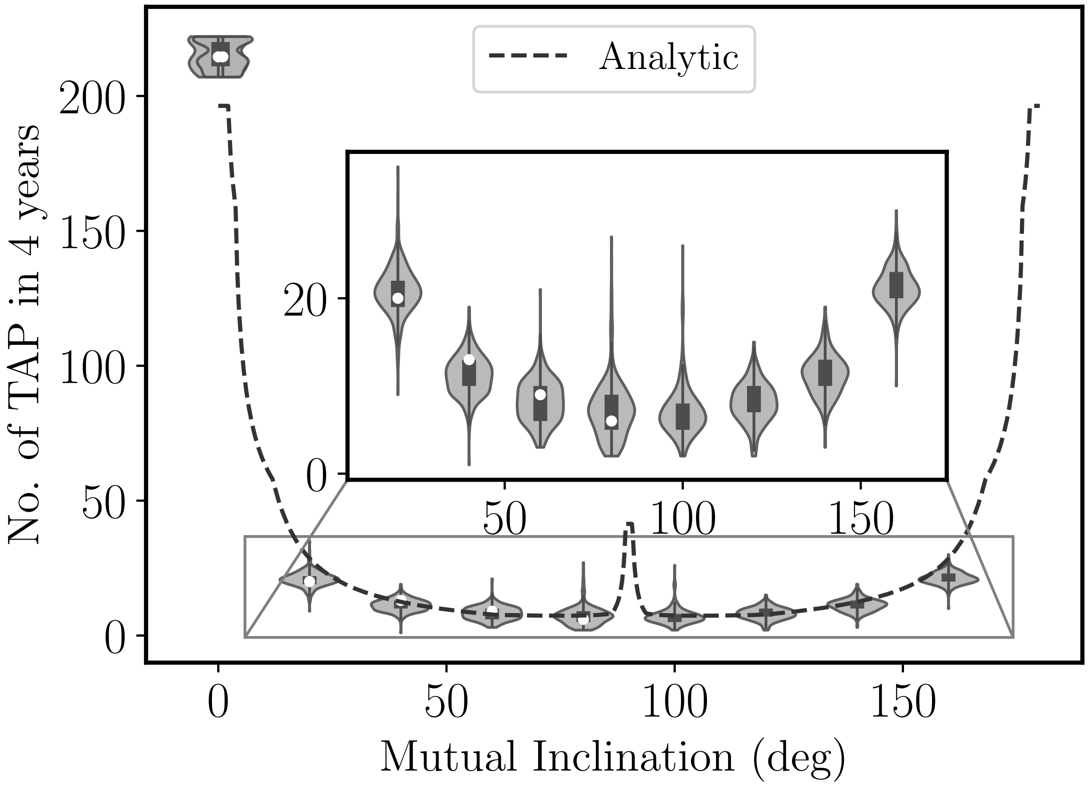

Figure 4.19 The distribution in number of transits across the primary (TAP) in four years as a function of mutual inclination in degrees for a 7.4d CBP around a 2d EB, based on $\sim$ 300 simulations with different $\Delta\Omega, i_p$, and initial planet phase per δi node. The dark grey boxes represent the first and third quartile ranges while the white marker denotes number of TAP for $\Delta\Omega = 0$ cases. Overall, the average numerical results agree with the analytic approximation (dashed line).

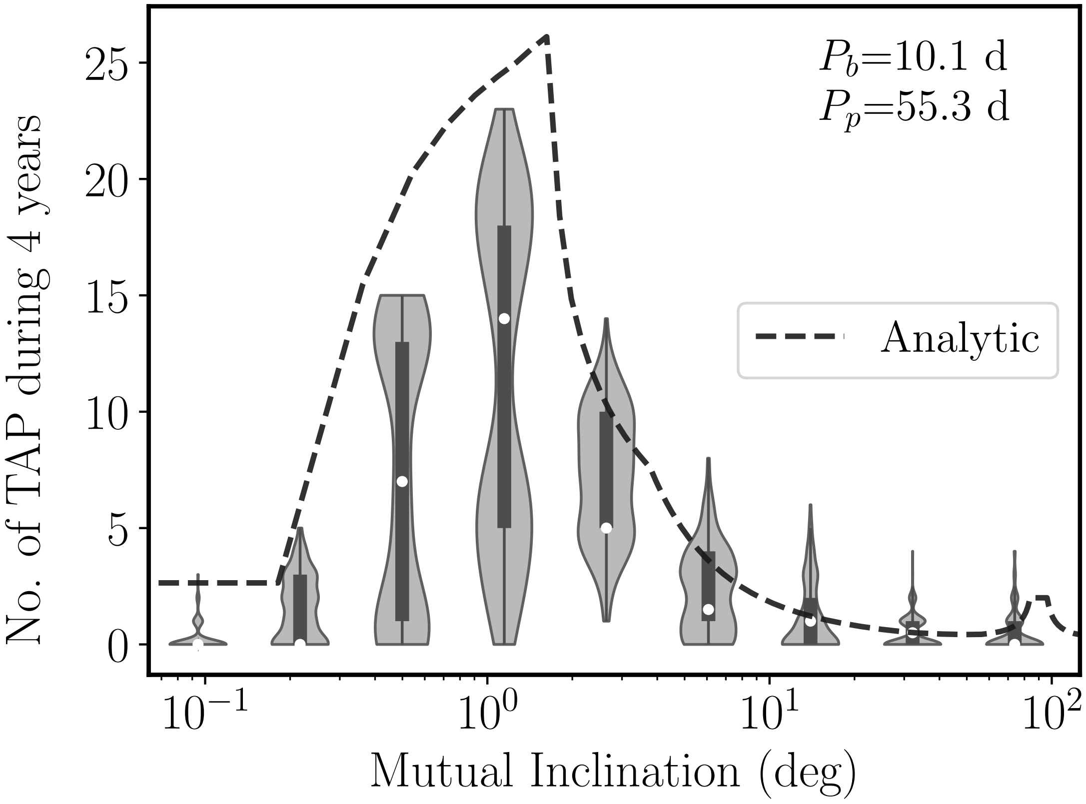

Figure 4.20 Same as Figure 4.19, but for a 55.3d CBP around a 10.1d EB and sampling δi in log space. The median number of transits for $\Delta\Omega = 0$ cases fall within the respective quartile ranges marginalized over possible $\Delta\Omega, i_p$ pairs and do not exhibit large systematic bias.

subpopulations.

4.4.1 The Likelihood Function

To make the population inference, we first model the process by which CBP candidates are detected. We use a forward model to generate the observed rate density $\hat{\Gamma}_\alpha(\boldsymbol{\theta})$.

$$\hat{\Gamma}_\alpha(\theta) = Q_c(\theta)\Gamma_\alpha(\theta) \ , \tag{4.11}$$

Here, the *expected* or observed rate density in bin volume V_j is the (unknown and yet to be defined) true rate density, censored by the cumulative detection efficiency Q_c (also called the censoring function; see Equation 4.10 in § 4.3.3). The "α" subscript is a reminder that the true CBP rate density is generated from, i.e., may be a function of, population-level parameters $\boldsymbol{\alpha}$.

Following Youdin (2011); Foreman-Mackey et al. (2014), we model the CBP catalogue candidates (§4.2) as Poisson realizations of the *observed* CBP rate density $\hat{\Gamma}(\theta)$. If the detections are represented in a 2D histogram, with J fixed bin volumes V_j and number of counts per bin K_j, the total likelihood is the product of Poisson distributions in each bin

$$p(\{\boldsymbol{\theta_i}\}|\boldsymbol{\alpha}) = \prod_{j=1}^{J} \left(\frac{(N_{\rm targ}\hat{\Gamma}_{\alpha,j}(\boldsymbol{\theta_i})V_j)^{K_j}}{K_j!} \right) \exp\left(-\sum_{j=1}^{J} N_{\rm targ}\hat{\Gamma}_{\alpha,j}V_j \right) \tag{4.12}$$

Here, $\{\boldsymbol{\theta_i}\}$ is the set of vectors of planet and binary physical parameters corresponding to the ith candidate system, and the detections implicitly depend on $\boldsymbol{\theta}$. α describes the population parameters[2], yet to be specified.

Substituting Equation 4.11 into Equation 4.12, the log-likelihood function can be expressed as

$$\mathcal{L} = \sum_j \left(K_j(\ln Q_{c,j} + \ln \Gamma_{\alpha,j}) - N_{\rm targ} Q_{c,j}\Gamma_{\alpha,j}V_j \right) + {\rm const} \tag{4.13}$$

The first term is the likelihood associated with actual (candidate) detections with parameters $\boldsymbol{\theta_i}$; the second term is a penalty term that specifies the likelihood of expected detections

---

[2] Note Foreman-Mackey et al., 2014, 2016 use w to represent the vector of physical parameters corresponding to planetary systems and θ to parameterize the population occurrence rate density.

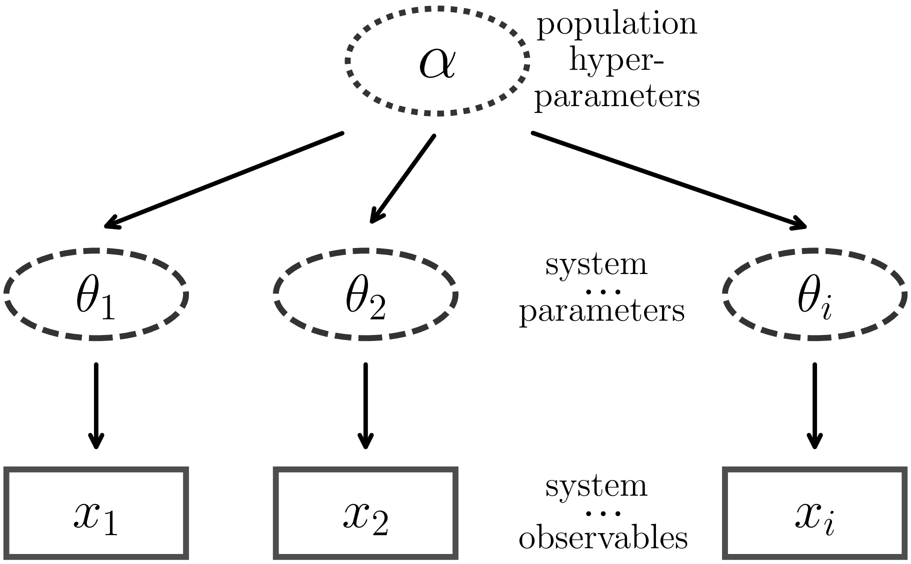

Figure 4.21 A simplified schematic of hierarchical framework to model the CBP population, following the notation of Wolfgang et al., 2016. Concretely, θ_i is a vector of physical parameters describing the binary $\theta_{\mathrm{b},i}$ and planet $\theta_{\mathrm{p},i}$ in the ith system, e.g., $\{P_\mathrm{b}, e_\mathrm{b}, M_1, M_2, R_1, P_\mathrm{p}, R_\mathrm{p}, ...\}$.

across all $\boldsymbol{\theta}$ space; the third term collects all the constants in the derivation (due to fixed bin size).

Taking the derivative of $\mathcal{L}$ with respect to $\Gamma_{\alpha,j}$, we can solve for the maximum likelihood solution to 4.13. The ML solution for the jth volume bin is

$$\Gamma_{\alpha,j}(\theta) = \frac{K_j}{N_\mathrm{targ} V_j Q_{c,j}} \tag{4.14}$$

where the numerator is the count of CBP candidates within V_j, and the denominator is the sum of cumulative detection efficiency within V_j (based on injections) multiplied by the bin volume V_j and total number of EB targets.

4.4.2 Priors and Posterior Sampling

Using the likelihood equation, we can directly fit for the true occurrence rate density for each bin, i.e., $\boldsymbol{\alpha}$ is the set of Γ_j free parameters. This assumes Γ_j values are independent of each other, and the caveat here is that the number of free parameters scale with the number of histogram bins. Alternatively, we may use a functional form to quantify correlations between Γ_j, i.e., constrain the shape of Γ as a function of $\ln R_p$ and $\ln(P_p/P_c)$. In this case, our fitting parameters $\boldsymbol{\alpha}$ is the set of hyper-parameters that specifies $\Gamma(\boldsymbol{\alpha})$. In the limit of sparse data, the choice of prior strongly influences the inferred results. Consequently, we provide derivations for a generalized parametric prior in Appendix D, and opt to use the direct fitting method for the remainder of our analysis.

Given the small number of detected candidates, we reduce the dimensionality of our 2D bins in $\ln R_p$ and $\ln P_p/P_c$ to $R_p/R_\oplus = \{2, 4, 10, 20\}$ and $P_p/P_c = \{1, 35\}$ in our frequency analysis, and then directly and independently fit for $\boldsymbol{\alpha} = \{\Gamma_j\}$, assuming flat priors $\in$ [0, 1000). We repeat this analysis for different j bins, κ values, and HM/LM subsamples.

We infer the true CBP frequency using Bayes' theorem, i.e., compute the posterior distribution of α given our input assumption (prior on $\boldsymbol{\alpha}$) and the likelihood expression given in Equation 4.13

$$p(\boldsymbol{\alpha}|\{\boldsymbol{\theta_i}\}) = \frac{p(\{\boldsymbol{\theta_i}\}|\boldsymbol{\alpha})p(\boldsymbol{\alpha})}{\int p(\{\boldsymbol{\theta_i}\}|\boldsymbol{\alpha})p(\boldsymbol{\alpha})d\boldsymbol{\alpha}} \ . \tag{4.15}$$

In practice, we run an affine-invariant MCMC (`emcee`; Foreman-Mackey et al., 2013) on the (sparse or empty) set of detected candidates and detection efficiency as function of R_p and P_p/P_c, and use the chain samples post burn-in to evaluate the posterior density distribution. We report the 50th percentile values for η at various bins, as well as their corresponding 50% confidence and 95% confidence intervals.

For small dimensions in and simple prescriptions for $\boldsymbol{\alpha}$, we can analytically integrate the denominator (the Bayesian "evidence") and evaluate the posterior probability density function. We use this as a calibration check for our MCMC analysis, and show in Figure 4.22 that the MCMC results and analytic computations agree.

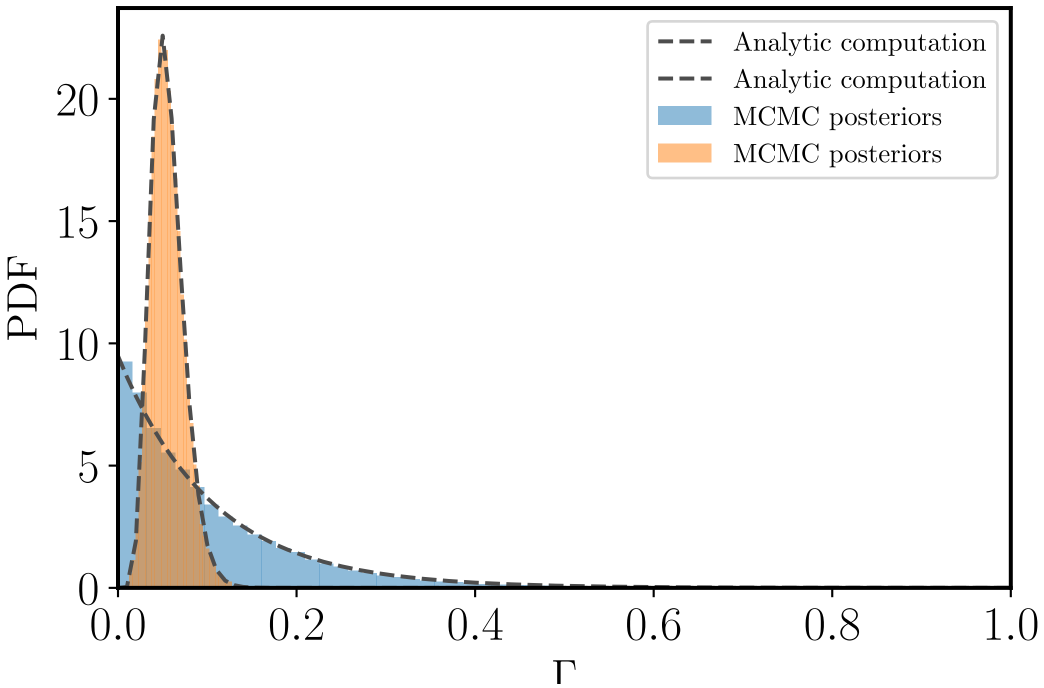

Figure 4.22 Posterior probability density function for Γ in an arbitrary $R_p, P_p/P_c$ bin for HM and LM, using MCMC (blue and orange histograms, respectively) vs. analytic expression (dashed lines). The results agree and provide a calibration check on our method.

Table 4.4 Occurrence Rates (%) for CBPs within $35P_c$ around LM ($P_b \gtrsim 5$ d)

κ	$2-4\mathrm{R}_\oplus$ ($\mathrm{N}_{\mathrm{det}}$=0)	$4-10\mathrm{R}_\oplus$ ($\mathrm{N}_{\mathrm{det}}$=8)	$10-20\mathrm{R}_\oplus$ ($\mathrm{N}_{\mathrm{det}}$=0)	$2-20\mathrm{R}_\oplus$ ($\mathrm{N}_{\mathrm{det}}$=8)
0.1	$73.1^{146.0\;404.3}_{30.5\;2.6}$	$82.7^{102.9\;149.2}_{65.6\;40.0}$	$2.7^{5.4\;14.8}_{1.1\;0.1}$	$59.4^{74.3\;107.9}_{46.7\;27.8}$
1	$67.7^{135.7\;369.1}_{28.6\;2.6}$	$77.4^{96.0\;140.6}_{61.2\;36.4}$	$2.7^{5.2\;13.8}_{1.1\;0.1}$	$56.0^{69.8\;102.2}_{44.2\;26.7}$
3	$49.4^{97.6\;258.6}_{20.4\;2.1}$	$59.3^{73.5\;107.4}_{47.0\;28.3}$	$2.0^{4.0\;10.6}_{0.9\;0.1}$	$43.8^{54.7\;79.9}_{34.8\;20.9}$
10	$25.5^{51.2\;136.0}_{10.8\;1.0}$	$36.4^{45.7\;66.6}_{28.5\;16.9}$	$1.4^{2.7\;7.1}_{0.6\;0.0}$	$28.2^{35.1\;50.7}_{22.3\;13.5}$
30	$15.2^{30.7\;81.0}_{6.2\;0.6}$	$25.2^{31.2\;45.3}_{19.9\;11.8}$	$1.0^{1.9\;5.2}_{0.4\;0.0}$	$20.8^{25.8\;37.9}_{16.4\;9.7}$
100	$11.0^{22.6\;59.8}_{4.5\;0.4}$	$19.4^{24.0\;34.8}_{15.3\;9.2}$	$0.8^{1.6\;4.2}_{0.3\;0.0}$	$16.6^{20.6\;30.1}_{13.1\;8.0}$
300	$9.2^{18.5\;50.0}_{3.8\;0.4}$	$17.9^{22.2\;31.9}_{14.1\;8.3}$	$0.8^{1.5\;4.2}_{0.3\;0.0}$	$15.5^{19.3\;28.0}_{12.2\;7.4}$
700	$8.7^{17.3\;45.3}_{3.6\;0.3}$	$17.5^{21.8\;31.8}_{13.8\;8.3}$	$0.8^{1.7\;4.3}_{0.3\;0.0}$	$15.8^{19.7\;29.3}_{12.5\;7.6}$

4.5 The Occurrence Rate of CBPs

We present the integrated occurrence rates as a function of mutual inclination distribution, binary period (HM vs LM), and coarse planet radius & period bins. Unless otherwise specified, the η values are derived using the clean candidates (e.g., SNR>12; see §4.2). For reference, we show a complete list of analysis results for conservative and all detected candidates (e.g., HMc, LMc, HMd, LMd) in Appendix E; their 50% confidence intervals typically overlap.

Table 4.4 shows the occurrence rates as a function of mutual inclination distribution for CBPs around low morphology ($P \gtrsim 5$ d) *Kepler* eclipsing binaries. Each table entry displays the 50th percentile value, with 25th and 75th percentile values as the first set of sub- and super-script, and 2.5th and 95th percentile values as the second set of sub/superscripts, which correspond to the mean, 50% and 95% confidence intervals of the η distribution, respectively. Note that the frequency distributions described here correspond to independent fits to each planet size bin (column), using the log-likelihood expression derived in Equation 4.13; as a result the occurrence rate results from the 2–4$\mathrm{R}_\oplus$, 4–10$\mathrm{R}_\oplus$, and 10–20$\mathrm{R}_\oplus$ bins do not sum up to those for the 2–20R$_\oplus$ bin. Moreover, for null detections, the 95% confidence intervals as upper limits are more meaningful than the 50th percentile values.

We find that the occurrence rate of CBPs with orbital periods $< 35P_c$ and radii between 4–10 R$_\oplus$ is $18^{+7}_{-5}\%$, if CBPs are preferentially coplanar with respect to their binary hosts. This frequency grows to $83^{+31}_{-24}\%$ if CBP mutual inclinations are isotropically distributed. Note that the super- and sub-scripts associated with the mean values refer to $\pm1\sigma$ uncertainties, which differ from the 50% and 95% confidence intervals reported in Table 4.4.

Around LM systems, the occurrence rate for Jovian-size or larger gas giants is, in general, significantly lower, with a 95% confidence upper limit of $< 4\%$ and $< 15\%$ for coplanar and isotropic δi distributions, respectively. The upper limit for sub-Neptune size CBPs is not as well constrained at $< 45\%$ in preferentially coplanar CBPs, due to the rapid drop in detection efficiency across $R \sim 4$ R$_\oplus$ threshold (see Figure 4.12). We do not report an upper limit for terrestrial-size CBPs here, as the low detection efficiency renders frequency quantification not meaningful.

Figure 4.23 illustrates η distributions of sub-Neptune, Neptune/Saturn, and Jovian+ size CBPs around LM systems for $\kappa = 700$. The upper panel shows the occurrence rate PDFs for each size bin, and bottom panel shows the corresponding "box-and-whiskers" plot, where thicker, box regions denote 50% confidence intervals and thinner lines/whiskers represent 95% confidence intervals. The dearth of $10 - 20$R$_\oplus$ CBPs relative to Neptune/Saturn size gas giants is agnostic to the underlying mutual inclination distribution, i.e., the relative abundances does not vary strongly as a function of κ.

We focus additional analysis in the LM sample in the region where most candidates are detected, in the 4–10R$_\oplus$ radius range and 1–12P_c period range. In particular, we test the hypothesis that the apparent "pile up" of CBPs near the critical stability semi-major axis is robust against observational or detection bias. Figure 4.24 shows the PDF (upper) and box-and-whiskers (lower) representation of the occurrence rate of Neptune/Saturn size CBPs in log uniform bins of $P_p/P_c \in \{1.0, 1.6, 2.7, 4.4, 7.3, 12\}$, conditioned on $\kappa = 700$, i.e., coplanar δi distribution. If there is a physical pile up, we would expect the η distribution in the

$P_p/P_c = 1 - 1.6$ bin to deviate substantially from values in the adjacent bin. While the mean η values between the 1–1.6 and 1.6–2.7 bins differ by a factor of three, the η distributions are all within 1σ from each other; this trend is observed across all κ values. Thus, the current data do not strongly support a physical pile-up of planets near a_c. However, we emphasize that not having strong evidence for a pile-up is not the same as having strong evidence against it. More detections and/or a larger target sample is crucial to robustly claim a physical origin to the observed proximity to a_c.

Finally, we compare the occurrence rates of CBPs around HM (typically $P \lesssim 5$ d) and LM (typically $P \gtrsim 5$ d) *Kepler* EBs. Figure 4.25 represents the 50% and 95% confidence intervals for 4–10$\mathrm{R}_\oplus$ CBPs within $35P_c$ as box-and-whiskers, where blue corresponds to LM and grey corresponds to HM. The 95th percentile η values for HM overlap with LM mean values when $\kappa > 1$. The large error bars in HM η values prohibit robust interpretation of the frequency of CBPs around short period binaries relative to those around longer period EBs. Expanding the target sample would help to reduce the uncertainty in HM, although achieving a large sample may be challenging, as the target sample requires mass and accurate binary orbital information to correct for large-scale binary-induced TTVs. In principle, however, one can expand the CBP target search to include a grid search in, e.g., binary mass ratio, to bypass detailed photometric modeling or time-intensive RV observations.

Furthermore, for reference, we also overplot in Figure 4.25 occurrence rate estimates from other transit surveys/detection pipelines. Armstrong et al. (2014a) (brown box-and-whiskers) searched ~ 1700 morph< 0.7 *Kepler* EBs and calculated η for various bins, the closest (4–10$\mathrm{R}_\oplus$ with $P_p < 300$ d) to our interval is plotted here. Klagyivik et al. (2017) (red, $P_b < 2.5$ d; pink, $P_b < 1$ d) estimated 50% upper limits to the CBP frequency based on non-detections in a transit search around *CoRoT* EBs. Owing to *CoRoT*'s shorter observing time span, the maximum searched period is $P_p < 50$ d around short period $P < 1$ d and $P < 2.5$ d binaries (roughly $P_p/P_c \sim 17$ and ~ 7, respectively), and their result is most comparable to that of our HM sample. In general, the occurrence rates derived here are consistent with literature estimates.

That multiple, independent CBP frequency analyses converge toward similar estimates indicate that the results, with their current uncertainties, are robust and not method-dependent. The challenge of future studies is to reduce these uncertainties, in order to extricate meaningful estimates on the frequency of terrestrial-size circumbinary worlds and determine planet distributions as a function of orbital period and mutual inclination. These endeavours necessitate a dramatically larger sample of *binaries* (i.e., thousands or tens of thousands) upon which to search CBPs; more robust modeling of binary-induced noise to increase detection sensitivity; and alternative avenues of detection with novel data sets that probe different CBP parameter space. We expand upon these ideas in Chapter 5.

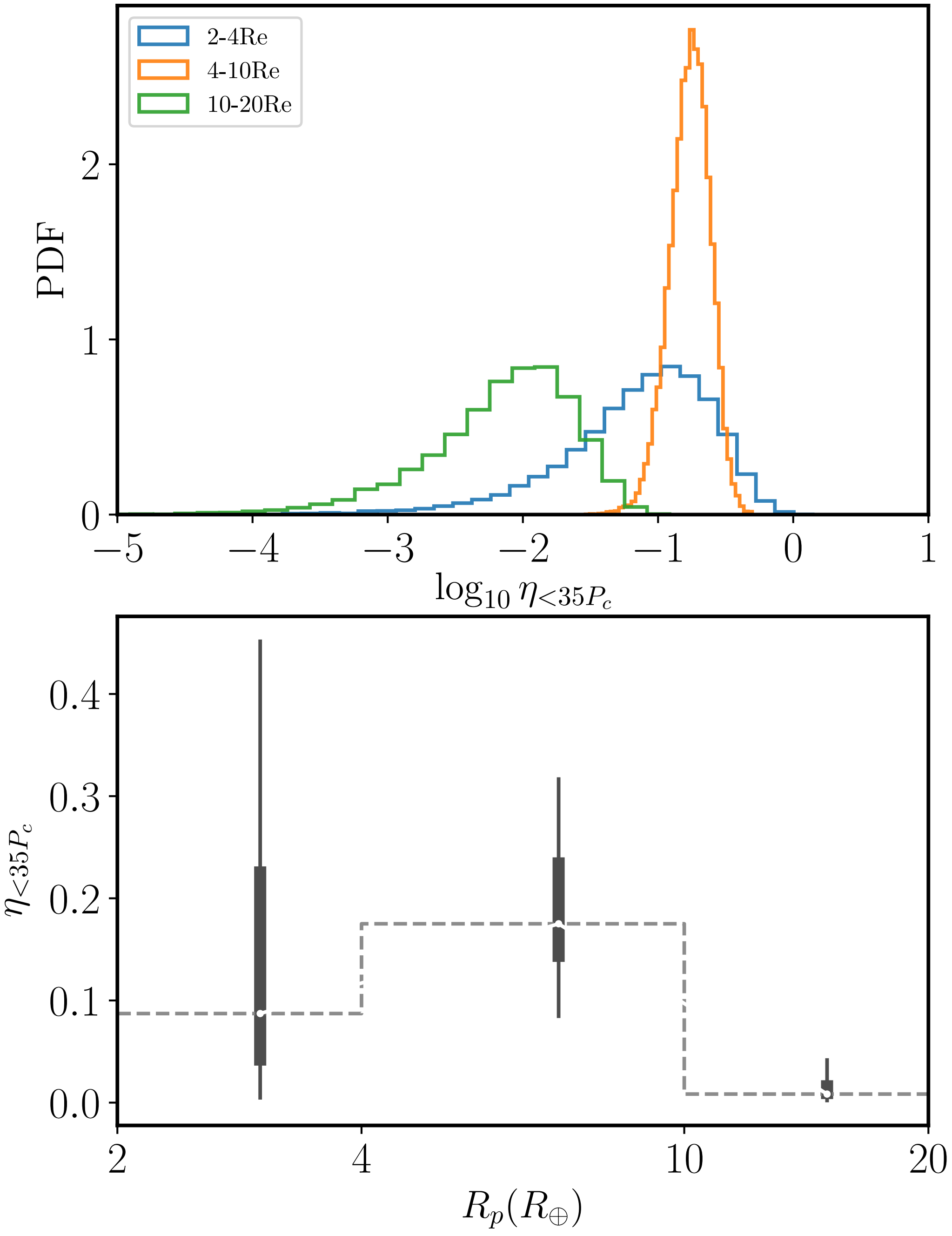

Figure 4.23 The occurrence rate of preferentially coplanar circumbinary sub-Neptunes (2–4R$_\oplus$), Neptunes/Saturns (4–10R$_\oplus$), and Jupiters (10–20R$_\oplus$) within $35P_c$ for LM binaries. Upper panel shows the η distribution while bottom panel shows 50% and 95% confidence intervals as "box-and-whiskers" values. Here, the 95% confidence upper limit for Jovian CBPs is 4%, a factor of 4 times smaller than the mean frequency of smaller gas giants.

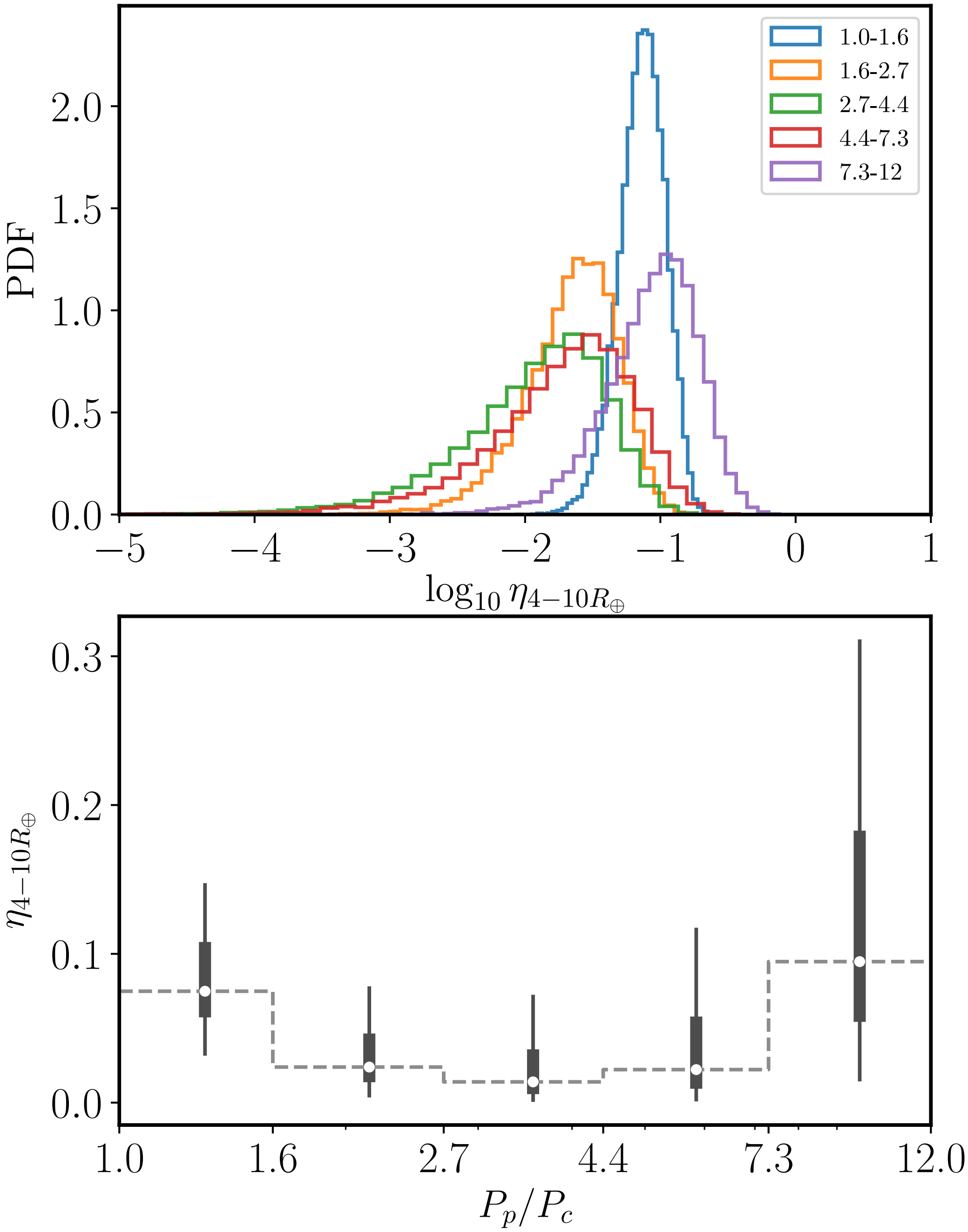

Figure 4.24 Frequency of CBPs with radius range 4–10R$_{\oplus}$ in bins of $P_p/P_c \in \{1, 1.6, 2.7, 4.4, 7.3, 12\}$, preferentially coplanar orbits around LM binaries. In the lower panel, the box and whiskers correspond to 50% and 95% confidence intervals, respectively. The data does not currently support a physical "pile-up" of planets near the critical stability period.

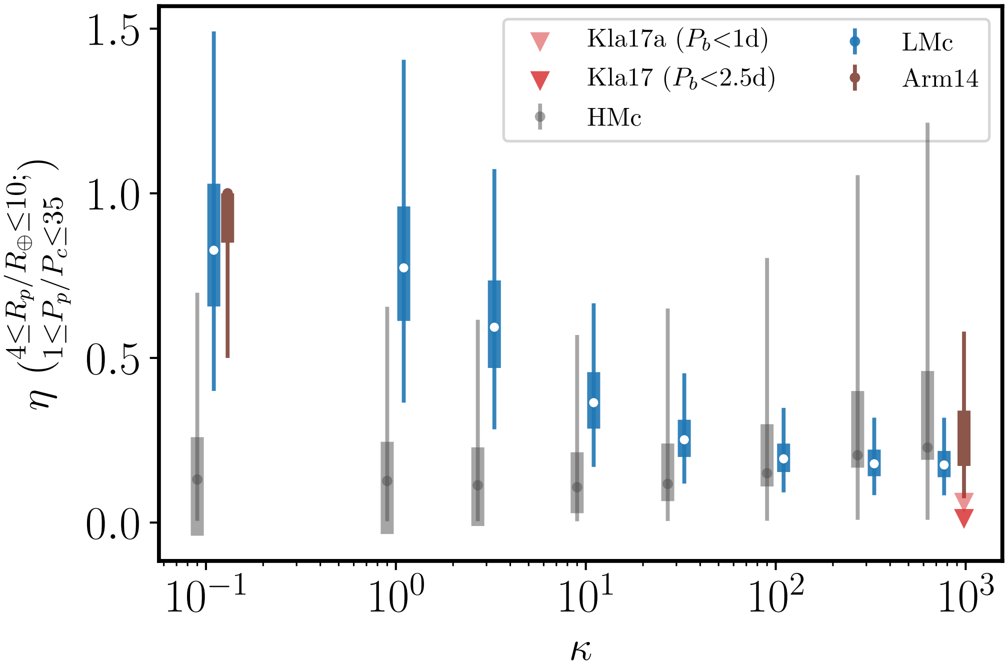

Figure 4.25 η box-and-whiskers distributions for HM (grey) vs. LM (blue) CBPs in the 4–10R$_\oplus$ range with orbital periods $< 35P_c$, as a function of κ. For reference, we overplot occurrence rates with planet size, period, and binary period bins closest to ours from literature. Armstrong et al. (2014a) values (brown) correspond to 4–10R$_\oplus$ CBPs with orbital periods $<$ 300 d, around *Kepler* LM *and* HM EBs. Using *CoRoT* data, Klagyivik et al. (2017) reported upper limits based on a binomial probability that true planets have a non-detection chance of 50%. Their $P_b < 1$ d and $P_b < 2.5$ d sample is most analogous to our HM sample, although their abundance constraints only go out to $P_p < 50$ d (corresponding roughly to $P_p/P_c \sim 17$ and ~ 7, respectively), due to *CoRoT*'s shorter $\mathcal{T}_{\rm obs}$.

Chapter 5

SUMMARY

Population-level analyses of planets orbiting binary stars have lagged behind those of their circumstellar counterparts. This thesis aims to develop a better understanding of circumbinary planet demographics by providing an independent, automated transit search and population analysis based on quantifiable detection statistics. I build toward this goal in three main efforts.

Effort one involves a Bayesian characterization of 728 *Kepler* EBs and their orbital and stellar parameters. Eclipsing binaries constitute excellent targets upon which to search for transiting CBPs, owing to their already eclipsing geometry. Because unknown binary parameters form a bottleneck in designing a sensitive transit search for CBPs, a fast and accurate method to characterize large ensembles of EBs is essential. The gold standard for the most precise and direct measurements of full system parameters requires eclipsing, double-lined spectroscopic binaries. These systems, however, are relatively rare, because they require both stellar lines to be resolved, and the observations are time-intensive. In Chapter 2, I describe a method to establish full orbital and stellar parameters of eclipsing binaries that bypasses the need for time-intensive spectroscopic observations. This technique leverages existing stellar evolutionary models against time-series, multi-band, and positional photometry to extract full system dimensions, including mass. Because photometric surveys are more efficient to operate, this technique enables mass and absolute orbital parameter estimation for large ensembles of EBs. Additionally, this effort generated 35 new systems which show evidence of eclipse timing variations, potentially due to tertiary companions and/or apsidal motion from binary tides.

Effort two involves creating an effective CBP transit detection scheme that is robust to large, binary-induced transit timing and duration variations. In Chapter 3, I introduced a novel, hybrid CBP transit detection routine which accounts for these variations, which can be of order days, in two important ways. First, it corrects for large scale variations due to binary reflex motion using a Keplerian model and binary parameters from Chapter 2 to approximate binary and CBP orbits. It subsequently uses QATS, a quasi-periodic signal detection algorithm, on the corrected light curves, to empirically treat e.g., inaccuracies arising from the Keplerian approximation and unaccounted companions. This dual approach improves CBP detection significance by greater than a factor of 2 from previous automated detection efforts.

Finally, Chapter 4 culminates in an applied CBP search on the ∼700 EBs from effort one and using the detection scheme from effort two. The target search yields 8 robust (SNR>12) candidates corresponding to confirmed CBPs, and 4 marginal candidates (SNR>8) which require additional vetting, as well as 4 multiply eclipsing binary candidates. I infer physical, population-level trends for CBPs, using the results from the automated target search and a thorough audit of detection biases to reconcile CBPs missed by the search. In particular, I find that:

1. Mutual inclination: The absolute frequency of CBPs depends on the underlying mutual inclination distribution (see also Armstrong et al., 2014a). Currently, this distribution is not robustly constrained, although some studies suggest that the *Kepler* discoveries may prefer a coplanar δi distribution (Armstrong et al., 2014a; Li et al., 2016), and Martin (2018) estimates that the spread in δi is <10° based on null detection from a RV survey. Dynamical and CBP formation studies predict that torque from the binary naturally induces an eccentric central cavity (Artymowicz & Lubow, 1994; Papaloizou et al., 2001; Thun & Kley, 2018) and inner regions of circumbinary disks to be eccentric, warped, and misaligned (Larwood & Papaloizou, 1997; Pierens et al., 2020); such misalignments around tight ($\lesssim$1 AU) binaries are observed in nature, ranging from nearly coplanar ($\delta i \lesssim 3°$; Czekala et al., 2019) to moderately misaligned

($\delta i \sim 15^\circ$ e.g., KH 15D; Herbst et al., 2010), to polar (e.g., HD 98800; Kennedy et al., 2019).

Hydrodynamical simulations of CBP formation within gasesous disks find that CBPs born in small or moderately misaligned ($\lesssim$20) disks damp toward a coplanar alignment with the binary as the disk dissipates, although this realignment may not operate for highly misaligned or polar disks (Pierens & Nelson, 2018). Additional dynamical processing due to planet-planet resonance/scattering (Sutherland & Fabrycky, 2016; Gong & Ji, 2017; Sutherland & Kratter, 2019), distant tertiary stellar companion (Muñoz & Lai, 2015; Martin et al., 2015; Hamers et al., 2016), or stellar fly-bys in birth star cluster environments (Ma et al., 2020) may excite mutual inclinations to larger values. The consequence of this is that perhaps the underlying δi distribution is not a single distribution, but bi- or multi-modal in nature. Testing this would require additional CBP discoveries and synthesizing multiple modes for detection which are less sensitive to geometric alignment, such as RV, astrometry, ETV, and direct imaging.

2. NEPTUNE/SATURN-SIZE CBP FREQUENCY: Around $P_b \gtrsim 5$ d binaries, the occurrence rate of Neptune- and Saturn-size (4–10R$_\oplus$) CBPs with $P_p < 35P_c$ ($\approx$480 d) is $18^{+7}_{-5}\%$, if planets are preferentially coplanar to their binary hosts. This frequency increases for more broad mutual inclination distributions, reaching to $83^{+31}_{-24}\%$ for isotropic δi. The values derived here provide tighter constraints than and are consistent with those from Armstrong et al. (2014a), who used a population synthesis approach to estimate CBP frequencies. Morever, the CBP frequency (in the coplanar scenario) appears broadly comparable to CSP values, ~15–20% for $R_p = 4 - 10\mathrm{R}_\oplus$ and $P_p < 400$ d (Foreman-Mackey et al., 2014; Hsu et al., 2019).

3. “PILE-UP” NEAR STABILITY REGION: The observed data do not currently support a peak in planet frequency, i.e., “pile-up” near the stability region. This analysis concludes that the observed pile-up of transiting CBPs appears indistinguishable from

detection bias (see, e.g., Martin & Triaud, 2014; Li et al., 2016; Quarles et al., 2018 for consenting and dissenting arguments). The occurrence rate density as a function of a_p has large associated error bars due to sparsity of detected and target sample size. Given the cumulative efficiency of this work, resolving a physical pile-up at the 3σ level would require a factor of $\sim$6 times more detections in the $P_p/P_c = 1.0$–1.6 bin relative to the adjacent 1.6–2.7 bin.

4. CBPs around (very) short period EBs: CBP transit probability is a complex function of binary inclination (with respect to the observer) and mutual inclination (with respect to binary orbit), as well as other binary and planet parameters. The allowable range of binary inclinations are larger for EBs with smaller orbital separations to still satisfy the eclipsing condition. Consequently, CBP transit probability is maximized at larger mutual inclination values for $P \lesssim 5$ d EBs, which may take on larger i_b values. In other words, short period EBs are the best targets to search for moderately misaligned CBPs (see also, e.g., Martin & Triaud, 2014). There are strong theoretical reasons to expect the population of CBPs around short period binaries to be misaligned. Dynamical studies predict that the Kozai-Lidov + tidal circularization mechanism, which hardens inner binaries with tertiary stellar companions, also destabilizes planets lying between the inner and outer stellar orbits. CBPs that survive this process typically have orbits that are further out from and misaligned relative to inner binary (Muñoz & Lai, 2015; Martin et al., 2015; Hamers et al., 2016). Moreover, in isolated binaries, numerical simulations show that pre-MS stellar and tidal co-evolution can enlarge and shrink the binary orbit on 1 - 100 Myr timescales, which cause the critical semi-major axis to evolve. The expansion in a_c removes CBPs initially located near it. This scenario may operate as an alternative or in parallel to the KL+tides mechanism. The W19a sample only contains $\sim$100 short period/high morphology EBs, due to poor recovery of stellar mass and radius using only Keplerian photodynamic modeling. Consequently, the small sample size is insufficient to place tight constraints

on CBP frequency around short period binaries. An ad-hoc solution may be to include all non-eccentric short period *Kepler* EBs and bypass detailed mass modeling by adding binary mass ratio Q as a third search dimension, after CBP period and size.

5. CB Gas Giant Frequency: Around $P_b \gtrsim 5$ d EBs, the frequency of Jovian-size or larger gas giants CBPs is $< 4\%$ and $< 15\%$ for coplanar and isotropic δi distributions, respectively. If the mutual inclination distribution is not a strong function of planet mass, then $> 10R_\oplus$ CBPs is a factor of ∼4 times lower than for 4–$10R_\oplus$ CBPs, for all δi distributions. This result is consistent with the work of Pierens & Nelson (2008), which predict that Saturn-mass CBPs are more common than Jovian-mass CBPs. In their hydrodynamic simulations of CBPs embedded in circumbinary disks, they observed that that Jovian mass planets are more likely than smaller gas giants to enter into a destabilising resonance with the binary, and become ejected. The fall-off in Jovian-size planet frequency is also observed in CS counterparts, which have a ∼10% occurrence rate (Mayor et al., 2011; Foreman-Mackey et al., 2014; Hsu et al., 2019). For the occurrence rates of CB Jupiters to be comparable to CP Neptune/Saturns, the former must be preferentially isotropically distributed while the latter, coplanar, invoking a sharp dichotomy not predicted in current formation theories. Moreover, Martin et al. (2019) recently conducted a RV survey to search for Jovian-mass companions to single-lined EBs, and found a frequency upper limit of $< 10\%$ for $P_p < 500$ d, reinforcing that Jovian-size gas giants are less common than Neptune/Saturn-size CBPs.

6. Earth-size CBP: Finally, the search for terrestrial-size CBPs continues. Despite the improved detection significance compared to previous automated CBP detection efforts, terrestrial-size CBPs were not detectable in the current data set. The sensitivity to CB Earth-size planets is severely hindered by the combination of host stars skewing slightly earlier-type and increased correlated noise associated with binarity. If future EB target catalogues have similar properties to *Kepler* EBs, and terrestrial-size CBPs are as abundant as Neptune- and Saturn-size ones, then this pipeline would require

an expanded target sample size of ∼35,000 EBs to secure one detection. Future CBP transit search pipelines should focus on fast, flexible noise modeling in binary time-series data and assembling a large (∼1000s) target sample of EBs with solar-type primary components.

Based on these results, it is abundantly clear that increasing the sample size of binary targets and additional avenues for CBP detection are needed to place meaningful demographic constraints. Increasing the sample size of CBP detections hinges upon dramatically increasing the sample size of binary targets, not simply improving the detection algorithm. Increasing the number of detection modalities would not only expand the size of target catalogues, but also sample different planetary parameter space, and thus yield tighter constraints on, e.g., mutual inclination distributions.

The upcoming PLATO mission, which is slated to launch in 2026, promises ultra-high precision, high cadence, uninterrupted photometric monitoring of $V \leq 11 - 13$ mag stars for a baseline duration of at least 2 years[1]. The EB modeling and CBP detection technique described here may be applicable to efficiently characterize MS eclipsing binaries monitored by PLATO and search for transiting CBPs around them.

The immediate successors to *Kepler*, K2 and TESS, have relatively short observing baselines (typically ∼30 d) and poorer photometric precision, which hinder CBP transit detections using quasi-periodic, multi-transit approaches. The two CBPs discovered – by eye – using K2 and TESS data, KOI-3152 (Welsh et al., 2020, Orosz et al., in prep) and TOI-1338 (Kostov et al., 2020) both fall on multiple observing sectors resulting in an effective baseline ∼200 d. Rather than searching multiple transits across either the primary or secondary stellar components, an alternative approach is to exploit consecutive transits across *both* primary and secondary stars. In this “1-2 punch” scenario (Kostov et al., in press), the multiplicity of transits derives from a single conjunction of the planet and host binary. The advantage of this technique is that detection occurs on the binary orbit timescale. However, such a

---

[1] PLATO Definition Study Report (Red Book): `https://sci.esa.int/web/plato/-/59252-plato-definition-study-report-red-book`

detection method strongly biases *against* non-equal mass binaries, and results in higher false alarm and less robust planet period estimates, although K2/TESS targets are more amenable to follow-up observations. Nonetheless, the "1-2 punch" is a promising method to enable statistical CBP transit searches on K2 and TESS eclipsing binaries.

An additional avenue for CBP detection is from analyzing EBs with eclipse timing variations (Sybilski et al., 2010; Schwarz et al., 2011), which encode dynamical information about the perturbing third body. The advantage of ETVs is that CBPs do not need to be geometrically aligned relative to the observer, thus expanding discovery potential. However, non-degenerate, reliable solutions (e.g., mass and mutual inclination of third body) to ETV signals require an observing campaign covering at least 2 orbital periods of the outer third body and resolving timing variations of both primary and secondary eclipses (Borkovits et al., 2015), which biases towards binary stars with similar temperatures. Zhang & Fabrycky (2019) recently showed that polar CBPs can be differentiated from coplanar configurations, based on simultaneous analysis of primary and secondary eclipse timings, although degeneracies arise for moderately misaligned ($\sim 15^\circ$) CBPs. Borkovits et al. (2016) and Hajdu et al. (2017) conducted comprehensive ETV analyses on eclipsing binaries in *Kepler* and *CoRoT*, respectively, and found the bulk of third body perturbers to be brown dwarf or stellar mass.

Another way to detect misaligned CBPs is to look for transits around non-eclipsing binaries. Although the transit probability is low for individual systems, and consecutive transits more rare, the majority of binaries are non-eclipsing (Martin & Triaud, 2014). Consequently, the cumulative transit probability for misaligned CBPs around non-eclipsing binaries is significant, if CBPs are not preferentially coplanar. Given that RVs are time-intensive and ETVs due to CBPs may not be sufficiently resolved even with *Kepler* photometric precision[2] (Sybilski et al., 2010; Muñoz & Lai, 2015), searching for transits around non-eclipsing/inclined binaries may be a complementary method to statistically constrain misaligned CBPs, similar to the statistical approach taken by Foreman-Mackey et al. (2016) to estimate long period

---

[2] ETV amplitude is of order 0.1-1 s for 1 AU Jovian mass CBP around a 5 d EB (Muñoz & Lai, 2015), and typical detectable timing amplitude for *Kepler* targets (13-14 mag) is 2-3 s (Sybilski et al., 2010).

Kepler transiting CSPs that only exhibit single transits. A natural reservoir to establish such a binary target sample is to select $P_{\mathrm{rot}} < 10$ d rapid rotator stars from photometric surveys, which may likely be tidally-synchronized, non-eclipsing short-period binaries (Angus et al., 2018; Simonian et al., 2019).

Finally, future space-based, coronagraphic, direct imaging missions such as LUVOIR[3] (Bolcar et al., 2017) will have 10^{-10} contrast capability to detect habitable zone, exo-Earth candidates. The focus of these study concepts has been on the exo-Earth yield around nearby, single FGK stellar systems (Stark et al., 2019). Given that the multiplicity frequency of solar-type stars is $\sim 50\%$ (Duchêne & Kraus, 2013; Moe & Di Stefano, 2017), direct imaging surveys of nearby stellar systems may be an invaluable way to probe circumbinary planet statistics and potentially detect habitable zone, Earth-size CBPs.

In particular, unresolved tight binaries are ideal coronagraphic targets, as they are effectively treated as single sources by wavefront sensors. The Search for Planets Orbiting Two Stars (SPOTS; Asensio-Torres et al., 2018) survey recently demonstrated the technological feasibility of directly imaging CBPs around young, tight binaries from ground-based facilities with adaptive optics. For LUVOIR, a solar twin binary is effectively unresolved at 30 pc when $P_b < 30$ d and $P_b < 80$ d, for the 15m and 8m concepts corresponding to LUVOIR-A and -B, respectively. The multiplicity frequency of MS companions to solar type primaries with $P < 80$ d is small but non-negligible at 5% (Moe & Di Stefano, 2017), yielding ~100 potential targets based on the nominal target catalogue (5449 sources) for exo-Earth yield calculations (Stark et al., 2014). With LUVOIR's $\leq 10^{-10}$ contrast, $1\mathrm{R}_{\oplus}$ CBPs are detectable at maximum elongation with $a \leq 1.36$ AU, within the inner and outer working angles of the coronagraph and within the HZ of circular binaries with solar type components. The potential to directly image Earth-size CBPs is an exciting opportunity to observationally constrain the conditions for habitability and quantify the distribution of habitable worlds in circumbinary environments.

---

[3] LUVOIR Final Report: https://asd.gsfc.nasa.gov/luvoir/reports/.

Appendix A

SINGLE TRANSIT PER STELLAR CONJUNCTION CRITERION

As discussed in §3.4 and §3.4.3, the QATS-EB algorithm assumes only a single planetary transit across one of the stellar components will occur at each passage of the planet across the binary. We refer to this as the "single-transit-per-stellar-conjunction" – or the abbreviated "single-transit" – criterion. For some binary and planet configurations, multiple transits across the same star can occur as the planet crosses the line-of-sight between observer and binary component (Deeg et al., 1998).

In this appendix, we estimate the fraction of time that this single-transit criterion is met, in the approximation that both the binary and planet are on circular, edge-on orbits. Here, we approximate the planet's motion as linear, as its orbital frequency is at least ∼three times slower than that of the binary, for stability (Holman & Wiegert, 1999). Figure A.1 shows the sky-projected orbital position as a function of time for one of the binary components and the planet (see also Figure 1 of Deeg et al., 1998). For only one transit to occur, the planet's path must only intersect the sky position of each binary star once.

To translate this constraint into physical parameters requires comparing the orbital speed of the planet, v_{p}, to the orbital speed of each binary star, $v_{1,2}$. We define the ratio of maximal velocities between the planet and one of the stellar components as

$$\alpha_{1,2} = \left(\frac{a_{\mathrm{p}}}{P_{\mathrm{p}}}\right)\left(\frac{P_{\mathrm{b}}}{a_{1,2}}\right) \tag{A.1}$$

This α value must be sufficiently large, i.e., steep as a function of binary orbital phase, so that it only intersects the binary star once.

In Figure A.1, we show three examples of the relative planetary speed α (here, we omit specification of primary or secondary star and thus drop the subscripts 1 and 2) . For $\alpha = 1$,

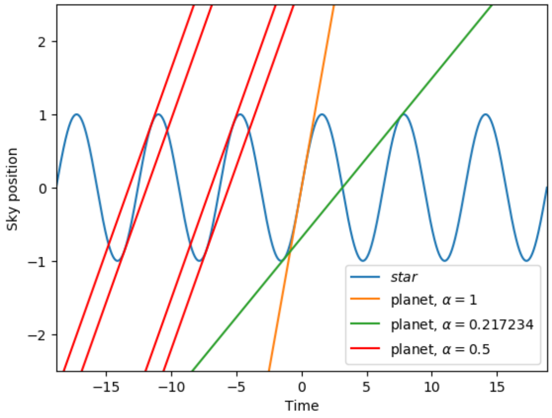

Figure A.1 Sky position versus time of one component of the binary star (blue) and planets with various speeds. The x-axis has units in which the binary orbital period is 2π, while the y-axis is in units of the amplitude of the binary star's orbit. The speed of the planet's orbit, α, is in units of the speed of the binary star's orbit.

the planet's speed matches the maximum speed of the binary star, and thus the planet will only cross the star's path once at any orbital phase. For $\alpha = 0.217234$, the planet is moving slowly enough that it will always intersect the star's position three times as it crosses the binary. For intermediate values of α there will be either one or three transits as the star crosses the binary. An example is shown on the left with $\alpha = 1/2$ for which there are three transits in between the closely spaced phases, and one transit elsewhere.

We now consider the fraction of binary phases that satisfy the single-transit criterion for *both* stellar components of the binary. Even if the velocity constraint $v_\mathrm{p} \geq v_{1,2}$ is violated, the QATS-EB algorithm may still apply, as the assumption of single transits is still valid at certain ranges in binary phase. Figure A.2 shows the fraction of binary phases that meet the single-transit criterion for both stars. From Equation A.1 and defining $Q = M_2/M_1$, we

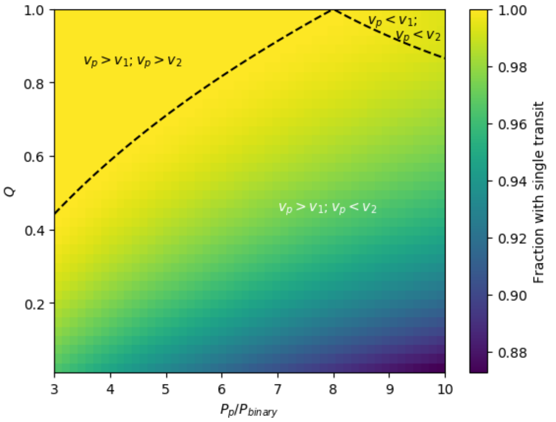

Figure A.2 Fraction of phases for either star, $(\phi(m_1)+\phi(m_2))/2$, at which a transiting planet will have a single transit for both stars. The range of binary mass-ratio, Q, and period ratio, $P_p/P_{\rm binary}$, for which the planet speed exceeds the stellar speed assuming circular, edge-on orbits is indicated with the black dashed lines.

derive

$$\alpha_1 = \frac{1+Q}{Q}\left(\frac{P_{\rm p}}{P_{\rm b}}\right)^{-1/3} \tag{A.2}$$

$$\alpha_2 = (1+Q)\left(\frac{P_{\rm p}}{P_{\rm b}}\right)^{-1/3}, \tag{A.3}$$

This implies, as Figure A.1 illustrates, that one transit per stellar conjunction occurs at all phases for $\alpha_1, \alpha_2 > 1$. When $\alpha_1, \alpha_2 < \alpha_{\rm crit}$, where $\alpha_{\rm crit} = 0.217234$, then there are 3 or more transits. For $\alpha_{\rm crit} < \alpha_1, \alpha_2 < 1$, the fraction of binary phase (time) during which there is one transit is given by:

$$\phi_{\rm b}(\alpha) = \begin{cases} 0 & \alpha \leq \alpha_{\rm crit} \\ 1 - \frac{1}{\pi}\left(\frac{\sqrt{1-\alpha^2}}{\alpha} - \cos^{-1}(\alpha)\right) & \alpha_{\rm crit} < \alpha \leq 1 \\ 1 & \alpha > 1 \end{cases} \tag{A.4}$$

The function $(\phi_{\rm b}(\alpha_1) + \phi_{\rm b}(\alpha_2))/2$ is plotted in Figure A.2. Thus, across a wide swath of parameter space in Q and $P_{\rm p}/P_{\rm b}$, the single-transit-per-stellar-conjunction criterion is satisfied for most eclipsing binary phases, under the assumption of circular orbits for the binary and the planet.

Appendix B

CBP QATS-EB CANDIDATE DETECTION & DIAGNOSTIC PLOTS

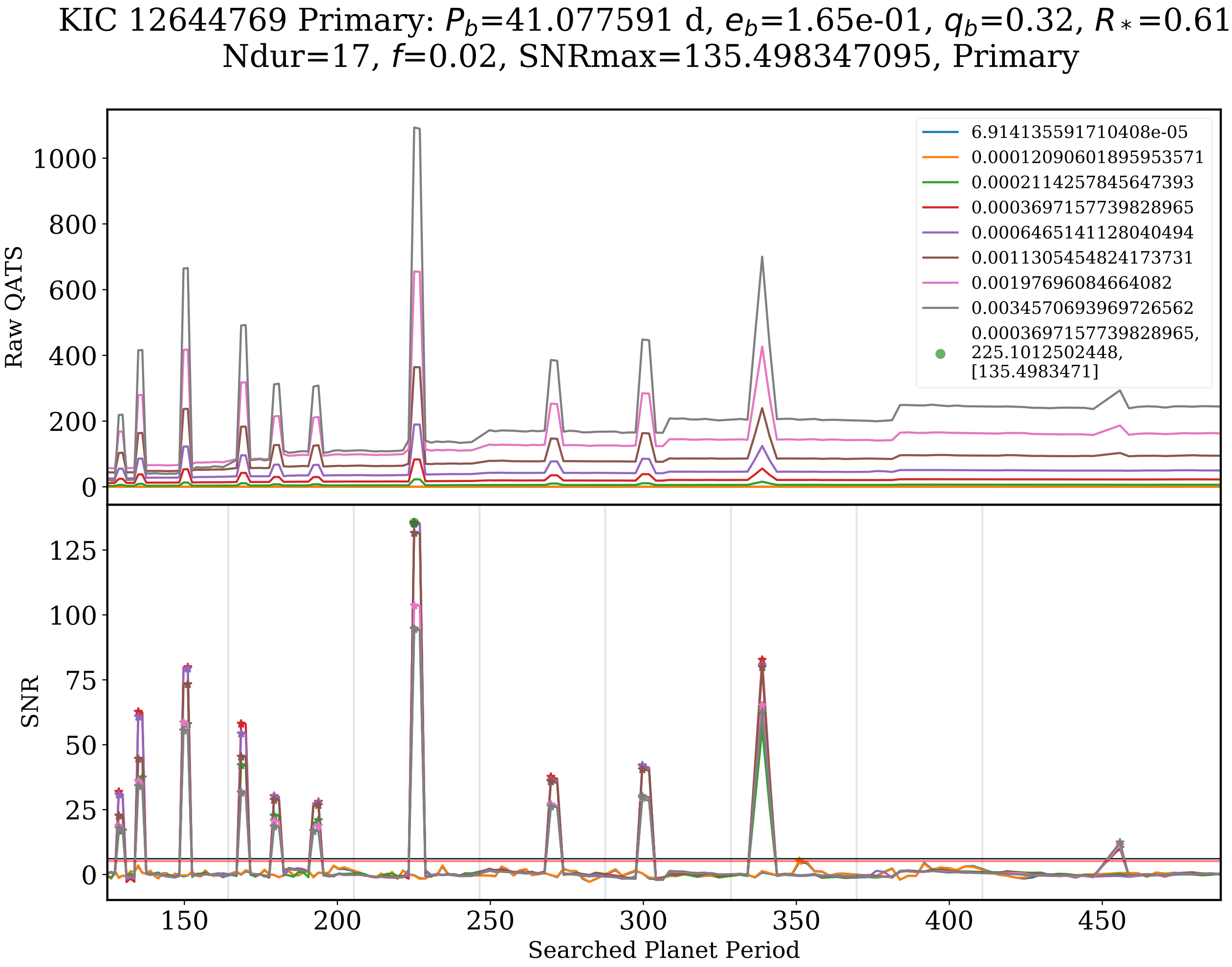

Figure B.1 QATS-EB detection and diagnostic plots for KIC 12644769, in the same format as Figure 4.5.

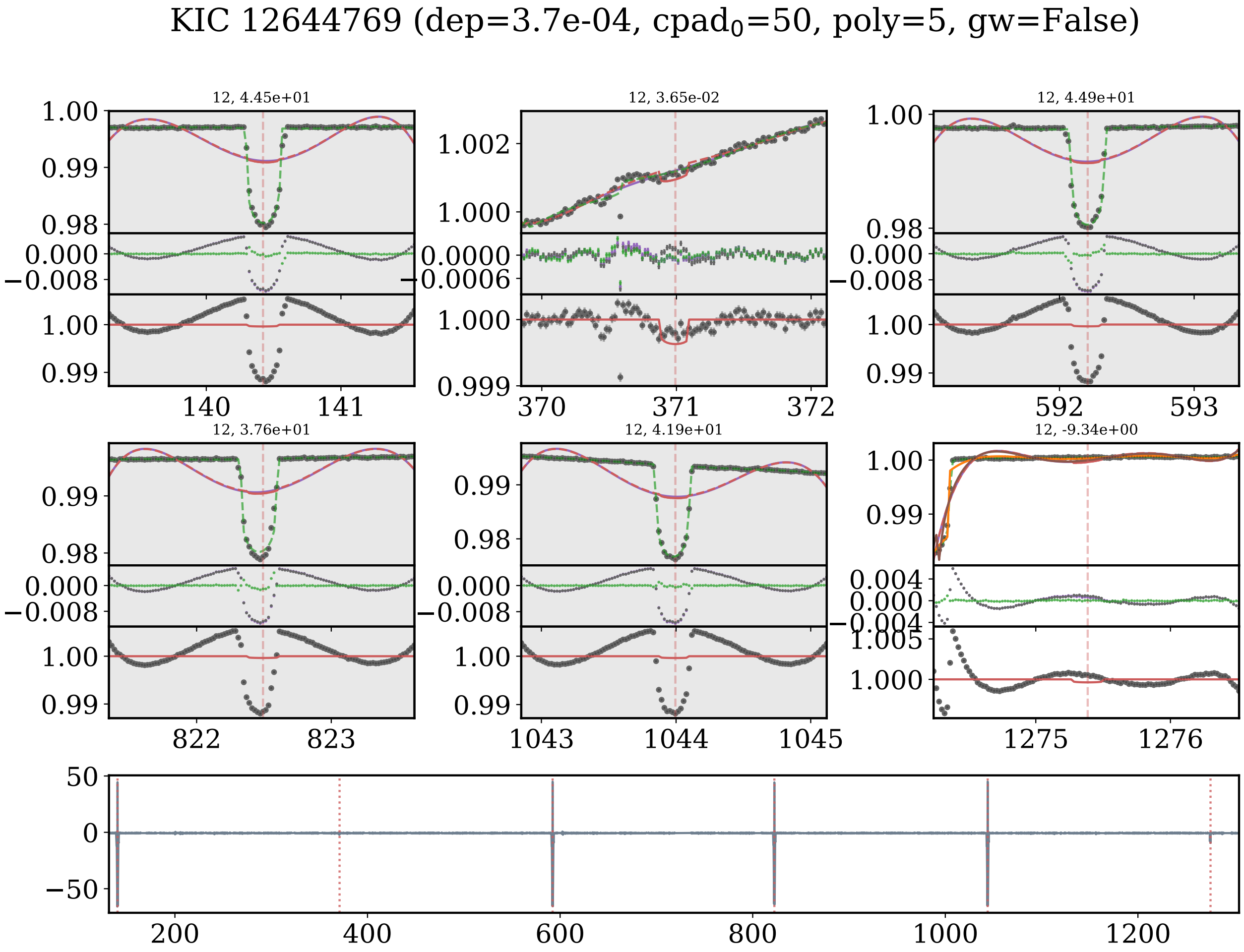

Figure B.2 QATS-EB detection and diagnostic plots for KIC 12644769, in the same format as Figure 4.5.

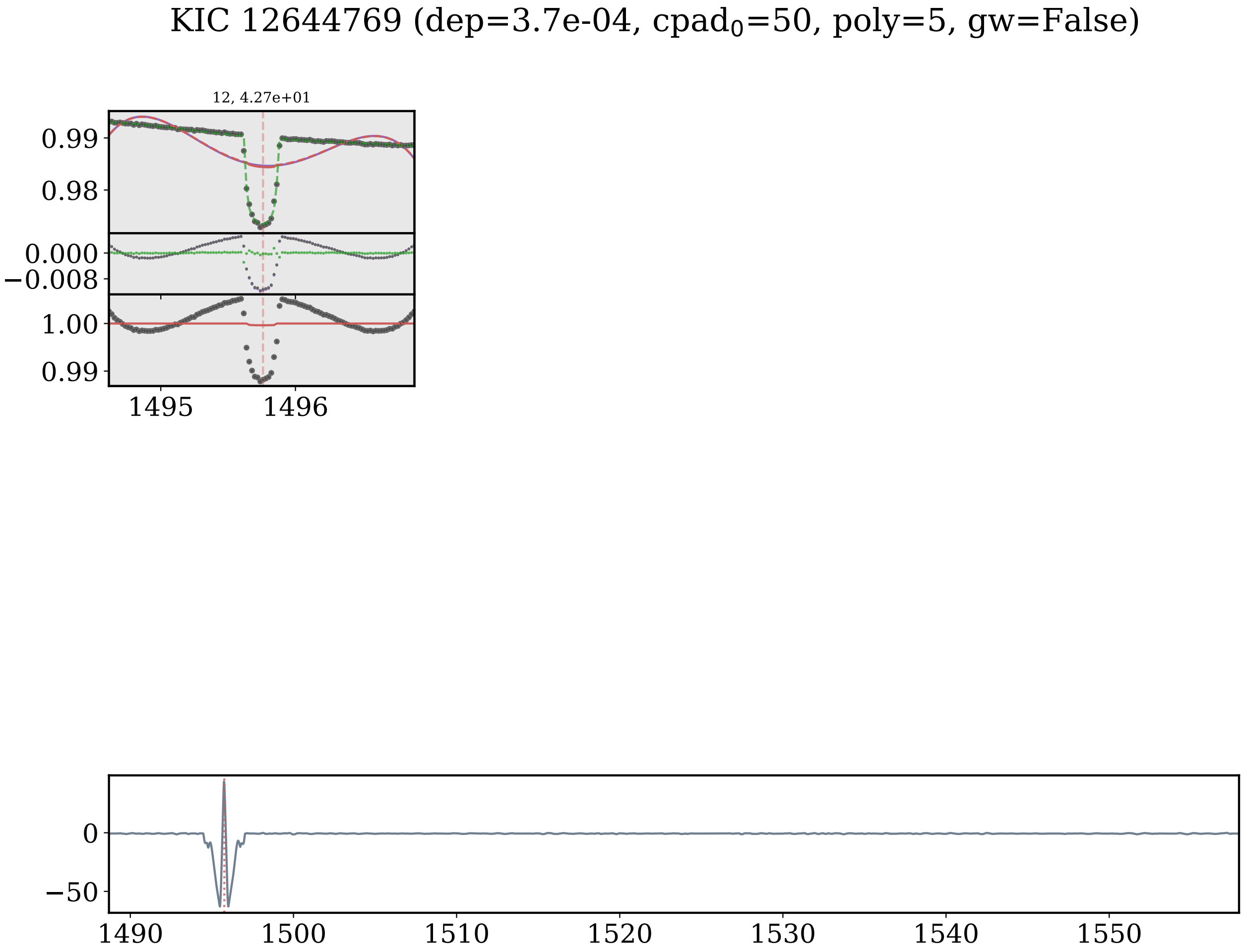

Figure B.3 QATS-EB detection and diagnostic plots for KIC 12644769, in the same format as Figure 4.5.

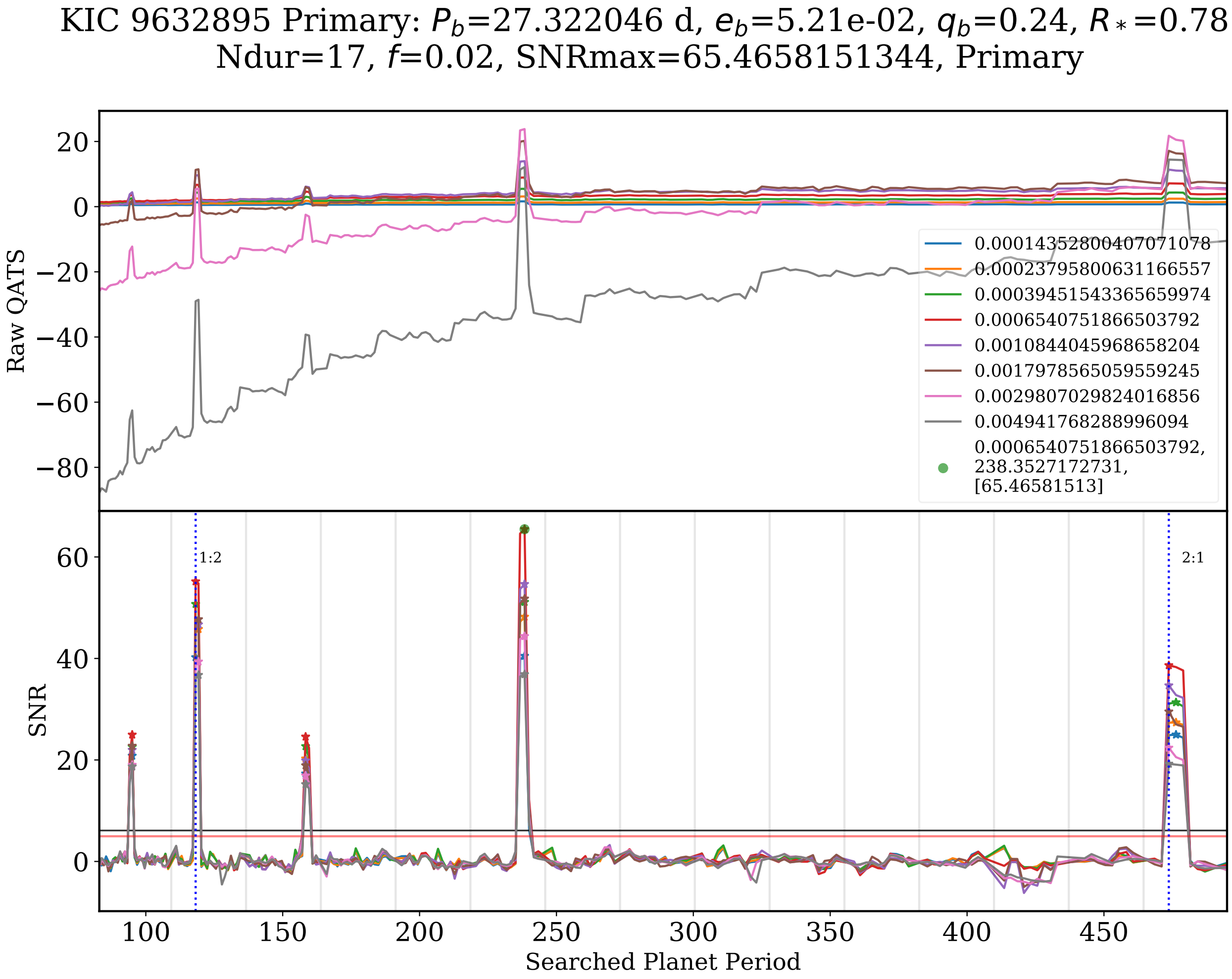

Figure B.4 QATS-EB detection and diagnostic plots for KIC 9632895, in the same format as Figure 4.5.

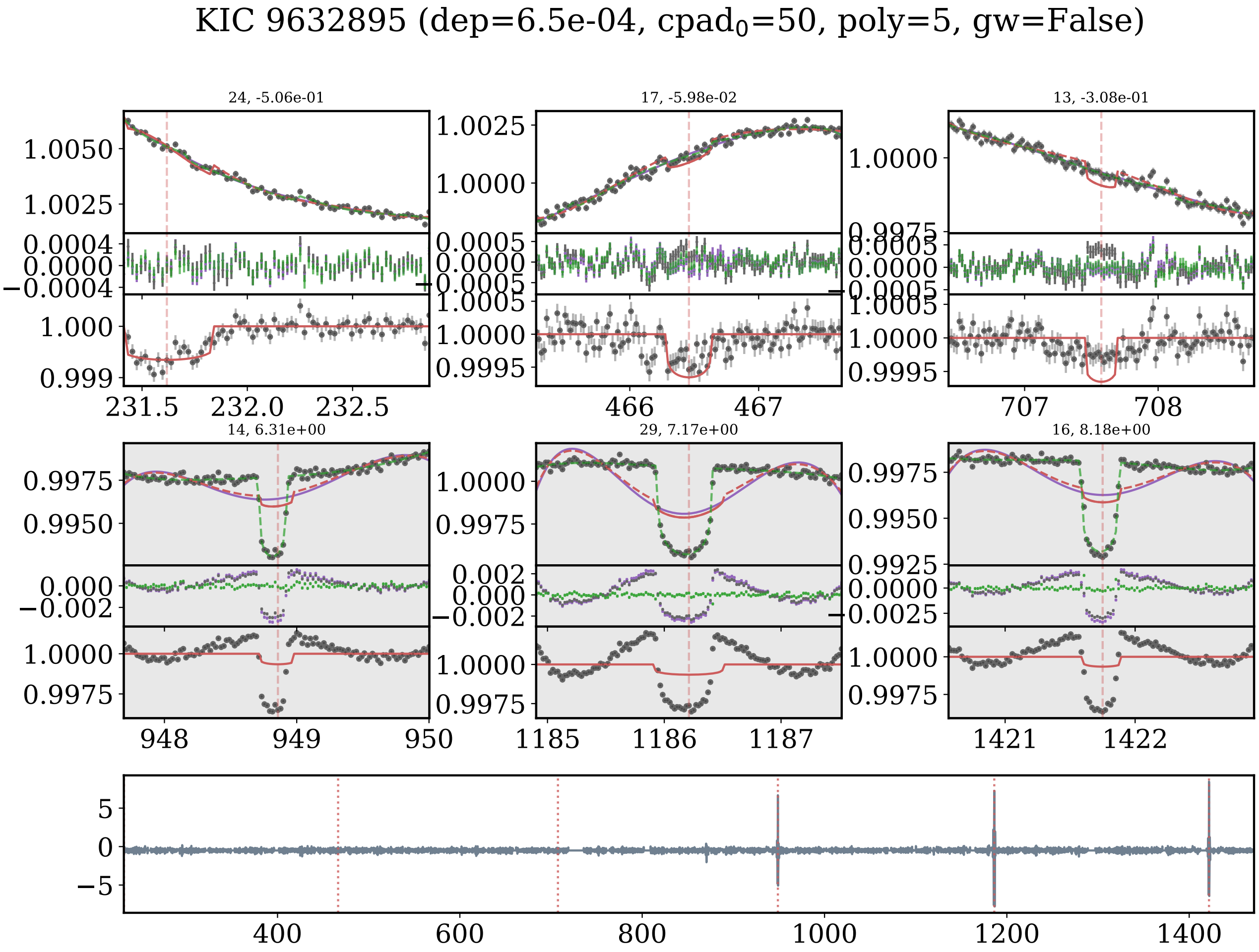

Figure B.5 QATS-EB detection and diagnostic plots for KIC 9632895, in the same format as Figure 4.5.

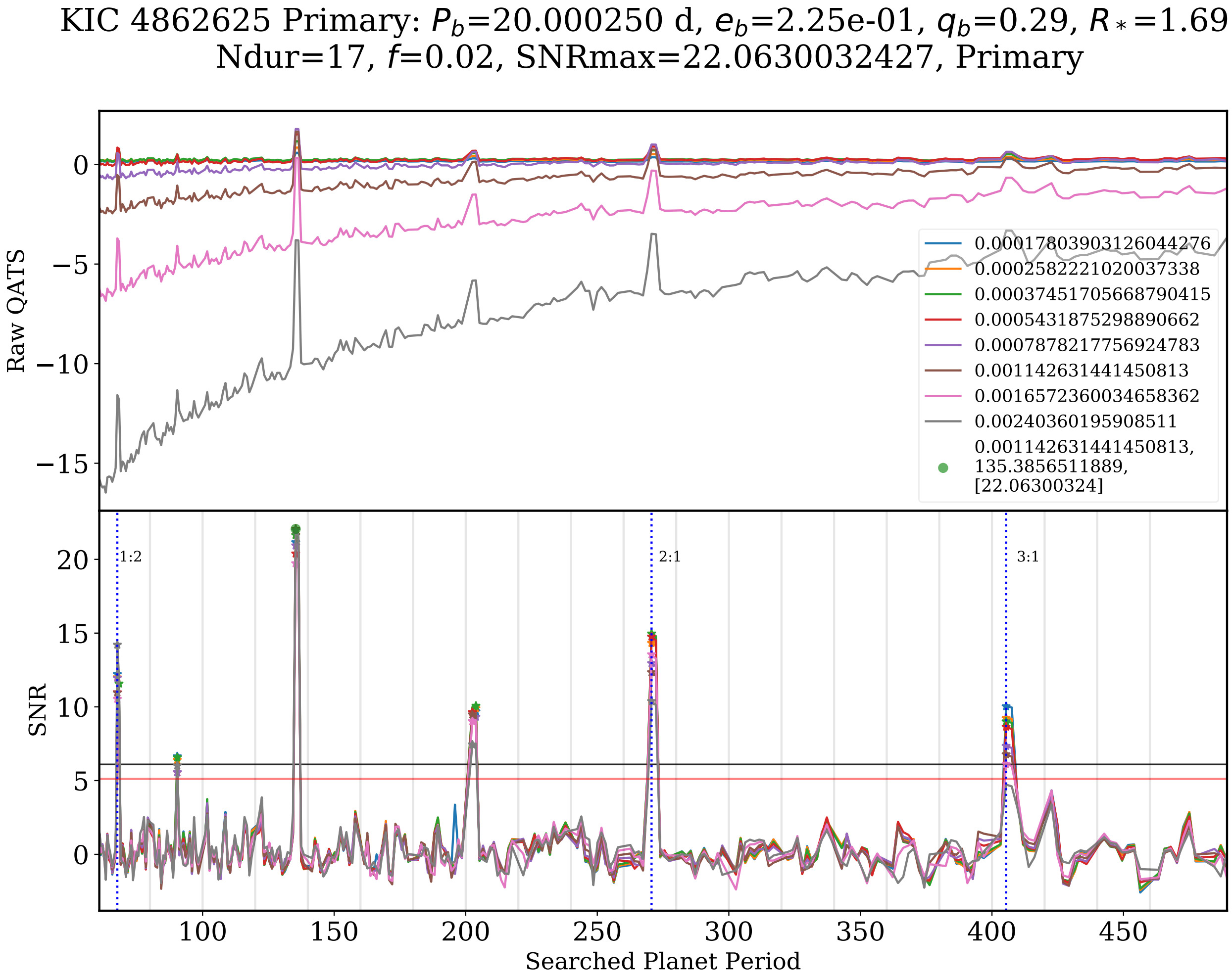

Figure B.6 QATS-EB detection and diagnostic plots for KIC 4862625, in the same format as Figure 4.5.

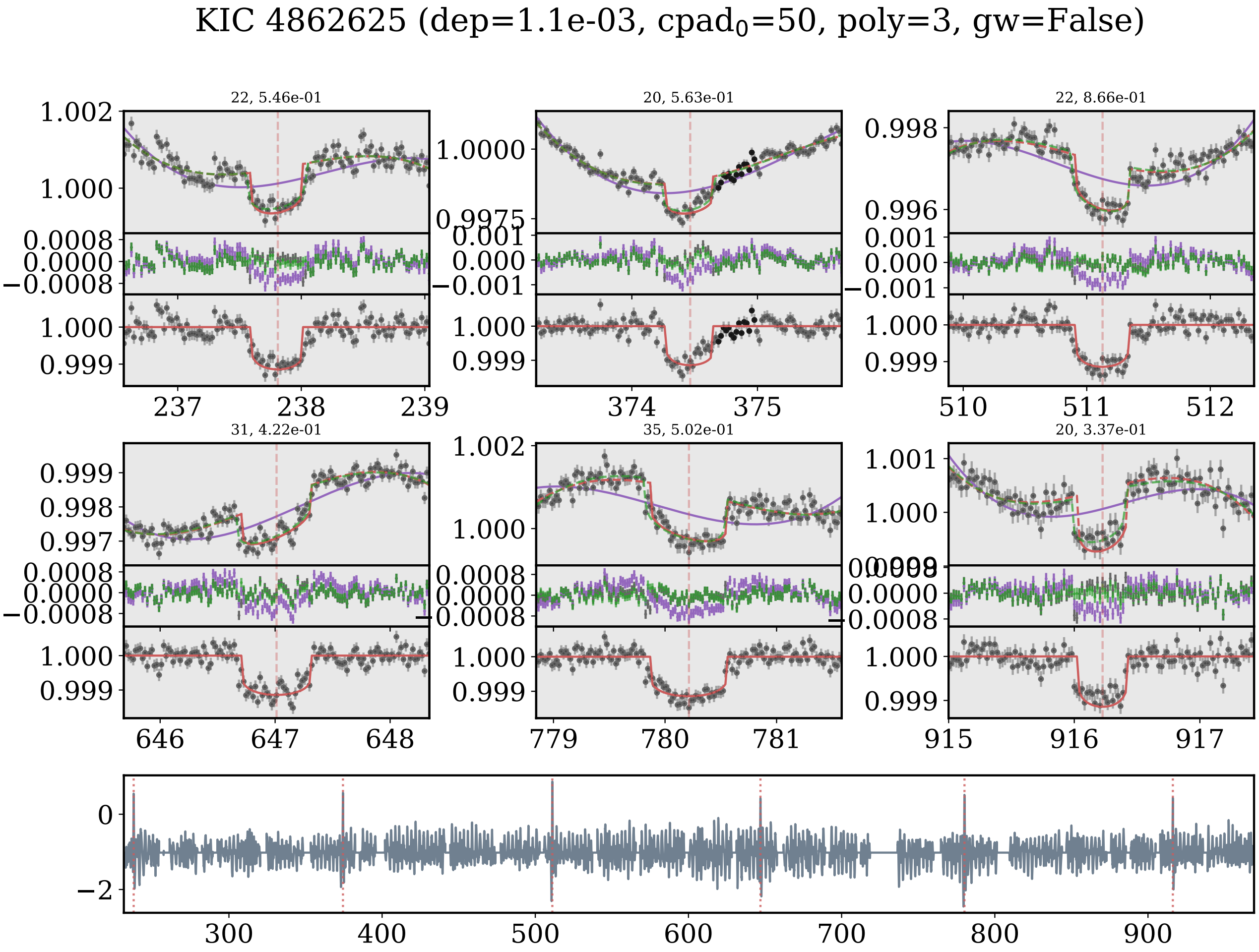

Figure B.7 QATS-EB detection and diagnostic plots for KIC 4862625, in the same format as Figure 4.5.

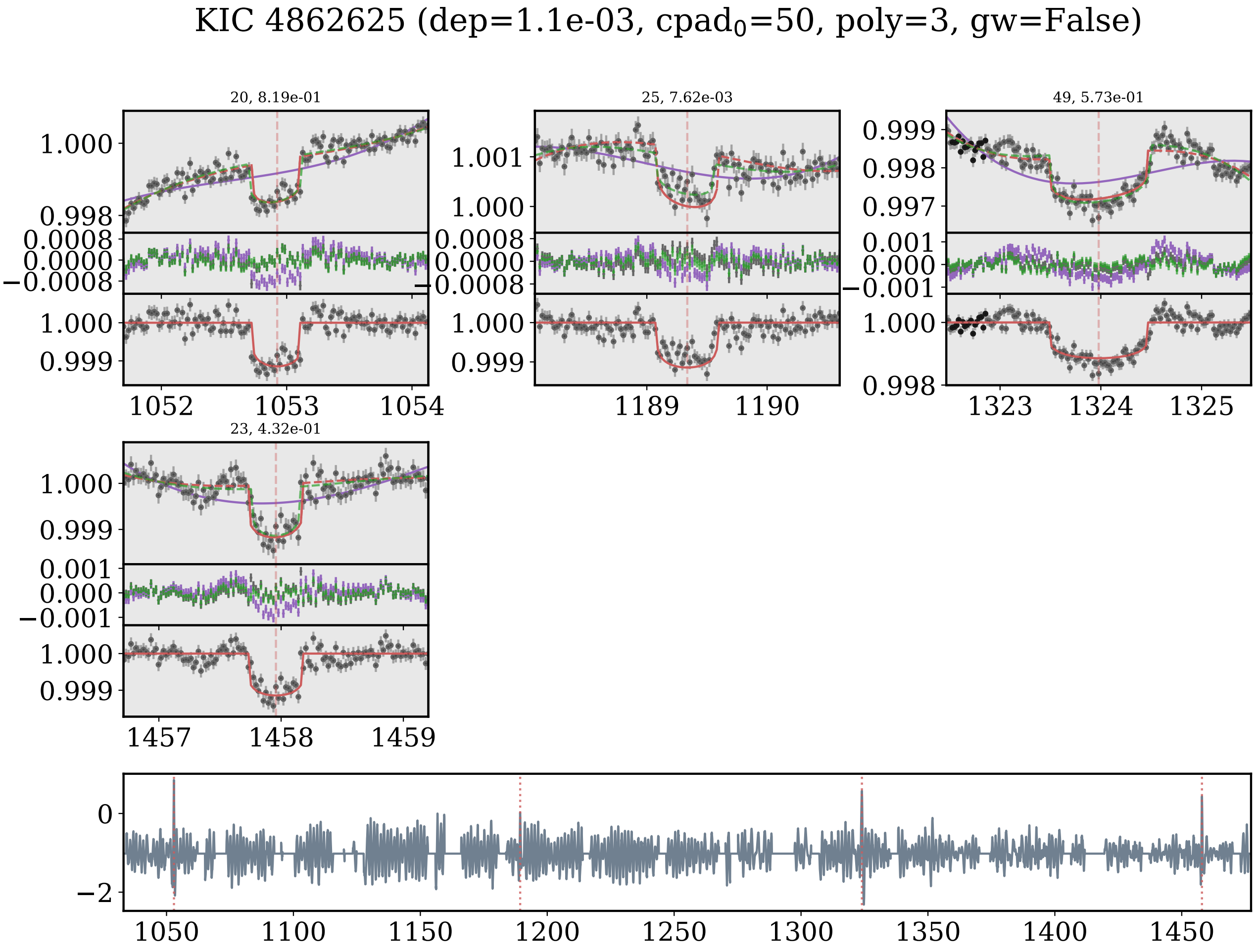

KIC 4862625 (dep=1.1e-03, cpad_0=50, poly=3, gw=False)

20, 8.19e-01

25, 7.62e-03

49, 5.73e-01

23, 4.32e-01

Figure B.8 QATS-EB detection and diagnostic plots for KIC 4862625, in the same format as Figure 4.5.

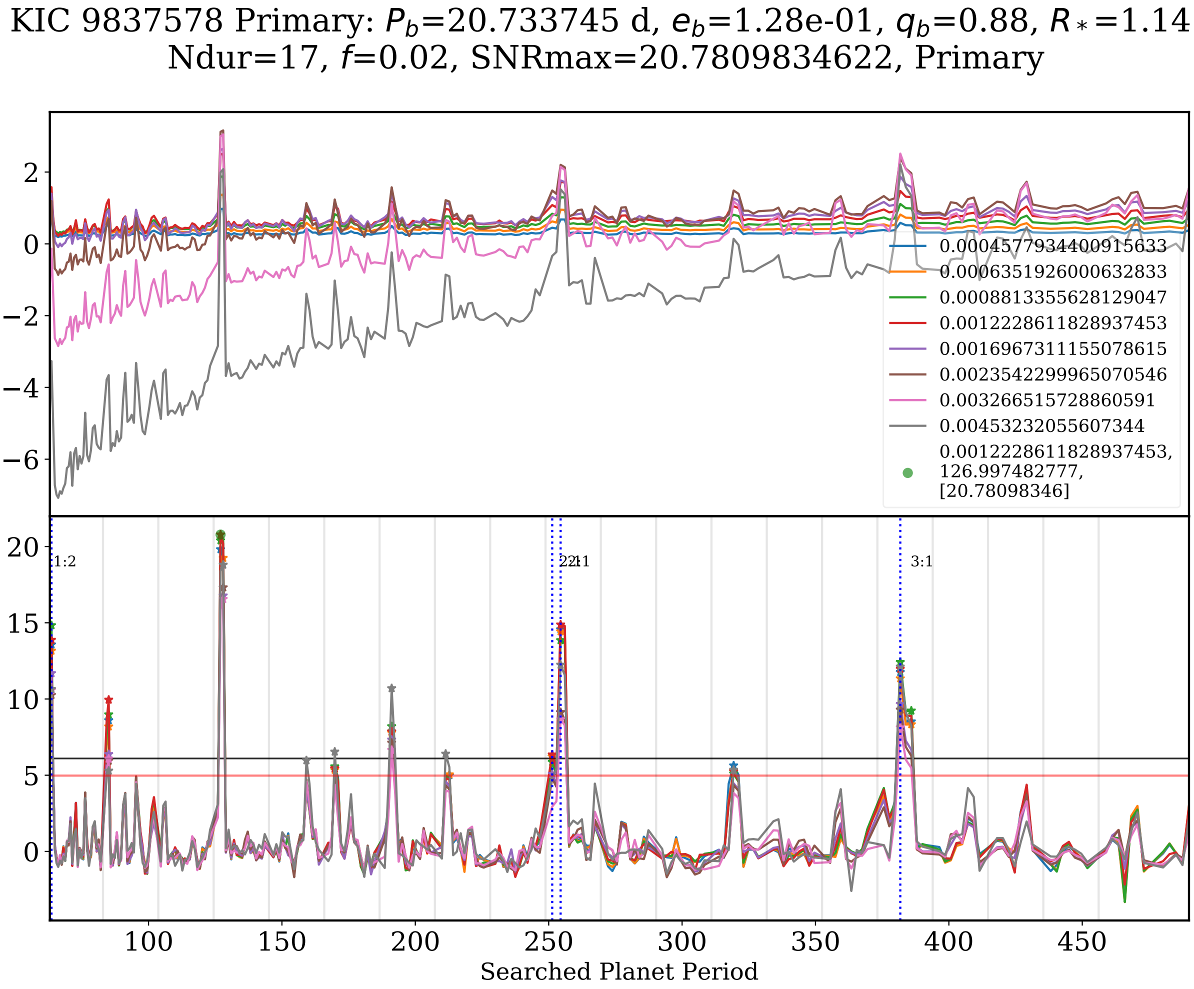

Figure B.9 QATS-EB detection and diagnostic plots for KIC 9837578, in the same format as Figure 4.5.

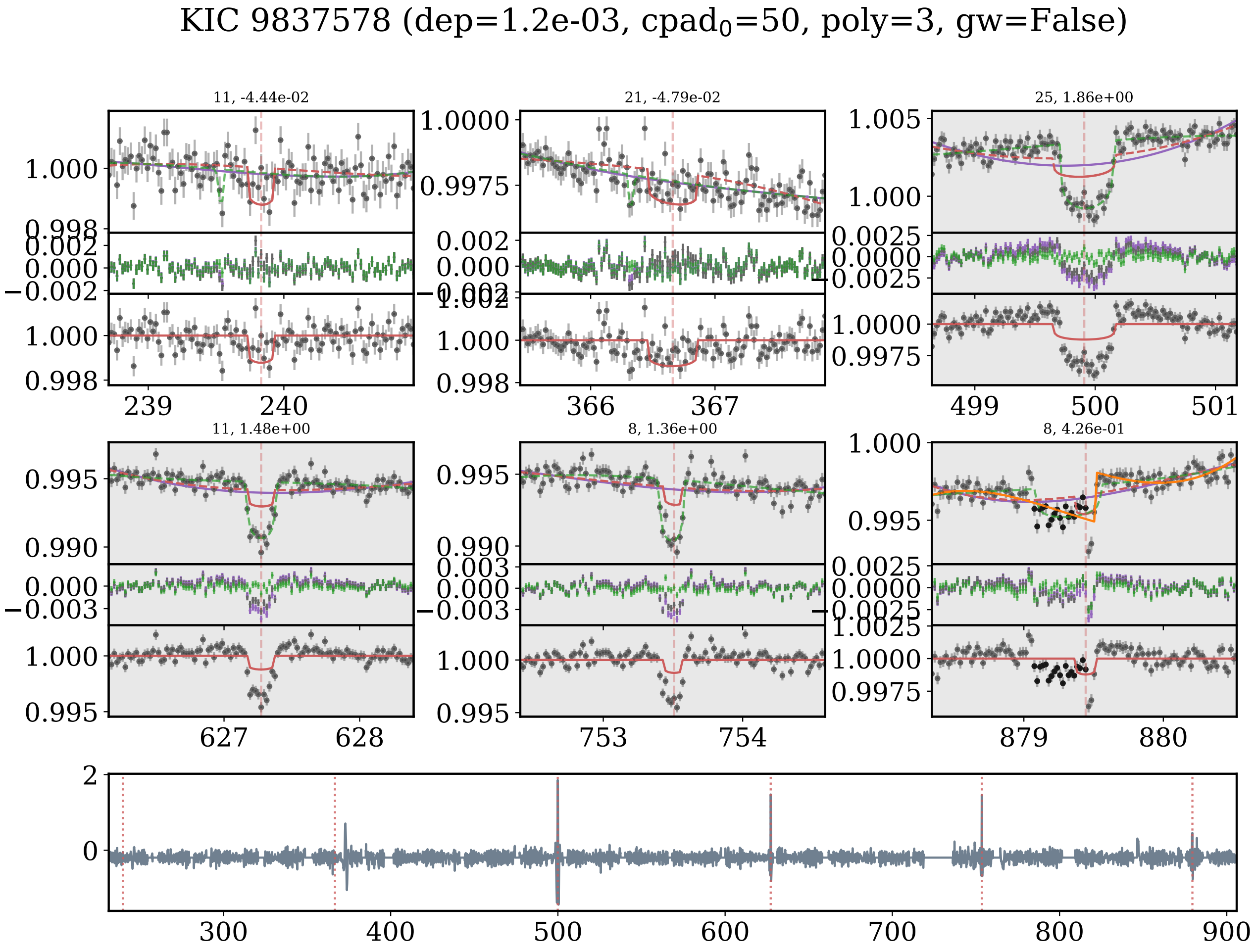

Figure B.10 QATS-EB detection and diagnostic plots for KIC 9837578, in the same format as Figure 4.5.

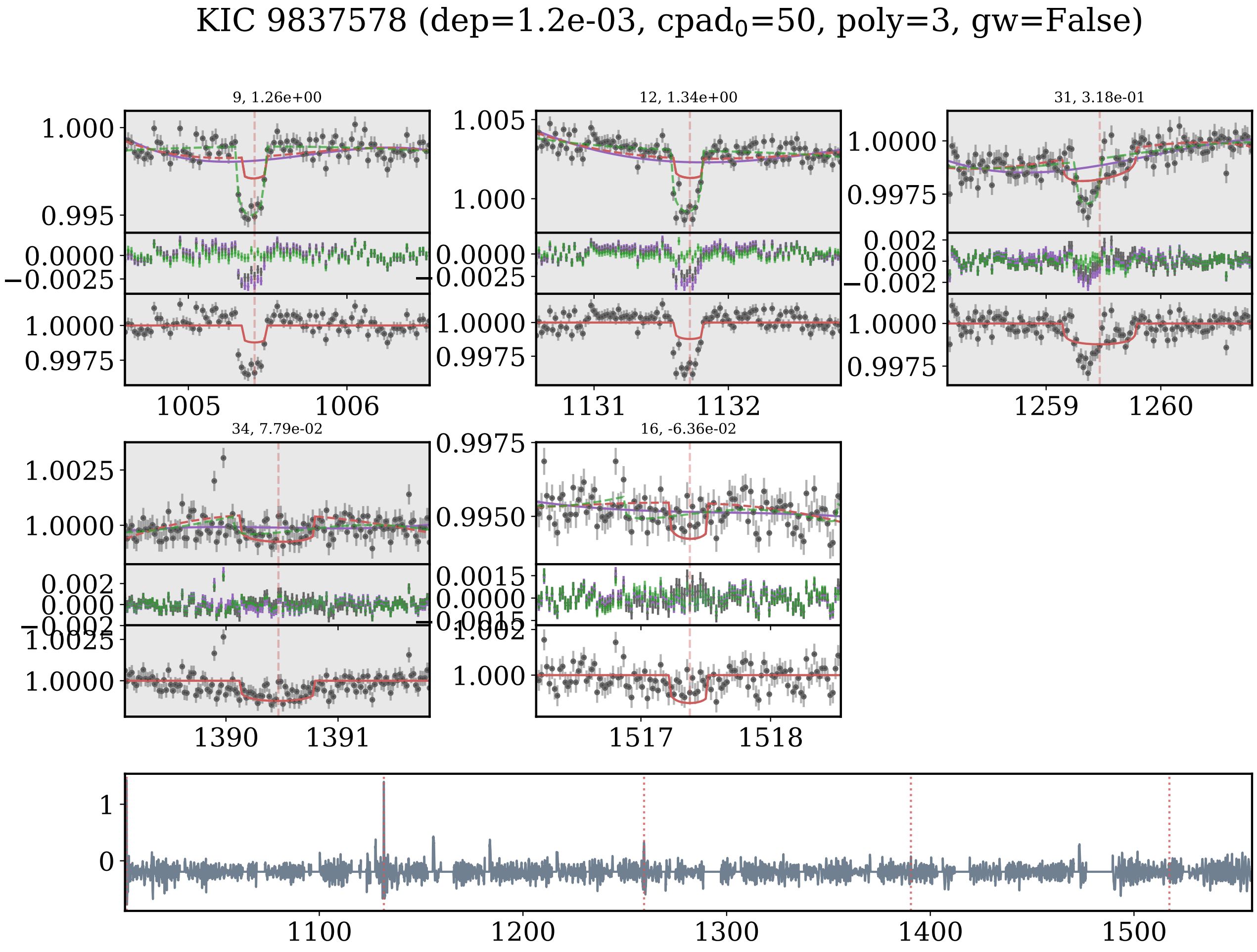

Figure B.11 QATS-EB detection and diagnostic plots for KIC 9837578, in the same format as Figure 4.5.

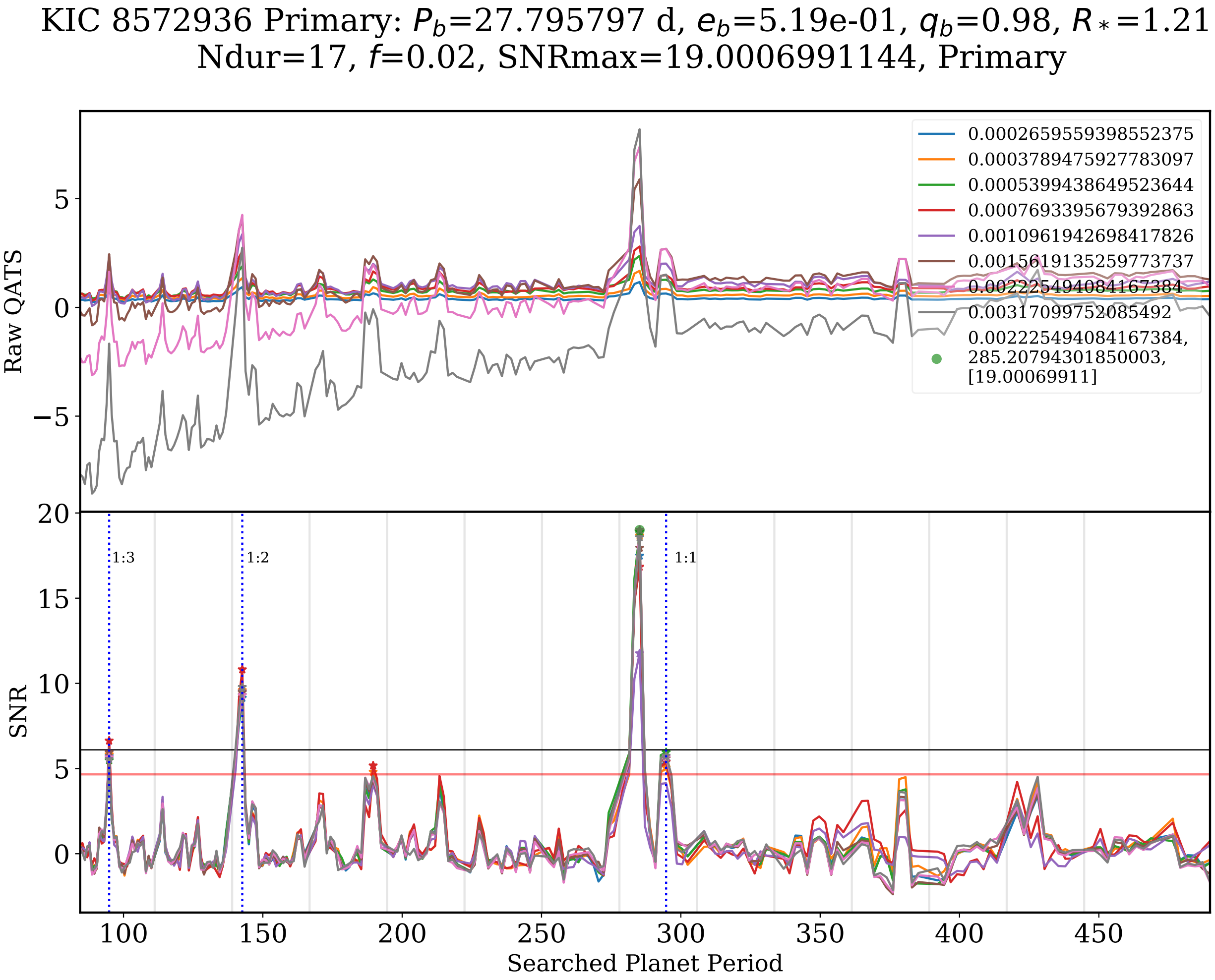

Figure B.12 QATS-EB detection and diagnostic plots for KIC 8572936, in the same format as Figure 4.5.

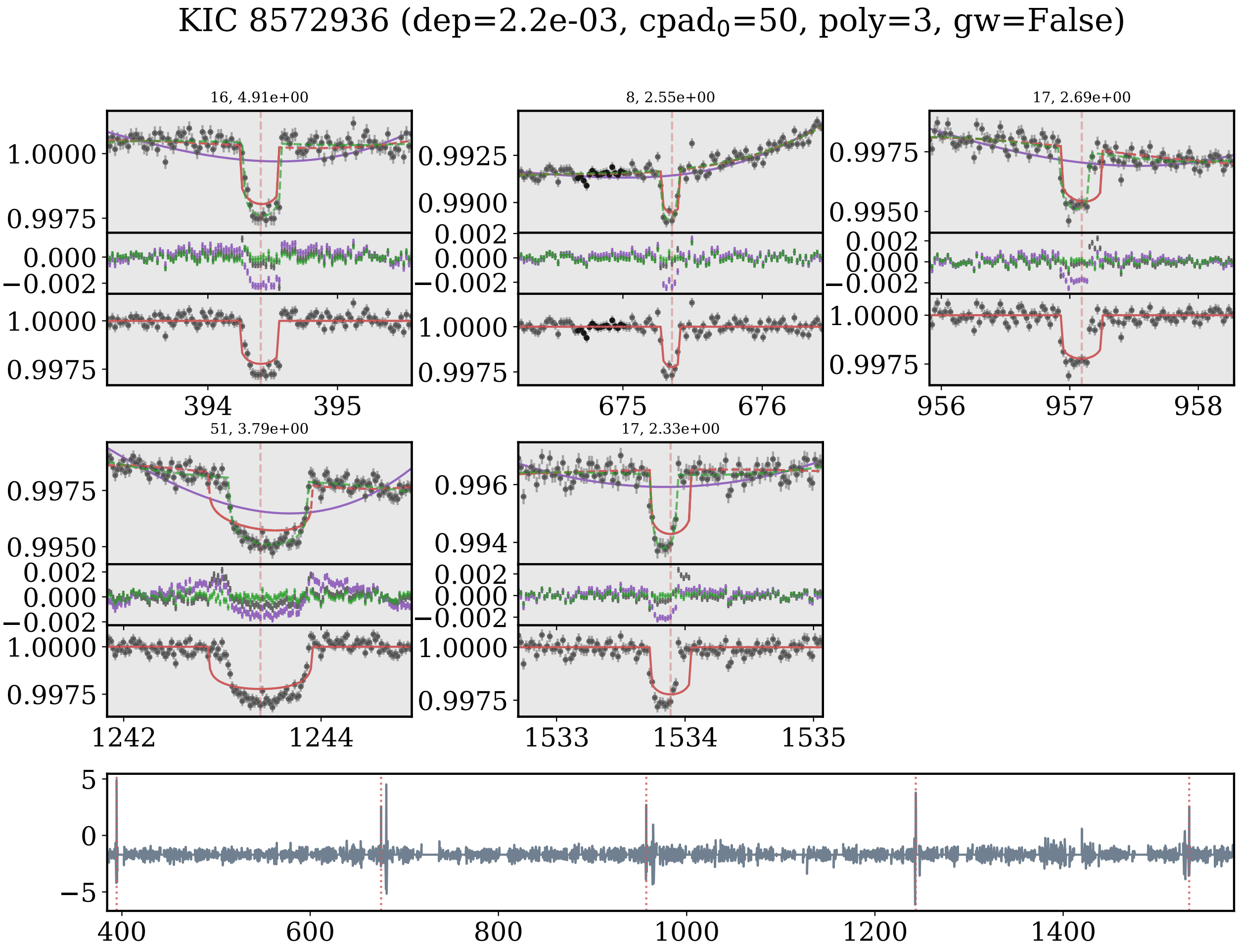

Figure B.13 QATS-EB detection and diagnostic plots for KIC 8572936, in the same format as Figure 4.5.

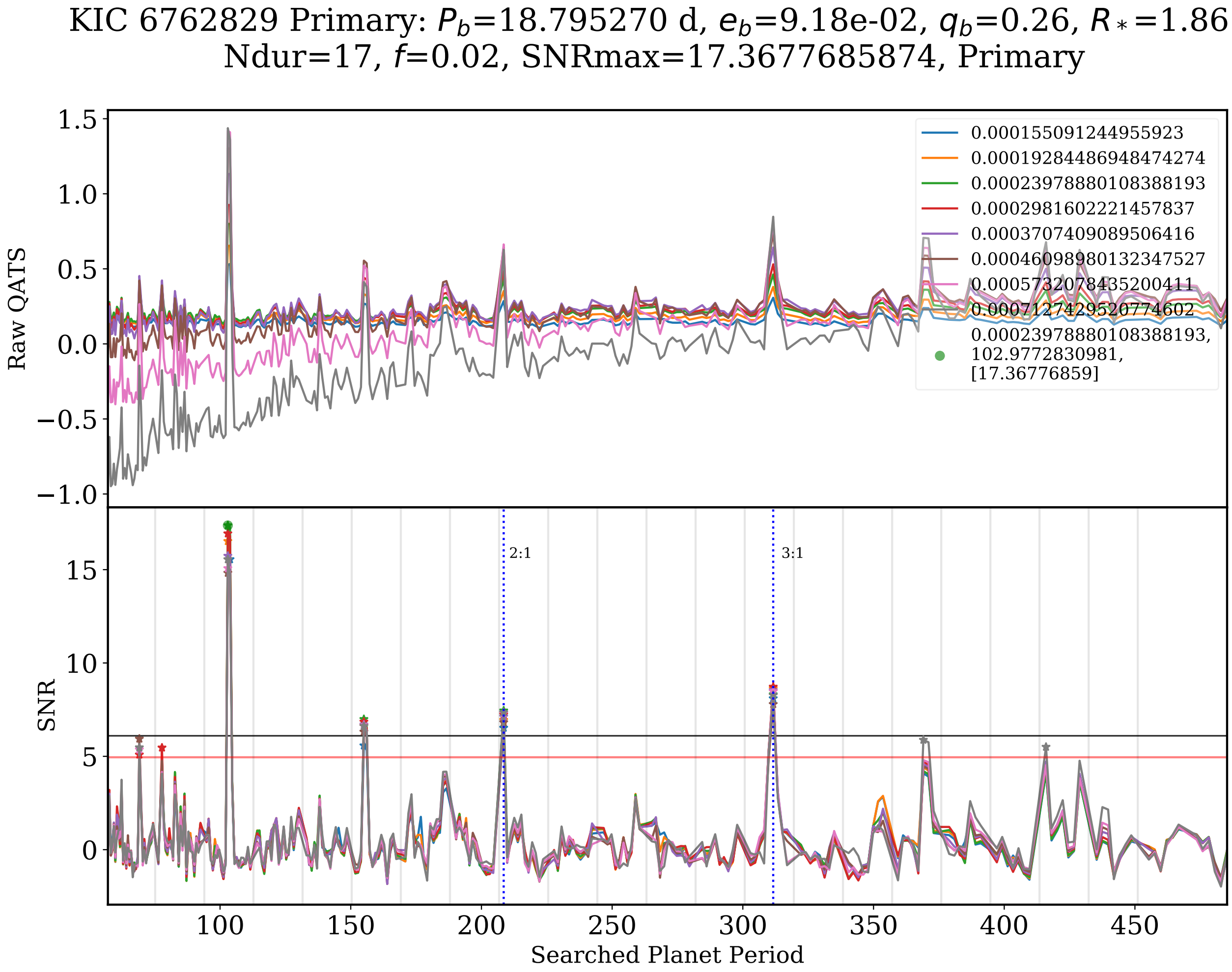

Figure B.14 QATS-EB detection and diagnostic plots for KIC 6762829, in the same format as Figure 4.5.

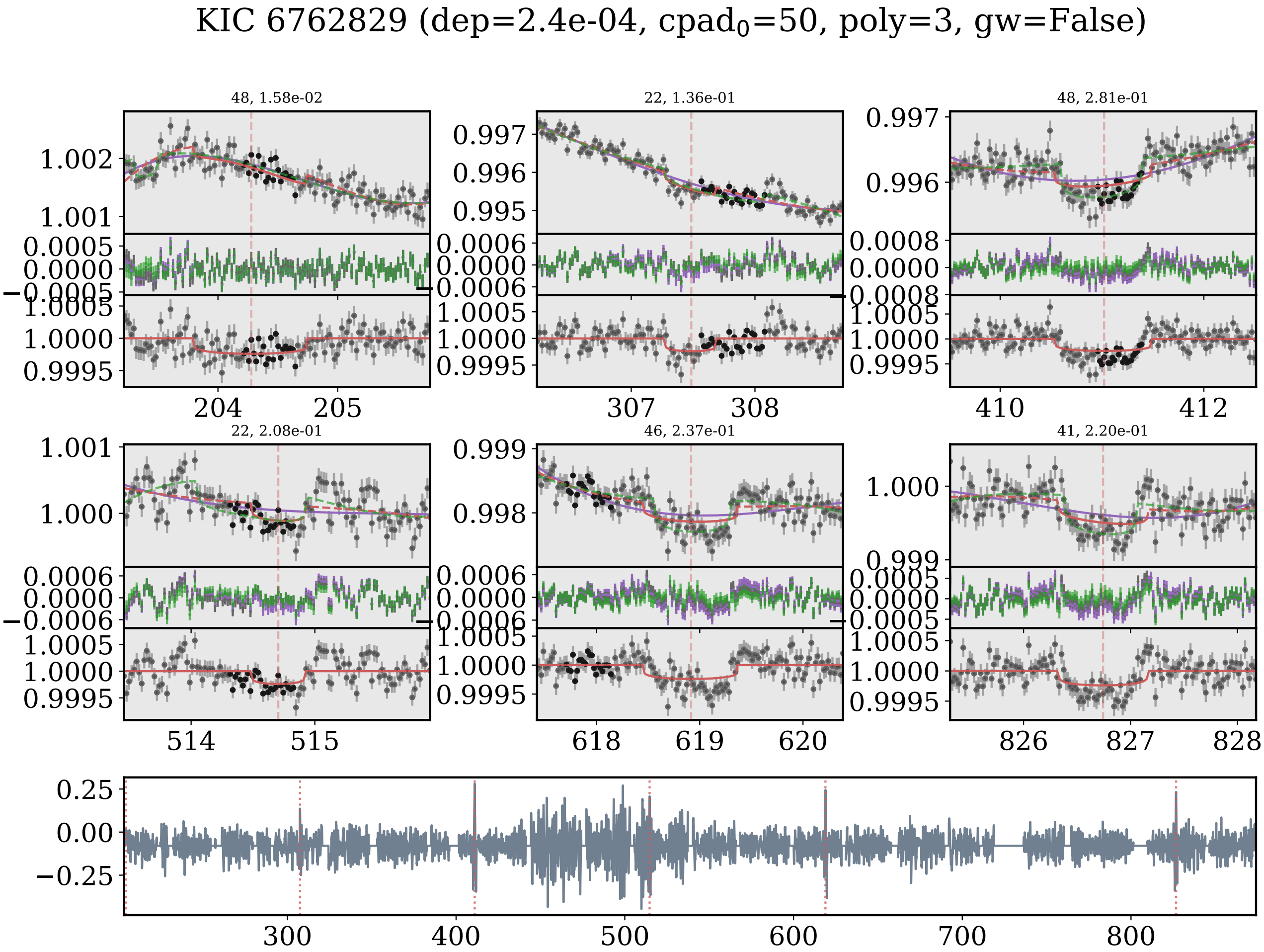

Figure B.15 QATS-EB detection and diagnostic plots for KIC 6762829, in the same format as Figure 4.5.

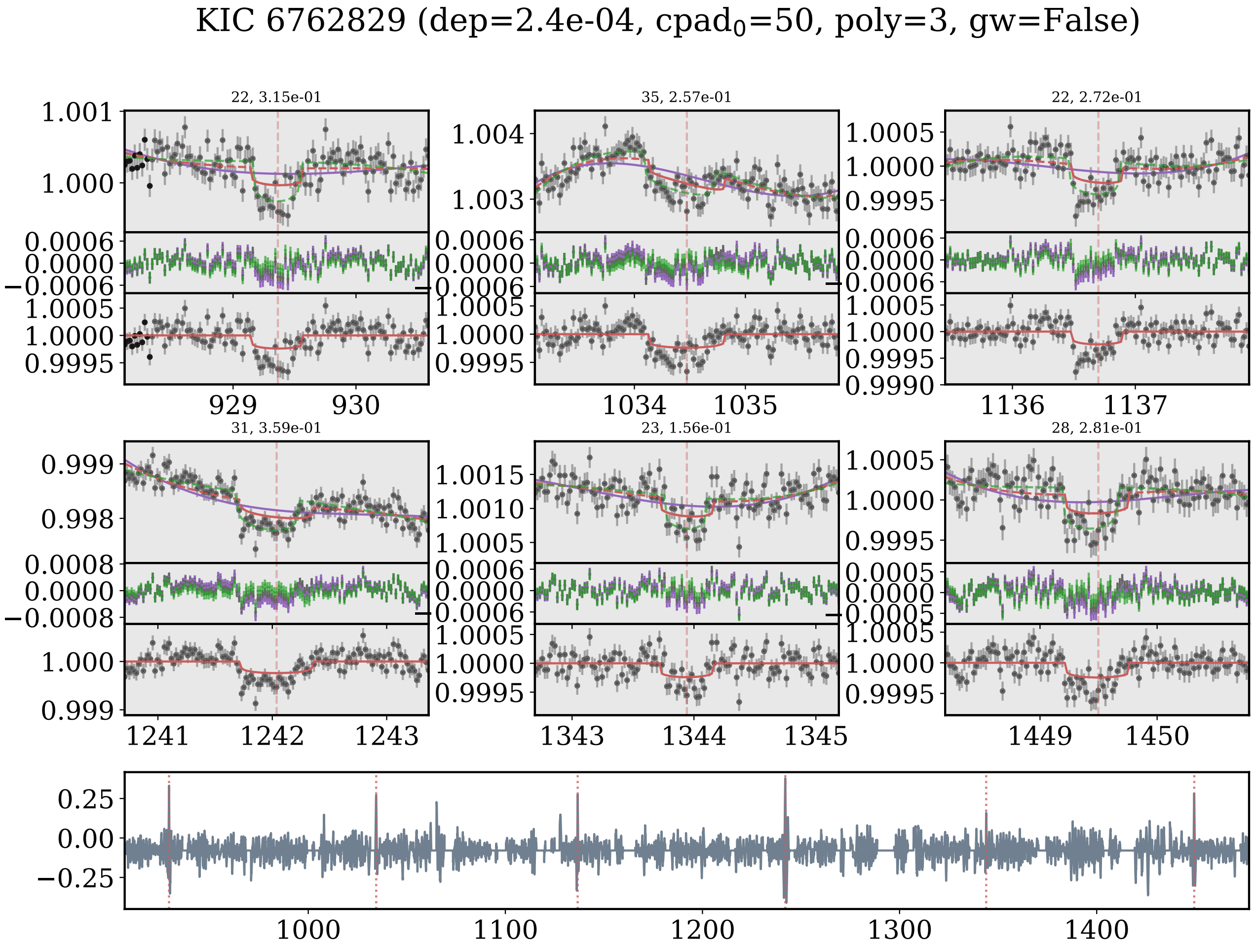

Figure B.16 QATS-EB detection and diagnostic plots for KIC 6762829, in the same format as Figure 4.5.

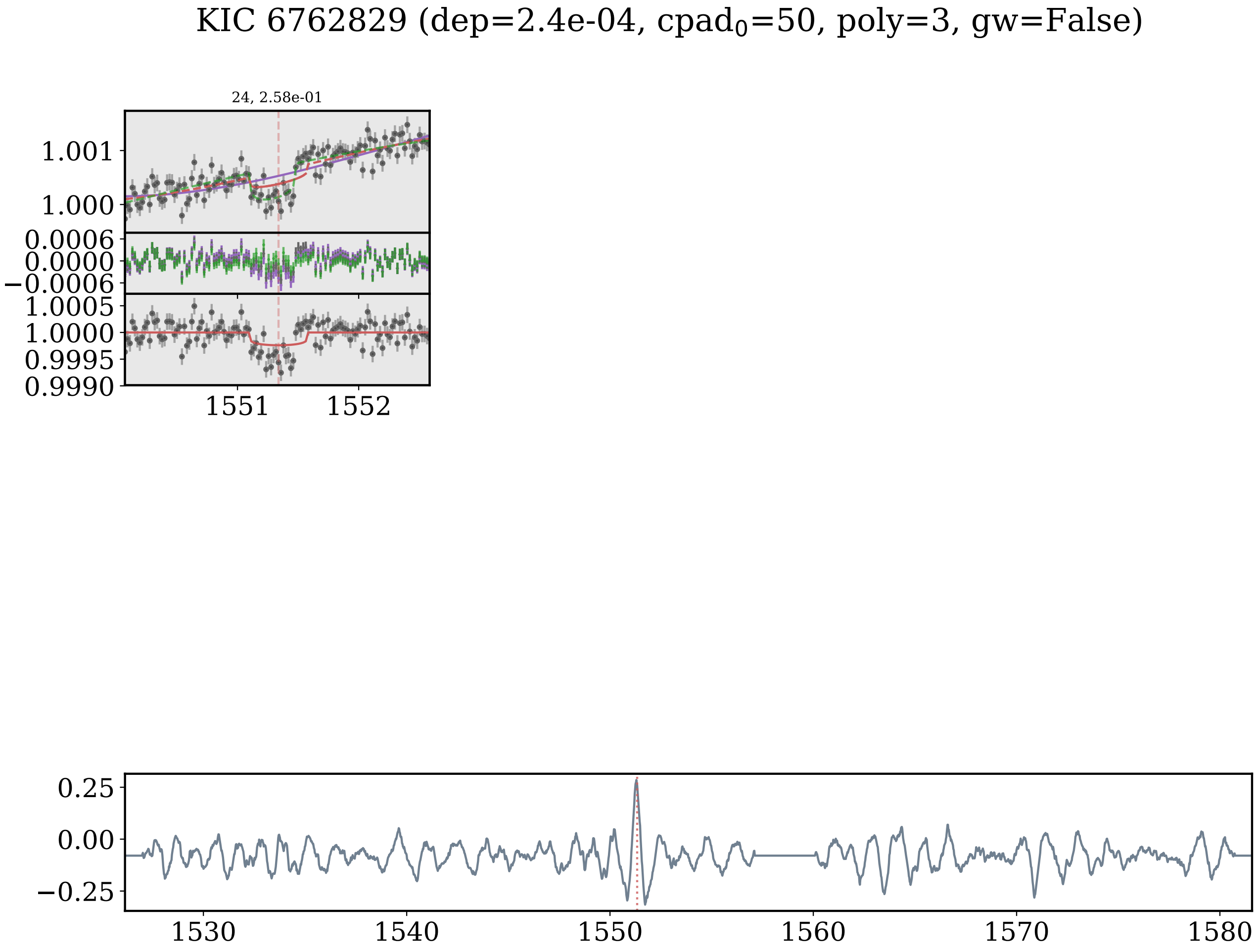

Figure B.17 QATS-EB detection and diagnostic plots for KIC 6762829, in the same format as Figure 4.5.

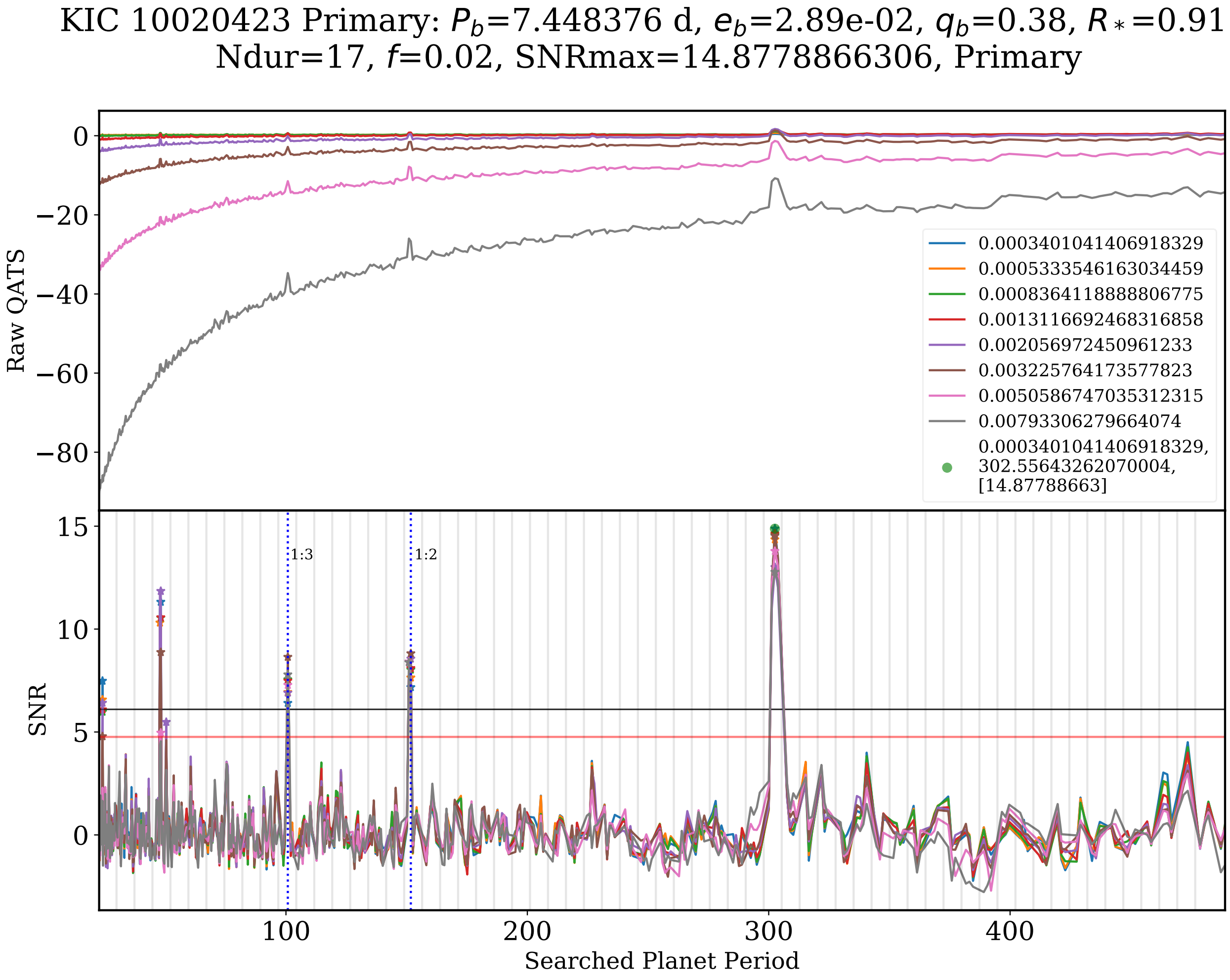

Figure B.18 QATS-EB detection and diagnostic plots for KIC 10020423, in the same format as Figure 4.5.

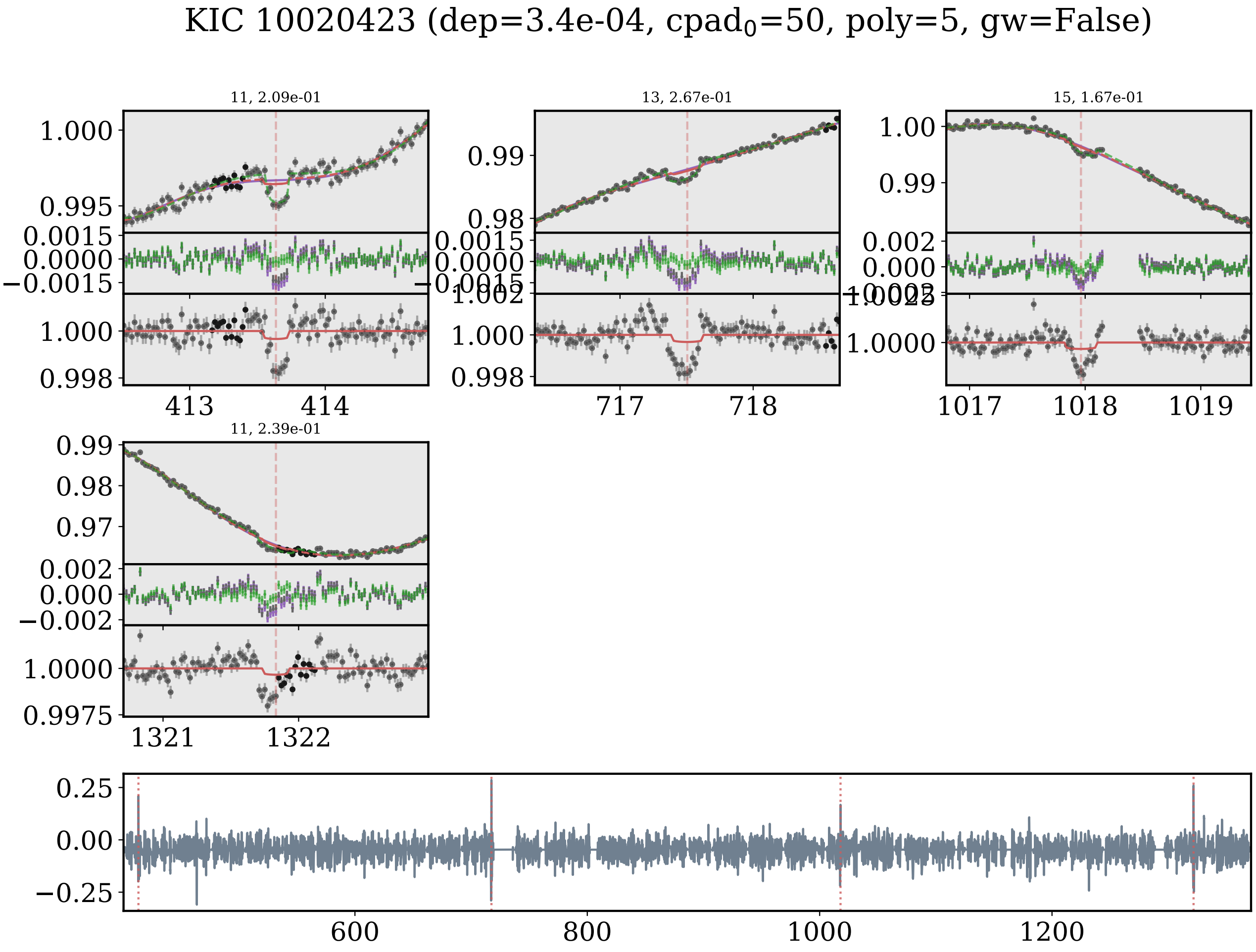

Figure B.19 QATS-EB detection and diagnostic plots for KIC 10020423, in the same format as Figure 4.5.

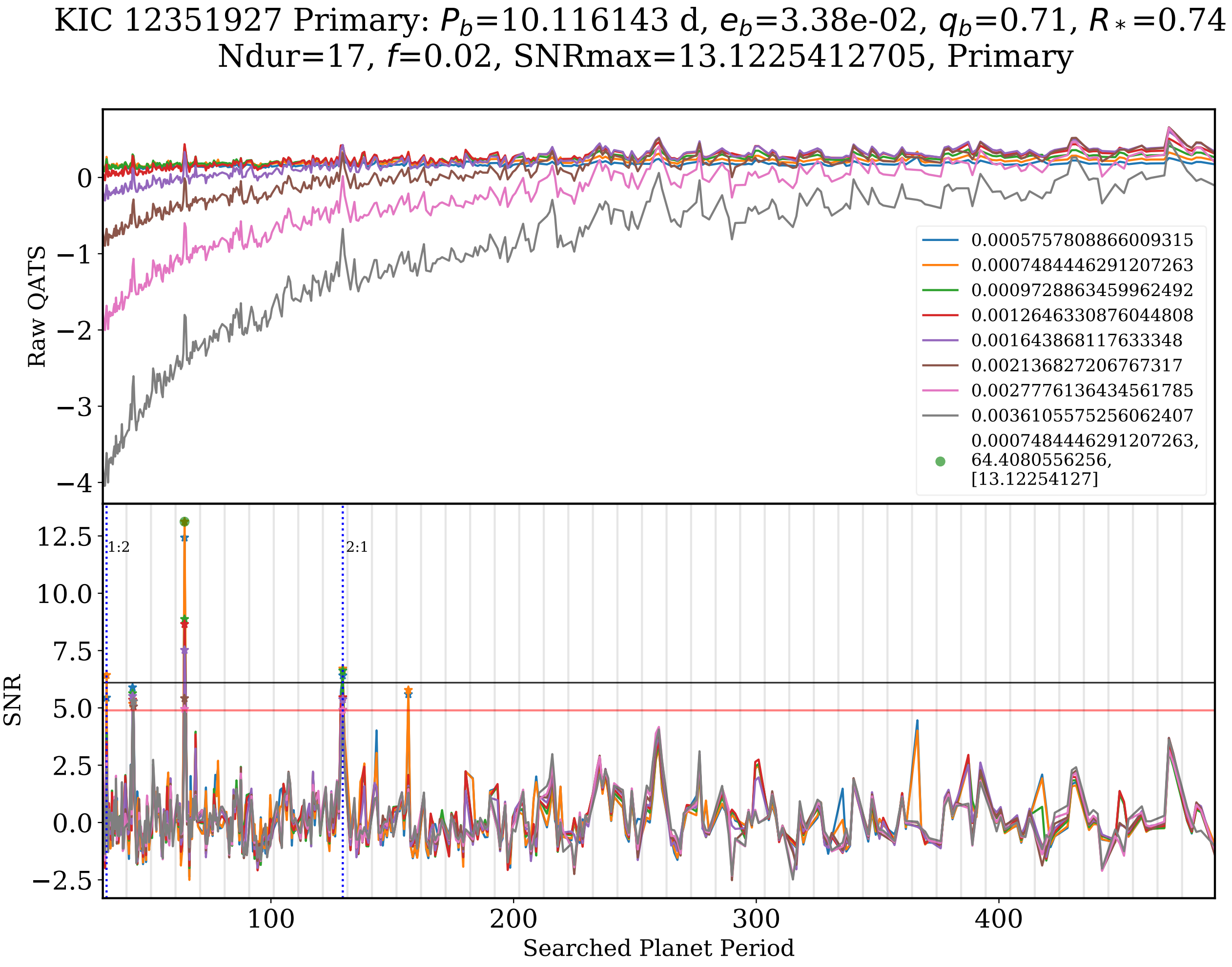

Figure B.20 QATS-EB detection and diagnostic plots for KIC 12351927, in the same format as Figure 4.5.

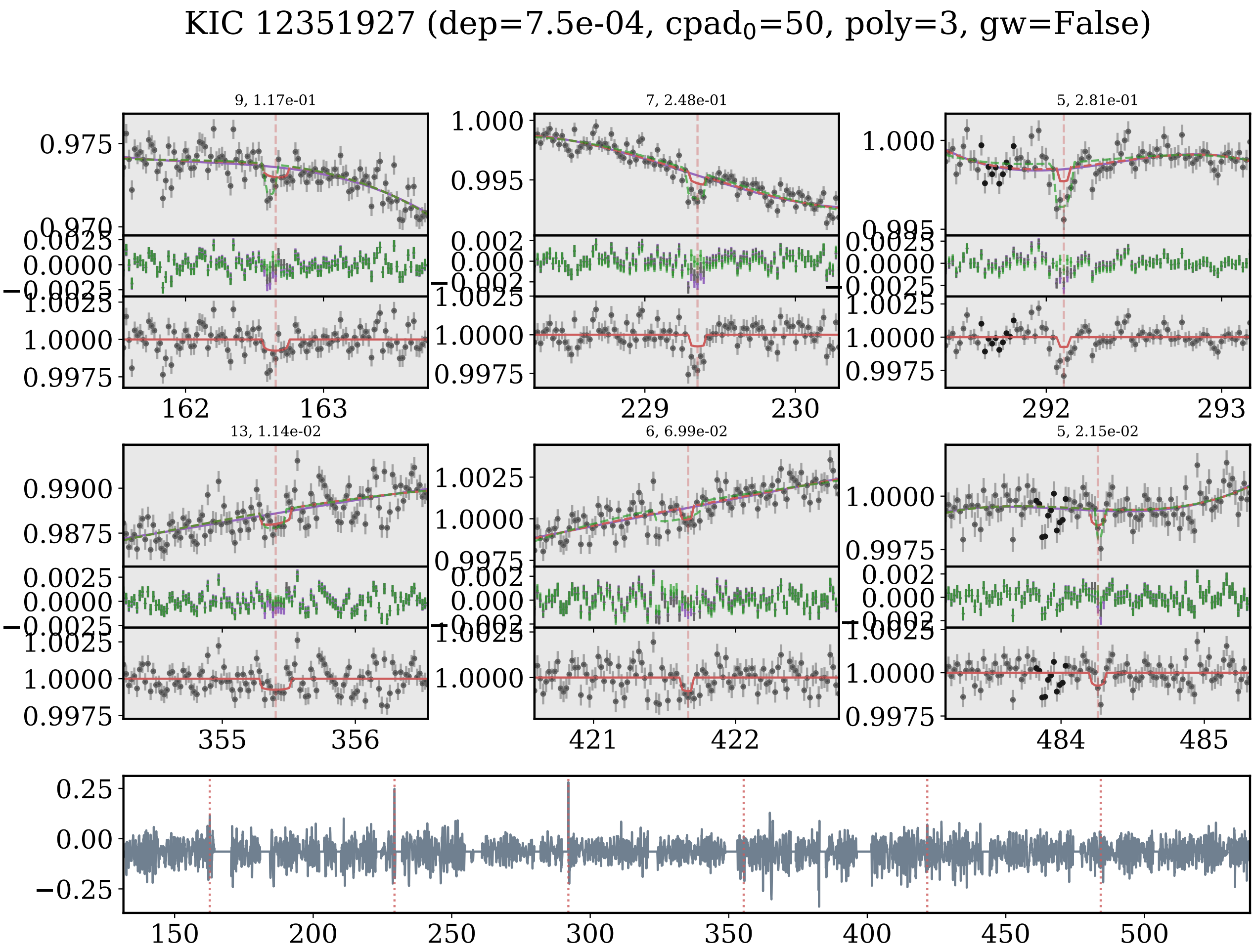

Figure B.21 QATS-EB detection and diagnostic plots for KIC 12351927, in the same format as Figure 4.5.

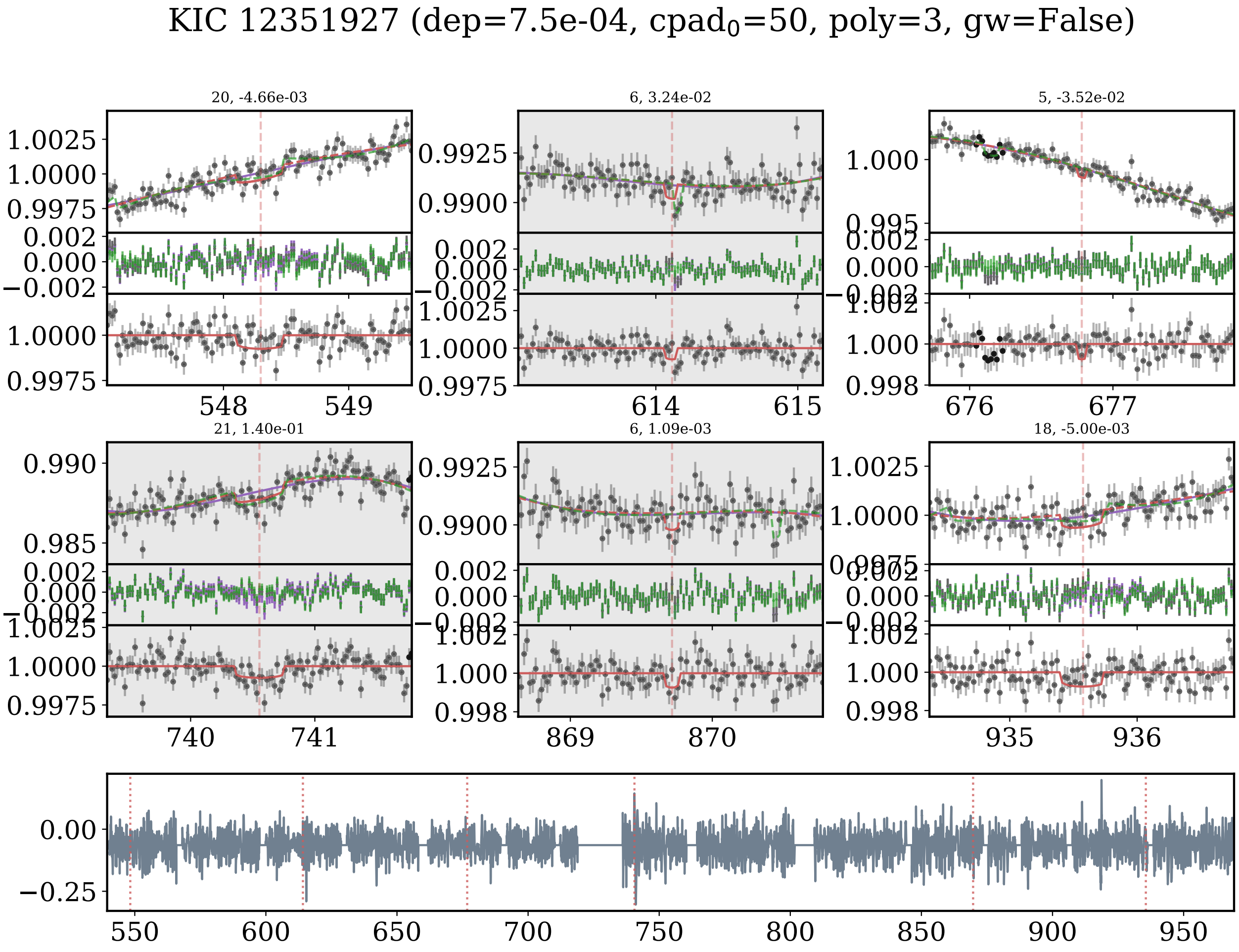

Figure B.22 QATS-EB detection and diagnostic plots for KIC 12351927, in the same format as Figure 4.5.

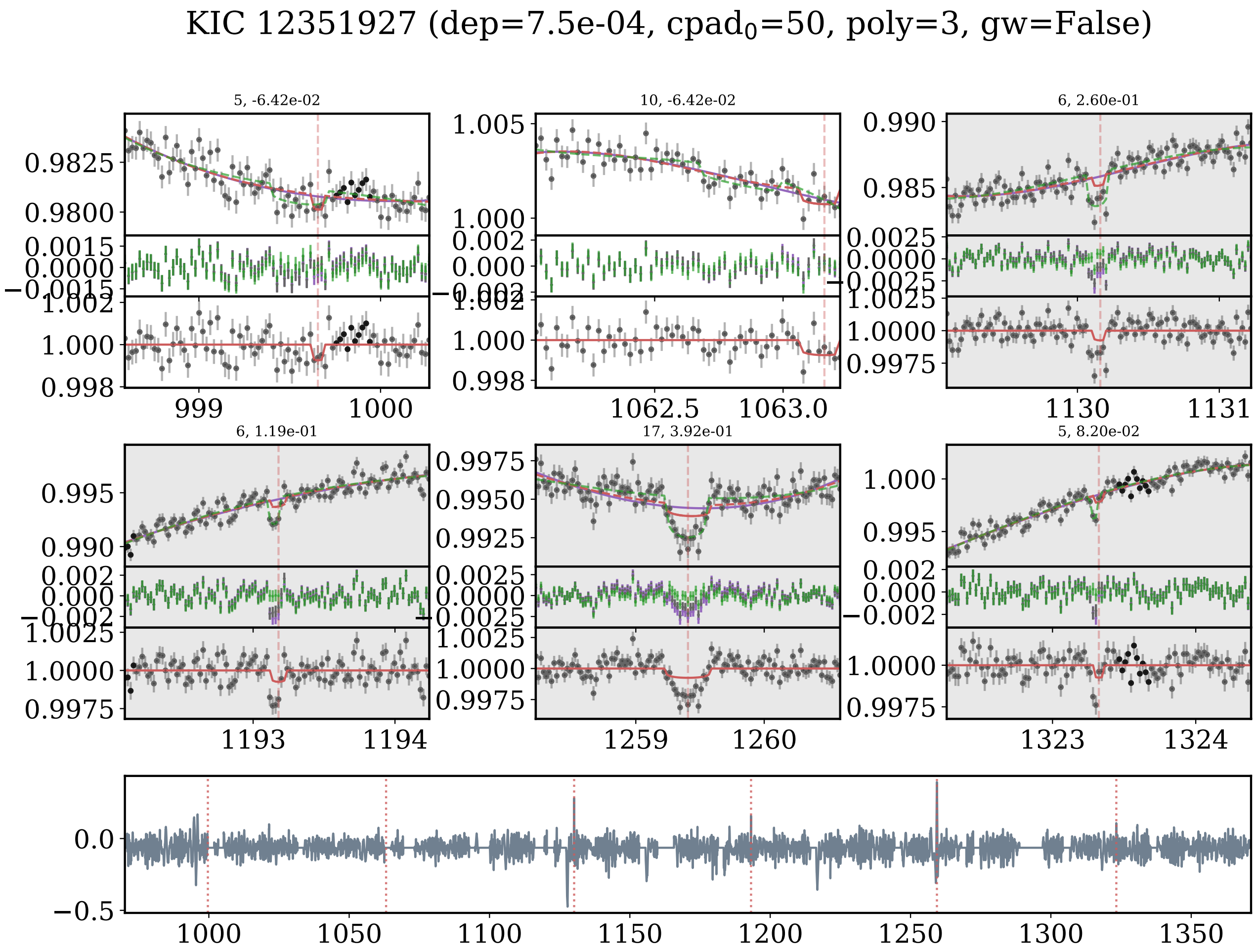

Figure B.23 QATS-EB detection and diagnostic plots for KIC 12351927, in the same format as Figure 4.5.

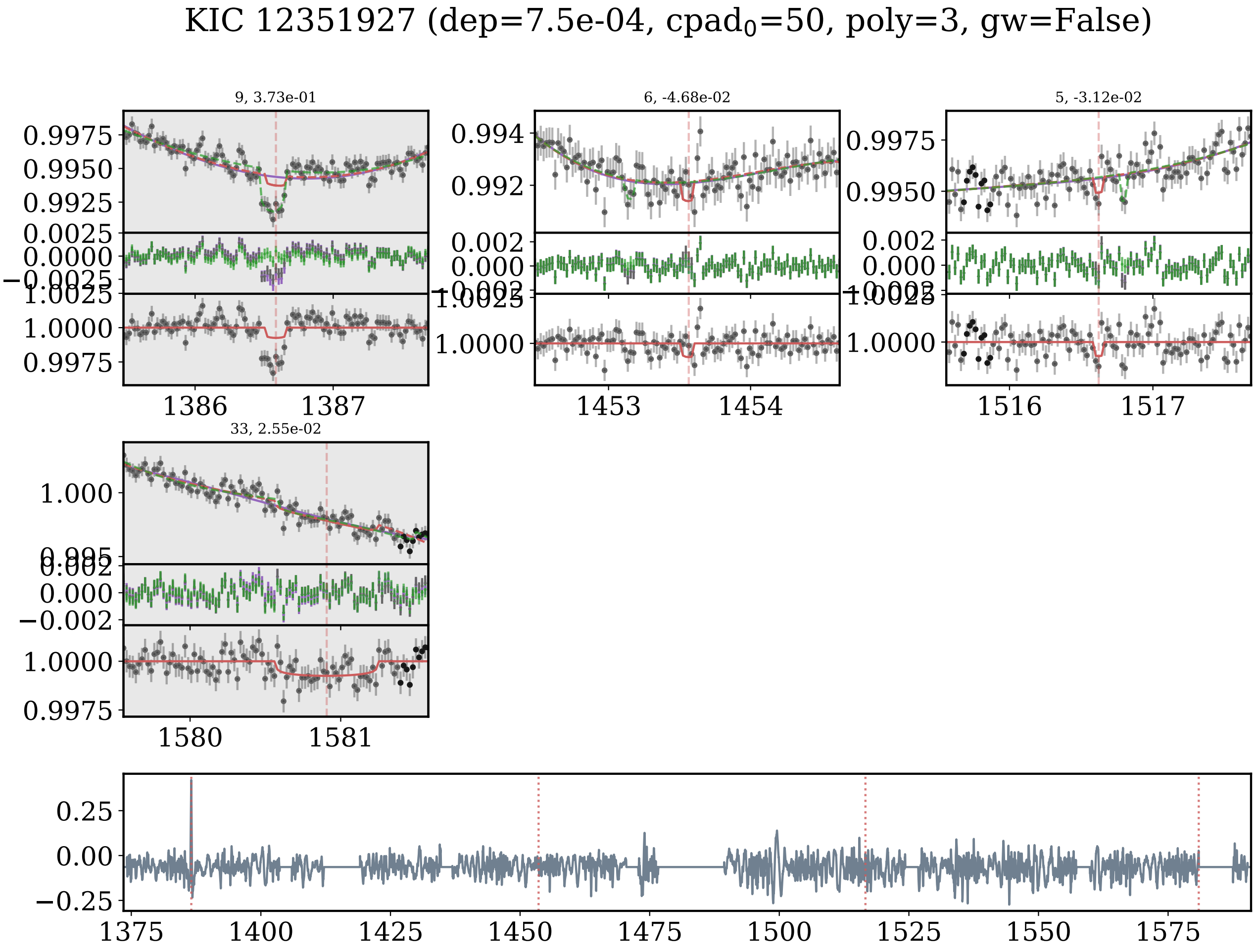

Figure B.24 QATS-EB detection and diagnostic plots for KIC 12351927, in the same format as Figure 4.5.

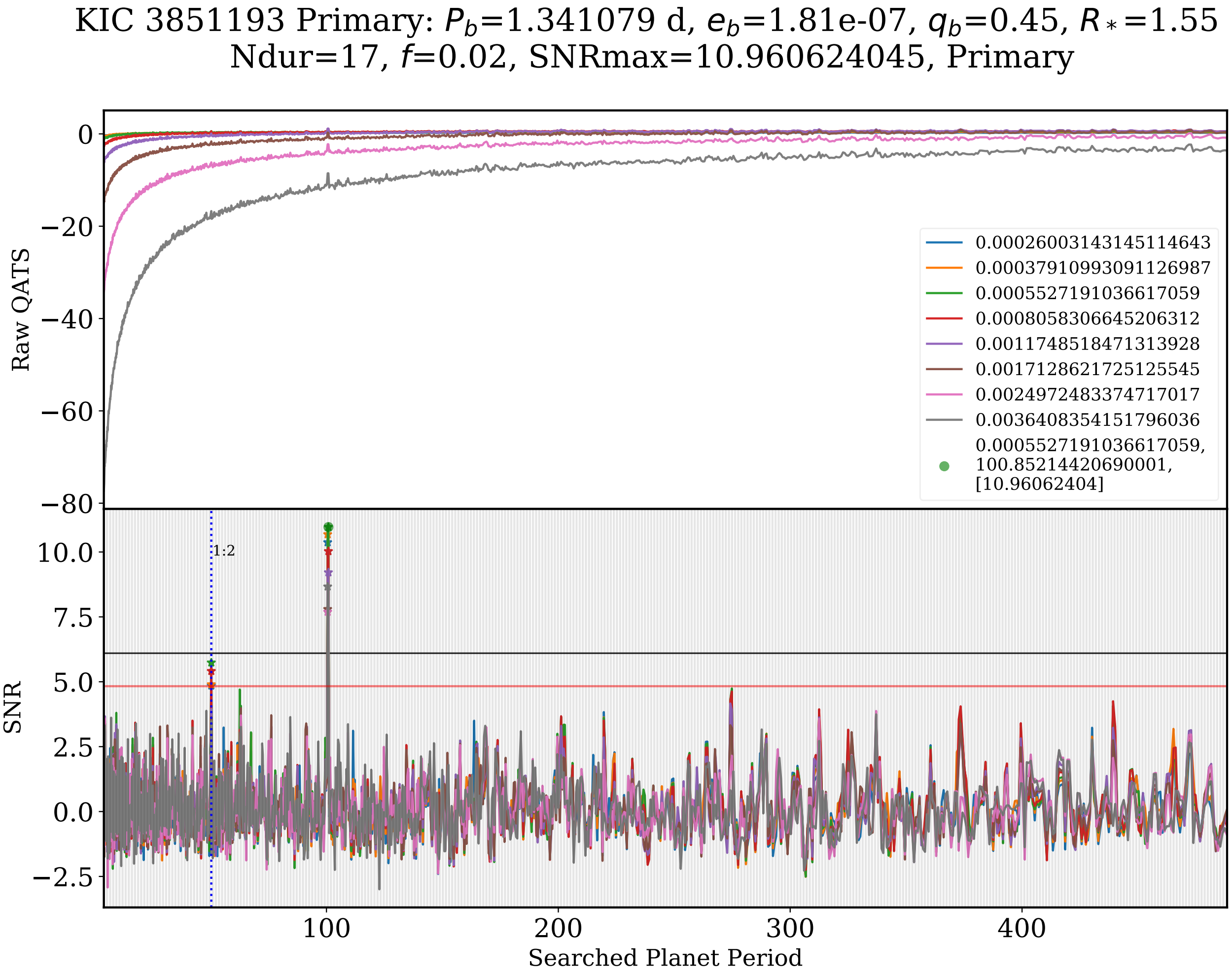

Figure B.25 QATS-EB detection and diagnostic plots for KIC 3851193, in the same format as Figure 4.5.

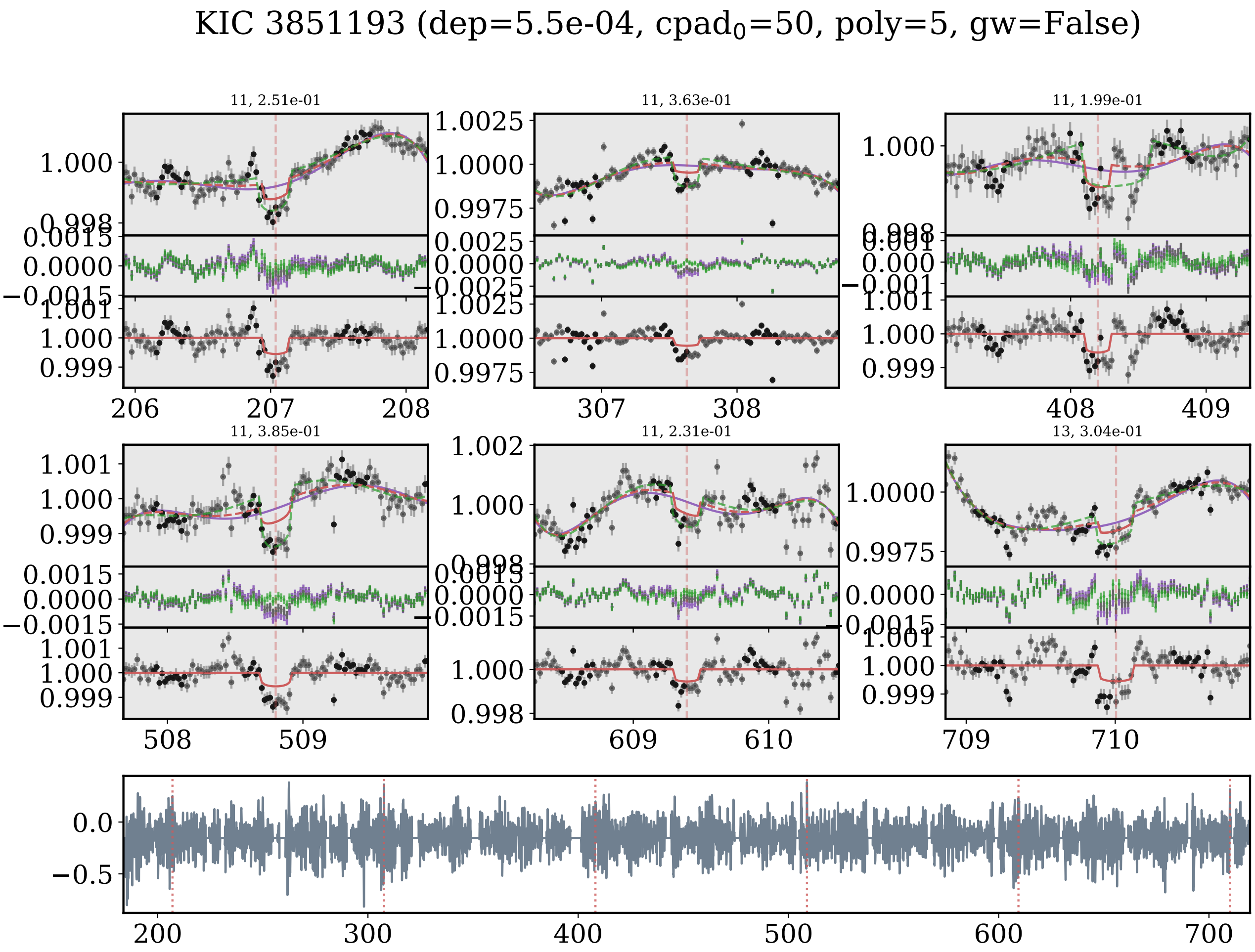

Figure B.26 QATS-EB detection and diagnostic plots for KIC 3851193, in the same format as Figure 4.5.

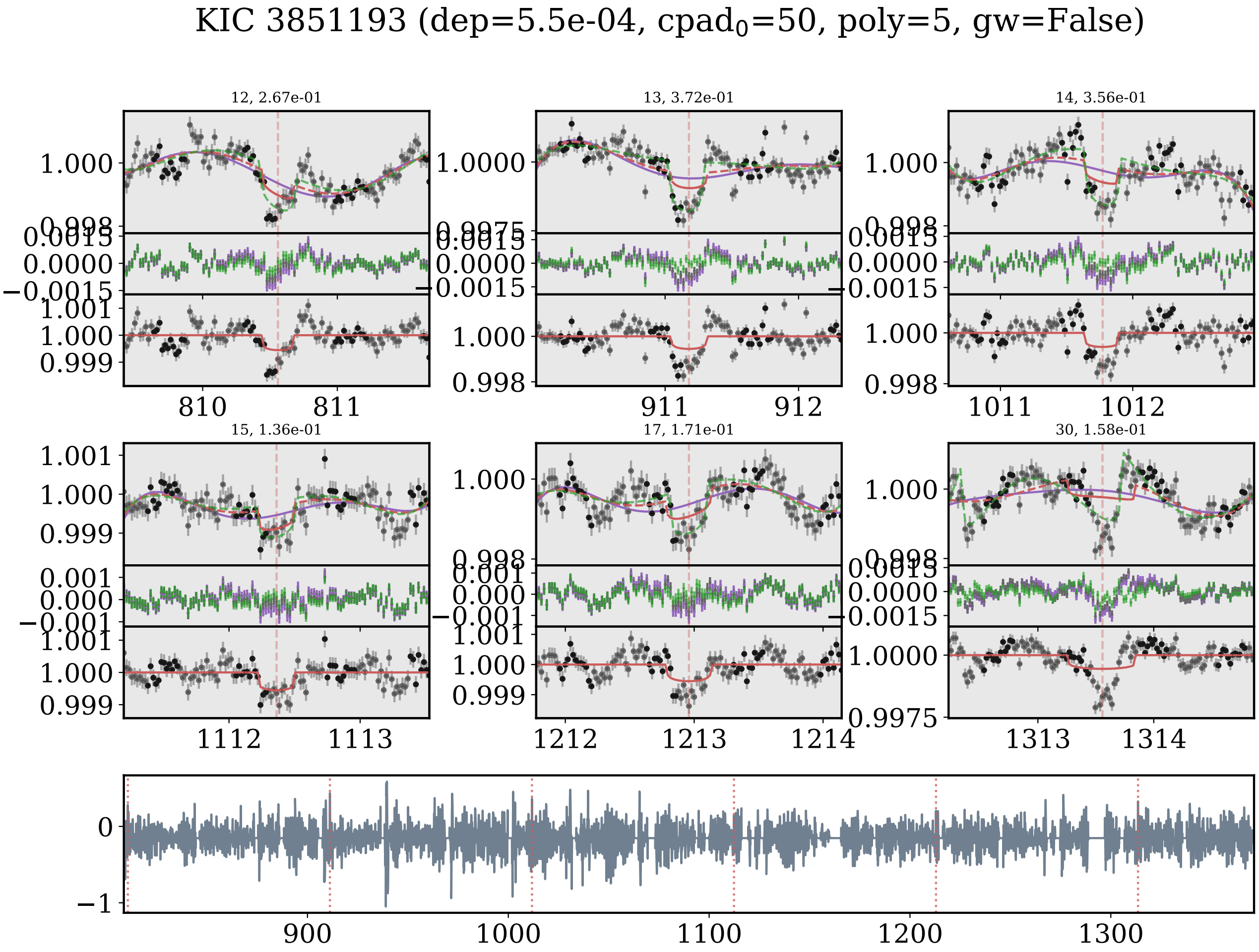

Figure B.27 QATS-EB detection and diagnostic plots for KIC 3851193, in the same format as Figure 4.5.

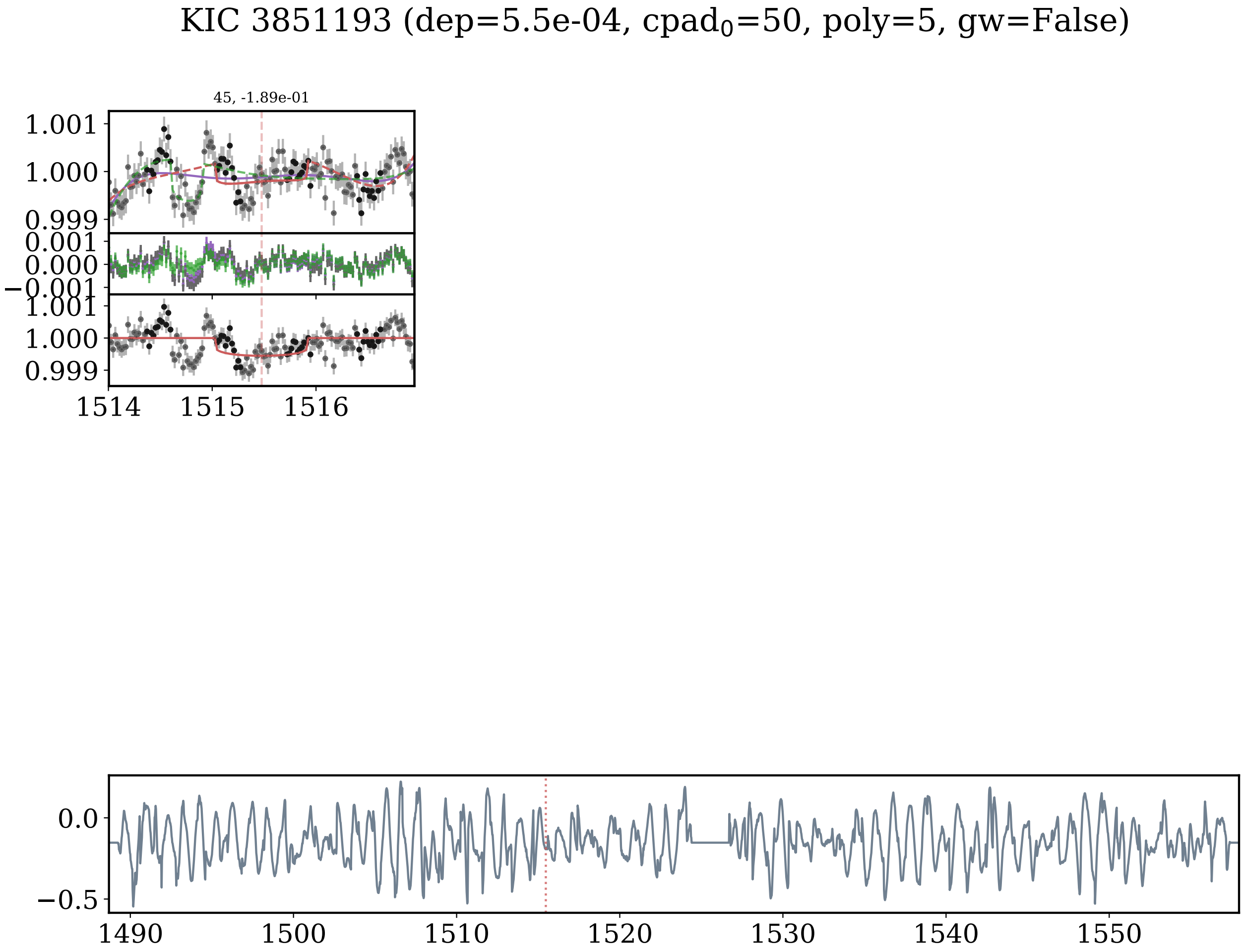

Figure B.28 QATS-EB detection and diagnostic plots for KIC 3851193, in the same format as Figure 4.5.

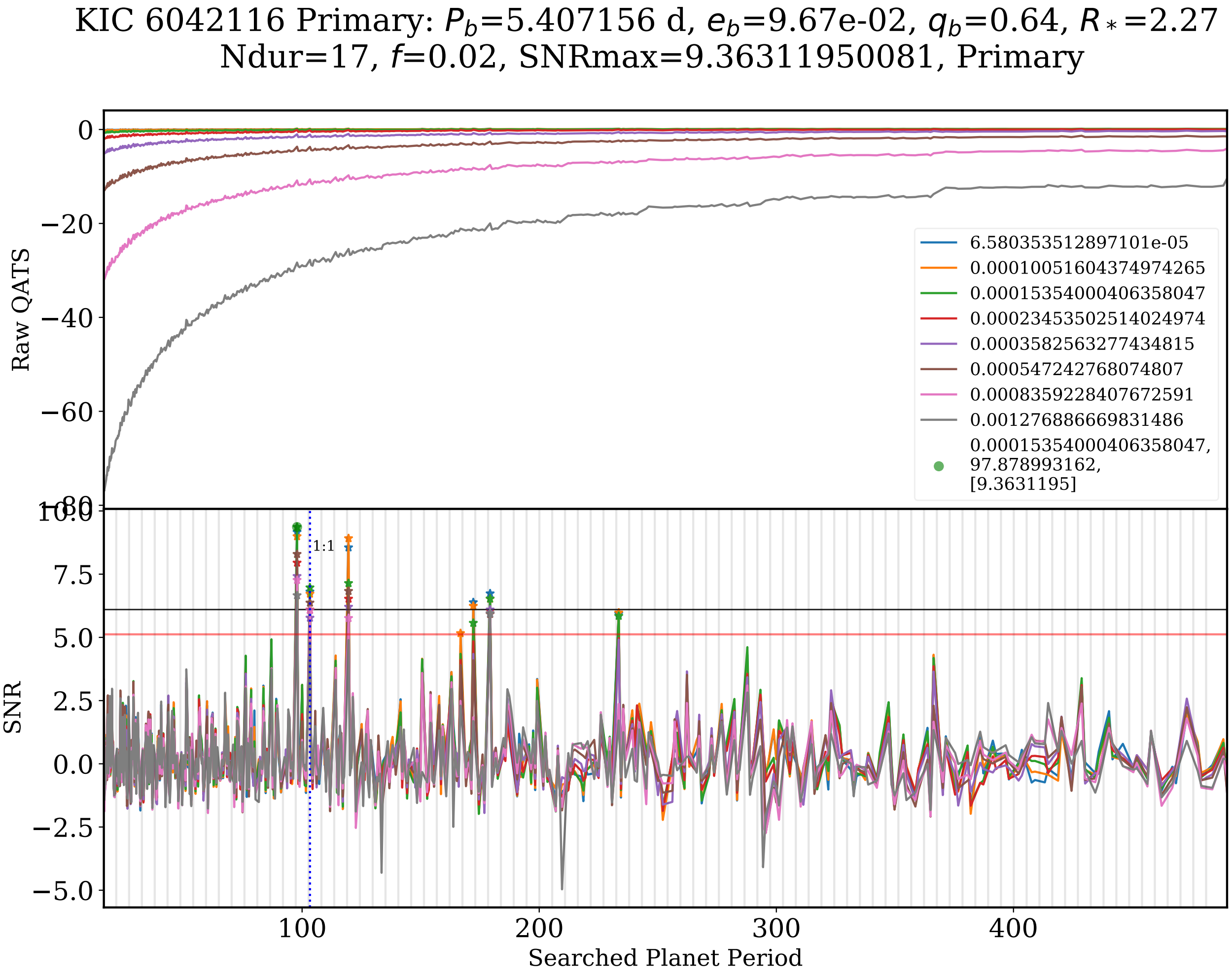

Figure B.29 QATS-EB detection and diagnostic plots for KIC 6042116, in the same format as Figure 4.5.

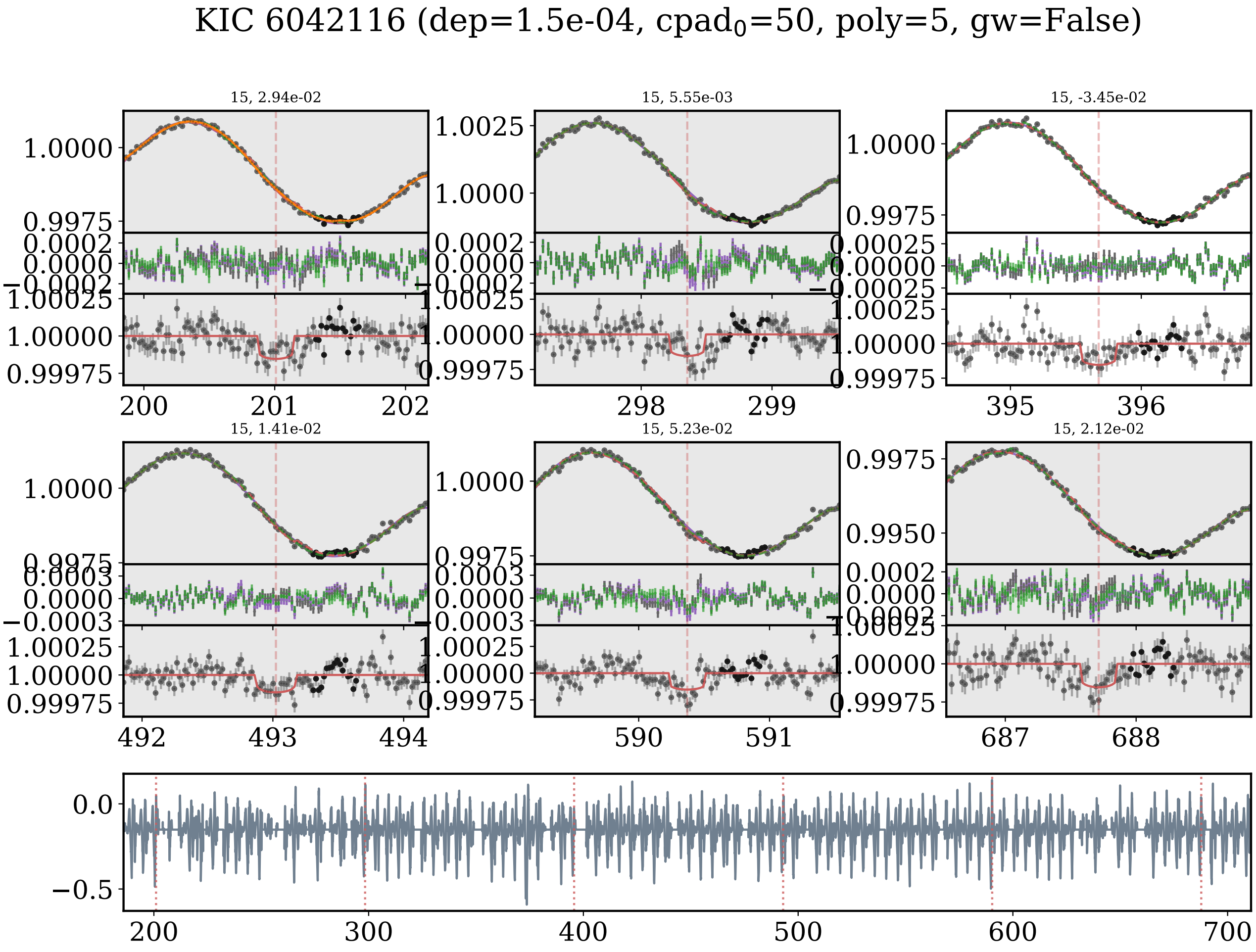

Figure B.30 QATS-EB detection and diagnostic plots for KIC 6042116, in the same format as Figure 4.5.

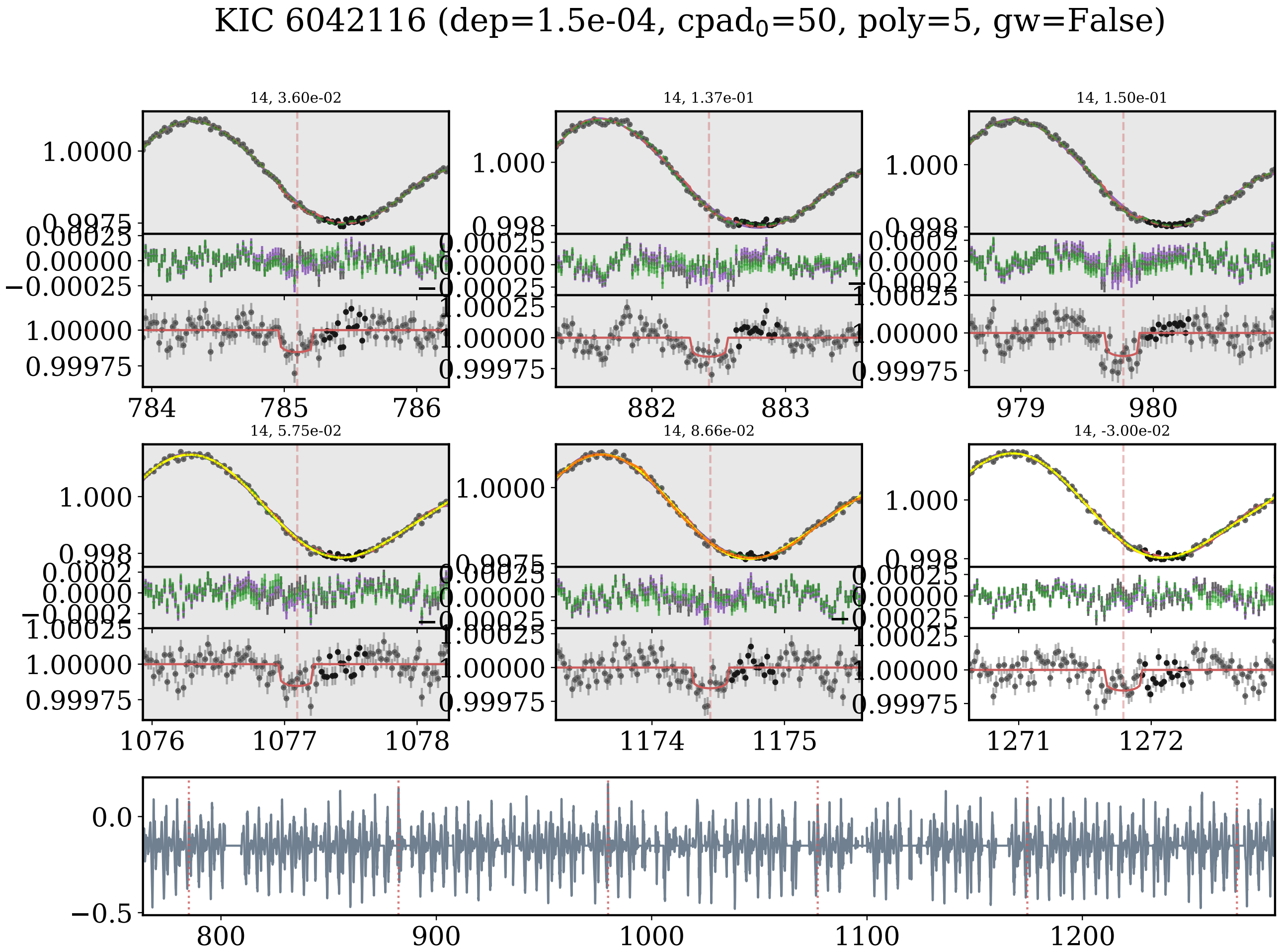

Figure B.31 QATS-EB detection and diagnostic plots for KIC 6042116, in the same format as Figure 4.5.

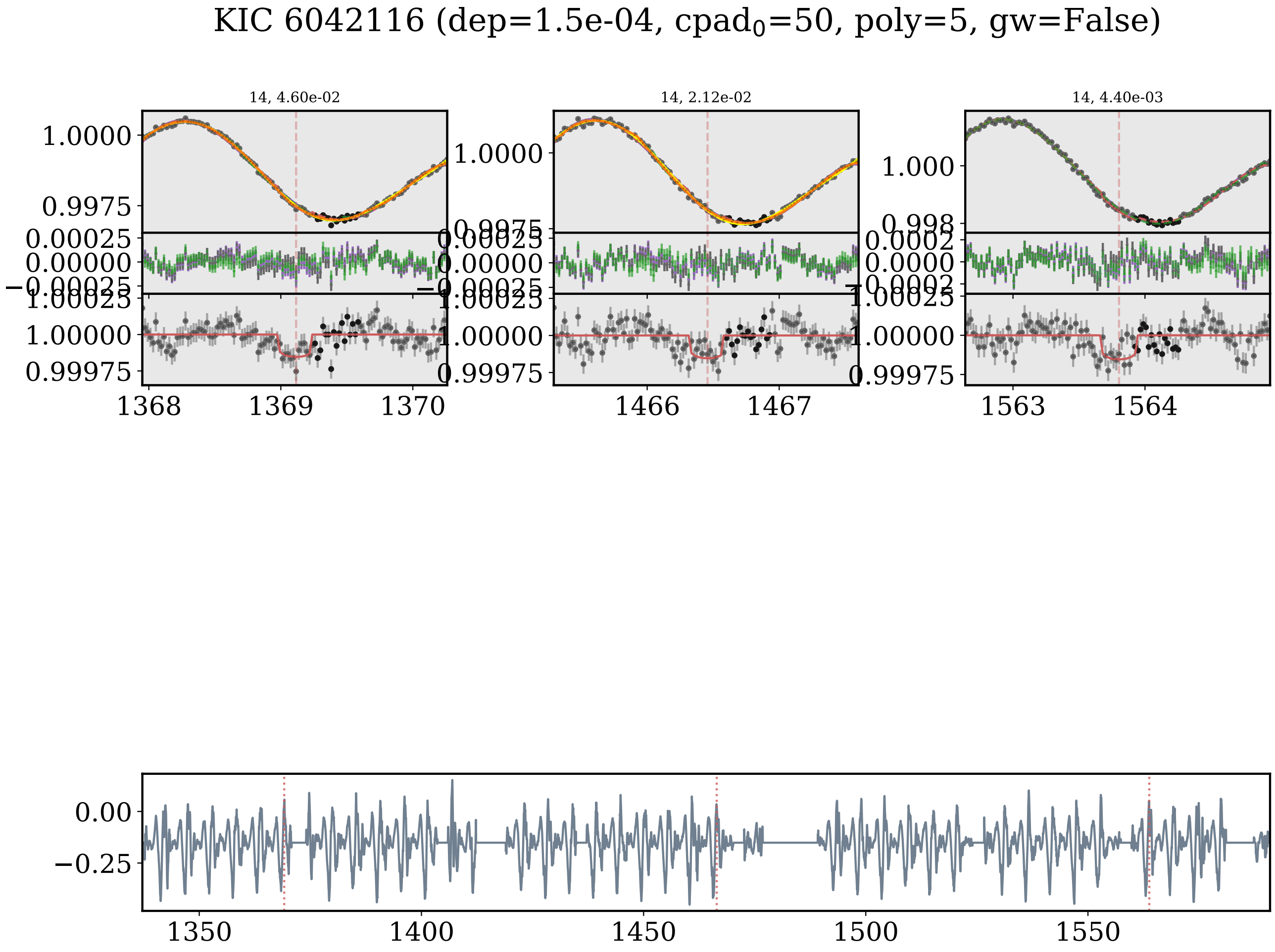

Figure B.32 QATS-EB detection and diagnostic plots for KIC 6042116, in the same format as Figure 4.5.

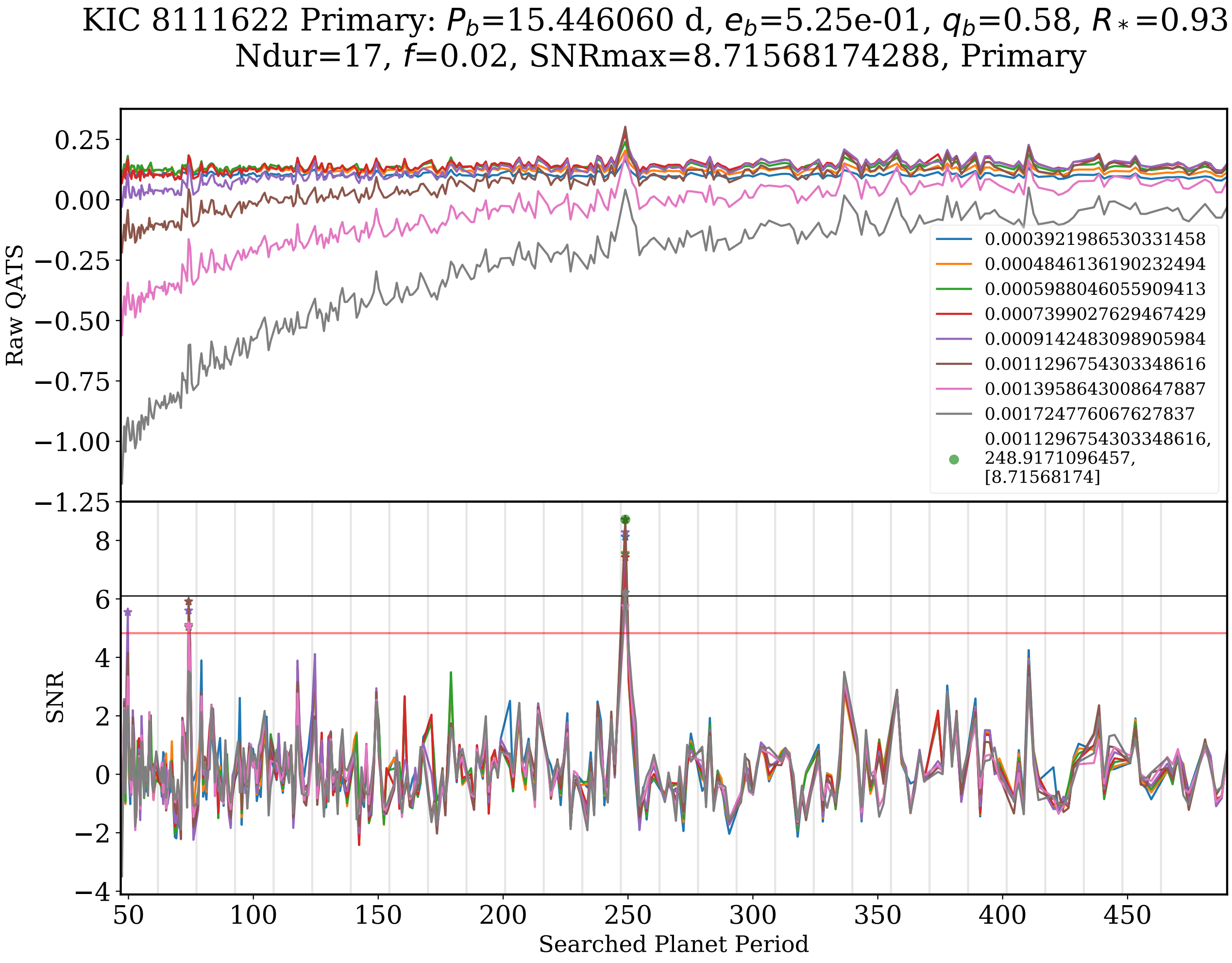

KIC 8111622 Primary: P_b=15.446060 d, e_b=5.25e-01, q_b=0.58, R_*=0.93
Ndur=17, f=0.02, SNRmax=8.71568174288, Primary

Figure B.33 QATS-EB detection and diagnostic plots for KIC 8111622, in the same format as Figure 4.5.

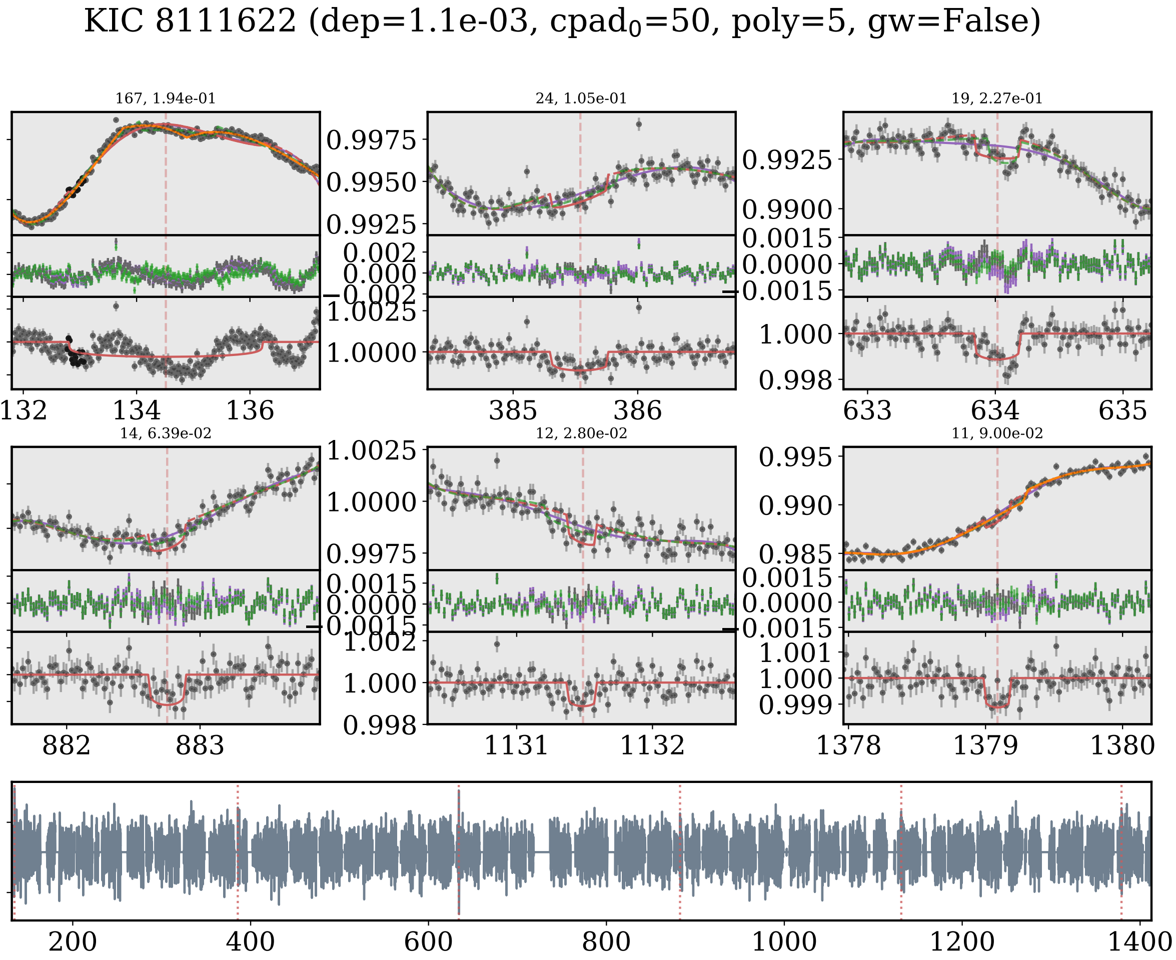

Figure B.34 QATS-EB detection and diagnostic plots for KIC 8111622, in the same format as Figure 4.5.

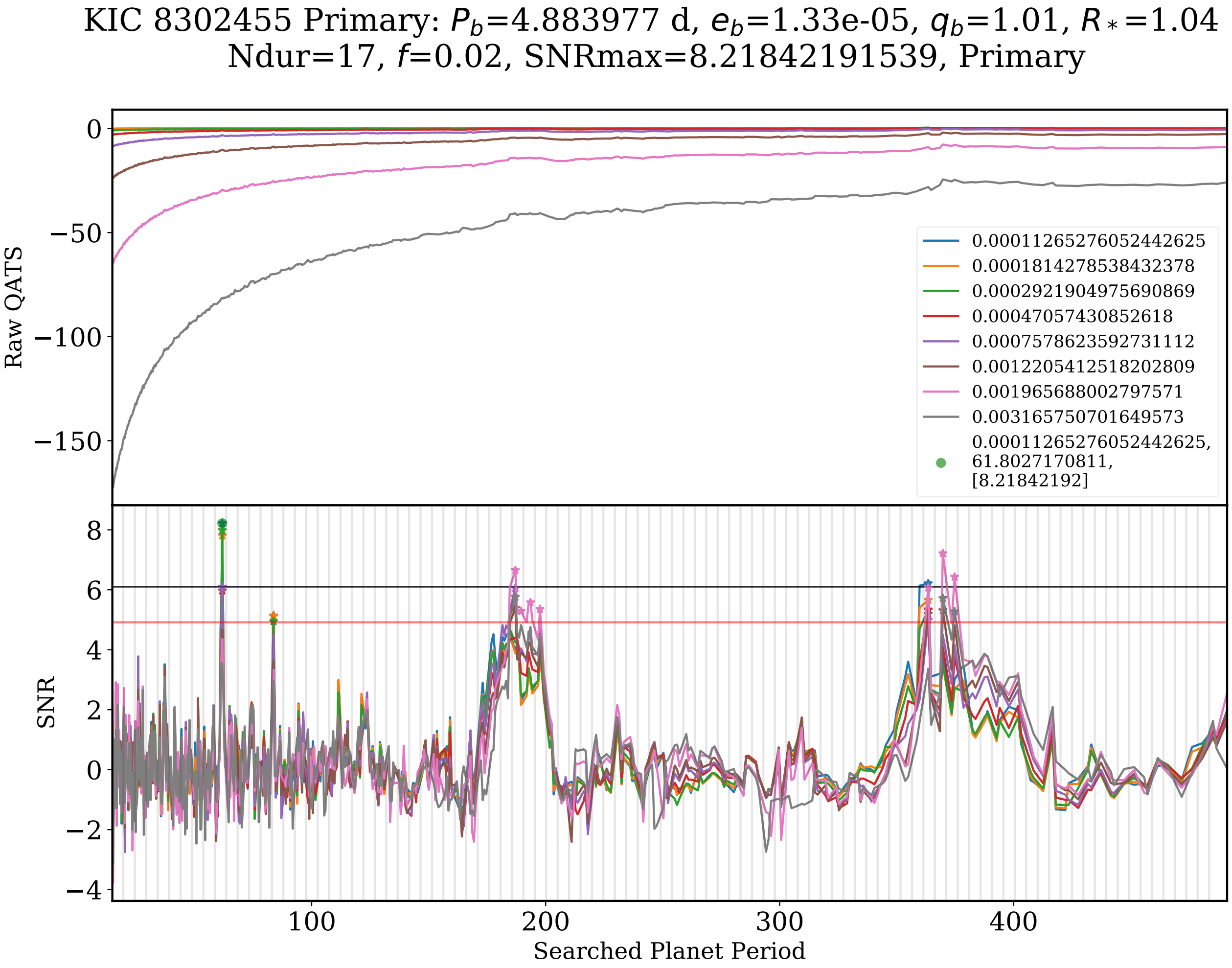

Figure B.35 QATS-EB detection and diagnostic plots for KIC 8302455, in the same format as Figure 4.5.

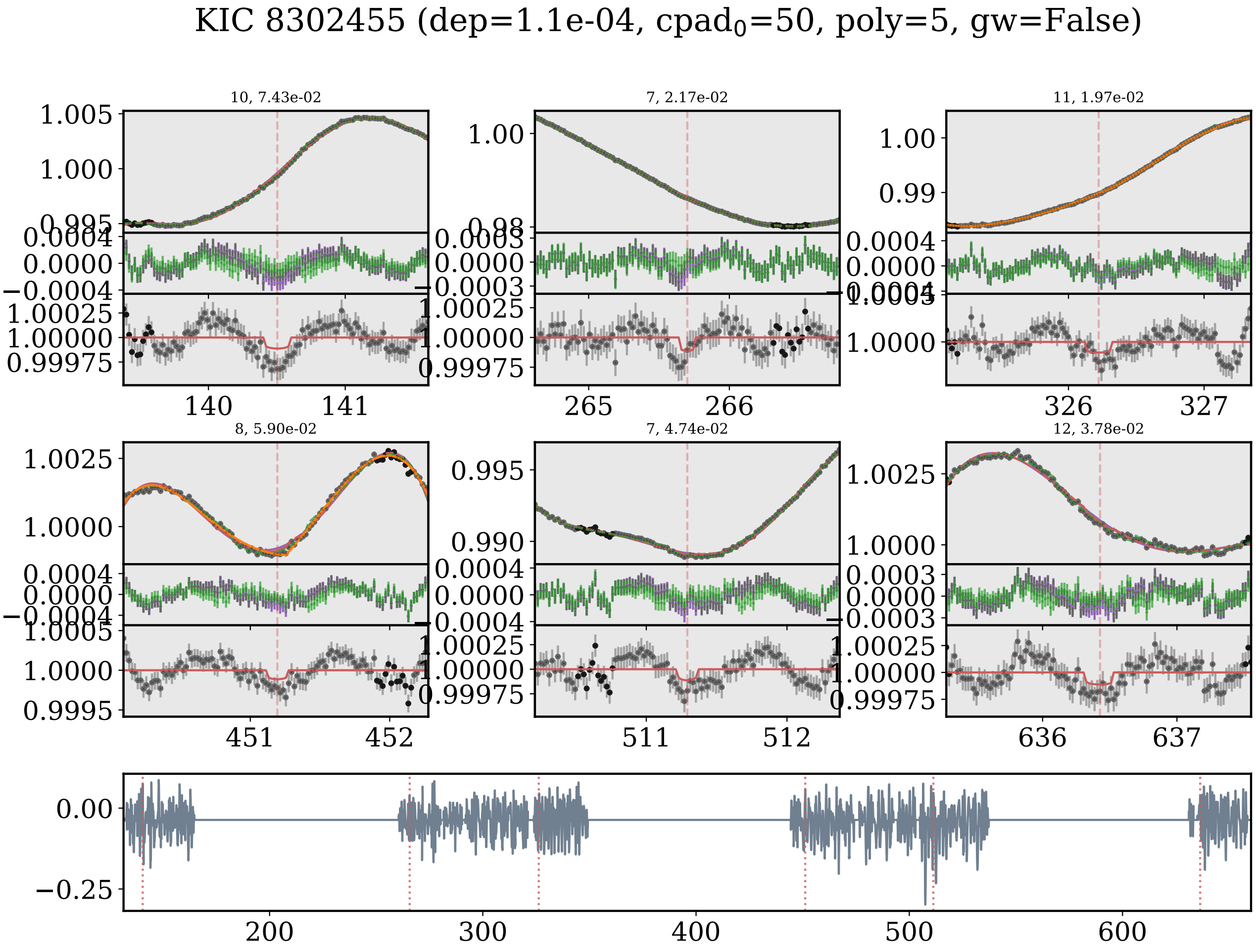

Figure B.36 QATS-EB detection and diagnostic plots for KIC 8302455, in the same format as Figure 4.5.

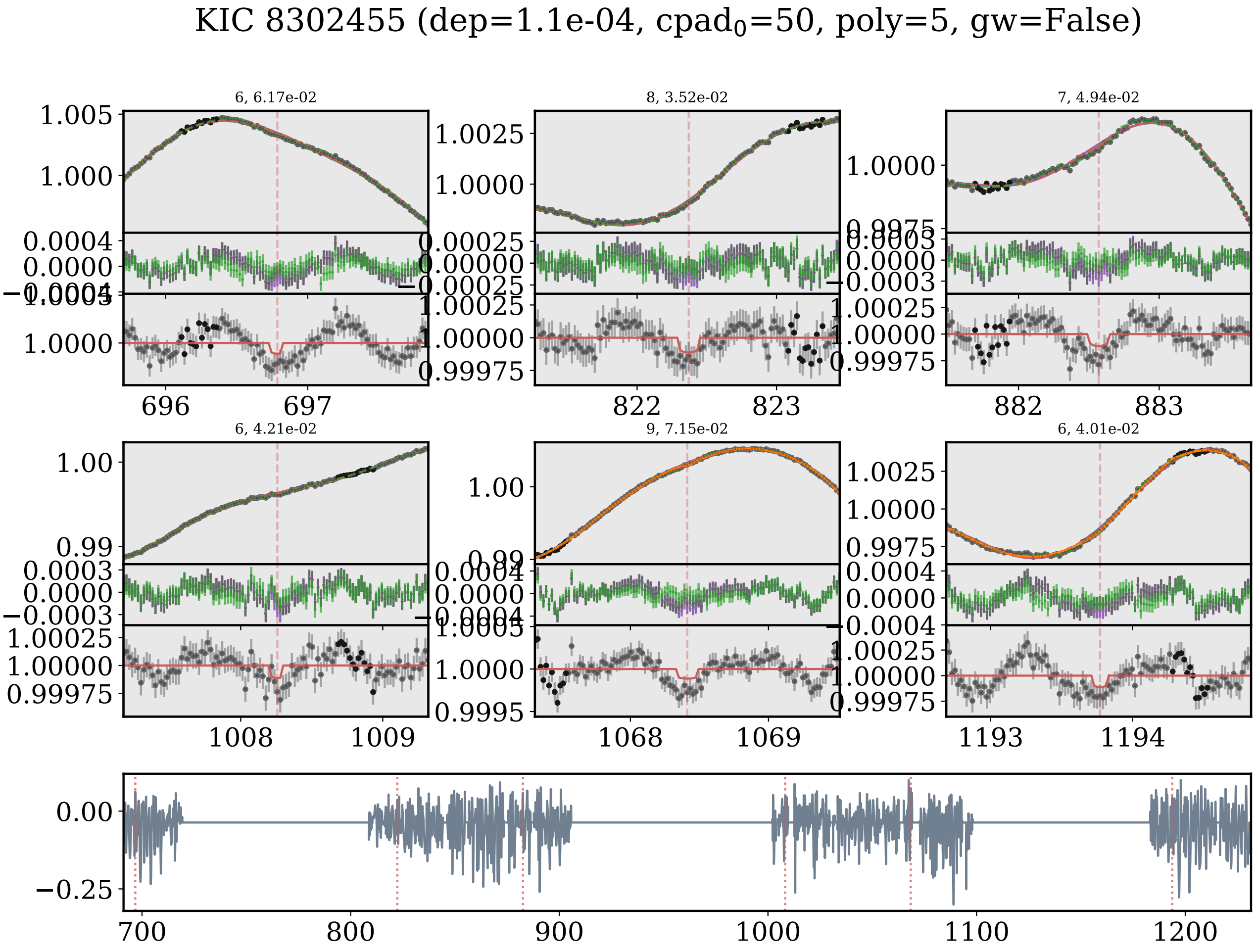

Figure B.37 QATS-EB detection and diagnostic plots for KIC 8302455, in the same format as Figure 4.5.

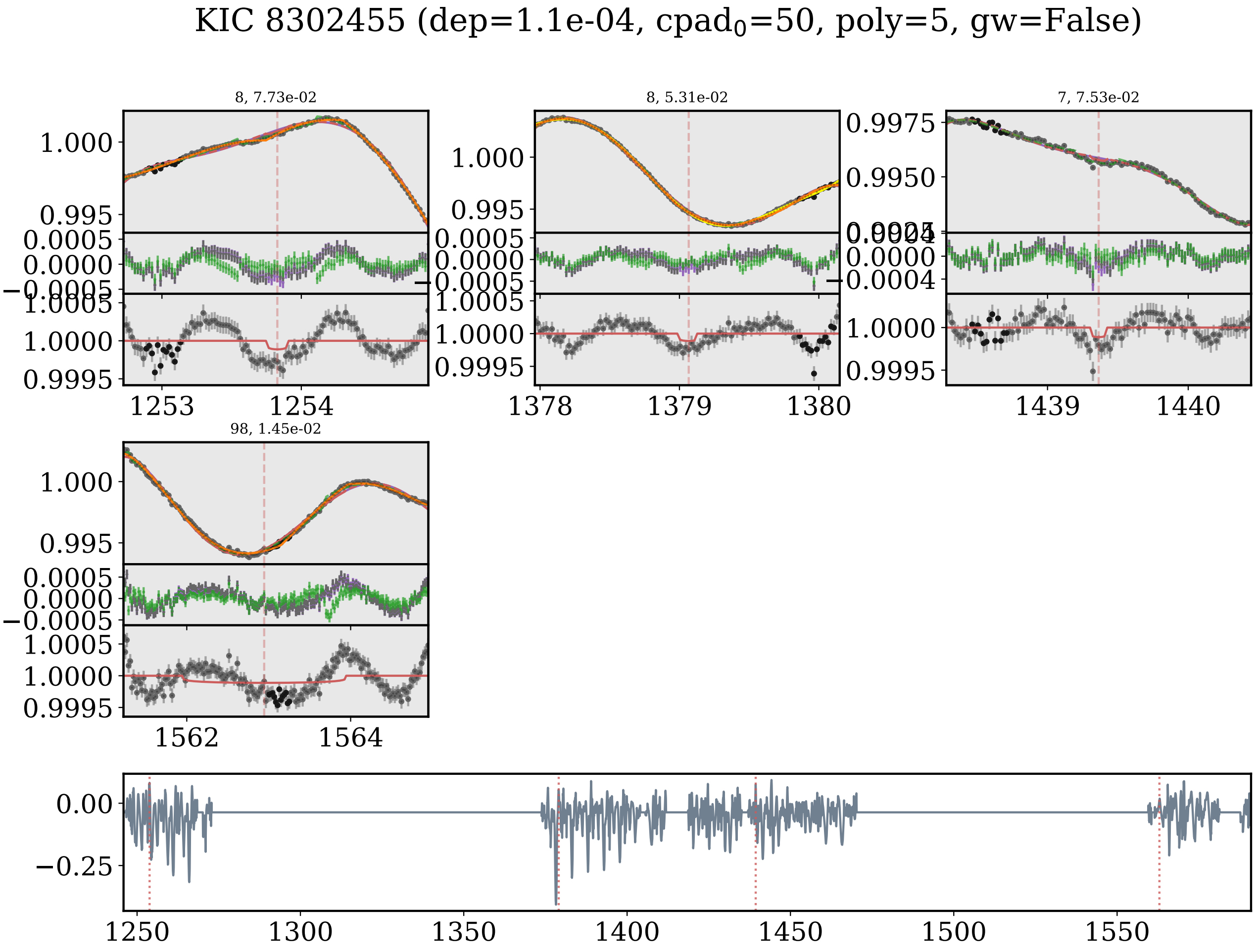

Figure B.38 QATS-EB detection and diagnostic plots for KIC 8302455, in the same format as Figure 4.5.

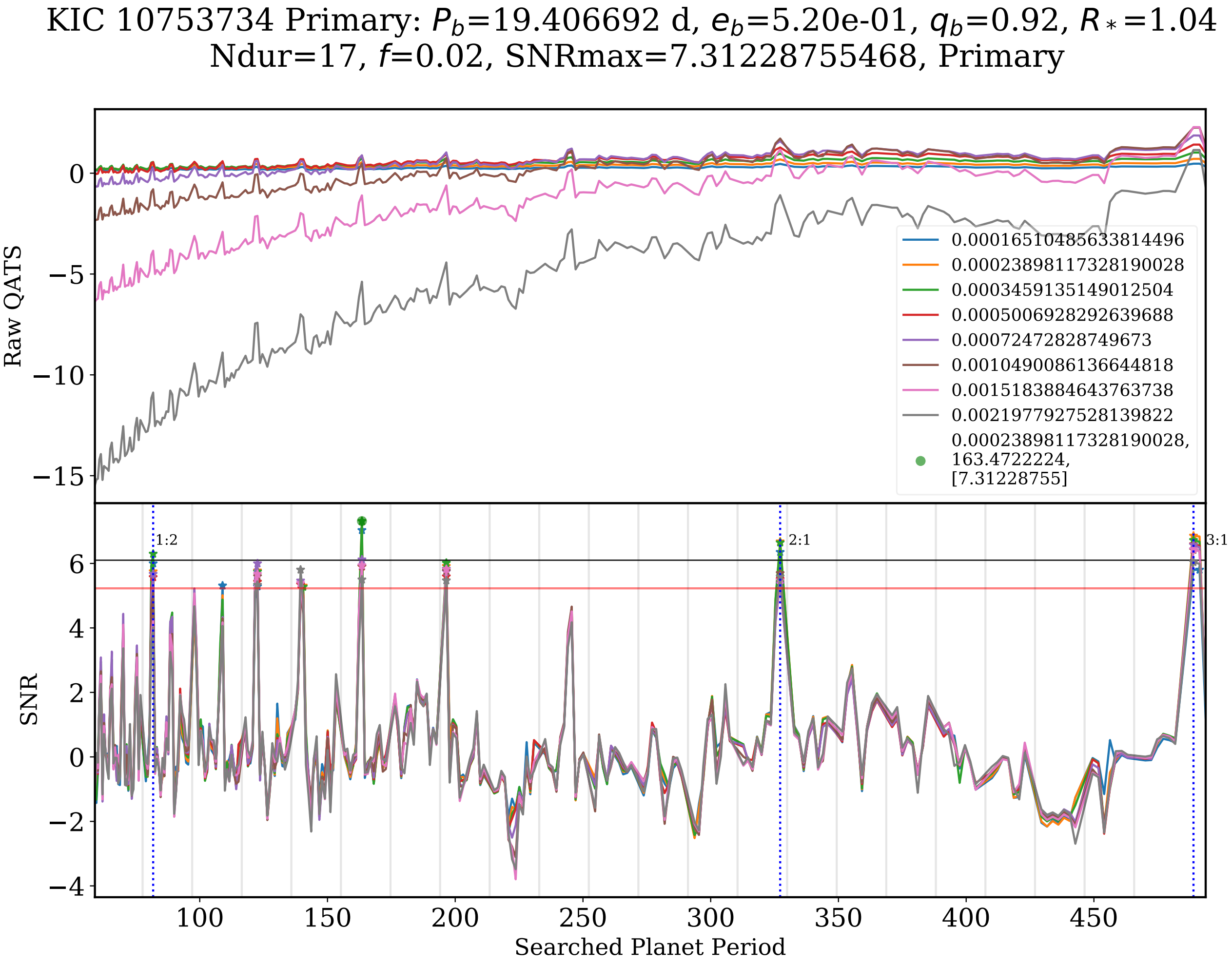

Figure B.39 QATS-EB detection and diagnostic plots for KIC 10753734, in the same format as Figure 4.5.

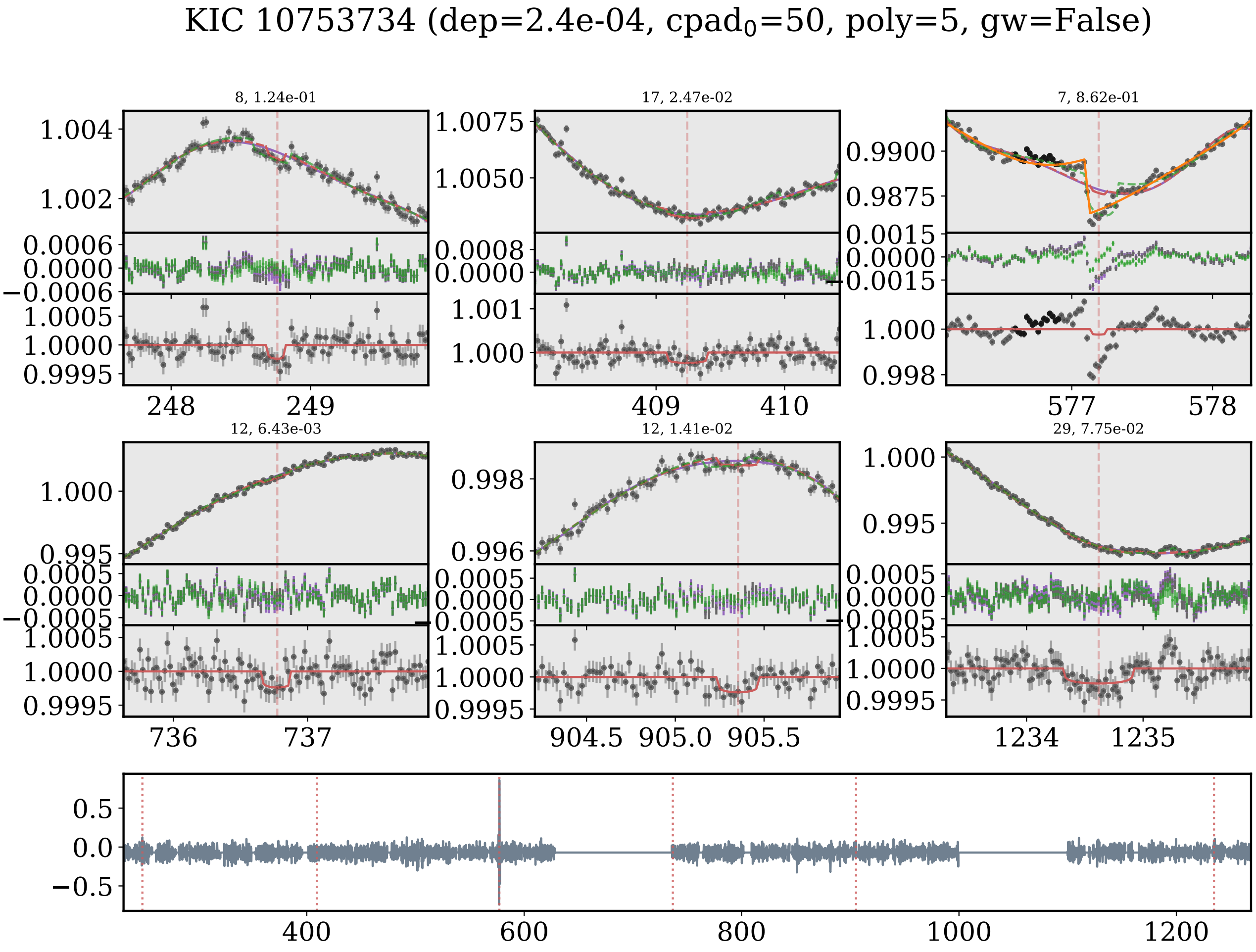

Figure B.40 QATS-EB detection and diagnostic plots for KIC 10753734, in the same format as Figure 4.5.

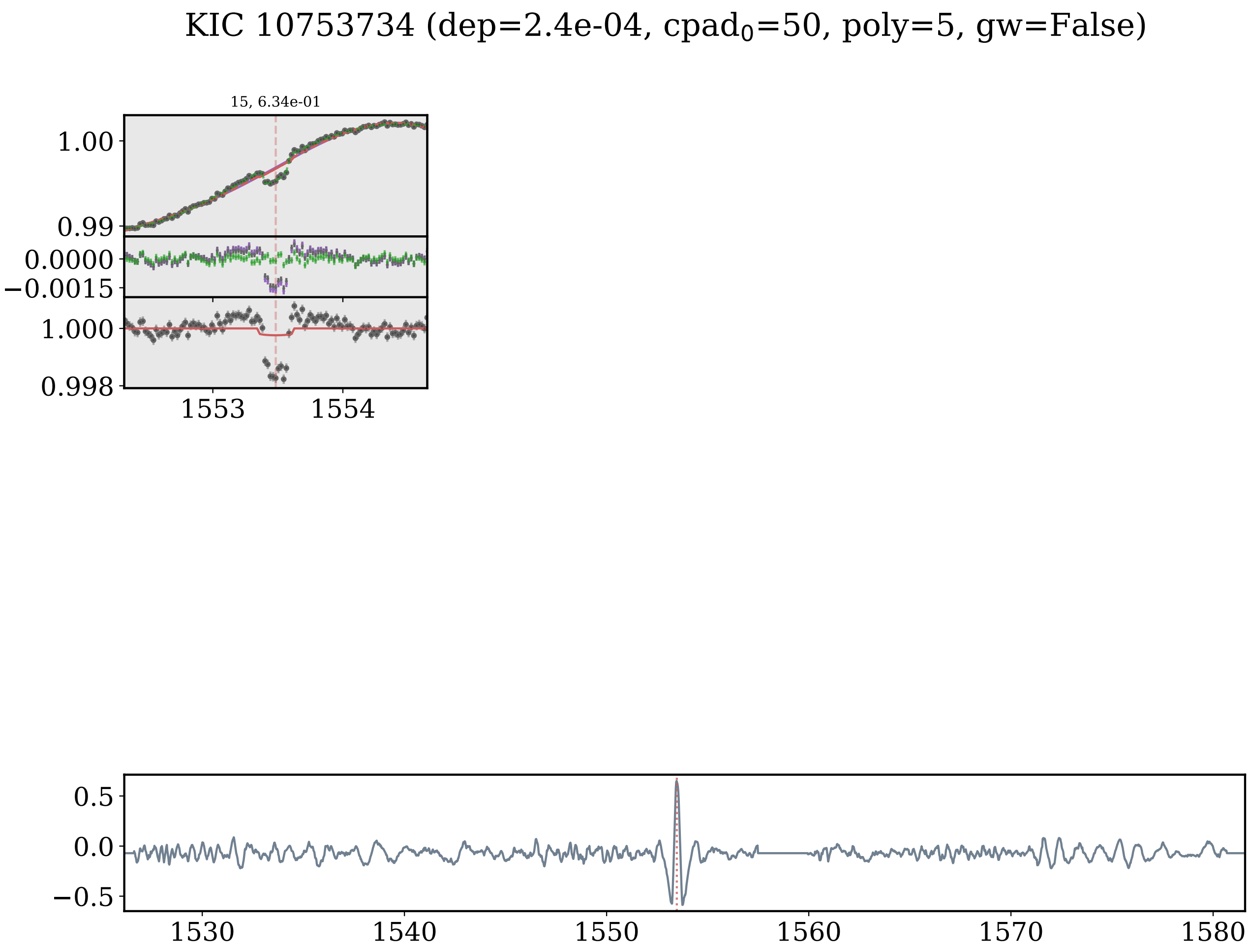

Figure B.41 QATS-EB detection and diagnostic plots for KIC 10753734, in the same format as Figure 4.5.

Appendix C

KIC 3848919, A DOUBLY ECLIPSING BINARY

KIC 3848919 is a known eclipsing binary with $P_b = 1.047$ d. As mentioned in Chapter 4.3.1, I discovered an additional periodic signal close to the known binary period in the search for transiting CBPs. I find the second set of eclipse signals have a period $P_{\rm companion} = 0.92726$ d. Because CBP target search limits the minimum period searched to $\sim 3P_b$ (the critical stability period), the raw QATS detection identified a peak signal at an alias period at ∼4.6 d. Figure C.1 shows a follow-up Lomb-Scargle periodogram analysis on the light curve of KIC 3848919, with the known binary signal at $P_b = 1.047$ d removed. The periodogram has a highly significant peaks at 0.2318 d and 0.4636 d, which are 4:1 and 2:1 aliases of the best-fit period $P_{\rm companion} = 0.92726$ d. The corresponding phased light curve is plotted in the bottom two panels, showing weak (grazing) primary and secondary eclipses.

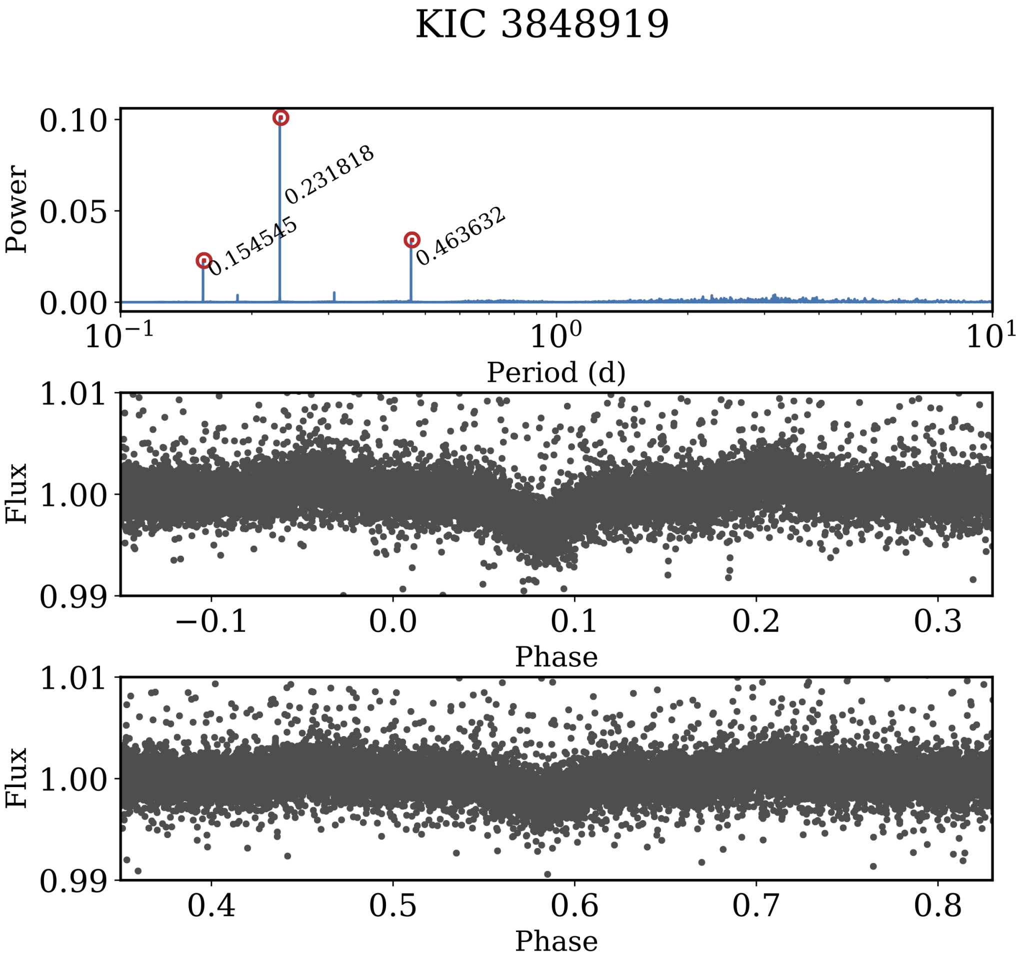

Figure C.1 Top: Lomb-Scargle periodogram on the *Kepler* light curve, with known EB signal at $P_b = 1.047$ d removed, revealing strong power at 4:1 and 2:1 aliases of the best-fit period $P_{\text{companion}} = 0.92726$ d. Middle and Bottom: $P_b = 1.047$ d EB removed light curve phased to $P_{\text{companion}} = 0.92726$ d, which show shallow and V-shaped primary and secondary eclipses indicative of grazing geometry.

Appendix D

PARAMETRIC PRIORS FOR OCCURRENCE RATE DENSITY

Here, we derive a generalized form using a lognormal function as a prior constraint for CBP occurrence rate density distribution $\Gamma = \frac{d^2\eta}{d\ln R_p d\ln(P_p/P_c)}$. Explicitly, we assume the R_p and P_p distributions are independent of each other, such that the joint prior probability on α in bins of R_p and P_p can be expressed as $p(\alpha, R_p, P_p) = p(\alpha, R_p)p(\alpha, P_p)$.

We model the distribution of Γ with respect to $x = \ln R_p, y = \ln(P_p/P_c)$ as a joint log-normal distribution:

$$\Gamma(\boldsymbol{\alpha}) = \Gamma(A, \mu_x, \sigma_x, \mu_y, \sigma_y) = A\exp\left(-\frac{(x-\mu_x)^2}{2\sigma_x^2}\right)\exp\left(-\frac{(y-\mu_y)^2}{2\sigma_y^2}\right) , \tag{D.1}$$

where $\mu_{x,y}$ and $\sigma_{x,y}$ are the mean and standard deviation in x, y, and A is the volumetric normalization constant. The (log-) normal distribution is easy to manipulate analytically, and generic enough that different combinations of μ, σ can approximate other frequently used distributions (given some x, y interval), such as (log-) uniform and power law, with the associated reductions in free parameters. For example, we can approximate a log-uniform distribution by holding constant $\sigma_{x,y}$ at large values and $\mu_{x,y}$ at arbitrary values.

Given that our data is discretized into large bins, the average value of Γ in a bin may differ from Γ evaluated at bin center via Equation D.1. The average value in the jth x, y, or $(\ln R_p, \ln P_p/P_c)$ volume bin is then

$$\begin{aligned}\bar{\Gamma}_j &= \frac{\int_{x_i}^{x_o}\int_{y_i}^{y_o} \Gamma(A, \mu_x, \sigma_x, \mu_y, \sigma_y)dxdy}{(x_o - x_i)(y_o - y_i)} \\ &= \frac{A \text{ erf}\left(\frac{\mu_x - x}{\sqrt{2}\sigma_x}\right)\Big|_{x_i}^{x_o} \text{erf}\left(\frac{\mu_y - y}{\sqrt{2}\sigma_y}\right)\Big|_{y_i}^{y_o}}{4(x_o - x_i)(y_o - y_i)}\end{aligned} \tag{D.2}$$

where the subscripts i and o denote inner and outer bin edge values, and erf is the error function. Thus, the free parameters are effectively reduced from $\mathrm{N_{xbins}} \times \mathrm{N_{ybins}} = \mathrm{J}$ total parameters to those controlling the shape of Γ.

Appendix E

OCCURRENCE RATE TABLES

Table E.1 Occurrence rates for $R_p = 2 - 20R_\oplus; P_p < 35P_c$ “Clean” Sample

	HMc					LMc				
κ	$\eta_{2.5}$	η_{25}	η_{50}	η_{75}	$\eta_{97.5}$	$\eta_{2.5}$	η_{25}	η_{50}	η_{75}	$\eta_{97.5}$
0.1	0.002	0.028	0.069	0.135	0.350	0.278	0.467	0.594	0.743	1.079
1	0.002	0.026	0.062	0.126	0.344	0.267	0.442	0.560	0.698	1.022
3	0.002	0.024	0.059	0.119	0.322	0.209	0.348	0.438	0.547	0.799
10	0.002	0.024	0.060	0.119	0.318	0.135	0.223	0.282	0.351	0.507
30	0.002	0.026	0.063	0.123	0.317	0.097	0.164	0.208	0.258	0.379
100	0.003	0.035	0.083	0.165	0.443	0.080	0.131	0.166	0.206	0.301
300	0.004	0.047	0.114	0.230	0.626	0.074	0.122	0.155	0.193	0.280
700	0.005	0.058	0.136	0.268	0.735	0.076	0.125	0.158	0.197	0.293

Table E.2 Occurrence rates for $R_p = 2 - 20R_\oplus; P_p < 35P_c$ “Dirty” Sample

	HMd					LMd				
κ	$\eta_{2.5}$	η_{25}	η_{50}	η_{75}	$\eta_{97.5}$	$\eta_{2.5}$	η_{25}	η_{50}	η_{75}	$\eta_{97.5}$
0.1	0.024	0.095	0.165	0.263	0.535	0.430	0.657	0.804	0.970	1.346
1	0.022	0.091	0.155	0.251	0.538	0.401	0.621	0.757	0.912	1.285
3	0.021	0.082	0.144	0.232	0.471	0.314	0.481	0.590	0.713	0.989
10	0.022	0.082	0.140	0.220	0.454	0.199	0.306	0.374	0.454	0.629
30	0.022	0.086	0.150	0.241	0.500	0.147	0.226	0.277	0.335	0.467
100	0.029	0.112	0.195	0.310	0.645	0.119	0.183	0.225	0.272	0.382
300	0.039	0.154	0.267	0.429	0.910	0.113	0.173	0.212	0.256	0.357
700	0.047	0.187	0.327	0.524	1.084	0.113	0.173	0.212	0.257	0.361

Table E.3 Occurrence rates for $R_p = 4 - 10R_\oplus; P_p < 35P_c$ “Dirty” Sample

	HMd					LMd				
κ	$\eta_{2.5}$	η_{25}	η_{50}	η_{75}	$\eta_{97.5}$	$\eta_{2.5}$	η_{25}	η_{50}	η_{75}	$\eta_{97.5}$
0.1	0.044	0.173	0.297	0.479	0.976	0.530	0.824	1.015	1.243	1.754
1	0.043	0.167	0.292	0.467	0.970	0.490	0.762	0.944	1.151	1.634
3	0.041	0.163	0.281	0.449	0.931	0.380	0.589	0.728	0.886	1.244
10	0.037	0.150	0.263	0.419	0.860	0.230	0.361	0.448	0.545	0.770
30	0.042	0.166	0.292	0.467	0.956	0.162	0.253	0.312	0.379	0.536
100	0.054	0.209	0.367	0.591	1.210	0.123	0.195	0.243	0.296	0.416
300	0.072	0.284	0.492	0.792	1.610	0.112	0.174	0.216	0.264	0.375
700	0.084	0.334	0.573	0.915	1.902	0.110	0.173	0.214	0.260	0.366

Table E.4 Occurrence rates for $R_p = 4 - 10R_\oplus; P_p < 35P_c$ “Clean” Sample

	HMc					LMc				
κ	$\eta_{2.5}$	η_{25}	η_{50}	η_{75}	$\eta_{97.5}$	$\eta_{2.5}$	η_{25}	η_{50}	η_{75}	$\eta_{97.5}$
0.1	0.005	0.054	0.131	0.259	0.698	0.400	0.656	0.827	1.029	1.492
1	0.004	0.051	0.126	0.245	0.655	0.364	0.612	0.774	0.960	1.406
3	0.004	0.047	0.113	0.228	0.616	0.283	0.470	0.593	0.735	1.074
10	0.004	0.044	0.107	0.214	0.570	0.169	0.285	0.364	0.457	0.666
30	0.005	0.049	0.117	0.240	0.650	0.118	0.199	0.252	0.312	0.453
100	0.006	0.061	0.150	0.299	0.804	0.092	0.153	0.194	0.240	0.348
300	0.008	0.086	0.205	0.400	1.055	0.083	0.141	0.179	0.222	0.319
700	0.008	0.093	0.228	0.460	1.214	0.083	0.138	0.175	0.218	0.318

BIBLIOGRAPHY

Abt, H. A. 1979, AJ, 84, 1591

Agol, E., Steffen, J., Sari, R., & Clarkson, W. 2005, MNRAS, 359, 567

Ahn, C. P., Alexandroff, R., Allende Prieto, C., et al. 2012, ApJS, 203, 21

Angus, R., Morton, T., Aigrain, S., Foreman-Mackey, D., & Rajpaul, V. 2018, MNRAS, 474, 2094

Armstrong, D., Martin, D. V., Brown, G., et al. 2013, MNRAS, 434, 3047

Armstrong, D. J., Gómez Maqueo Chew, Y., Faedi, F., & Pollacco, D. 2014a, MNRAS, 437, 3473

Armstrong, D. J., Osborn, H. P., Brown, D. J. A., et al. 2014b, MNRAS, 444, 1873

Artymowicz, P., & Lubow, S. H. 1994, ApJ, 421, 651

Asensio-Torres, R., Janson, M., Bonavita, M., et al. 2018, A&A, 619, A43

Badenes, C., Mazzola, C., Thompson, T. A., et al. 2018, ApJ, 854, 147

Bailer-Jones, C. A. L., Rybizki, J., Fouesneau, M., Mantelet, G., & Andrae, R. 2018, AJ, 156, 58

Ballard, S., & Johnson, J. A. 2016, ApJ, 816, 66

Bastien, F. A., Stassun, K. G., Basri, G., & Pepper, J. 2013, Nature, 500, 427

Batalha, N. M. 2014, Proceedings of the National Academy of Sciences, 111, 12647

Batalha, N. M., Rowe, J. F., Bryson, S. T., et al. 2013, ApJS, 204, 24

Berger, T. A., Huber, D., Gaidos, E., & van Saders, J. L. 2018, ApJ, 866, 99

Birkby, J., Nefs, B., Hodgkin, S., et al. 2012, MNRAS, 426, 1507

Bolcar, M. R., Aloezos, S., Bly, V. T., et al. 2017, in Society of Photo-Optical Instrumentation Engineers (SPIE) Conference Series, Vol. 10398, Society of Photo-Optical Instrumentation Engineers (SPIE) Conference Series, 1039809

Borkovits, T., Hajdu, T., Sztakovics, J., et al. 2016, Monthly Notices of the Royal Astronomical Society, 455, 4136

Borkovits, T., Rappaport, S., Hajdu, T., & Sztakovics, J. 2015, MNRAS, 448, 946

Borkovits, T., Derekas, A., Fuller, J., et al. 2014, MNRAS, 443, 3068

Bressan, A., Marigo, P., Girardi, L., et al. 2012, MNRAS, 427, 127

Bromley, B. C., & Kenyon, S. J. 2015, ApJ, 806, 98

Brown, T. M., Latham, D. W., Everett, M. E., & Esquerdo, G. A. 2011, AJ, 142, 112

Burke, C. J., & McCullough, P. R. 2014, ApJ, 792, 79

Burke, C. J., Christiansen, J. L., Mullally, F., et al. 2015, ApJ, 809, 8

Carter, J. A., & Agol, E. 2013, ApJ, 765, 132

Cassisi, S. 2017, in European Physical Journal Web of Conferences, Vol. 160, European Physical Journal Web of Conferences, 04002

Castelli, F., & Kurucz, R. L. 2003, in IAU Symposium, Vol. 210, Modelling of Stellar Atmospheres, ed. N. Piskunov, W. W. Weiss, & D. F. Gray, A20

Chabrier, G., Gallardo, J., & Baraffe, I. 2007, A&A, 472, L17

Chatterjee, S., & Tan, J. C. 2014, ApJ, 780, 53

Chavez, C. E., Georgakarakos, N., Prodan, S., et al. 2014, Monthly Notices of the Royal Astronomical Society, Volume 446, Issue 2, p.1283-1292, 446, 1283

Cheetham, A. C., Kraus, A. L., Ireland, M. J., et al. 2015, ApJ, 813, 83

Chen, H., & Rogers, L. A. 2016, ApJ, 831, 180

Chen, J., & Kipping, D. 2017, ApJ, 834, 17

Chen, Y., Girardi, L., Bressan, A., et al. 2014, MNRAS, 444, 2525

Claret, A., & Torres, G. 2018, ApJ, 859, 100

Clark Cunningham, J. M., Rawls, M. L., Windemuth, D., et al. 2019, AJ, 158, 106

Cockell, C. S., Bush, T., Bryce, C., et al. 2016, Astrobiology, 16, 89

Conroy, K. E., Prša, A., Stassun, K. G., et al. 2014, AJ, 147, 45

Cruz, P., Diaz, M., Birkby, J., et al. 2018, MNRAS, 476, 5253

Cuello, N., & Giuppone, C. A. 2019, A&A, 628, A119

Cukier, W., Kopparapu, R. k., Kane, S. R., et al. 2019, PASP, 131, 124402

Cuntz, M., & M. 2014, The Astrophysical Journal, Volume 798, Issue 2, article id. 101, 17 pp. (2015)., 798, 1409.3796

Cutri, R. M., & et al. 2014, VizieR Online Data Catalog, II/328

Czekala, I., Chiang, E., Andrews, S. M., et al. 2019, ApJ, 883, 22

Davenport, J. R. A. 2016, ApJ, 829, 23

Davenport, J. R. A., Hawley, S. L., Hebb, L., et al. 2014, ApJ, 797, 122

Dawson, R. I. 2014, ApJ, 790, L31

Deacon, N. R., Kraus, A. L., Mann, A. W., et al. 2016, MNRAS, 455, 4212

Deeg, H. J., Doyle, L. R., Kozhevnikov, V. P., et al. 1998, A&A, 338, 479

del Burgo, C., & Allende Prieto, C. 2018, MNRAS, 479, 1953

Devor, J., Charbonneau, D., O'Donovan, F. T., Mandushev, G., & Torres, G. 2008, AJ, 135, 850

Doolin, S., & Blundell, K. M. 2011, MNRAS, 418, 2656

Dotter, A. 2016, ApJS, 222, 8

Doyle, L. R., Jenkins, J. M., Deeg, H. J., et al. 1995, in American Astronomical Society Meeting Abstracts, Vol. 187, American Astronomical Society Meeting Abstracts, 70.18

Doyle, L. R., Carter, J. A., Fabrycky, D. C., et al. 2011, Science, 333, 1602

Dressing, C. D., Adams, E. R., Dupree, A. K., Kulesa, C., & McCarthy, D. 2014, AJ, 148, 78

Duane, S., Kennedy, A., Pendleton, B. J., & Roweth, D. 1987, Physics Letters B, 195, 216

Duchêne, G. 2010, ApJ, 709, L114

Duchêne, G., & Kraus, A. 2013, ARA&A, 51, 269

Duquennoy, A., Mayor, M., & Halbwachs, J. L. 1991, A&AS, 88, 281

Eldridge, J. J., Stanway, E. R., Xiao, L., et al. 2017, PASA, 34, e058

Everett, M. E., Howell, S. B., & Kinemuchi, K. 2012, PASP, 124, 316

Fabrycky, D., & Tremaine, S. 2007, ApJ, 669, 1298

Fabrycky, D. C., & Winn, J. N. 2009, ApJ, 696, 1230

Faigler, S., Kull, I., Mazeh, T., et al. 2015, ApJ, 815, 26

Faigler, S., & Mazeh, T. 2011, MNRAS, 415, 3921

Faigler, S., Tal-Or, L., Mazeh, T., Latham, D. W., & Buchhave, L. A. 2013, ApJ, 771, 26

Farago, F., & Laskar, J. 2010, MNRAS, 401, 1189

Fedurco, M., & Parimucha, Š. 2018, Ap&SS, 363, 267

Feiden, G. A., & Chaboyer, B. 2014, ApJ, 789, 53

Fitzpatrick, E. L. 1999, PASP, 111, 63

Fleming, D. P., Barnes, R., Davenport, J. R. A., & Luger, R. 2019, ApJ, 881, 88

Fleming, D. P., Barnes, R., Graham, D. E., Luger, R., & Quinn, T. R. 2018, ApJ, 858, 86

Foreman-Mackey, D., Hogg, D. W., Lang, D., & Goodman, J. 2013, PASP, 125, 306

Foreman-Mackey, D., Hogg, D. W., & Morton, T. D. 2014, ApJ, 795, 64

Foreman-Mackey, D., Morton, T. D., Hogg, D. W., Agol, E., & Schölkopf, B. 2016, AJ, 152, 206

Forgan, D. H., & Duncan. 2016, Monthly Notices of the Royal Astronomical Society, Volume 463, Issue 3, p.2768-2780, 463, 2768

Fulton, B. J., Petigura, E. A., Howard, A. W., et al. 2017, AJ, 154, 109

Furlan, E., Ciardi, D. R., Everett, M. E., et al. 2017, AJ, 153, 71

Gaulme, P., McKeever, J., Jackiewicz, J., et al. 2016, ApJ, 832, 121

Gazeas, K. D., & Niarchos, P. G. 2006, MNRAS, 370, L29

Gies, D. R., Williams, S. J., Matson, R. A., et al. 2012, AJ, 143, 137

Giles, H. A. C., Collier Cameron, A., & Haywood, R. D. 2017, MNRAS, 472, 1618

Gilliland, R. L., Chaplin, W. J., Jenkins, J. M., Ramsey, L. W., & Smith, J. C. 2015, AJ, 150, 133

Ginzburg, S., Schlichting, H. E., & Sari, R. 2018, MNRAS, 476, 759

Gong, Y.-X., & Ji, J. 2017, AJ, 154, 179

Gong, Y.-X., & Yan-Xiang. 2016, The Astrophysical Journal, 834, 55

Guo, Z., Gies, D. R., Matson, R. A., & García Hernández, A. 2016, ApJ, 826, 69

Guo, Z., Gies, D. R., Matson, R. A., et al. 2017, ApJ, 837, 114

Hadden, S., & Lithwick, Y. 2014, ApJ, 787, 80

Haghighipour, N., & Kaltenegger, L. 2013, The Astrophysical Journal, Volume 777, Issue 2, article id. 166, 13 pp. (2013)., 777, arXiv:1306.2890

Hajdu, T., Borkovits, T., Forgács-Dajka, E., et al. 2017, Monthly Notices of the Royal Astronomical Society, 471, 1230–1245

Halbwachs, J. L., Boffin, H. M. J., Le Bouquin, J. B., et al. 2016, MNRAS, 455, 3303

Hamers, A. S., Perets, H. B., & Portegies Zwart, S. F. 2016, MNRAS, 455, 3180

Han, E., Muirhead, P. S., & Swift, J. J. 2019, AJ, 158, 111

Han, E., Muirhead, P. S., Swift, J. J., et al. 2017, AJ, 154, 100

Haqq-Misra, J., Wolf, E. T., Welsh, W. F., et al. 2019, Journal of Geophysical Research (Planets), 124, 3231

Harris, R. J., Andrews, S. M., Wilner, D. J., & Kraus, A. L. 2012, ApJ, 751, 115

Hauschildt, P. H., Allard, F., & Baron, E. 1999, ApJ, 512, 377

Hełminiak, K. G., Ukita, N., Kambe, E., et al. 2017, MNRAS, 468, 1726

Herbst, W., LeDuc, K., Hamilton, C. M., et al. 2010, AJ, 140, 2025

Hinse, T. C., Haghighipour, N., Kostov, V. B., & Goździewski, K. 2015, ApJ, 799, 88

Hintze, J. L., & Nelson, R. D. 1998, The American Statistician, 52, 181

Hirsch, L. A., Ciardi, D. R., Howard, A. W., et al. 2017, AJ, 153, 117

Hodgson, R., Bailey, D., Naylor, M., Ng, A., & McNeill, S. 1985, Image and Vision Computing, 3, 3

Hogg, D. W., Bovy, J., & Lang, D. 2010, arXiv e-prints, arXiv:1008.4686

Holman, M. J., & Wiegert, P. A. 1999, AJ, 117, 621

Holman, M. J., Fabrycky, D. C., Ragozzine, D., et al. 2010, Science, 330, 51

Horch, E. P., Howell, S. B., Everett, M. E., & Ciardi, D. R. 2014, ApJ, 795, 60

Hsu, D. C., Ford, E. B., Ragozzine, D., & Ashby, K. 2019, AJ, arXiv:1902.01417

Huang, S.-S. 1960, PASP, 72, 106

Hut, P. 1981, A&A, 99, 126

Ibanoğlu, C., Soydugan, F., Soydugan, E., & Dervişoğlu, A. 2006, MNRAS, 373, 435

Izzard, R. G., & Halabi, G. M. 2018, arXiv e-prints, arXiv:1808.06883

Jaime, L. G., Aguilar, L., & Pichardo, B. 2014, Monthly Notices of the Royal Astronomical Society, 443, 260

Jenkins, J. M., Doyle, L. R., & Cullers, D. K. 1996, Icarus, 119, 244

Jin, S., Mordasini, C., Parmentier, V., et al. 2014, ApJ, 795, 65

Johnstone, C. P., Pilat-Lohinger, E., Lüftinger, T., Güdel, M., & Stökl, A. 2019, A&A, 626, A22

Jontof-Hutter, D., Ford, E. B., Rowe, J. F., et al. 2016, The Astrophysical Journal, 820, 39

Jørgensen, B. R., & Lindegren, L. 2005, A&A, 436, 127

Kane, S. R., & Hinkel, N. R. 2013, ApJ, 762, 7

Kasting, J. F., Whitmire, D. P., & Reynolds, R. T. 1993, Icarus, 101, 108

Kennedy, G. M., & Wyatt, M. C. 2012, MNRAS, 426, 91

Kennedy, G. M., Matrà, L., Facchini, S., et al. 2019, Nature Astronomy, 3, 230

Kesseli, A. Y., Muirhead, P. S., Mann, A. W., & Mace, G. 2018, AJ, 155, 225

Kiefer, F., Halbwachs, J. L., Arenou, F., et al. 2016, MNRAS, 458, 3272

Kiefer, F., Halbwachs, J. L., Lebreton, Y., et al. 2018, MNRAS, 474, 731

Kipping, D. M. 2010, MNRAS, 408, 1758

—. 2013, MNRAS, 435, 2152

Kirk, B., Conroy, K., Prša, A., et al. 2016, AJ, 151, 68

Kjurkchieva, D., Vasileva, D., & Atanasova, T. 2017, AJ, 154, 105

Kjurkchieva, D., Vasileva, D., & Dimitrov, D. 2016, AJ, 152, 189

Klagyivik, P., Deeg, H. J., Cabrera, J., Csizmadia, S., & Almenara, J. M. 2017, A&A, 602, A117

Kley, W., & Haghighipour, N. 2014, Astronomy & Astrophysics, 564, A72

Kley, W., & Haghighipour, N. 2015, A&A, 581, A20

Kley, W., Thun, D., & Penzlin, A. B. T. 2019, A&A, 627, A91

Kopparapu, R., Ramirez, R., Kasting, J. F., et al. 2013, The Astrophysical Journal, Volume 765, Issue 2, article id. 131, 16 pp. (2013)., 765, arXiv:1301.6674

Kostov, V. B., McCullough, P. R., Hinse, T. C., et al. 2013, ApJ, 770, 52

Kostov, V. B., McCullough, P. R., Carter, J. A., et al. 2014, ApJ, 784, 14

Kostov, V. B., Orosz, J. A., Welsh, W. F., et al. 2016, ApJ, 827, 86

Kostov, V. B., Orosz, J. A., Feinstein, A. D., et al. 2020, AJ, 159, 253

Kovács, G., Zucker, S., & Mazeh, T. 2002, A&A, 391, 369

Kraus, A. L., Ireland, M. J., Hillenbrand, L. A., & Martinache, F. 2012, ApJ, 745, 19

Kraus, A. L., Ireland, M. J., Huber, D., Mann, A. W., & Dupuy, T. J. 2016, AJ, 152, 8

Kraus, A. L., Tucker, R. A., Thompson, M. I., Craine, E. R., & Hillenbrand, L. A. 2011, ApJ, 728, 48

Kruse, E., & Agol, E. 2014, Science, 344, 275

Kruse, E., Agol, E., Luger, R., & Foreman-Mackey, D. 2019, ApJS, 244, 11

Larwood, J. D., & Papaloizou, J. C. B. 1997, Monthly Notices of the Royal Astronomical Society, 285, 288–302

Lee, E. J., & Chiang, E. 2016, ApJ, 817, 90

Lehmann, H., Zechmeister, M., Dreizler, S., Schuh, S., & Kanzler, R. 2012, A&A, 541, A105

Li, G., Holman, M. J., & Tao, M. 2016, ApJ, 831, 96

Lines, S., Leinhardt, Z. M., Paardekooper, S., Baruteau, C., & Thebault, P. 2014, ApJ, 782, L11

Liu, S.-F., Hori, Y., Lin, D. N. C., & Asphaug, E. 2015, ApJ, 812, 164

Lopez, E. D., & Fortney, J. J. 2014, ApJ, 792, 1

Lopez, E. D., & Rice, K. 2018, MNRAS, 479, 5303

Lurie, J. C., Vyhmeister, K., Hawley, S. L., et al. 2017, AJ, 154, 250

Ma, C.-T., Gong, Y.-X., Wu, X.-M., & Ji, J. 2020, MNRAS, 493, 1907

Majewski, S. R., Schiavon, R. P., Frinchaboy, P. M., et al. 2017, AJ, 154, 94

Mandel, K., & Agol, E. 2002, ApJ, 580, L171

Martin, D. V. 2017, MNRAS, 465, 3235

—. 2018, Populations of Planets in Multiple Star Systems, 156

—. 2019, MNRAS, 488, 3482

Martin, D. V., Mazeh, T., & Fabrycky, D. C. 2015, MNRAS, 453, 3554

Martin, D. V., & Triaud, A. H. M. J. 2014, A&A, 570, A91

—. 2015, MNRAS, 449, 781

—. 2016, MNRAS, 455, L46

Martin, D. V., Triaud, A. H. M. J., Udry, S., et al. 2019, A&A, 624, A68

Martin, R. G., Armitage, P. J., & Alexand er, R. D. 2013, ApJ, 773, 74

Martin, R. G., & Lubow, S. H. 2018, MNRAS, 479, 1297

Marzari, F., & Scholl, H. 2000, ApJ, 543, 328

Mason, P. a., Zuluaga, J. I., Clark, J. M., & Cuartas-Restrepo, P. a. 2013, ApJ, 774, L26

Mason, P. A., Zuluaga, J. I., Cuartas-Restrepo, P. A., & Clark, J. M. 2014, arXiv:1408.5163

Mathur, S., Huber, D., Batalha, N. M., et al. 2017, ApJS, 229, 30

Matijevič, G., Prša, A., Orosz, J. A., et al. 2012, AJ, 143, 123

Matson, R. A., Gies, D. R., Guo, Z., & Williams, S. J. 2017, AJ, 154, 216

May, E. M., & Rauscher, E. 2016, The Astrophysical Journal, 826, 225

Mayor, M., Marmier, M., Lovis, C., et al. 2011, arXiv e-prints, arXiv:1109.2497

Meschiari, S. 2012, ApJ, 761, L7

Moe, M., & Di Stefano, R. 2017, ApJS, 230, 15

Mohanty, S., & Basri, G. 2003, ApJ, 583, 451

Moré, J. J. 1978, The Levenberg-Marquardt algorithm: Implementation and theory, Vol. 630, 105–116

Moriwaki, K., & Nakagawa, Y. 2004, ApJ, 609, 1065

Morton, T. D. 2012, ApJ, 761, 6

Muñoz, D. J., & Lai, D. 2015, Proceedings of the National Academy of Science, 112, 9264

Mullally, F., Coughlin, J. L., Thompson, S. E., et al. 2016, PASP, 128, 074502

Neal, R. M. 2012, MCMC using Hamiltonian dynamics, arXiv:1206.1901

Newville, M., Stensitzki, T., Allen, D. B., & Ingargiola, A. 2014, LMFIT: Non-Linear Least-Square Minimization and Curve-Fitting for Python, doi:10.5281/zenodo.11813

Ngo, H., Knutson, H. A., Hinkley, S., et al. 2016, ApJ, 827, 8

North, T. S. H., Chaplin, W. J., Gilliland , R. L., et al. 2017, MNRAS, 465, 1308

Ofir, A. 2008, MNRAS, 387, 1597

Orosz, J. A. 2015, Astronomical Society of the Pacific Conference Series, Vol. 496, Triple Stars Observed by Kepler, ed. S. M. Rucinski, G. Torres, & M. Zejda, 55

Orosz, J. A., & Hauschildt, P. H. 2000, A&A, 364, 265

Orosz, J. A., Welsh, W. F., Carter, J. A., et al. 2012a, Science, 337, 1511

—. 2012b, ApJ, 758, 87

Orosz, J. A., Welsh, W. F., Short, D. R., et al. 2016, in American Astronomical Society Meeting Abstracts, Vol. 228, American Astronomical Society Meeting Abstracts #228, 316.07

Orosz, J. A., Welsh, W. F., Haghighipour, N., et al. 2019, AJ, 157, 174

Owen, J. E., & Wu, Y. 2013, ApJ, 775, 105

Paardekooper, S.-J., Leinhardt, Z. M., Thébault, P., & Baruteau, C. 2012, ApJ, 754, L16

Papaloizou, J. C. B., Nelson, R. P., & Masset, F. 2001, A&A, 366, 263

Petigura, E. A., Howard, A. W., & Marcy, G. W. 2013, Proceedings of the National Academy of Science, 110, 19273

Pierens, A., McNally, C. P., & Nelson, R. P. 2020, MNRAS, arXiv:2005.14693

Pierens, A., & Nelson, R. P. 2007, A&A, 472, 993

—. 2008, A&A, 483, 633

—. 2013, A&A, 556, A134

—. 2018, MNRAS, 477, 2547

Pierrehumbert, R. T. 2013, Nature Geoscience, 6, 81

Popova, E. A., & Shevchenko, I. I. 2013, ApJ, 769, 152

Popp, M., Eggl, S., Lindner, V., Kasting, J. F., & Clough, S. A. 2017, Nature Communications, 8, 14957

Price-Whelan, A. M., & Goodman, J. 2018, ApJ, 867, 5

Prša, A., Batalha, N., Slawson, R. W., et al. 2011, AJ, 141, 83

Prša, A., Conroy, K. E., Horvat, M., et al. 2016, ApJS, 227, 29

Quarles, B., Musielak, Z. E., & Cuntz, M. 2012, The Astrophysical Journal, 750, 14

Quarles, B., Satyal, S., Kostov, V., Kaib, N., & Haghighipour, N. 2018, ApJ, 856, 150

Rabl, G., & Dvorak, R. 1988, A&A, 191, 385

Rafikov, R. R. 2013, ApJ, 764, L16

Raghavan, D., McAlister, H. A., Henry, T. J., et al. 2010, ApJS, 190, 1

Rappaport, S., Deck, K., Levine, A., et al. 2013, ApJ, 768, 33

Rein, H., & Liu, S. F. 2012, A&A, 537, A128

Rogers, L. A. 2015, ApJ, 801, 41

Rucinski, S. M. 2001, AJ, 122, 1007

Schlafly, E. F., & Finkbeiner, D. P. 2011, ApJ, 737, 103

Schneider, J. 1994, Planet. Space Sci., 42, 539

Schwamb, M. E., Orosz, J. A., Carter, J. A., et al. 2013, ApJ, 768, 127

Schwarz, R., Haghighipour, N., Eggl, S., Pilat-Lohinger, E., & Funk, B. 2011, Monthly Notices of the Royal Astronomical Society, 414, 2763

Segura, A., Walkowicz, L. M., Meadows, V., Kasting, J., & Hawley, S. 2010, Astrobiology, 10, 751

Shabram, M., Demory, B.-O., Cisewski, J., Ford, E. B., & Rogers, L. 2016, ApJ, 820, 93

Simonian, G. V. A., Pinsonneault, M. H., & Terndrup, D. M. 2019, The Astrophysical Journal, 871, 174

Skrutskie, M. F., Cutri, R. M., Stiening, R., et al. 2006, AJ, 131, 1163

Skumanich, A. 1972, ApJ, 171, 565

Slawson, R. W., Prša, A., Welsh, W. F., et al. 2011, AJ, 142, 160

Smullen, R. A., Kratter, K. M., & Shannon, A. 2016, MNRAS, 461, 1288

Southworth, J., Maxted, P. F. L., & Smalley, B. 2005, A&A, 429, 645

Stark, C. C., Roberge, A., Mandell, A., & Robinson, T. D. 2014, The Astrophysical Journal, 795, 122

Stark, C. C., Belikov, R., Bolcar, M. R., et al. 2019, The ExoEarth Yield Landscape for Future Direct Imaging Space Telescopes, arXiv:1904.11988

Stassun, K. G., Hebb, L., López-Morales, M., & Prša, A. 2009, in IAU Symposium, Vol. 258, The Ages of Stars, ed. E. E. Mamajek, D. R. Soderblom, & R. F. G. Wyse, 161–170

Stassun, K. G., Kratter, K. M., Scholz, A., & Dupuy, T. J. 2012, ApJ, 756, 47

Stassun, K. G., & Torres, G. 2016, AJ, 152, 180

Steffen, J. H., & Coughlin, J. L. 2016, Proceedings of the National Academy of Sciences of the United States of America, 113, 12023

Sutherland, A. P., & Fabrycky, D. C. 2016, ApJ, 818, 6

Sutherland, A. P., & Kratter, K. M. 2019, MNRAS, 487, 3288

Sybilski, P., Konacki, M., & Kozłowski, S. 2010, Monthly Notices of the Royal Astronomical Society, 405, 657

Tegmark, M., Strauss, M. A., Blanton, M. R., et al. 2004, Phys. Rev. D, 69, 103501

Thompson, S. E., Coughlin, J. L., Hoffman, K., et al. 2018, ApJS, 235, 38

Thun, D., & Kley, W. 2018, A&A, 616, A47

Tilley, M. A., Segura, A., Meadows, V., Hawley, S., & Davenport, J. 2019, Astrobiology, 19, 64

Tingley, B. 2004, in ESA Special Publication, Vol. 538, Stellar Structure and Habitable Planet Finding, ed. F. Favata, S. Aigrain, & A. Wilson, 71–78

Tokovinin, A. 2008, MNRAS, 389, 925

Tokovinin, A., Thomas, S., Sterzik, M., & Udry, S. 2006, A&A, 450, 681

Van Eylen, V., Winn, J. N., & Albrecht, S. 2016, ApJ, 824, 15

Virtanen, P., Gommers, R., Oliphant, T. E., et al. 2020, Nature Methods, 17, 261

Wang, Z., & Cuntz, M. 2019, ApJ, 873, 113

Weiss, L. M., & Marcy, G. W. 2014, ApJ, 783, L6

Welsh, W., Orosz, J., Quarles, B., & Haghighipour, N. 2015a, in AAS/Division for Extreme Solar Systems Abstracts, Vol. 47, AAS/Division for Extreme Solar Systems Abstracts, 402.01

Welsh, W., Orosz, J., & Socia, Q. 2020, in American Astronomical Society Meeting Abstracts, American Astronomical Society Meeting Abstracts, 349.04

Welsh, W. F., Orosz, J. A., Carter, J. A., & Fabrycky, D. C. 2014, in IAU Symposium, Vol. 293, Formation, Detection, and Characterization of Extrasolar Habitable Planets, ed. N. Haghighipour, 125–132

Welsh, W. F., Orosz, J. A., Carter, J. A., et al. 2012, Nature, 481, 475

Welsh, W. F., Orosz, J. A., Short, D. R., et al. 2015b, ApJ, 809, 26

Wilson, R. E., & Devinney, E. J. 1971, ApJ, 166, 605

Windemuth, D., Agol, E., Ali, A., & Kiefer, F. 2019a, MNRAS, 489, 1644

Windemuth, D., Agol, E., Carter, J., et al. 2019b, MNRAS, 490, 1313

Winn, J. N. 2010, Exoplanet Transits and Occultations, ed. S. Seager, 55–77

Winn, J. N., & Fabrycky, D. C. 2015, ARA&A, 53, 409

Wolfgang, A., & Lopez, E. 2015, ApJ, 806, 183

Wolfgang, A., Rogers, L. A., & Ford, E. B. 2016, The Astrophysical Journal, 825, 19

Wyithe, J. S. B., & Wilson, R. E. 2002, ApJ, 571, 293

Yakut, K., & Eggleton, P. P. 2005, ApJ, 629, 1055

Yamanaka, A., & Sasaki, T. 2019, Earth, Planets, and Space, 71, 82

Youdin, A. N. 2011, ApJ, 742, 38

Zahn, J. P., & Bouchet, L. 1989, A&A, 223, 112

Zanazzi, J. J., & Lai, D. 2018, MNRAS, 473, 603

Zasowski, G., Johnson, J. A., Frinchaboy, P. M., et al. 2013, AJ, 146, 81

Zhang, J., Qian, S.-B., & He, J.-D. 2017, Research in Astronomy and Astrophysics, 17, 22

Zhang, Z., & Fabrycky, D. C. 2019, The Astrophysical Journal, 879, 92

Ziegler, C., Law, N. M., Morton, T., et al. 2017, AJ, 153, 66

Zucker, S., & Mazeh, T. 1994, ApJ, 420, 806

Zucker, S., Mazeh, T., & Alexander, T. 2007, ApJ, 670, 1326

Zucker, S., Mazeh, T., Santos, N. C., Udry, S., & Mayor, M. 2003, A&A, 404, 775

Zuluaga, J. I., Mason, P. A., & Cuartas-Restrepo, P. A. 2016, The Astrophysical Journal, 818, 160

VITA

Diana K. Windemuth was born on December 1, 1988 in Changchun, China, and moved to the United States when she was 10. She graduated from Barnard College in 2011 with a Bachelor's in astronomy, minoring in French. She has a M.A. in astronomy from Wesleyan University, and went on to pursue her PhD in astronomy at the University of Washington.